

**Fundamental studies and bioanalytical applications of  
nanostructured-initiator mass spectrometry (NIMS)**

(Spine title: Studies and applications of NIMS)

(Thesis format: Monograph)

By

**Jin Li**

Graduate Program in Chemistry

A thesis submitted in partial fulfillment  
of the requirements for the degree of  
Doctor of Philosophy

Faculty of Graduate Studies  
The University of Western Ontario  
London, Ontario, Canada

© Jin Li 2012

THE UNIVERSITY OF WESTERN ONTARIO  
The School of Graduate and Postdoctoral Studies

**CERTIFICATE OF EXAMINATION**

Supervisor

\_\_\_\_\_  
Dr. Robert H. Lipson

Co-Supervisor

\_\_\_\_\_  
Dr. Yining Huang

Supervisory Committee

\_\_\_\_\_  
Dr. Martin Stillman

Examiners

\_\_\_\_\_  
Dr. Zhifeng Ding

\_\_\_\_\_  
Dr. François Lagurné-Labarthet

\_\_\_\_\_  
Dr. Yujun Shi

\_\_\_\_\_  
Dr. Jin Zhang

The thesis by

**Jin Li**

entitled:

**Fundamental studies and bioanalytical applications of nanostructured-initiator  
mass spectrometry (NIMS)**

is accepted in partial fulfillment of the  
requirements for the degree of  
Doctor of Philosophy

Date \_\_\_\_\_

\_\_\_\_\_  
Chair of the Thesis Examination Board

## Abstract

Nanostructured-Initiator Mass Spectrometry (NIMS), which uses ‘initiator’ molecules trapped within a nanostructured material to assist the release and ionization of intact molecules adsorbed on that material's surface upon laser or ion irradiation, is a new soft desorption/ ionization technique with several positive attributes including extraordinarily high detection sensitivities, relatively simple sample preparation protocols, and can be initiated using photon or ion irradiation sources. As a result NIMS has a great deal of potential for the ready detection of small molecules from complex biofluids including metabolites, and for tissue imaging.

In the thesis, a variety of nanostructured materials including porous silicon (pSi),  $\text{WO}_3$  and  $\text{TiO}_2$  were fabricated with a home-made apparatus as substrates for NIMS. The benefit of pSi-based NIMS using  $\text{BisF}_{17}$  as an initiator over Desorption Ionization On Silicon (DIOS) and Matrix-Assisted Laser Desorption Ionization (MALDI) mass spectrometry (MS) was demonstrated by comparing the signal intensities of protonated polypeptide Dalargin, using the three techniques. A wide range of biological and pharmaceutical compounds were analyzed by NIMS that ionize in different ways to illustrate the versatility of this method.

Secondly, a fluororous-affinity NIMS chip was developed using a fluororous tag containing a 3-(perfluorooctyl)-propyl-1-maleimide moiety, to selectively capture peptides that contain cysteine residues. The fluororous tag was held to the NIMS chip by non-covalent fluorine-fluorine interactions. This methodology was utilized to effectively separate and enrich on-chip cysteine-containing peptides from mixtures, perform kinases (PKA and Abl) activity assays, as well as to quantitatively analyze enzymatic inhibition.

It was shown that fluororous-affinity NIMS chips have the potential to be used as high throughput enzyme inhibitor screening methodology for drug discovery. Fluororous NIMS chips were also shown to be able to measure the enantiomeric excess (ee) of chiral analytes based on kinetic resolution.

An exploration of new micro/nanostructured substrates and laser sources for NIMS was also carried out using microstructured  $\text{WO}_3$  and porous  $\text{TiO}_2$ , and the 532 nm output of a frequency-doubled Nd-YAG laser. It was shown that NIMS mass spectra of peptide (Dalargin) with good intensity could be obtained by these substrates and visible laser source using  $\text{BisF}_{17}$  as an initiator.

Lastly, the Surface-Assisted Laser Desorption Ionization (SALDI) mechanism was investigated by measuring the ion signal,  $I$ , as a function of laser fluence,  $F$ . Evidence is presented that shows that desorption is driven by a thermal process, and desorption activation energies were derived for pSi,  $\text{WO}_3$  and  $\text{TiO}_2$ , respectively. A new ionization mode, Surface Assisted Multiphoton Ionization (SAMPI), is postulated that explains the observation of radical cations and the strong dependence of these ion signals on the position of laser focus relative to the substrate surface. The SAMPI mechanism which appears to be generic for all the porous SALDI substrates studied in this thesis, may prove to be useful for delivering biomolecules into the gas-phase for spectroscopy.

**Keywords:** Nanostructured-Initiator Mass Spectrometry (NIMS), Surface-Assisted Laser Desorption/Ionization (SALDI), Surface-Assisted Multiphoton Ionization (SAMPI), fluororous affinity biochip, enzymatic activity assay, enzyme inhibitor screening, enantiomeric excess analyses, desorption/ionization mechanism, visible-NIMS, porous Si,  $\text{WO}_3$  and  $\text{TiO}_2$ .

**To my wife, Bo Li, our daughter, Ruishan Li, and my family**

## Acknowledgements

I would like to express my sincere gratitude to my supervisor, Professor Robert Lipson, for his guidance, support and encouragement throughout my graduate studies at the University of Western Ontario. I have greatly appreciated his invaluable suggestions, comments and edits on my thesis, as well as his kind consideration on my family unity each year. I am deeply inspired by his patience and passion for research. It has been an honor and a privilege for me to do research under his supervision.

I would also like to extend my heartfelt thanks to my co-supervisor, Professor Yining Huang, for his guidance on my routine work and courses, especially for his precious suggestions for my first year report. Thanks are also extended to Dr. Xiaokun Hu for his nice discussions, MDS-Sciex for generous in-kind donation of the MALDI mass spectrometer, Dr. Stamen S. Dimov for his assistance with the laser instrument, Dr. Todd Simpson for his help in SEM, and Mr. John Vanstone for his help in maintaining and modifying the experimental apparatus. In addition, I am also very grateful to other members of Lipson's group, Dr. Cheng Lu, Dr. Weiping Shi, Dr. Xiujuan Yang, M.Sc. Chunyang Yang and M.Sc. JP. McCool, for their friendship and interesting discussions. Above all, I am deeply indebted to my family in China for their endless love and continuous support in every single moment of my life.

Finally, I would like to extend again my warmest thanks to all who have contributed to this thesis and to all the people who have assisted me during these years.

## Table of Contents

Abstract .....	iii
Dedication .....	v
Acknowledgements .....	vi
Table of Contents .....	vii
List of Figures .....	xi
List of Tables .....	xix
List of Abbreviations .....	xx
Chapter 1: Introduction .....	1
1.1: Background on Surface Assisted Laser Desorption/Ionization (SALDI) .....	1
1.1.1: The development and limitations of MALDI .....	2
1.1.2: The development of DIOS .....	4
1.1.3: Methods for fabricating porous silicon .....	5
1.1.4: Applications of DIOS .....	6
1.2: The overview of Nanostructure-Initiator Mass Spectrometry (NIMS) .....	6
1.2.1: Fundamental characteristics of NIMS .....	6
1.2.2: The applications of NIMS .....	12
1.2.2.1: Complex biofluid analyses .....	12
1.2.2.2: Metabolites analysis .....	14
1.2.2.3: NIMS imaging .....	15
1.3: Immobilization method on chip surface .....	16
1.3.1: Covalent immobilization .....	17
1.3.2: Non-covalent immobilization .....	17
1.4: Fluorous affinity techniques .....	19
1.4.1: The fundamental features of fluorous chemistry .....	19
1.4.2: The application of fluorous tags on chemical biology .....	21
1.5: The goals of the thesis .....	22
Chapter 2: Experimental .....	26
2.1: Materials and Chemicals .....	26
2.2: Instrumentation .....	30

2.2.1: The set-up for preparation of pSi .....	30
2.2.2: Mass spectrometer .....	30
2.2.3: Laser equipment.....	33
2.2.4: Other pieces of equipment .....	34
2.3: Experimental methods .....	35
2.3.1: Preparation of a fluorous-affinity NIMS chip.....	35
2.3.2: NIMS MS experimental procedure.....	39
2.3.3: Enrichment of cysteine-containing peptides.....	41
2.3.4: Enzyme activity assay.....	44
2.3.5: Measurement of enantiomeric excess by kinetic resolution and NIMS ..	44
2.3.6: Methodology to fabricate WO <sub>3</sub> and TiO <sub>2</sub> substrates.....	45
Chapter 3: Optimization and characterization of NIMS .....	46
3.1: Optimized conditions for preparing NIMS chip.....	46
3.1.1: Effect of etching time on the NIMS performance .....	47
3.1.2: Effect of current density on the NIMS performance .....	50
3.1.3: Effect of etching solution and pre-etching cleaning on the NIMS performance .....	50
3.2: Characterization of NIMS.....	57
3.2.1: SEM imaging of the NIMS chips .....	57
3.2.2: Comparison of MALDI, DIOS and NIMS .....	57
3.2.3: The effect of sample storage time.....	60
3.3: Analyses of small molecule drugs and peptides using NIMS.....	65
3.3.1: NIMS spectra of molecules that form radical cations.....	65
3.3.2: NIMS spectra of molecules that form protonated cations .....	71
3.3.3: NIMS spectra of molecules that form cationized adducts .....	73
Chapter 4: On-chip enrichment and analysis of peptide subsets using maleimide- functionalized fluorous affinity biochip and NIMS .....	77
4.1: Background.....	77
4.2: Results and discussions.....	79
4.2.1: Characterization of the binding reaction and washing conditions .....	82
4.2.2: Comparison of the NIMS mass spectra without fluorous affinity tags,	



before washing and after washing.....	84
4.2.3: Enrichment of a cysteine-containing peptide residue from a BSA digest.....	86
4.2.4: Compatibility of fluoruous-affinity enrichment methodology with MS/MS sequencing.....	89
Chapter 5: Label-free kinase activity assay and inhibitor screening using a fluoruous- affinity NIMS chip .....	93
5.1: Background.....	93
5.2: Results and discussion .....	98
5.2.1: Enzymatic activity assay of PKA with fluoruous-affinity NIMS chip ....	100
5.2.2: NIMS chips for multiple kinase activity assays.....	104
5.2.3: Quantitative analysis of enzyme inhibition by product/substrate ratio measurements.....	106
5.2.4: A potential platform for enzyme inhibitor screening .....	113
Chapter 6: Measurement of enantiomeric excess by kinetic resolution and NIMS.....	117
6.1: Overview.....	117
6.2: Determination of ee based on kinetic resolution and NIMS.....	120
6.3: Results and discussions.....	121
Chapter 7: An exploration of visible-NIMS and NIMS using WO <sub>3</sub> and TiO <sub>2</sub> substrates.....	125
7.1: Visible laser NIMS.....	125
7.1.1: Overview of visible MALDI and SALDI.....	125
7.1.2: Results and Discussion .....	126
7.2: New NIMS substrates: microstructured WO <sub>3</sub> and porous TiO <sub>2</sub> .....	129
7.2.1: WO <sub>3</sub> chip as a NIMS substrate .....	130
7.2.2: TiO <sub>2</sub> chip used for NIMS substrate.....	132
Chapter 8: Mechanisms of laser desorption/ionization by MALDI and NIMS.....	134
8.1: MALDI .....	134
8.1.1: Desorption in MALDI .....	134
8.1.2: Ionization in MALDI .....	137
8.1.2.1: Primary ion formation.....	137

8.1.2.2: Secondary ion formation.....	140
8.1.3: Some key parameters influencing desorption/ionization process .....	143
8.1.3.1: Laser wavelength and matrice absorption.....	143
8.1.3.2: The effect of laser fluence on MALDI ion signal intensity .....	144
8.1.3.3: Sample preparation protocols .....	144
8.2: DIOS .....	145
8.2.1: The desorption process in DIOS .....	145
8.2.2: Ion formation in DIOS .....	147
8.2.2.1 Primary and secondary ionization.....	147
8.2.2.2: Proton source .....	149
8.2.3: Some pSi properties influencing DIOS performance .....	150
8.2.3.1: Porosity and surface structure of the pSi .....	150
8.2.3.2: Chemical properties of pSi surface .....	151
8.2.3.3: Other influencing factors .....	152
8.3: NIMS .....	153
Chapter 9: The SALDI ionization mechanism.....	155
9.1: Introduction.....	155
9.2: Small molecule ionization experiments using a pSi substrate.....	156
9.2.1 Ionization when the output of the laser is focussed at the surface of the pSi chip .....	158
9.2.2: Ionization when the output of the laser is focussed above the surface of the pSi chip .....	158
9.2.3: Improving the ionization efficiency using two lasers .....	163
9.3: Peptide ionization using a pSi substrate .....	168
9.4 Ionization process using different substrates .....	171
9.5: Discussion.....	177
Chapter 10: Conclusions and future work .....	185
10.1: Conclusions.....	185
10.2: Future work.....	189
REFERENCES .....	191
VITA .....	215

## List of Figures

Fig. 1.1: Experimental configuration for a DIOS experiment .....	3
Fig.1.2: Schematic diagram of a typical NIMS analysis.....	8
Fig.1.3: Illustration of some of the main applications of NIMS .....	13
Fig.1.4a) a bifunctional linker covalently immobilized on the chip to form a maleimide-functionalized surface; b) a reaction showing how the treated biochip can be used to capture selectively a compound containing a thiol group by simple Michael addition reaction.....	18
Fig.1.5: Representative examples of noncovalent immobilization used to fabricate SMM chips: a) a schematic showing how libraries of small molecules which are encoded by a specific PNA codon may be captured selectively onto an oligonucleotide micro- array by a hybridization reaction; b) a schematic showing how a small polyfluoro- carbon attaches non-covalently to a fluoroalkylsilane-coated chip surface .....	20
Fig.1.6: Illustration of some main applications of fluorophilic affinity technology: a) a F-PSE column which uses perfluoroalkyl chains as bonded phase instead of a resin to facilitate analyte separation, is employed to enrich and separate specific classes of peptides in fluorophilic proteomics. Firstly it is selectively labelled with a fluorophilic tag and then loaded onto a F-PSE column, followed by washing and collection based on fluorine content; b) a Nimzyme assay process in which enzymatic substrate with fluorophilic tags is immobilized onto NIMS chip surface by fluorophilicity followed by incubation of the surface with the samples to screen for enzymatic activity.....	23
Fig.1.7: Flow chart illustrating the goals of this thesis .....	25
Fig. 2.1: The Teflon cell assembly used for etching Si wafers electrochemically. a) The silicon wafer or chip is placed with its polished side facing the O-ring. A section of conductive copper tape is attached on its backside with a section sticking outside of the assembly; b) The Teflon base is attached to the top half of the assembly with the chip sandwiched between; c) The positive (+) (red) electrode is attached to the silicon wafer chip by clipping a lead to the conductive copper foil while the negative (-) (black) electrode was attached to a platinum wire. ....	31
Fig. 2.2: A schematic of the experimental apparatus used to perform NIMS. The SEM image (lower right) of the pSi substrate shows the typical morphology of the NIMS chip surfaces used in this work (lower left). ....	32
Fig. 2.3: The photo on the left shows a NIMS chip mounted onto the face of an in-house modified MALDI target plate with double-sided adhesive tape. The photo on the right shows the NIMS chip being spotted with analyte solution using a pipette...	40
Fig. 2.4: Schematic diagram of the experimental arrangement used to fabricate a microstructured WO <sub>3</sub> NIMS chip by laser irradiation. ....	44
Fig. 3.1: The chemical structure of the hexapeptide Dalargin .....	47

Fig. 3.2: A plot of the NIMS Dalargin ion signal as a function of pSi chip etching time..	48
Fig. 3.3: A SEM image of pSi chip produced by electrochemical etching for 35 min at a current density = 45mA/cm <sup>2</sup> and using 50% (by volume) hydrofluoric acid ethanol solution. ....	48
Fig. 3.4: NIMS spectra of protonated Dalargin as a function of pSi etching time using BisF <sub>17</sub> as initiator. ....	49
Fig. 3.5: A plot of protonated Dalargin NIMS signal as a function of current density. ....	51
Fig. 3.6: The appearances of pSi etched at a normal electrical potential (< 2.0V; upper picture) and after electropolishing at an overpotential (> 2.0 V; lower picture). ....	52
Fig. 3.7: NIMS spectra of protonated Dalargin as a function of current density using BisF <sub>17</sub> as initiator. ....	53
Fig. 3.8: The NIMS ion intensity (ion counts) of protonated Dalargin as a function of the etching solution volume ratio. ....	54
Fig. 3.9: NIMS spectra obtained from pSi substrates formed using different etching solution volume ratios. ....	55
Fig. 3.10: Comparison of the NIMS spectra of Dalargin using pSi prepared with and without Piranha solution cleaning before electrochemical etching. a) NIMS spectrum of Dalargin obtained using a chip that was not cleaned with Piranha solution; b) NIMS spectrum of Dalargin obtained with a chip that was cleaned with Piranha solution. BisF <sub>17</sub> was used as the initiator in both experiments. ....	56
Fig. 3.11: SEM image of the nanostructured surface of a pSi chip obtained using the experimental conditions listed in the Table 3.1. ....	58
Fig. 3.12: A plot of the S/N ratio of the Dalargin NIMS ion signal versus the number of moles of Dalargin in the sample of the irradiated laser spot. ....	59
Fig. 3.13: a) MALDI mass spectrum of Dalargin using a CHCA matrix (1μL, 1mM); b) DIOS mass spectrum of Dalargin; c) NIMS spectrum of Dalargin using BisF <sub>17</sub> as initiator. Each sample contained the same amount of Dalargin (1μL, 10μM). The same laser energy per pulse (5μJ) was used in each experiments and the mass spectrometer was scanned over the same mass range of 100-800 amu. ....	61
Fig. 3.14: Protonated Dalargin signal intensities obtained by NIMS (initiator, BisF <sub>17</sub> ) and DIOS as a function of pSi storage time in air. Note that 0 days implies a freshly prepared pSi chip. ....	62
Fig. 3.15: NIMS spectra of Dalargin as a function of storage time in air. Note that 0 days indicates a freshly prepared pSi chip. BisF <sub>17</sub> served as the initiator for each run. ....	63
Fig. 3.16: DIOS mass spectra of Dalargin as a function of storage time in air. Note that 0 days indicates a freshly prepared pSi chip ....	64
Fig. 3.17: The chemical structure of Fluorouracil .....	66
Fig. 3.18: NIMS spectrum of Fluorouracil (200 fmol) obtained by using BisF <sub>17</sub> as the initiator and placing the focus of the N <sub>2</sub> laser (337 nm; 10 μJ/pulse) a distance of 0.4 mm above the surface of the pSi chip.....	67

Fig. 3.19: A plot of the S/N ratio of the 5-FU NIMS signal at $m/z$ 130 versus the number of moles of sample within the laser spot.....	67
Fig. 3.20: The chemical structure of Quinidine .....	68
Fig. 3.21: NIMS spectrum of Quinidine (200 fmol) obtained by using BisF <sub>17</sub> as the initiator and placing the focus of the N <sub>2</sub> laser (337 nm; 10 μJ/pulse) a distance of 0.4 mm above the surface of the pSi chip .....	69
Fig. 3.22: A plot of the S/N ratio of the Quinidine NIMS radical cation signal at $m/z$ 324 versus the number of moles of sample with the laser spot.....	69
Fig. 3.23: The chemical structure of Bradykinin .....	70
Fig. 3.24: NIMS mass spectrum of Bradykinin (100 fmol) on a pSi substrate using the BisF <sub>17</sub> initiator and a N <sub>2</sub> laser (337 nm) energy of 5 μJ/pulse .....	71
Fig. 3.25: A plot of the S/N ratio of the Bradykinin NIMS signal ( $m/z$ 1061) versus the number of moles of sample within the laser spot.....	71
Fig. 3.26: The chemical structure of Erythromycin .....	73
Fig. 3.27: The chemical structure of Dexamethasone.....	73
Fig. 3.28: NIMS spectrum of Erythromycin (100 pmol) on a pSi substrate using the BisF <sub>17</sub> initiator and a N <sub>2</sub> laser (337 nm) energy of 5 μJ/pulse .....	74
Fig. 3.29: A plot of the S/N ratio of the Erythromycin NIMS signal ( $m/z$ 757) versus the number of moles of sample within the laser spot.....	74
Fig. 3.30: NIMS spectrum of Dexamethasone (100 pmol) on a pSi substrate coated with BisF <sub>17</sub> initiator and AgNO <sub>3</sub> (5 nmol). The spectrum was obtained using the output of a N <sub>2</sub> laser (337 nm) having an energy of 5 μJ/pulse.....	75
Fig. 3.31: A plot of the S/N ratio of the Dexamethasone NIMS signal ( $m/z$ 499) versus the number of moles of sample in the laser spot.....	76
Fig. 4.1: The chemical structure of fluorine-affinity tag, 3-(perfluorooctyl)-propyl-1-maleimide (RF <sub>17</sub> ) .....	79
Fig. 4.2: Schematic diagram for the methodology: <b>1.</b> a thin film of initiator is coated in the surface of porous Si produced by electrochemical etching; <b>2.</b> a fluorine affinity tag is immobilized on the NIMS chip by fluorine-fluorine interactions; <b>3.</b> a specific peptide is captured by the affinity tag; <b>4.</b> mass analysis by NIMS.....	80
Fig. 4.3: The binding chemical reaction occurring between RF <sub>17</sub> and Pep2 .....	81
Fig. 4.4: The chemical structure of Pep2 (LRRASLGC) .....	81
Fig. 4.5: The effect of temperature on cysteine residue binding efficiency. The square and circle dots show the ion intensities produced by NIMS of Pep2 plus 3-(perfluoroalkyl) propyl-1-maleimide and untagged Pep2, respectively, with different reaction temperature .....	83
Fig. 4.6: The effect of temperature on cysteine residue binding efficiency. The solid and dash lines show the ion intensities produced by NIMS of Pep2 plus 3-(perfluoroalkyl) propyl-1-maleimide and untagged Pep2, respectively, with	

different reaction temperature .....	83
Fig. 4.7: Optimization of the washing solvent composition for cysteine residue enrichment on a fluorous-affinity NIMS chip determined by plotting the ion intensity of the tagged and untagged peptides as a function of the percentage of methanol used .....	84
Fig. 4.8a): NIMS spectrum of the mixture Pep1, Pep2 and Pep3; b): NIMS spectrum of the mixture Pep1, Pep2 and Pep3 which has been incubated with the fluorous-affinity NIMS chip before washing; c): NIMS spectrum of the mixture Pep1, Pep2 and Pep3 which has been incubated with the fluorous-affinity NIMS chip after washing with a 40% methanol water solution containing TFA .....	85
Fig. 4.9: a): NIMS spectrum of a group of residues from a 200 fmol BSA tryptic digest before washing. 4.9b): NIMS spectrum produced at the same condition as 4.9a), but recorded after washing the chip with 40% methanol in water solution containing 0.1% TFA. # corresponds to peptide peaks detected by NIMS not containing cysteine residues; * corresponds to peptide peaks containing cysteine residues; & corresponds to one peptide fragment containing two cysteine residues .....	90
Fig. 4.10: A MS/MS spectrum of fluorous-affinity labeled peptide, C <sup>RF17</sup> ASIQK, produced by CID using [M+H] <sup>+</sup> as precursor. The top shows the complete peptide sequence of Y and B ions which were assigned from mass differences corresponding to the mass of amino acid residues. The graphic in the top right corner exhibits how Y and B ions are cleaved. The a <sub>2</sub> ion, which is obtained by loss CO(28) from a b <sub>2</sub> ion, is often observed as a diagnostic for b <sub>2</sub> . # is an immonium ion peak of fluorous-tagged cysteine residue at m/z = 633 with a structure [H <sub>2</sub> N=CH-C <sup>RF17</sup> ] <sup>+</sup> , where C <sup>RF17</sup> is fluorous-tagged cystenyl. * correspond to ions which have lost water or ammonia .....	92
Fig. 5.1: The crystal structure of protein kinase A (PKA) .....	97
Fig. 5.2: The crystal structure of Abl protein tyrosine kinase (Abl) .....	98
Fig. 5.3: Schematic diagram for NIMS-based assays: 1. A specific class of substrate peptides is captured by fluorous phase interactions with a fluorous affinity tag immobilized on a NIMS chip. 2. An enzyme such as protein kinase A (PKA) is added onto the NIMS chip; 3. A product such as phosphorylated peptide is produced by the enzyme reaction. 4. The substrate and product are detected by NIMS .....	99
Fig. 5.4: a) The mass spectrum of a substrate (Pep2) with fluorous tag before adding the PKA enzyme. b) The mass spectrum after adding PKA. The major peak corresponds to phosphorylated Pep2 resulting from the reaction of the substrate with PKA .....	101
Fig. 5.5: Schematic diagram of phosphorylation reaction under assistance of protein kinase A (PKA), which can catalyse the transfer of ATP terminal phosphate to peptide or protein substrates at serine or threonine residues .....	102
Fig. 5.6: a) Mass spectrum of a mixture of peptides (Pep1, Pep2 and Pep3) obtained using	

a fluororous-affinity NIMS MS chip before adding kinase PKA. b) Mass spectrum of the products formed from the mixture in a) after the addition of PKA and rinse using a 40% methanol water solution .....	103
Fig. 5.7: The chemical structure of Pep4 (IYAAPKKKC) .....	104
Fig. 5.8: NIMS spectra of obtained for the simultaneous measurement of multiple kinase activities. a) the NIMS spectrum of substrate peptides of LRRASLGC (Pep2) for PKA and IYAAPKKKC (Pep4) for Abl. b) the NIMS spectrum obtained after adding PKA. Only Pep2 has been phosphorylated. c) the NIMS spectrum obtained after the addition of Abl. Only Pep4 has been phosphorylated.....	105
Fig. 5.9: Plots of the percent product measured by MALDI-TOF MS using CHCA as matrix versus the indicated molar ratios onto the MALDI target plate demonstrated validation of product/substrate for enzyme ratios served as a quantitative enzyme assay without internal standards. The dashed line represents the theoretical linear relationship if the MS readout matched the molar ratios (i.e., the substrate and product had equal ionization and detection efficiencies) .....	108
Fig. 5.10: Validation of the simple quantitative kinase PKA enzyme assay without internal standards by NIMS detection. In this experiment a standard substrate peptide, LRRASLGC, was used which was phosphorylated by the enzyme to produce the product peptide, LRRAS(p)LGC. The against percent product peptide ion intensity over the intensity sum of substrate and product peptide from NIMS detection in positive ion mode is plotted against the percent number of moles of phosphorylated peptide in the 5 replicates with 200 fmol peptide mixture each.....	110
Fig. 5.11: The chemical structure of the PKA inhibitor staurosporine .....	111
Fig. 5.12: The chemical structure of the Abl inhibitor imatinib .....	111
Fig. 5.13: a) a 10-point dose-dependent inhibition assay curve obtained by plotting the log [Stsp] against degree of enzyme inhibition, %MA. b) a similar assay curve of the Abl inhibitor imatinib. Note that X means the log inhibition concentration..	112
Fig. 5.14: A cartoon of a 2 x 2 NIMS chip array. Dot1 is a control region of the chip where an enzyme and substrate have been added but not an inhibitor. Dot 2 is a region of the NIMS chip where the enzyme, the substrate in Dot 1, and a known inhibitor have been added. Dot 3 corresponds to a region of the NIMS chip where the enzyme, substrate, and potential inhibitor calix[4]arene have been added. Dot 4 corresponds to a region of the NIMS chip where the enzyme, substrate, and potential inhibitor C-methylcalix[4]resorcinarene have been added. Note that the area of each dot is ~3.14 mm <sup>2</sup> , and here the dots are not drawn to scale .....	114
Fig. 5.15: The chemical structure of compound C-Methylcalix[4]resorcinarene.....	115
Fig. 5.16: The chemical structure of compound Calix[4]arene .....	115
Fig. 5.17: The fluororous-affinity NIMS chip was used to perform enzymatic inhibitor screening in 4-dot format. a): NIMS spectrum of phosphorylation of substrate Pep2 for PKA without inhibitor and other compounds (Control); b): NIMS spectrum after adding a known inhibitor, staurosporine; c): NIMS spectrum after	

adding compound A, Calix[4]arene; d): NIMS spectrum after adding compound B, C-Methylcalix[4] resorcinarene .....	116
Fig. 6.1: A scheme showing the reaction of 1-phenylethanol (enantiomers of different ratios or an enantiomerically pure sample) with equivalent fluororous-mass tagged chiral acids .....	119
Fig.6.2: A schematic diagram of the generalized reactions of chiral alcohols with mass-tagged chiral acids in a kinetic resolution process .....	120
Fig.6.3: A typical 337 nm NIMS spectrum of the products from the reaction of pure R-1-phenylethanol with equimolar mixture of pseudoenantiomeric fluororous mass-tagged chiral acylating agents (b) and c)). The initiator used was BisF <sub>17</sub> ..	123
Fig. 6.4: A scheme of 1-phenylethanol (an R configuration enantiomerically pure sample) reacting with equivalent fluororous-mass tagged chiral acids .....	124
Fig. 7.1: Visible NIMS spectrum of Dalargin (2 pmol) using BisF <sub>17</sub> as initiator and the 532 nm output of a Nd-YAG laser operating at a 10 Hz repetition rate .....	127
Fig.7.2: A plot of the S/N ratio of the protonated Dalargin visible-NIMS signal versus the number of moles of Dalargin in the sample .....	128
Fig. 7.3: SEM image of a microstructured WO <sub>3</sub> substrate for NIMS produced by irradiating W foil for 40 minutes in methanol with the 355 nm output of a frequency-tripled Nd-YAG laser at an intensity of ~ 4-5 W/cm <sup>2</sup> , followed by heat activation.....	131
Fig. 7.4: NIMS spectrum of Dalargin (0.5 pmol) from a microstructured WO <sub>3</sub> substrate using BisF <sub>17</sub> as an initiator. The NIMS process was initiated using 337 nm output of a N <sub>2</sub> laser operating at a 10 Hz repetition rate and having an energy of 10 μJ/pulse .....	131
Fig. 7.5: SEM image of porous TiO <sub>2</sub> substrate for NIMS produced by electrochemical etching in 1 M H <sub>3</sub> PO <sub>4</sub> containing 0.5 wt% HF acid. Here the potential was ramped from 0 V to 10 V at a sweep rate of 500 mV/s followed by holding the potential at 10 V for 500 seconds.....	132
Fig. 7.6: NIMS spectrum of Dalargin (1pmol) from a porous TiO <sub>2</sub> substrate using BisF <sub>17</sub> as an initiator. The NIMS process was initiated using the 337 nm output of a N <sub>2</sub> laser operating at a 10 Hz repetition rate and having an energy of 15 μJ/pulse ..	133
Fig. 8.1: Density changes with time during plume expansion in a MALDI process. The inset shows the initial behaviour in which the lower and upper curves represent a typical laser pulse and an average lifetime of matrix excited state, respectively; the dashed line is for a phase explosion while the solid line is for desorption ....	135
Fig. 8.2: Schematic of the pooling and hopping processes involving neighbouring matrix molecules. S <sub>0</sub> is the electronic ground state, S <sub>1</sub> the first singlet excited state, and S <sub>n</sub> an excited state above S <sub>1</sub> .....	138
Fig. 9.1: Chemical structure of caffeine; C <sub>8</sub> H <sub>10</sub> N <sub>4</sub> O <sub>2</sub> ; molar mass = 194.2 gmol <sup>-1</sup> .....	156
Fig. 9.2: DIOS mass spectra of caffeine obtained a) when the incident laser was focussed at the surface of the pSi chip and b) when the laser was focussed above the	



surface of the pSi chip.....	157
Fig. 9.3: Schematic diagram illustrating a) the incident laser focused at the surface of pSi chip and b) the laser focussed above the surface of the pSi chip.....	157
Fig. 9.4: The ln-ln plots of the DIOS signal intensity of the protonated caffeine ion (upper plot) and radical caffeine ion (bottom plot) versus laser fluence when the output of the N <sub>2</sub> laser (337 nm) was focussed at the surface of the pSi substrate.....	159
Fig. 9.5: The DIOS-MS signal intensity of the radical caffeine ion as a function of the distance between the laser focus and the surface of the pSi chip .....	160
Fig.9.6: The ln-ln plots of the DIOS-MS signal intensity of caffeine versus laser fluence for the radical cation (upper plot) and the protonated ion (bottom plot) when the output of the N <sub>2</sub> laser (337 nm) is focussed 0.4 mm above the surface of the pSi substrate .....	161
Fig.9.7: The ln-ln plots of the NIMS signal intensity of caffeine versus laser fluence, for the radical cation (upper plot) and protonated caffeine ion (bottom trace), using BisF <sub>17</sub> as an initiator and placing the focus of incident N <sub>2</sub> laser beam (337 nm) 0.4 mm above the surface of the pSi chip.....	162
Fig.9.8: NIMS spectrum of caffeine obtained using BisF <sub>17</sub> as the initiator and placing the focus of the incident N <sub>2</sub> laser (337 nm) 0.4mm above the surface of the pSi chip.....	163
Fig.9.9: Time delay sequence for a two-laser post-ionization DIOS experiment. The time axis as shown is not drawn to scale .....	165
Fig.9.10: A plot showing the enhancement of the radical caffeine cation signal intensity at <i>m/z</i> 194.2 produced by two-laser DIOS over a DIOS experiment performed with a single laser, as a function of delay time .....	166
Fig.9.11: DIOS spectra of caffeine obtained in a two-laser experiment where a) DIOS was initiated with a N <sub>2</sub> laser (337 nm) while the visible output of a doubled Nd-YAG laser (532nm) was used for post-ionization and b) DIOS was initiated with a double Nd:YAG laser (532 nm) while the UV output of a N <sub>2</sub> laser (337 nm) was used for post-ionization.....	167
Fig.9.12: ln-ln plots of the protonated Dalargin ion intensity formed by DIOS versus laser fluence when a) the focus of N <sub>2</sub> laser (337nm) was placed at the surface of the pSi chip, and b) when the output of the incident N <sub>2</sub> laser (337 nm) was focused 0.4 mm above the surface of the pSi chip.....	169
Fig.9.13: ln-ln plots of the protonated Dalargin NIMS signal intensity versus laser fluence using BisF <sub>17</sub> as an initiator a) when the focus of N <sub>2</sub> laser (337 nm) was placed 0.4 mm above the surface of the pSi chip and b) when the focus of N <sub>2</sub> laser (337 nm) was placed at the surface of the pSi chip .....	170
Fig. 9.14: ln-ln plots of the SALDI ion signal intensity of protonated caffeine (upper plot) and the radical cation (bottom plot) versus laser fluence using WO <sub>3</sub> as a substrate when the focus of the N <sub>2</sub> laser (337 nm) was placed at the surface of the chip... 172	
Fig.9.15: ln-ln plots of the SALDI ion signal intensity of protonated caffeine (upper plot)	

and the radical cation (bottom plot) versus laser fluence using $\text{WO}_3$ as a substrate when the focus of the $\text{N}_2$ laser (337 nm) was located $d = 0.4$ mm above the surface of the chip .....	173
Fig.9.16: In-In plots of the SALDI ion signal intensity of protonated caffeine (upper plot) and the radical cation (bottom plot) versus laser fluence using $\text{TiO}_2$ as a substrate when the focus of $\text{N}_2$ laser (337 nm) was placed at the surface of the chip .....	174
Fig.9.17: In-In plots of the SALDI ion signal intensity of the caffeine radical cation (upper plot) and the protonated species (bottom plot) versus laser fluence using $\text{TiO}_2$ as a substrate and placing the focus of $\text{N}_2$ laser $d = 0.4$ mm above the surface of the chip .....	175
Fig.9.18: Plots of $\ln(I)$ for the protonated caffeine ion versus $1/(T_0 + \eta F)$ using pSi, $\text{WO}_3$ and $\text{TiO}_2$ as substrates when the focus of $\text{N}_2$ laser was located at the chip surfaces .....	180
Fig.9.19: Plots of $\ln(I)$ for the caffeine radical cation versus $1/(T_0 + \eta F)$ using pSi, $\text{WO}_3$ and $\text{TiO}_2$ as substrates when the focus of $\text{N}_2$ laser was located $d = 0.4$ mm above the chip surfaces.....	181
Fig. 9.20: A schematic diagram showing the Surface Assisted Multiphoton Ionization (SAMPI) process. $A_{\text{ad}}$ and $A_{\text{g}}$ correspond to adsorbed and gas-phase analyte molecules, respectively .....	184

## List of Tables

Table 1.1 Compounds utilized as a NIMS initiator.....	9
Table 2.1: The list of all chemicals used in this work.....	26
Table 2.2: Mass spectrometer operating settings for NIMS experiments in positive ion mode.....	40
Table 2.3: Abbreviations used for amino acids.....	42
Table 3.1 Critical parameters and their optimum values for making pSi.....	57
Table 4.1: Assignments of peptides from a BSA tryptic digest using NIMS.....	87
Table 6.1: NIMS analysis of phenylethanol enantiomeric excess using fluoros mass tags b and c.....	124
Table 9.1: Slopes derived from plots of $\ln(I)$ versus $\ln(F)$ in term of protonated ions and radical cations using pSi, $WO_3$ and $TiO_2$ as substrates of DIOS .....	176
Table 9.2: Physical parameters for the SALDI substrates used in this thesis.....	178
Table 9.3: The slope and $\eta$ values from plots of $\ln(I)$ for protonated Caffeine ion versus $1/(T_0 + \eta F)$ when the focus of the $N_2$ laser was placed at the surface of the chip.....	180
Table 9.4: The slope and $\eta$ values from plots of $\ln(I)$ for Caffeine radical cation versus $1/(T_0 + \eta F)$ when the focus of the $N_2$ laser was located 0.4 mm above the surface of the chip.....	181

## List of Abbreviations

[A]	Analyte
Abl	Tyrosine kinase enzyme
ADP	Adenosine 5'-diphosphate
AP	Atmospheric pressure
ATP	Adenosine 5'-triphosphate
BisF <sub>17</sub>	1,3-Bis-(heptadecafluoro-1,1,2,2-tetrahydrodecyl) tetramethyldisiloxane
BSA	Bovine serum albumin
CD	Circular dichroism
CEM	Channeltron electron multiplier
CHCA	$\alpha$ -Cyano-4-hydroxycinnamic acid
CID	Collision-induced dissociation
DCC	1,3-Dicyclohexylcarbodiimide
DHB	2,5-Dihydroxybenzoic acid
DIOS	Desorption/ionization on silicon
DMAP	4-Dimethylaminopyridine
DTT	Dithiothreitol
Ee	Enantiomeric excess
ESI	Electrospray ionization
FAB	Fast atom bombardment
FIB	Fast ion beam
F-SPE	Fluorous Solid-Phase Extraction
5-FU	Fluorouracil
GC	Gas chromatography
GDP	5'-Guanylate diphosphate
GPB	Gas-phase basicities
GTP	Guanosine 5'-triphosphate
HPLC	High performance liquid chromatography
IC <sub>50</sub>	Half maximal inhibitory concentration

IMS	Imaging mass spectrometry
IP	Ionization potentials
IR	Infrared
KDP	Potassium dideuterium phosphate
LOD	Limit of detection
M/A	Matrix/analyte
MALDI	Matrix assisted laser desorption/ionization
MD	Molecular dynamics
MPI	Multiphoton ionization
MS	Mass spectrometry
MSE	Matrix suppression effect
MW	Molecular weight
m/z	mass/charge
Nd:YAG	Neodymium: yttrium aluminum garnet
Nimzyme	NIMS enzymatic assay
NIMS	Nanostructure-initiator mass spectrometry
PA	Proton affinity
PECVD	Plasma enhanced chemical vapor deposition
PEP	Phosphoenolpyruvate
PKA	Kinase A
PLs	Phospholipids
PNA	Peptide-Nucleic-Acid
pSi	Porous silicon
QqQ	Triple quadrupole
RF <sub>17</sub>	3-(Perfluorooctyl)-propyl-1-maleimide
RIE	Reactive ion etching
SALDI	Surface Assisted Laser Desorption/Ionization
SELDI	Surface enhancement laser desorption/ionization
SEM	Scanning electron micrograph
SIMS	Secondary ion mass spectrometry
SiNWs	Silicon nanowires

SLOS	Smith–Lemli–Opitz Syndrome
SMM	Small-Molecule Microarray
S/N	Signal-to-noise
SPI	Single-photon ionization
TFA	Trifluoroacetic acid
TOF	Time of flight
UHP	Ultra high purity
UV	Ultraviolet
VLS	Vapor-liquid-solid
VUV	Vacuum ultraviolet

## Chapter 1: Introduction

### 1.1: Background on Surface Assisted Laser Desorption/Ionization (SALDI)

#### 1.1.1: The development and limitations of MALDI

Matrix Assisted Laser Desorption/Ionization (MALDI) is a soft ionization technique discovered in the late 1980s which is widely utilized in mass spectrometry (MS) [1, 2]. It employs a solid molecular matrix which absorbs an incident laser energy and assists in the desorption and ionization of analytes imbedded within. In general, a matrix consists of small organic molecules or inorganic nanoparticle suspensions, and plays a crucial role in formation of intact gas-phase analyte ions. For example, the matrix prevents the analyte imbedded within the matrix from being photochemically and/or thermally degraded when the solid solution undergoes a phase transition from solid to gas under laser irradiation. It also prevents analyte molecules from aggregating by dilution within the solid solution [3]. Therefore MALDI MS has greatly expanded the applications of mass spectrometry for the analysis of a wide variety of compounds, especially large thermally labile biomolecules and synthetic polymers [4].

MALDI MS, however, has several well-known limitations including the need to have a variety of matrices on hand to study different classes of analyte molecules, the presence of ‘sweet spots’; that is, areas of the solid solution which produce more intense MALDI signals than others due to the uneven distribution of analytes within the matrix, and matrix interferences at low  $m/z$  values. The choice of a suitable matrix, which is typically determined by trial and error, is an extremely laborious but a vital step towards optimizing a MALDI spectrum because it influences the analyte ionization efficiency, the

mass resolution and the detection sensitivity. While there are a number of matrices which have been tested for different incident laser wavelengths and analyte types which can be used for some guidance, the selection process remains empirical [3]. The phenomenon of “sweet spots”, resulting in shot-to-shot ion signal variability is due in part to the method of preparation selected to make the solid solution [5]. Lastly, the MALDI technique suffers from excessive matrix background signals in the low molecular weight (mass/charge,  $m/z < 1000$ ) region of the mass spectrum. This background due to matrix ion fragments, clusters, and adducts obscures the ion signals from low molecular weight molecules of interest such as drug metabolites and small peptides. Moreover, the high abundance of matrix-related ions in the laser plume can lead to signal suppression and compromise the detection sensitivity for low-abundance analytes [6-8].

There has been considerable interest in developing matrix-free SALDI techniques to minimize or eliminate these problems. The most prevalent one for the analysis of small molecules is desorption/ionization on silicon (DIOS) [9]. However, other solid substrates have also been tested including sol-gels [10], carbon-based microstructures [11, 12], and metal-based nanostructure substrates [13].

In DIOS, porous Si (pSi) is used to assist in the ionization of analyte molecules instead of a MALDI matrix compound such as 2,5-dihydroxybenzoic acid, DHB and *o*-cyano-4-hydroxycinnamic acid, CHCA. Although not a commercial technique DIOS has been successfully used to analyze a wide variety of samples including small drugs, explosives, polymers, and forensic compounds [14, 15].

### **1.1.2: The development of DIOS**

DIOS MS, introduced by the Siuzdak group in 1999, was the first truly matrix-



free laser desorption/ionization mass spectrometric method. It involves spotting an analyte onto a sample of pSi, as shown in the Fig. 1.1[9]. As a desorption/ionization technique, DIOS offers good sensitivity, high tolerance to contaminants and no matrix interferences. Furthermore this approach is compatible with silicon-based microfluidics and microchip technologies [9].

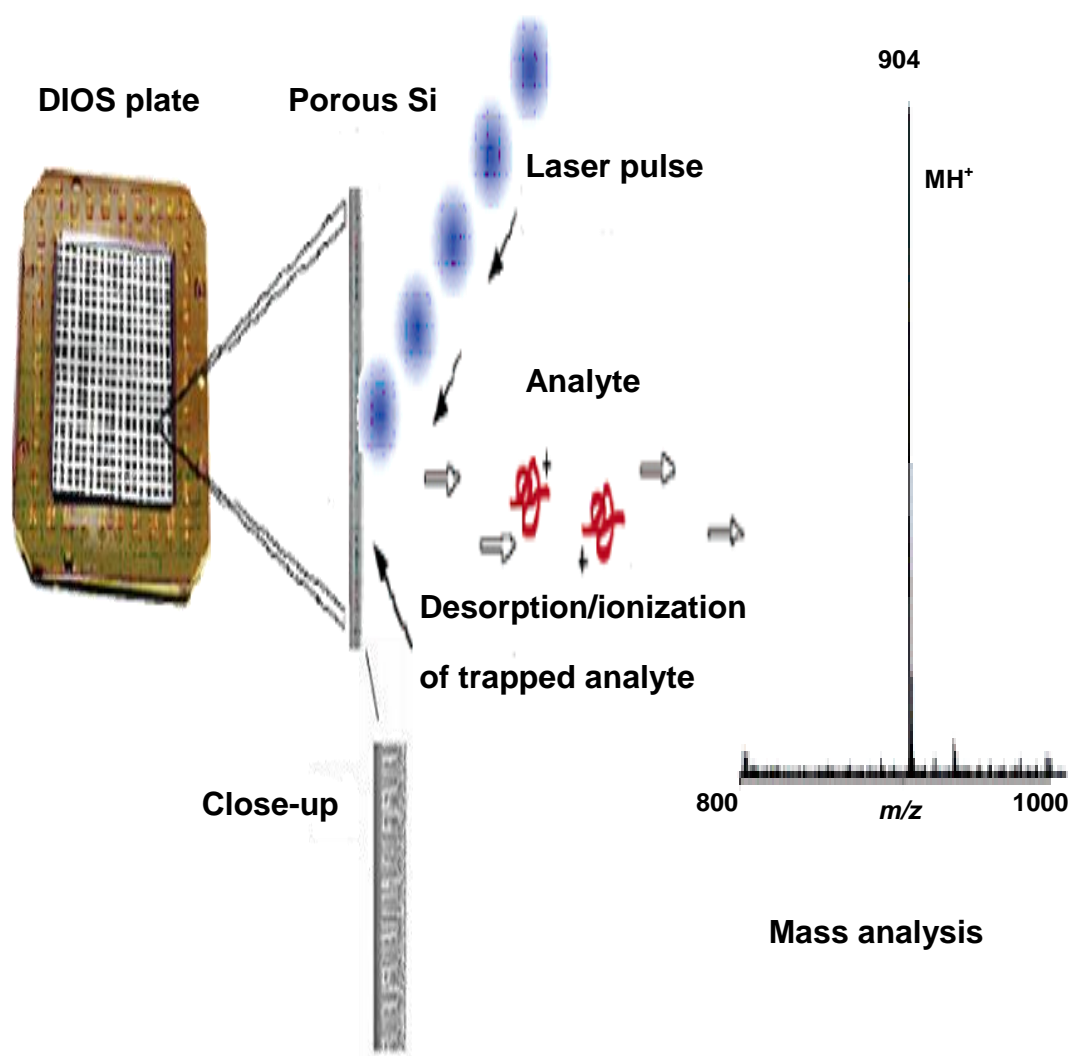


Fig. 1.1: Experimental configuration for a DIOS experiment [9].

A large number of DIOS-related methods have been subsequently developed. For example, atmospheric pressure-desorption/ionization on silicon (AP-DIOS), was introduced as a new analytical tool that is complementary to AP-MALDI [16] and shown to be superior at  $m/z < 1,100$ . The combined data of both AP-DIOS and AP-MALDI nearly doubled the number of identifiable mass spectral peaks in a bovine serum albumin (BSA) digest analysis compared to that obtained separately by only one approach.

Silicon nanowires (SiNWs) have been used instead of pSi as an alternate platform for DIOS-MS. Unlike a pSi surface, SiNWs are grown on the surface of a solid Si substrate. Sensitivity down to the attomole ( $10^{-18}$  moles) level has been achieved using these structures by optimizing the incident laser energy, Si surface chemistry, and the NW diameter, length, and orientation relative to the underlying substrate. Due to their high surface areas and fluid wicking capabilities, SiNWs are able to perform analyte chromatography separations prior to mass spectrometric analysis, thereby providing a unique platform that integrates these two functions on a single substrate [17].

The nanostructured silicon produced by electrochemical etching and laser processing are characterized by a morphology consisting of an array of  $\mu\text{m}$  high Si columns, each covered by nano-leaves. This morphology features a large surface area that is relatively stable against UV laser damage, and therefore able to generate reproducible DIOS mass spectra. This is expected to make DIOS suitable for routine analysis of low molecular weight analytes [18].

### **1.1.3: Methods for fabricating porous silicon**

A pSi surface is characterized by a large area and a nanostructured morphology. The material can then be spotted with analyte and directly irradiated for laser desorption

ionization MS with little or no background interference. So far, many different techniques including electrochemical etching [19], laser-induced transformations [20], high-density plasma deposition [21], reactive ion etching [22], and so on, have been used to produce pSi substrates.

In this work pSi was fabricated by electrochemically etching bulk Si wafers in dilute aqueous or ethanoic hydrofluoric acid (HF). Ethanol is frequently added to the hydrofluoric acid to minimize hydrogen bubble formation during anodization. This improves the pSi layer uniformity [23]. Electrochemical etching can be performed either in a potentiostatic (voltage-controlled) or galvanostatic (current-controlled) mode. The latter is normally preferred because it supplies the required charge for the reaction at constant rate regardless of any changes in cell electrical impedance, ultimately leading to more homogeneous and reproducible material.

Other fabrications used to produce nanostructured silicon substrates include nanosphere lithography-coupled reactive ion etching (RIE) which can be used to generate a regular microstructured surface [24]. A Au nanocluster-catalyzed vapour-liquid-solid (VLS) growth mechanism was used to produce dense arrays of single-crystal SiNWs platform for DIOS detection of small molecules, peptides, protein digests, and metabolites in biofluids [17]. Plasma-enhanced chemical vapour deposition (PECVD) can be used to form novel thin films consisting of a column/void-network of deposited silicon that does not require etching prior to its use for DIOS [21].

#### **1.1.4: Applications of DIOS**

The utility of DIOS for the analysis of small molecules, protein identification and functional characterization, and polymer analysis has been studied. The analysis of small

biomolecules such as drugs is one of the strengths of DIOS combined with MS due to the elimination of the matrix and subsequent matrix-related interferences [9, 15, 25]. DIOS combined with proteolytic digestion and database searching allows proteins and post-translational modifications to be identified. For example, on-plate digestion and DIOS with mass detection was used to identify the acetylcholine esterase (Ache) enzyme [26]. The potential that DIOS-MS has for making reliable quantitative analyses of polymers makes it promising for biological forensics. For example, DIOS-MS have been used to analyze ethoxylate polymers present in a contraceptive lubricant [14].

Since DIOS is a matrix-free desorption technique, it has the potential to monitor sequential reactions on the same surface via multiple mass spectrometric measurements. For example, DIOS-MS was used to determine the enantiomeric excess of a synthetic process during drug development [27]. It has also the potential to be used to measure the enantiomeric excess in high throughput systems to establish optimum reaction conditions quickly and easily [28]. Lastly, DIOS MS has been used as direct assays of tissues and cells.[29].

## **1.2: The overview of Nanostructured-Initiator Mass Spectrometry (NIMS)**

### **1.2.1: Fundamental characteristics of NIMS**

In 2007, the Siuzdak group introduced NIMS, which uses ‘initiator’ molecules trapped in a nanostructured surface like pSi to release and ionize intact adsorbed molecules on the surface. This approach overcomes the limitations that DIOS has in terms of robustness and reproducibility, which has limited its use to date [30]. NIMS takes advantage of the basic physical properties of the pSi DIOS platform such as its ability to absorb light and its low thermal conductivity to perform rapid surface heating and trigger

the desorption of adsorbed molecules. At the same time, NIMS also incorporates some features which are similar to MALDI such as the use of a liquid initiator like a fluorinated siloxane to facilitate desorption due to its sensitivity to temperature. However, unlike a matrix the initiator does not absorb laser energy due to its transparency to UV light, and thus are not ionized themselves. Furthermore, they are also not co-crystallized or incorporated with the analyte molecules [31]. Conceptually NIMS can be viewed as the inverse of one of the first MALDI experiments that involved the use of nanoparticles matrixes suspended in glycerol [2]. Furthermore NIMS is considerably softer than MALDI [3]. As shown in Fig. 1.2, in a typical NIMS process, after the pSi has absorbed the incident laser energy that causes rapid surface heating, the trapped initiator is vaporized, facilitating the desorption of the analyte without fragmentation [32].

NIMS has some exceptional features. For example, many different types of irradiation sources such as a N<sub>2</sub> laser and various ion sources (Au<sup>+</sup>, Ga<sup>+</sup>, Bi<sup>+</sup> and Bi<sub>3</sub><sup>+</sup>) have been found to produce NIMS activity. In general, a typical NIMS surface is composed of ~10 nm pores fabricated by electrochemically etching pSi on a bulk silicon wafer, (Section 1.1.3). A variety of NIMS initiator molecules have been successfully used with molecular weights ranging from 200 to 14,000 Da, including lauric acid, polysiloxanes, siloxanes and silanes (Table 1.1). However, the performance of perfluorinated siloxanes has been shown to be excellent for a wide range of analytes and therefore, is preferred for laser-NIMS. The reason for this is that perfluorinated siloxanes are effectively trapped within nanostructured pSi and have relatively low vapour pressures making them compatible for use in the vacuum environment of most MALDI instruments [31]. A higher molecular weight fluorinated siloxane (14,000 Da) is often

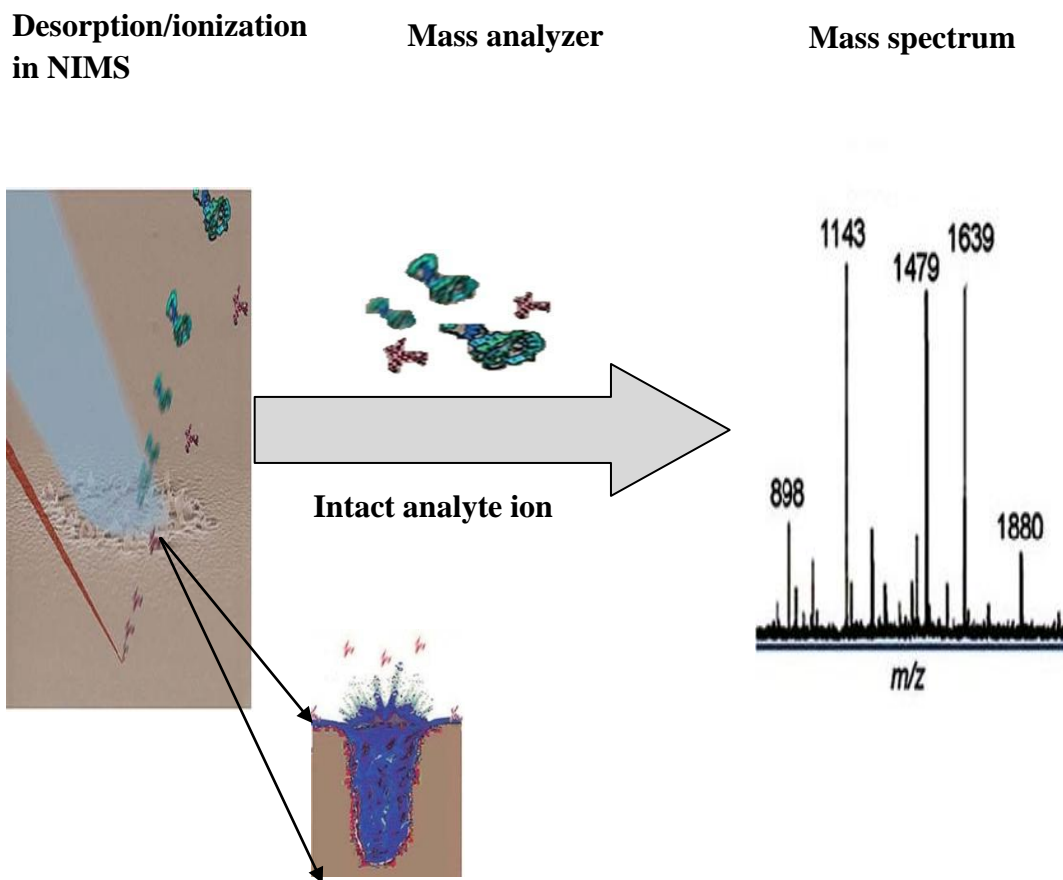
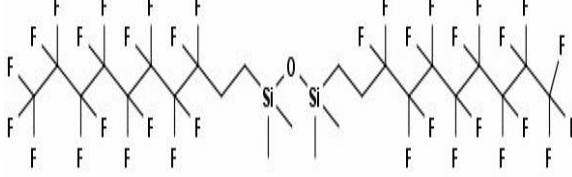
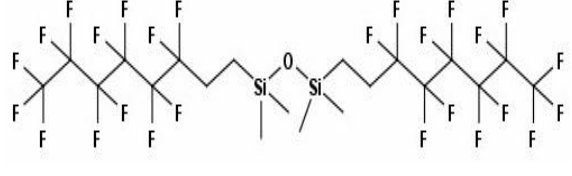
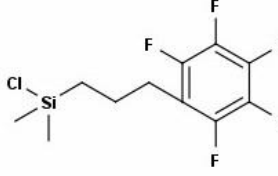
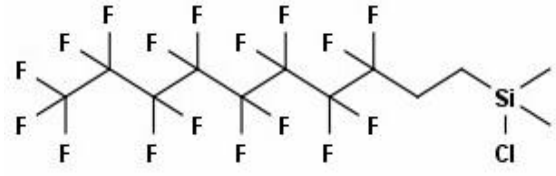
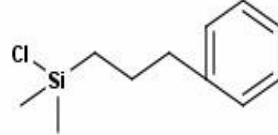
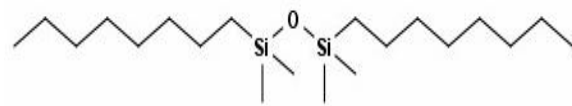
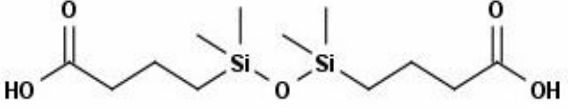
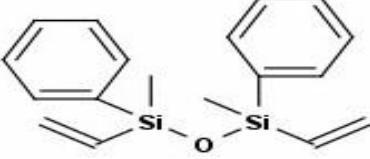
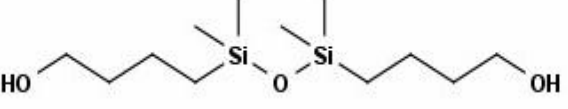

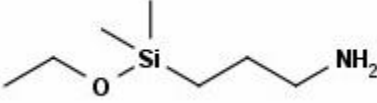
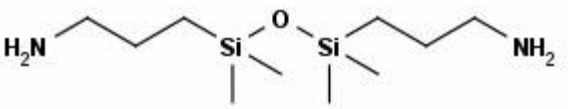
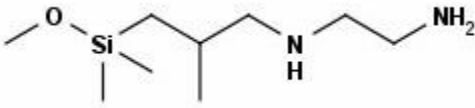
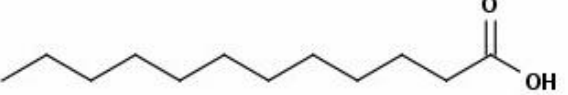


Fig.1.2: Schematic diagram of a typical NIMS analysis [30]

chosen for ion-initiated NIMS due to their very low vapour pressures; a necessity for use in time-of-flight-secondary-ion mass spectrometry (TOF-SIMS) instruments that have more stringent vacuum requirements [30]. It is essential that any initiator chosen does not absorb the incident laser energy and ionize to avoid introducing chemical noise into the mass spectra [32].

**Table 1.1: Compounds utilized as a NIMS initiator**

Name, molecular formula, molecular weight	Chemical structure	References
Bis(heptadecafluoro-1,1,2,2-tetrahydrodecyl)tetramethyldisiloxane, $C_{24}H_{20}F_{34}OSi_2$ , 1026.5		[33]
Bis(tridecafluoro-1,1,2,2-tetrahydrooctyl)tetramethyldisiloxane, $C_{20}H_{20}F_{26}OSi_2$ , 826.5		[34]
Pentafluorophenylpropyldimethylchlorosilane, $C_{11}H_{12}ClF_5Si$ , 302.7		[31]
(Heptadecafluoro-1,1,2,2-tetrahydrodecyl)dimethylchlorosilane, $C_{12}H_{10}ClF_{17}Si$ , 540.7		[35]
(3-Phenylpropyl)dimethylchlorosilane, $C_{11}H_{17}ClSi$ , 212.8		[31]
1,3-Dioctyltetramethyldisiloxane, $C_{20}H_{46}OSi_2$ , 358.7		[30]

<p>1,3-Bi(3-carboxypropyl) tetramethyldisiloxane, <math>C_{12}H_{26}O_5Si_2</math>, 306.5</p>		[30]
<p>1,3-Divinyl-1,3-diphenyl-1,3-dimethyldisiloxane, <math>C_{18}H_{22}OSi_2</math>, 310.5</p>		[30]
<p>1,3-Bis(hydroxybutyl) tetramethyl-disiloxane, <math>C_{12}H_{30}O_3Si_2</math>, 278.5</p>		[30]
<p>3-Cyanopropyldimethyl-chlorosilane, <math>C_6H_{12}ClNSi</math>, 161.7</p>		[27]
<p>3-Aminopropyldimethyl-ethoxysilane, <math>C_7H_{19}NOSi</math>, 161.3</p>		[31]
<p>1,3-Bis(3-aminopropyl) tetramethyldisiloxane, <math>C_{10}H_{28}N_2OSi_2</math>, 248.5</p>		[27]
<p>(Aminoethylamino)-3-isobutyl-dimethylmethoxysilane, <math>C_9H_{24}N_2OSi</math>, 204.1</p>		[30]
<p>Lauric acid, <math>C_{12}H_{24}O_2</math>, 200.3</p>		[30]





## **1.2.2: The applications of NIMS**

As shown in Fig. 1.3 the potential of NIMS for the detection of small molecules in the analyses of complex biofluids, metabolites and tissue imaging is immense [34].

### **1.2.2.1: Complex biofluid analyses**

Biofluids such as blood, urine and saliva are in many instances ideal diagnostic samples because they can contain a wealth of biochemical information related to pathology changes [39]. Typically, the nature and complexity of biofluid samples necessitate sample preparation such as organic solvent extraction or chromatography separation prior to conventional analyses such as gas chromatography (GC)/MS, high performance liquid chromatography (HPLC)/MS or MALDI MS [40-42]. Conversely, NIMS does not require prior sample preparation [37]. It has been demonstrated that ketamine, a drug used in human and veterinary medicine, and its metabolite, norketamine, could be analyzed by NIMS by directly spotting mouse urine and blood sample onto the chip surface without any additional sample preparation except for removal of excess urine or blood drops using a N<sub>2</sub> gas stream [37]. Similarly, direct NIMS analysis of some compounds from human saliva was also reported in the same article.

Furthermore, NIMS performance has been quantitatively evaluated using several standard xenobiotics (methamphetamine, codeine, apralozam and morphine spiked into rat serum). The limit-of-detection (LOD) values of all these analytes were in the attomole range and their response curves were linear in the range between 1 ng/mL and 150 ng/mL [37].

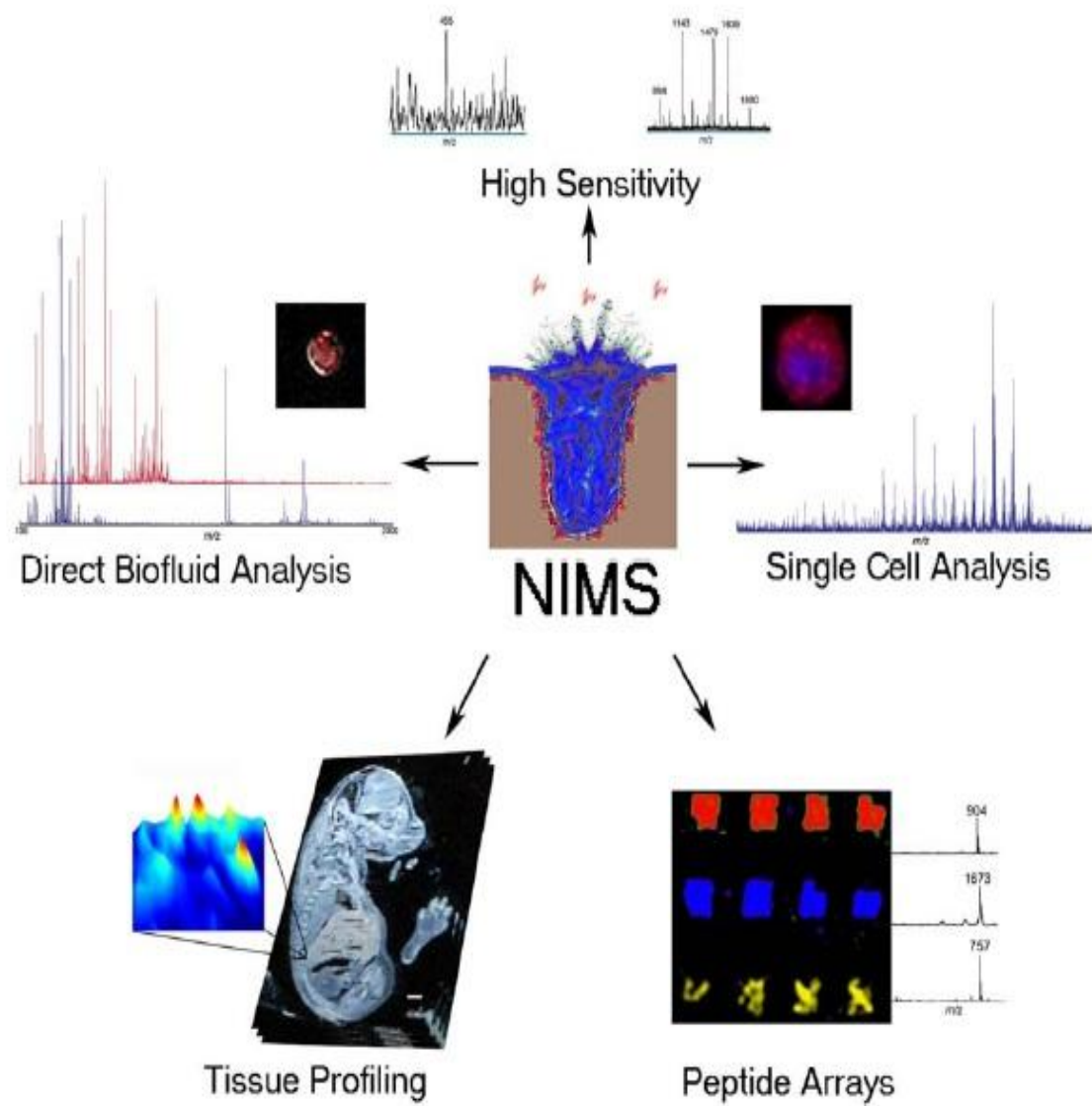


Fig.1.3: Illustration of some of the main applications of NIMS [34].

The potential applicability of cation-NIMS analysis in a clinical setting was demonstrated in a study which analyzed glucose and cholesterol in human serum. Here, cations were deposited on the NIMS surface by electrospray before adding the initiator [33]. It is well-known that carbohydrates and steroids are classes of important biological active molecules that are hard to detect by current surface-based MS methods due to their low ionization efficiencies [4, 43]. In general, they are more easily detected as cationic adducts instead of protonated  $[A+H]^+$  species [44]. The concentration of glucose in standard human serum obtained from Sigma-Aldrich was determined to be 4.1mM by  $Na^+$ -enhanced NIMS. The analyte detection exhibited good linearity ( $R^2 = 0.9975$ ) between 1  $\mu$ M and 200  $\mu$ M [33]. Interestingly, steroids such as cholesterol were best detected as silver adducts  $[A+Ag]^+$ . In this way,  $Ag^+$ -NIMS, used to quantitatively analyze the amount of cholesterol in human serum, found the concentration of the steroid to be ~4.2 mM (~164 mg/dL), which is within the normal cholesterol range of less than 200 mg/dL recommended by the American Heart Association [33].

#### **1.2.2.2: Metabolites analysis**

Although MALDI MS has been developed to be one of the most dominant analysis tools in proteomics, there is still a formidable challenge in analyzing metabolites due to interferences from the matrix. Metabolites closely correlate with an organism's phenotype [45] and include a wide variety of compounds such as amino acids, other organic acids and amines, nucleotides, lipids, and sugars which are the downstream end products of gene and protein activity. It was suggested that NIMS could provide a means of studying metabolites due to its extremely high sensitivity, the absence of matrix interference, and minimal sample preparation [30].

Phospholipids (PLs) have been proved to be effective cancer biomarkers and cell specific drug targets [46, 47]. It was demonstrated that laser-NIMS could be used to analyze endogenous PLs from metabolites of few or even a single cell in a highly metastatic breast cancer cell line [30]. Since the concentration of metabolites is often vital in clinical assays, it is important to reiterate that NIMS method has ability to perform direct quantitative analysis of metabolites from blood and urine [33, 37]. Laser-NIMS with negative-ion mode detection was also used to detect endogenous cell metabolites of phosphoenolpyruvate (PEP), 5'-guanylate diphosphate (GDP), adenosine 5'-triphosphate (ATP), adenosine 5'-diphosphate (ADP), and guanosine 5'-triphosphate (GTP) [35].

Interestingly, the selection of initiator can significantly impact the ion profiles observed in the mass spectrum of a biological sample. For example, there are substantially different ion profiles in NIMS spectra of urine samples obtained using bis-(heptadecafluoro-1,1,2,2-tetrahydrodecyl) tetramethyl-disiloxane as an initiator and a more polar compounds such as 1,3-bis (hydroxybutyl) tetramethyldisiloxane [32].

### **1.2.2.3: NIMS imaging**

NIMS is a powerful platform for MS imaging due to its high spatial resolution, an extended usable mass range, minimal sample preparation, the absence of matrix interferences and improved sensitivity [32]. For example, NIMS imaging of metabolites in mouse embryo slices was done by first ablating the surface tissue with a high energy laser ( $\sim 0.4 \text{ J/cm}^2$  per pulse), followed by direct interrogation of the interface between the tissue and chip surface with low-energy irradiation ( $\sim 0.01 \text{ J/cm}^2$  per pulse) [30].

Cation-enhanced NIMS imaging has also been used to acquire the distribution of sucrose in a flower stem and the distribution of cholesterol in a mouse brain [33].

Furthermore, it was utilized for the first time to localize the perturbations to metabolism within pathological brain tissue of mice having Smith–Lemli–Opitz Syndrome (SLOS) by imaging cholesterol and its precursors. These results suggest a role for cholesterol metabolites in the development of these brain regions and provide anatomical insight into the SLOS disease pathology [38]. Overall, NIMS imaging is complementary to imaging MALDI MS, which is better suited to the detection of peptides and small proteins in tissue samples [48].

### **1.3: Immobilization method on chip surface**

Currently one of the most cutting-edged biochemical analysis techniques is the combination of affinity fractionation based on the surface chemistry of a biochip, with label-free detection based on surface laser desorption/ionization mass spectrometry: Surface-Enhanced Laser Desorption/Ionization (SELDI) [49]. This approach allows enrichment and massively parallel analyses of particular subsets of analytes of interest from small volumes of complex mixtures. The functionalized surface of the biochip plays an active role by providing moieties that can immobilize specific target analytes, thereby reducing nonspecific interactions of molecules in the sample with the chip surface [50]. According to a general or specific physicochemical property of the analyte of interest, each biochip surface can be designed to immobilize specific molecules. A number of immobilization methods have been developed to prepare biochips, including covalent strategies such as a Michael addition reaction [51], silyl ether formation [52], etc. In addition, non-covalent approaches can be used that take advantage of electrostatic interactions [53], sequence-specific hybridizations [54], fluoros-base interactions [55], and so on.

### 1.3.1: Covalent immobilization

This immobilization strategy makes use of mild and chemically selective coupling reactions to capture desired analyte molecules onto a derivatized chip surface. For example, the first Small-Molecule Microarray (SMM) chip was prepared by a reaction to form a maleimide-functionalized surface using a bifunctional linker, as shown in the Fig.1.4a [51]. The treated biochip was then used to selectively capture compounds containing a free thiol group by a simple Michael addition reaction, (Fig.1.4b) [56].

Other covalent immobilization methods include a chloro-silanated chip surface which is produced by reacting  $\text{SOCl}_2$  with a glass surface. This substrate has been used to bind primary alcohol but not secondary alcohols or phenols due to their relatively slow reaction rates [57]. Similarly, an epoxide-coated chip surface has been used to capture hydrazide-tagged analytes and carbohydrates [58]. Likewise, a diazobenzylidene-functionalized surface was used to selectively immobilize acidic heteroatom-containing compounds such as phenols, carboxylic acids or sulphonamides [59]. Many other chemical reactions such as Diels–Alder cycloadditions, Staudinger Ligation and photocrosslinking have also been used to covalently immobilize analytes on chip surfaces [56].

### 1.3.2: Non-covalent immobilization

Non-covalent methods take advantage of adsorption phenomenon rather than chemical reactions to immobilize an analyte. For example, carbohydrate-lectin interactions were investigated using a chip on which carbohydrates with tails of saturated carbon chains consisting of 13~15 carbons were attached as an array on a hydrophobic

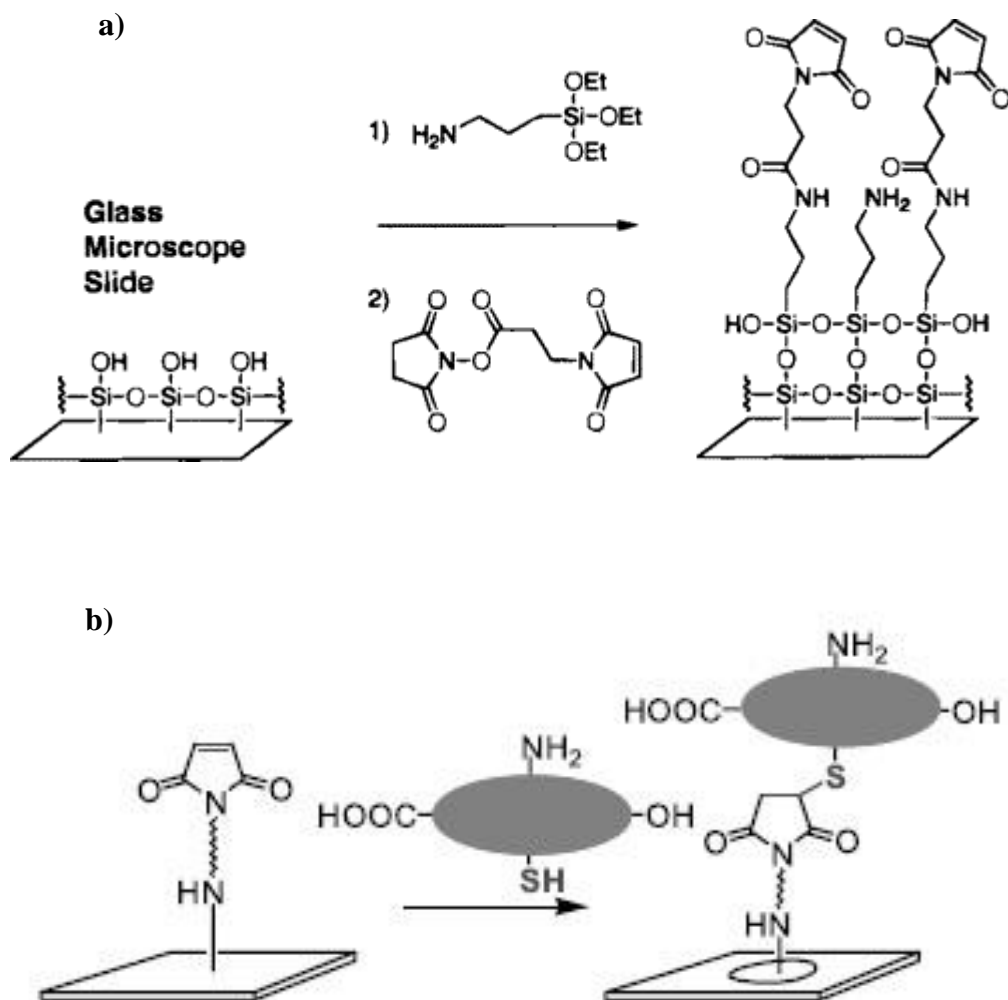


Fig.1.4a) a bifunctional linker covalently immobilized on the chip to form a maleimide-functionalized surface; b) a reaction showing how the treated biochip can be used to capture selectively a compound containing a thiol group by simple Michael addition reaction [51, 56].



surface [60]. In another strategy, a Peptide Nucleic Acid (PNA) tag containing a covalently bound small molecule or bifunctional linker was anchored non-covalently onto an oligonucleotide microarray chip surface by sequence-specific hybridization, as shown in Fig.1.5a [54].

#### **1.4: Fluorous affinity techniques**

Recently a new non-covalent immobilization strategy based on fluororous-fluorous interactions has been used to prepare small molecule microarrays for carbohydrate analysis (Fig.1.5b) [61]. Such fluororous-based microarray chips have also been used to perform high-throughput enzymatic inhibitor screening for drug discovery [55].

##### **1.4.1: The fundamental features of fluororous chemistry**

Since the introduction of fluororous biphasic catalysis techniques in the middle of 1990s [62], the field of fluorine-based chemistry has expanded rapidly in organic synthesis and purification [63, 64]. Recent innovations suggest that a wide range of potential applications of fluororous tags technology could be realized in chemical biology as well [65]. The word ‘fluorous’ refers to a bulk liquid phase distinct from organic solvents; it is a third phase orthogonal to the organic and aqueous phases [66]. Since at the molecular level, the perfluoroalkyl groups  $[-(\text{CF}_2)_n-]$  tend to repel organic and inorganic molecules but have attractive interactions with other perfluoroalkyl ( $\text{RF}_n$ ) groups, fluororous molecules can be separated from other molecules based on their  $\text{CF}_2$  content by several methods such as chromatography, liquid-liquid or solid-phase extractions, etc. [65].

Interestingly, although in principle a fluororous phase is immiscible in both aqueous and organic phases, the solubility of a fluororous compound in organic solvents is

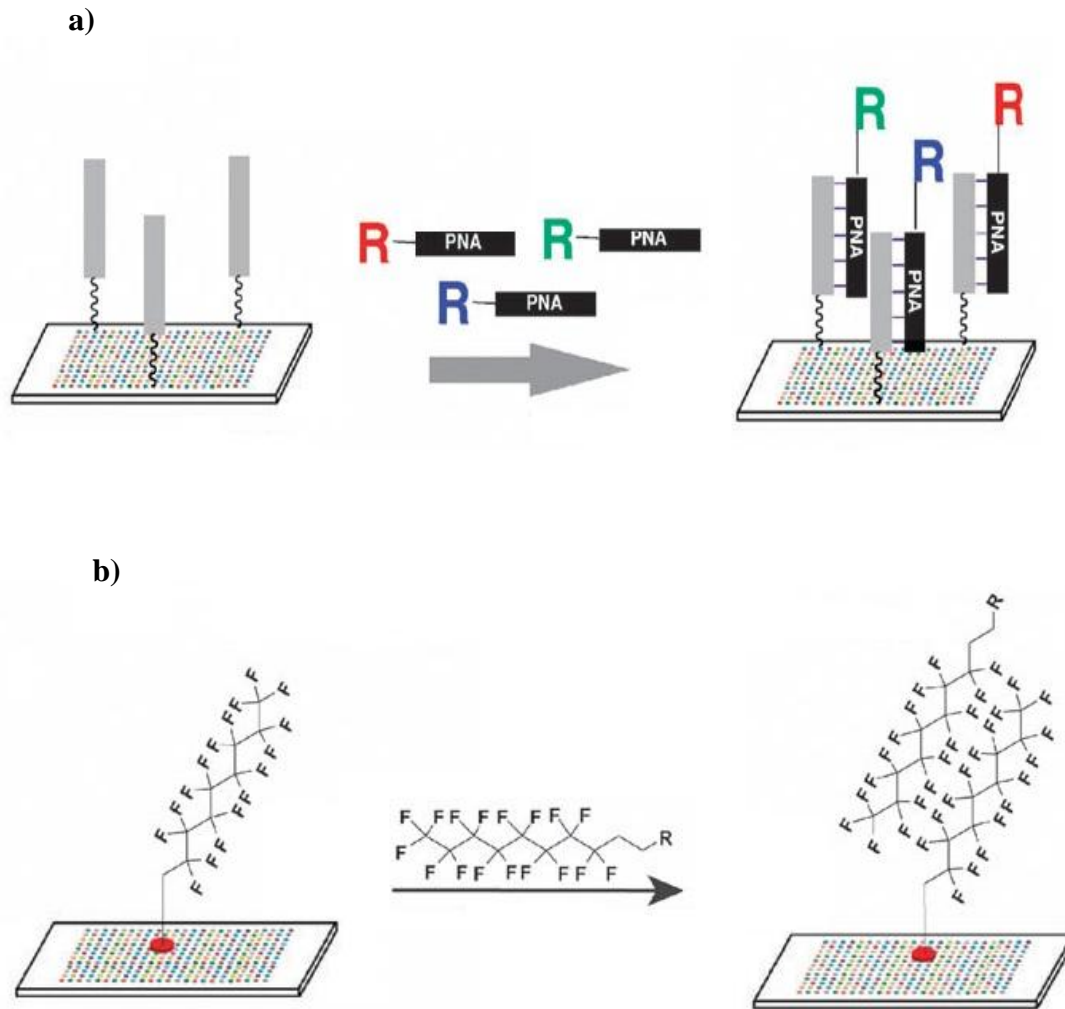


Fig.1.5: Representative examples of noncovalent immobilization used to fabricate SMM chips: a) a schematic showing how libraries of small molecules which are encoded by a specific PNA codon may be captured selectively onto an oligonucleotide microarray by a hybridization reaction; b) a schematic showing how a small polyfluorocarbon attaches non-covalently to a fluoroalkylsilane-coated chip surface [54, 61].

dependent on temperature and the fluorine content of the whole molecule [67]. This unique characteristic has been exploited in the development of fluorous tags for solution-phase syntheses and fluorous separations [68]. The fluorous phase methods can be seen as green because fluorous materials can be recovered and recycled for use after separation [67].

Typically, fluorous tags contain a perfluorinated domain ( $\text{RF}_n$ ) which is that portion of the molecule used for fluorous separation or immobilization. It also contains a parent molecule with a chemically reactive group and an alkyl segment  $(\text{CH}_2)_m$  that connects the parent molecule to the fluorous group and insulates the reactive site on the parent molecule from the electron-withdrawing fluorines. It is assumed that the immobilization does not alter or completely eliminate the activity of the molecule, which is a major concern for chip-based assays. In addition, the unique solvophobicity and fluorophilicity of a fluorous phase can prevent nonspecific adsorption of protein, which can often lead to denaturation and a subsequent loss of activity of the immobilized species [69].

#### **1.4.2: The application of fluorous tags on chemical biology**

Recently, fluorous affinity technology has been used to separate proteins, to assay enzymes (by NIMS) and to construct fluorous carbohydrate microarrays [61, 70, 71]. In general, fluorous-affinity tags used for separation and enrichment operate in one of two modes. The first is based on the use of a Fluorous Solid-Phase Extraction (F-SPE) column where perfluoroalkyl chains serve as a bonded phase instead of a resin to facilitate analyte separation (Fig.1.6a). In fluorous proteomics separations, for example, a complex peptide (or proteins) sample in solution is selectively labeled with a fluorous tag

containing a specific functional group and then loaded onto the fluororous solid-phase medium for separation. The unbound species and contaminants are subsequently washed away using a suitable organic solution. Finally, the desired bound species are eluted from the affinity column for MS analysis [70, 72].

The second strategy is based on a biochip where the analytes of interest are captured by a fluororous tag immobilized on a fluororous-silylated surface by fluorine-fluorine interactions (Fig.1.6b)). In proof-of-principle experiments, a NIMS enzymatic assay or Nimzyme was developed to detect both addition and cleavage reactions under enzymatic catalysis of sialyltransferase and galactosidase with extremely high sensitivity (sub-picogram levels), and to directly characterize the enzymatic activity of crude cell lysates from thermophilic bacteria [71].

As mentioned previously, fluororous-affinity interactions have also been exploited in the fabrication of small molecule microarrays. For example, fluororous-tagged saccharides have been non-covalently immobilized on a fluororous slide surface for the analysis of carbohydrates [61]. This arrangement was used to obtain information on the binding of heptoses to lectins and to identify small molecule inhibitors of the histone deacetylase enzyme [55, 73].

### **1.5: The goals of the thesis**

The projects described in this dissertation are motivated by the desire to apply the concepts developed from surface chemistry, fluororous chemistry and mass spectrometry to develop biochips that can be used to investigate the interactions between biological species and small molecules. The work in this thesis extends demonstrated concepts such as the use of fluororous affinity tags F-SPE column chromatography to enrich and

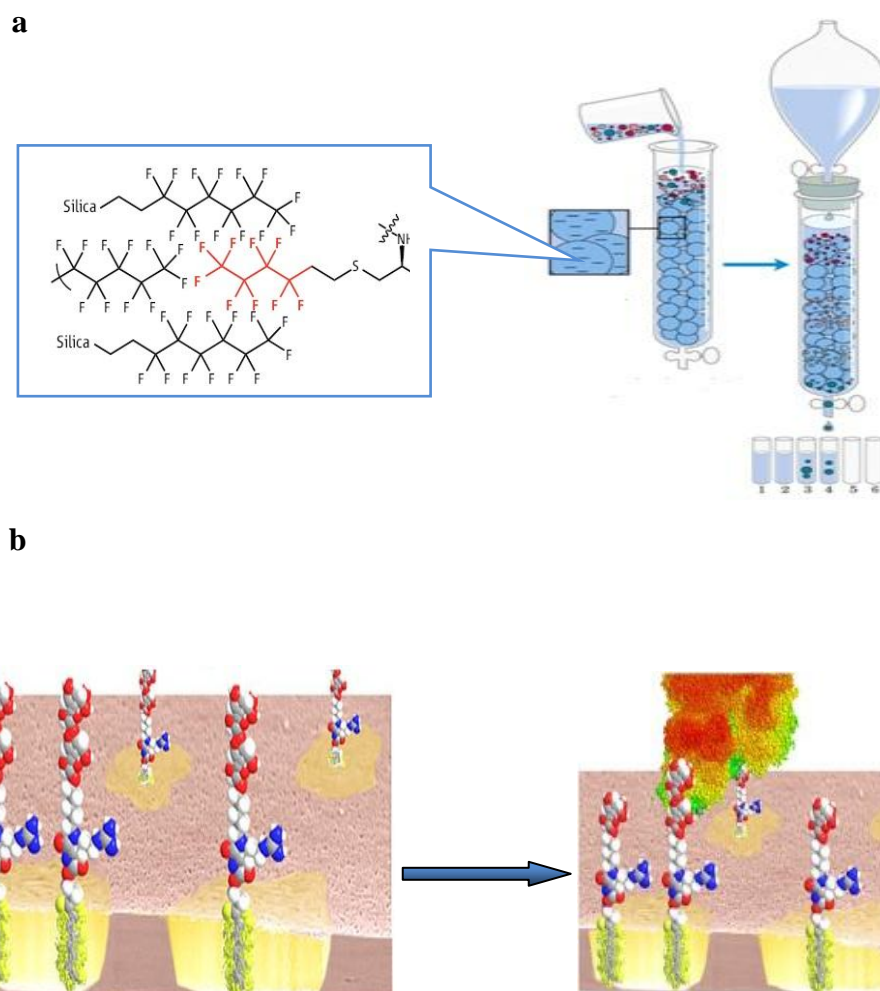


Fig. 1.6: Illustration of some main applications of fluoruous affinity technology: a) a F-SPE column which uses perfluoroalkyl chains as bonded phase instead of a resin to facilitate analyte separation, is employed to enrich and separate specific classes of peptides in fluoruous proteomics. Firstly it is selectively labelled with a fluoruous tag and then loaded onto a F-SPE column, followed by washing and collection based on fluorine content; b) a Nimzyme assay process in which enzymatic substrate with fluoruous tags is immobilized onto NIMS chip surface by fluorophilicity followed by incubation of the surface with the samples to screen for enzymatic activity [65, 71].

subsequently mass analyze peptide subsets from mixtures [70]. The work also exploits the fact that fluorinated liquid-coated NIMS surfaces can be used as tags to non-covalently attach enzyme substrates for assays [71].

A flow chart detailing the goals of this thesis is shown in Fig. 1.7. In Chapter 1 the background to understand various Surface Assisted Laser Desorption Ionization (SALDI) techniques including NIMS is presented. Details regarding the experimental apparatus used in this thesis are found in Chapter 2, as well as an assessment of the performance of pSi chips fabricated using a home-built electrochemical etching set-up. An evaluation of a NIMS chip based on a pSi substrate is provided in Chapter 3. Several new applications of a fluorinated affinity NIMS chip utilizing a 3-(perfluorooctyl)-propyl-1-maleimide tag are described in Chapters 4, 5 and 6. It is shown that initiators such as perfluorinated siloxanes trapped within the nanostructured surface of the NIMS chip not only increase the ionization efficiency of MS based on DIOS, but also exhibit an ability to attach the immobilized ligands by fluorinated phase interactions. This differs significantly from the immobilization methods above where chemical modifications of the chip surface were required before adding an affinity tag.

Specifically, the NIMS chip developed in this thesis was used to enrich a subset of peptides containing cysteine residues from a mixture. Similarly, a kinase activity assay for phosphorylation and enzymatic inhibitor screening was optimized. Lastly, the fluorinated-affinity NIMS chips were also used to measure enantiomeric excesses by kinetic resolution.

The use of visible lasers to drive NIMS and the development of microstructured tungsten oxide and titanium dioxide substrates for SALDI MS are discussed in Chapter 7.

The current state of our understanding of the laser desorption/ionization mechanisms of MALDI, DIOS and NIMS are compared in Chapter 8 while experimental results which provide insight into SALDI mechanism using porous Si, and microstructured WO<sub>3</sub> and TiO<sub>2</sub> can be found in Chapter 9. These experiments suggest under specific conditions a new ionization mode can occur in SALDI which we name Surface Assisted Multiphoton Ionization or SAMPI. Conclusions and possible future experiments are suggested in Chapter 10.

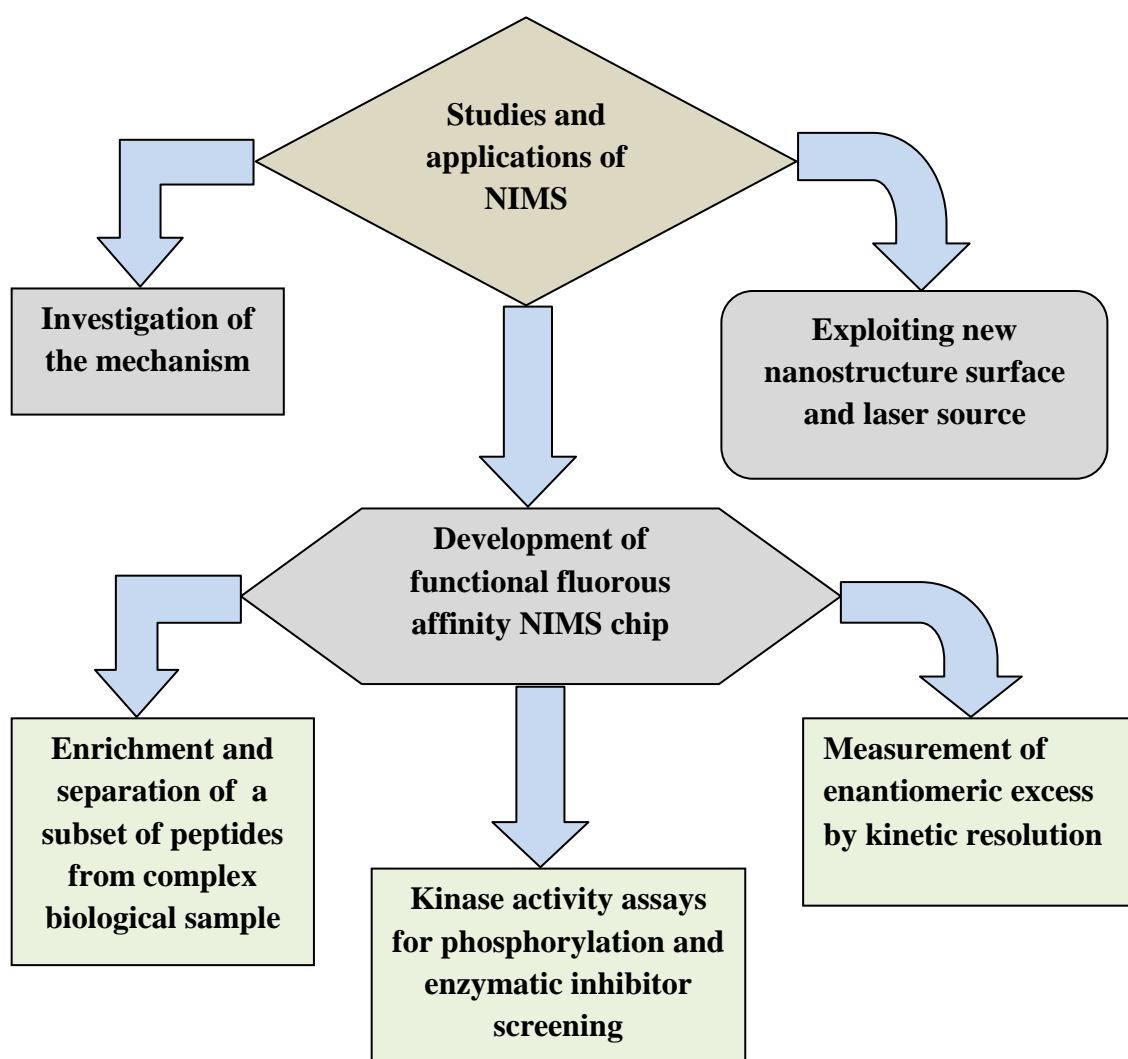


Fig. 1.7: Flow chart illustrating the goals of this thesis

## Chapter 2: Experimental

### 2.1: Materials and Chemicals

**Materials:** Single-side polished p-type (boron-doped) silicon <100> wafers ( $381 \pm 25 \mu\text{m}$  thickness and 76 mm diameter) exhibiting a low-resistivity of  $<0.005 \Omega\text{-cm}$  were purchased from Silicon Quest International (Santa Clara, CA, USA). The other materials used in this work include platinum wire, double-sided 3M XYZ-axis electrically conductive tape (TED PELLA, INC.), 3M<sup>TM</sup> copper conductive tape, Petri dishes, a stainless steel positioning lift, a ruler, a pair of tweezers, a diamond-tip scribe, vernier caliper (series No.530, Mitutoyo Corporation), as well as different 2 m or 5 m long Ultraviolet (UV)-Visible (Vis) optical fibers (Ocean Optics Inc.) having core diameters of 100  $\mu\text{m}$  and 200  $\mu\text{m}$ .

**Chemicals:** Table 2.1 lists all chemicals used in this work including their names, purities, formula, CAS number and manufacturers.

**Table 2.1: The list of all chemicals used in this work**

Name (purity), formula and CAS No.	Manufacturer
Dalargin (HPLC grade, >98% purity), $\text{C}_{35}\text{H}_{51}\text{N}_9\text{O}_8$	Bachem Americas, Inc. (California, USA)
Prednisolone ( $\geq 99\%$ purity), $\text{C}_{21}\text{H}_{28}\text{O}_5$ , 50-24-8	Sigma-Aldrich Chemical Co. (St. Louis, MO)
Bradykinin acetate (HPLC grade, $\geq 98\%$ purity), $\text{C}_{50}\text{H}_{73}\text{N}_{15}\text{O}_{11}$ , 5979-11-3	Sigma-Aldrich Chemical Co. (St. Louis, MO)
$\alpha$ -Cyano-4-hydroxycinnamic acid (CHCA), $\text{C}_{10}\text{H}_7\text{NO}_3$ , 28166-41-8	Sigma-Aldrich Chemical Co. (St. Louis, MO)



Methanol, CH <sub>4</sub> O, 67-56-1	Caledon Laboratories Ltd. (Georgetown, Ont., Canada)
Ethanol, C <sub>2</sub> H <sub>6</sub> O, 64-17-5	Caledon Laboratories Ltd. (Georgetown, Ont., Canada)
Acetonitrile, C <sub>2</sub> H <sub>3</sub> N, 75-05-8	Caledon Laboratories Ltd. (Georgetown, Ont., Canada)
Sodium chloride, NaCl, 7647-14-5	Caledon Laboratories Ltd. (Georgetown, Ont., Canada)
Hydrofluoric acid (48% by weight in water), HF, 7664-39-3	Caledon Laboratories Ltd. (Georgetown, Ont., Canada)
N <sub>2</sub> (UHP), 7727-37-9	Spectra Gases
1,3-Bis-(heptadecafluoro-1,1,2,2-tetrahydrodecyl)tetramethyldisiloxane, C <sub>24</sub> H <sub>20</sub> F <sub>34</sub> OSi <sub>2</sub> (BisF <sub>17</sub> ), 129498-18-6	Gelest (Morrisville, PA)
3-(Perfluorooctyl)-propyl-1-maleimide, C <sub>15</sub> H <sub>8</sub> F <sub>17</sub> NO <sub>2</sub> , 852527-40-3	Fluorous Technologies Inc. (Pittsburgh, PA)
A peptide of LRRASLGC (HPLC grade, ≥98% purity, custom synthesis), C <sub>35</sub> H <sub>67</sub> N <sub>14</sub> O <sub>10</sub> S	GenScript USA Inc. (Piscataway, NJ)
Bovine serum albumin (BSA)	Sigma-Aldrich Chemical Co. (St. Louis, MO)
Dithiothreitol (DTT), C <sub>4</sub> H <sub>10</sub> O <sub>2</sub> S <sub>2</sub> , 3483-12-3	Sigma-Aldrich Chemical Co. (St. Louis, MO)
Ammonium bicarbonate, NH <sub>4</sub> HCO <sub>3</sub> , 1066-33-7	Sigma-Aldrich Chemical Co. (St. Louis, MO)
Sequencing-grade modified trypsin	Promega (Madison, WI)
Hydrogen peroxide (30% solution), H <sub>2</sub> O <sub>2</sub> , 7722-84-1	EMD Chemicals Inc. (Gibbstown, NJ)
Trifluoroacetic acid (TFA), C <sub>2</sub> HF <sub>3</sub> O, 76-05-1	Caledon Laboratories Ltd. (Georgetown, Ont., Canada)

Sulfuric acid, H <sub>2</sub> SO <sub>4</sub> , 7664-93-9	Caledon Laboratories Ltd. (Georgetown, Ont., Canada)
Acetic acid, C <sub>2</sub> H <sub>4</sub> O <sub>2</sub> , 64-19-7	Caledon Laboratories Ltd. (Georgetown, Ont., Canada)
Protein kinase A(PKA)	New England Biolabs Ltd.( Pickering, Ontario)
Tyrosine kinase enzyme (Abl)	New England Biolabs Ltd.( Pickering, Ontario)
PKA reaction buffer (including 50mM Tris-HCl, 10mM MgCl <sub>2</sub> and pH 7.5 at 25 °C)	New England Biolabs Ltd.( Pickering, Ontario)
NEBuffer for Abl (including 50mM Tris-HCl, 10mM MgCl <sub>2</sub> , 1mM EGTA, 2mM DTT, 0.01% Brij 35 and pH 7.5 at 25 °C)	New England Biolabs Ltd.( Pickering, Ontario)
Peptide of IYAAPKKKC, C <sub>47</sub> H <sub>81</sub> N <sub>12</sub> O <sub>11</sub> S	GenScript USA Inc. (Piscataway, NJ)
Standard phosphorylation peptide, LRRASpLGC (HPLC grade, ≥98% purity, custom synthesis)	GenScript USA Inc. (Piscataway, NJ)
C-Methylcalix[4]resorcinarene, C <sub>32</sub> H <sub>32</sub> O <sub>8</sub> , 65338-98-9	Sigma-Aldrich Chemical Co. (St. Louis, MO)
Calix[4]arene, C <sub>28</sub> H <sub>24</sub> O <sub>4</sub> , 74568-07-3	Sigma-Aldrich Chemical Co. (St. Louis, MO)
Ammonium bicarbonate, NH <sub>4</sub> HCO <sub>3</sub> , 1066-33-7	Sigma-Aldrich Chemical Co. (St. Louis, MO)
Imatinib mesylate (a crystalline solid, purity, ≥98%), C <sub>29</sub> H <sub>31</sub> N <sub>7</sub> O, 152459-95-5	Cayman Chemical (Ann Arbor, MI)
Staurosporine (a solution in ethyl acetate, purity, ≥98%), C <sub>28</sub> H <sub>26</sub> N <sub>4</sub> O <sub>3</sub> , 62996-74-1	Cayman Chemical (Ann Arbor, MI)
Titanium foil (Ti, 0.1 mm thick, 99.99% purity), 7440-32-6	Sigma-Aldrich Chemical Co. (St. Louis, MO)

Tungsten foil (W, 0.127mm thick, 99.9% purity), 7440-33-7	Sigma-Aldrich Chemical Co. (St. Louis, MO)
Caffeine, C <sub>8</sub> H <sub>10</sub> N <sub>4</sub> O <sub>2</sub> , 58-08-2	Sigma-Aldrich Chemical Co. (St. Louis, MO)
Fluorouracil, C <sub>4</sub> H <sub>3</sub> FN <sub>2</sub> O <sub>2</sub> , 51-21-8	Sigma-Aldrich Chemical Co. (St. Louis, MO)
Quinidine, C <sub>20</sub> H <sub>24</sub> N <sub>2</sub> O <sub>2</sub> , 56-54-2	Sigma-Aldrich Chemical Co. (St. Louis, MO)
Dexamethasone, C <sub>22</sub> H <sub>29</sub> FO <sub>5</sub> , 50-02-2	Sigma-Aldrich Chemical Co. (St. Louis, MO)
Erythromycin, C <sub>37</sub> H <sub>67</sub> NO <sub>13</sub> , 114-07-8	Sigma-Aldrich Chemical Co. (St. Louis, MO)
Silver chloride, AgCl, 7783-90-6	Caledon Laboratories Ltd. (Georgetown, Ont., Canada)
(R)-(+)-1-Phenylethanol, 1517-69-7 and (S)-(-)-1-Phenylethanol, 1445-91-6, C <sub>8</sub> H <sub>10</sub> O	Sigma-Aldrich Chemical Co. (St. Louis, MO)
Fluorous mass-tagged N-acylprolines (custom synthesis), C <sub>20</sub> H <sub>16</sub> F <sub>13</sub> O <sub>3</sub> N and C <sub>22</sub> H <sub>16</sub> F <sub>17</sub> O <sub>3</sub> N	Fluorous Technologies Inc. (Pittsburgh, PA)
1,3-Dicyclohexylcarbodiimide (DCC), C <sub>13</sub> H <sub>22</sub> N <sub>2</sub> , 538-75-0	Sigma-Aldrich Chemical Co. (St. Louis, MO)
4-Dimethylaminopyridine (DMAP), C <sub>7</sub> H <sub>10</sub> N <sub>2</sub> , 1122-58-3	Sigma-Aldrich Chemical Co. (St. Louis, MO)
Dichloromethane, CH <sub>2</sub> Cl <sub>2</sub> , 75-09-2	Caledon Laboratories Ltd. (Georgetown, Ont., Canada)
Phosphoric acid, H <sub>3</sub> PO <sub>4</sub> , 7664-38-2	Caledon Laboratories Ltd. (Georgetown, Ont., Canada)

## **2.2: Instrumentation**

The following section is a description of the major pieces of equipment used in this thesis.

### **2.2.1: The set-up for preparation of pSi**

A home-made silicon wafer etching cell was built for this work which was composed of two circular Teflon sections, as shown in the Fig. 2.1; a bottom piece and a top piece sealed by an O-ring and held together by screws. The anode, connected to the silicon wafer using conductive copper tape attached to its backside, provided electrical contact as a working electrode, while a platinum wire acting as the cathode was positioned within the cell cavity as a counter electrode.

In galvanostatic mode, a VersaSTAT 3 potentiometer operating off the V3-Studio software package controlled the current between the counter and working electrodes at a specified voltage; specifically, the potential applied to the counter electrode was set to establish the desired cell current.

### **2.2.2: Mass spectrometer**

In general, any mass spectrometer designed for MALDI MS can be used for NIMS without further modification. In this work, an Applied Biosystems/MDS Sciex API-365 LC/MS/MS triple quadrupole (QqQ) electrospray ionization (ESI) MS reconfigured with a home-made MALDI ion source, was provided as an in-kind contribution to this research project by MDS Analytical Technologies. As shown in Fig. 2.2, NIMS chips were attached to the face of a home-made MALDI target plate using electrically conductive double-sided tape. The triple QqQ-MS was maintained at a

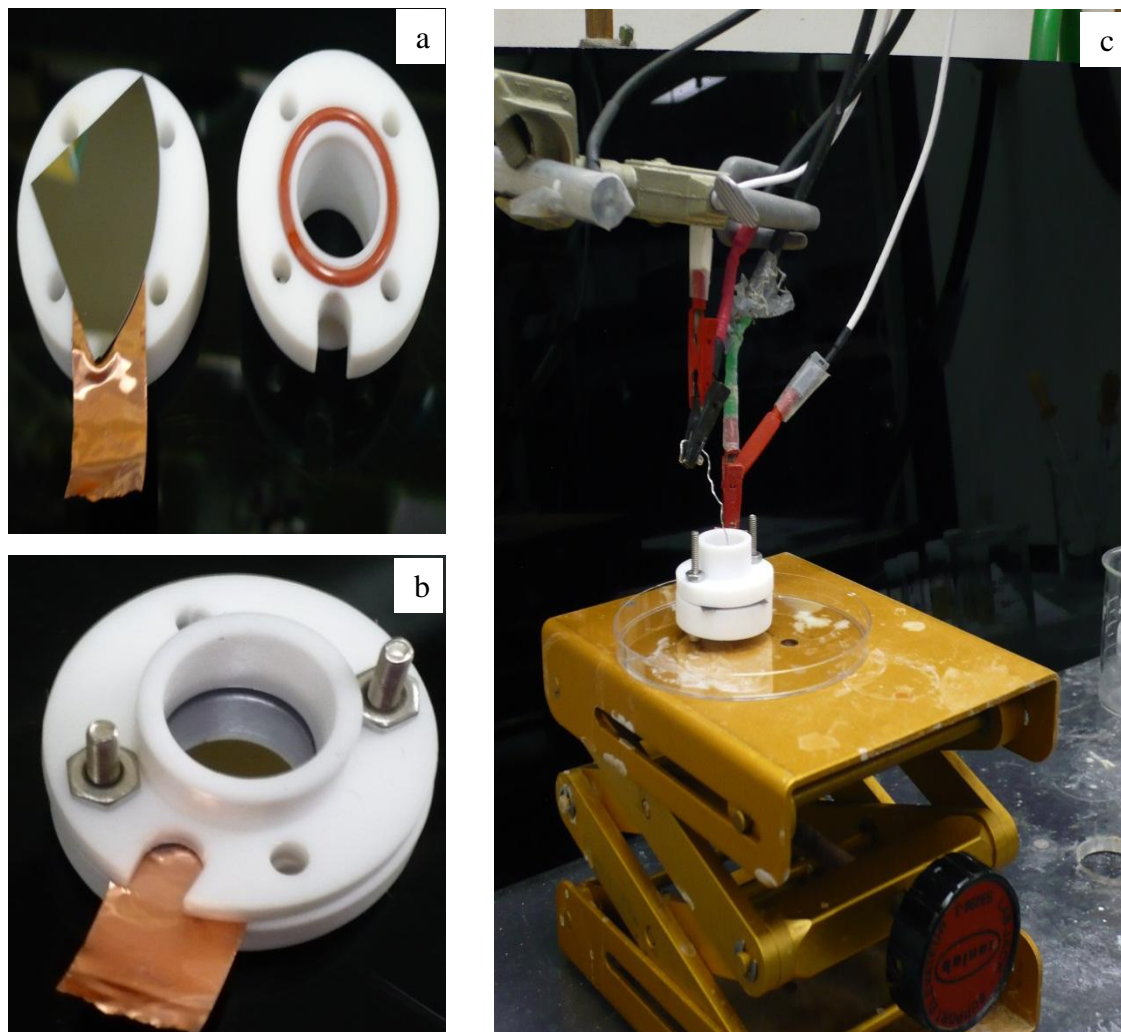


Fig. 2.1: The Teflon cell assembly used for etching Si wafers electrochemically. a) The silicon wafer or chip is placed with its polished side facing the O-ring. A section of conductive copper tape is attached on its backside with a section sticking outside of the assembly; b) The Teflon base is attached to the top half of the assembly with the chip sandwiched between; c) The positive (+) (red) electrode is attached to the silicon wafer chip by clipping a lead to the conductive copper foil while the negative (-) (black) electrode was attached to a platinum wire.

pressure less than  $\sim 10^{-5}$  Torr by two turbo pumps connected in parallel and backed by a mechanical pump.

UV pulses from a  $N_2$  laser were directed to the sample plate via an optical fiber and focused to a spot on the NIMS chip surface with an  $f = 10$  cm focal length lens.  $N_2$  gas (0.1 Torr, UHP) was introduced into the ionization region of the spectrometer to cool the ions and improve the ion focusing. The laser pulse energy was adjusted with a variable beam attenuator, and the laser intensity at the output of the optical fiber was measured with a NOVA Laser Power/Energy Monitor (OPHIR). The resultant ions were mass dispersed within the triple quadrupole and detected using a channeltron electron multiplier (CEM, Burle Industries).

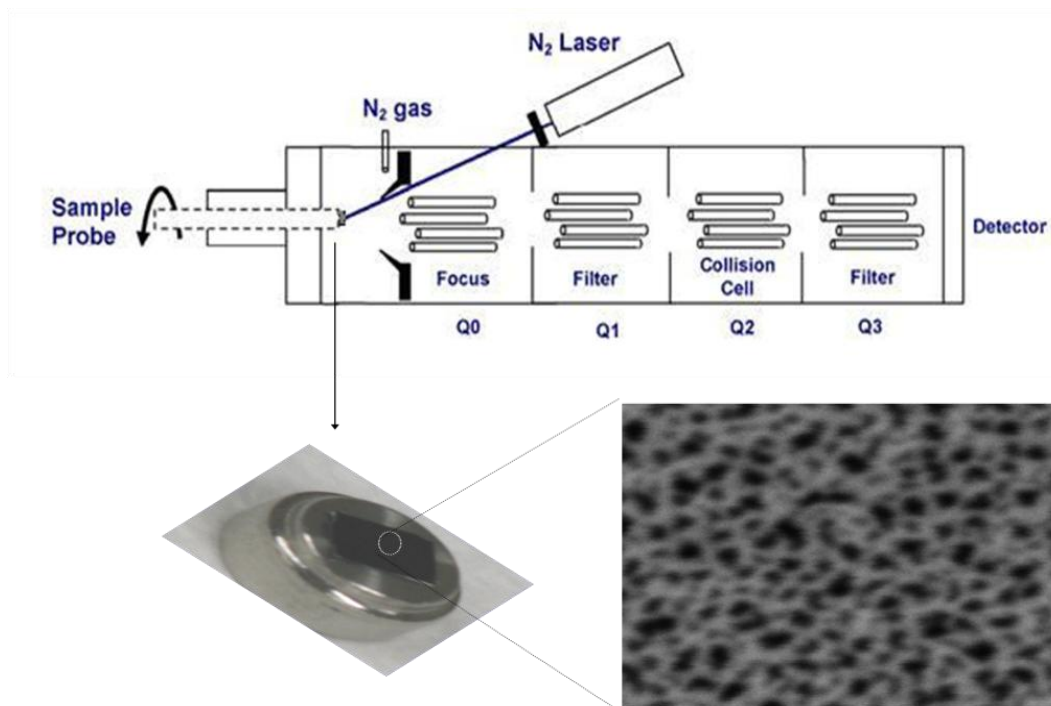


Fig. 2.2: A schematic of the experimental apparatus used to perform NIMS. The SEM image (lower right) of the pSi substrate shows the typical morphology of the NIMS chip surfaces used in this work (lower left).

### 2.2.3: Laser equipment

**Nitrogen laser:** In this work, two N<sub>2</sub> lasers having an output of 4 ns long pulses at wavelength  $\lambda = 337$  nm were operated at a repetition rate of 10 Hz. One was manufactured by Thermo Laser Science (model VSL-337ND-S) while the other was made by Laser Science, Inc. (LSI). They both use a replaceable and sealed laser cartridge which includes the laser cavity, high voltage storage capacitors, a switching element, and can be triggered internally or externally. A variable optical power attenuator (Mitutoyo) was mounted on the output side of the N<sub>2</sub> laser, allowing the laser energy to be manually changed and precisely controlled.

**Neodymium: Yttrium Aluminum Garnet (Nd:YAG ) laser operating at 355 nm:** 4 ns infrared (IR) laser pulses at  $\lambda = 1064$  nm were generated at a repetition rate of 20 Hz using a Q-switched Nd:YAG laser (Spectra Physics, PRO 250). The IR output was frequency-doubled to 532 nm in a nonlinear potassium dideuterium phosphate (KDP) crystal. The resultant 532 nm output was then frequency-mixed with the residual 1064 nm fundamental to produce UV light at 355 nm. The UV output was subsequently used for the MS experiments described in this thesis.

In general, the Spectra Physics Nd:YAG laser uses an injection seeder (Spectra Physics Model 6350) to achieve single mode operation by injecting very narrow line width radiation into the laser cavity at a time when the Q-switch is opened. In a Q-switched laser, energy is stored in the laser medium during flash-lamp pumping by ensuring the quality (Q) factor of the cavity is low. That energy is then released rapidly in a single, short burst by switching the Q-factor of the cavity to a high value. Specifically, in the Spectra Physics device during operation the flash lamp excites the Nd<sup>3+</sup> ions in the

YAG rods for  $\sim 200 \mu\text{s}$ , building up a large population inversion. When a high voltage pulse is applied to an opto-electronic Q-switch (Pockel cell), the threshold gain in the cavity is reduced. This results in a giant pulse of light (duration  $< 10 \text{ ns}$ ) with a peak optical power of tens of megawatts in the infrared ( $\lambda = 1064 \text{ nm}$ ). During seeded operation, a narrow line width laser emission from a diode laser is injected on-axis into the Nd:YAG laser cavity which is resonantly amplified by the flash-lamp/Q-switch assembly. As a result a Q-switched pulse of the seed emission builds up. Seeding prepopulates one specific longitudinal mode with photons, giving this mode an advantage of being amplified more rapidly and finally becoming the dominant output signal. The output of an injection seeded Nd:YAG laser is highly monochromatic, and consequently, has a long coherence length [74].

**Nd:YAG laser operating at 532 nm:** Coherent radiation at 532 nm was generated by frequency doubling the output of a Q-switched Nd: YAG laser (Quanta-Ray GCR-4;  $\lambda = 1064 \text{ nm}$ ) in a KDP nonlinear crystal. The 532 nm laser beam operating at a 10Hz repetition rate was introduced into a 100  $\mu\text{m}$  diameter optical fiber using a 5 cm focal length lens and directed towards the sample plate of the mass spectrometer. The laser intensity at the output of the optical fiber was regulated by a half-wave plate and polarizer combination, and measured with a laser power meter. This particular Nd:YAG laser is not injection seeded.

#### **2.2.4: Other pieces of equipment**

**The VersaSTAT 3:** The VersaSTAT 3 (Princeton Applied Research; Oak Ridge, TN) is a simple, flexible, and extremely powerful system for performing a wide range of electrochemical measurements. It can serve as either a potentiostat or galvanostat, and if



desired, a frequency response analyzer (FRA). The unit can be controlled by the V3-Studio electrochemistry software package using any PC equipped with a suitable Universal Serial Bus (USB) interface.

**Scanning electron microscopy (SEM):** Scanning electron microscopy (SEM) images were obtained using the LEO-ZEISS 1540XB CrossBeam instrument located in the Nanofabrication Laboratory in the Department of Physics and Astronomy of the University of Western Ontario. The instrument has a high resolution Fast Ion Beam (FIB) for precision milling, and can provide a high resolution images that allow fabricated nanostructures to be inspected in real time.

**Digital pulse generator:** A digital pulse generator (Stanford Systems Research Inc; Model DG535) was used to trigger the oscilloscope, the N<sub>2</sub> laser and the Nd:YAG laser, and synchronize the different optical and mechanical components of the apparatus used in two-laser system.

## **2.3: Experimental methods**

### **2.3.1: Preparation of a fluororous-affinity NIMS chip**

NIMS chips are not commercially available. The preparation of a fluororous-affinity NIMS chip involves a series of steps such as pre-etching treatment, assembling the Teflon cell, handling it after etching, loading initiators and immobilizing fluororous affinity tags. The details are as follows:

#### **Treatment before etching:**

- Silicon chips of an appropriate size are cut from a Si wafer using a diamond tip scribe and a ruler prior to insertion into the etching chamber.

- The cut wafers are soaked in glass Petri dishes containing Piranha solution for 60 minutes. A Piranha solution is composed of concentrated sulfuric acid and hydrogen peroxide in a fixed volume ratio of  $\text{H}_2\text{SO}_4:\text{H}_2\text{O}_2 = 2:1$ . In general, it was found that the cleaning is more effective using freshly prepared Piranha solution for each use presumably because concentrated sulfuric acid and hydrogen peroxide easily evaporate, changing the volume ratio with time and thereby decreasing the oxidation effectiveness of the solution.
- After cleaning, the silicon chips are removed from the Petri dish using stainless steel tweezers, rinsed immediately with deionized water, and blown dried rapidly by a jet of UHP  $\text{N}_2$ . The process is repeated approximately 3~5 times. It should be noted that methanol and other organic solvents cannot be used to rinse the just-soaked wafers, since the mixing of Piranha solution with organic solvents may cause a fire or an explosion.
- All experimental components (Teflon lid and base, electrodes, platinum wire, tweezers, etc) are cleaned in methanol for 15 minutes using an ultrasonic cleaner.

**Steps for assembling the Teflon cell, and for electrochemical etching:**

- An O-ring is placed into the groove of the Teflon lid.
- The silicon chip is placed with its polished side facing the O-ring. A section of conductive copper tape is attached in the other side of the chip with part of the copper tape sticking outside of the assembly.
- The Teflon base is joined with the top half of the assembly with the Si chip sandwiched between.

- The assembly is secured with screw caps.
- The assembly is leak tested by placing some methanol in the chamber. The methanol is poured out if the seal is good, and the assembly blown dry with UHP nitrogen.
- The assembly is placed in a Petri dish on a stainless steel lift, and positioned to ensure that the platinum wire is centered in the middle of the cell.
- The positive (+) electrode is attached directly to the conductive copper tape while the negative (-) electrode made from a platinum wire is mounted onto a support stand.
- The stainless steel base is lifted so that the platinum wire first makes contact with the top of the chip inside the chamber. The base is then lowered to ensure that the distance (~1 cm) between the platinum wire and silicon surface is the same for each experiment.
- An etching solution composed of a mixture of HF and ethanol is carefully added to the cell to just cover the platinum wire and chip.
- The electrochemical etching is processed in galvanostatic mode using the VersaSTAT 3 system for 30 minutes operating at a constant current of 96 mA. This corresponds to a current density of  $45 \text{ mA/cm}^2$ .

**After etching:**

- Both electrodes are removed from the etching cell and washed to remove any excess HF/ethanol solvent. This is especially important for the platinum electrode because it is in direct contact with the HF/ethanol solvent. Prolonged

exposure causes corrosion and contamination.

- The HF/ethanol solution is carefully poured out of the assembly into a plastic beaker. The assembly is subsequently thoroughly washed with methanol.
- The Teflon cell is dried under UHP nitrogen and then disassembled by reversing the assembly procedure provided above.
- The chip is carefully removed with a pair of tweezers and washed with methanol to remove any excess HF/ethanol solution. The chip is then dried under UHP nitrogen. This step is repeated ~3-4 times.
- Lastly, the chip is baked in an oven (Fisher Scientific) at 120°C for ~5 minutes.

#### **Loading the initiators**

- ~ 2  $\mu\text{L}$  of an initiator molecule such as BisF<sub>17</sub> is spotted to cover the pSi chip surface and kept in a Petri dish for approximately 30-60 minutes at room temperature.
- Excess initiator is blown off from the chip surface using a strong jet of UHP N<sub>2</sub> gas until a thin film of initiator is left covering the pSi chip.
- The resultant NIMS chip is briefly placed in a 100 °C oven for 3-5 seconds, and then placed under a UHP N<sub>2</sub> again to blow off the excess initiator. These steps are repeated about 3-5 times until the chip surface is partially dry. Drying the chip completely and leaving too much initiator on its surface impacts the NIMS performance.

#### **Immobilizing the fluorine affinity tag:**

- A 1 mM stock solution is prepared by adding 55.7 mg of 3-(perfluoroalkyl) propyl-1-maleimide ( $C_{15}H_8F_{17}NO_2$ , RF<sub>17</sub>) into 100 mL methanol solvent, and then diluting to 10  $\mu$ M using neat methanol solvent.
- 1  $\mu$ L of such solution (10  $\mu$ M) is spotted onto the NIMS chip. The fluororous-tagged molecules with a maleimide-functionalized group are held to the chip by non-covalent fluorine-fluorine interactions between the fluororous tag and the perfluorous initiator molecules trapped within the nanostructured surface.

### 2.3.2: NIMS MS experimental procedure

The surface of each NIMS chip, anchored to a sample probe using electrically-conducting double-sided carbon tape, were spotted with analyte using a pipette (Fig.2.3), and then placed inside the home-build MALDI mass spectrometer. The chips could be irradiated with the output of a pulsed N<sub>2</sub> laser ( $\lambda = 337$  nm), Nd:YAG laser ( $\lambda = 355$  nm) or Nd:YAG laser ( $\lambda = 532$  nm), operating at a 10 Hz repetition rate. In general, the total volume used per spotting was 1  $\mu$ L (unless stated otherwise) and the NIMS analysis was performed by scanning the Q1 quadrupole in positive ion mode. The optimal voltage and gas pressure settings used for operating the triple quadrupole mass spectrometer are listed in Table 2.2.

Typically, each mass spectrum is acquired using ~1000 laser shots, each pulse having 5  $\mu$ J of energy. Spectra were collected from at least 5 different positions on the NIMS chip. The peak intensity of a specific mass peak is reported after normalizing to the intensity of the strongest feature in the spectrum.

Collision-induced dissociation (CID) spectra of certain species could also be

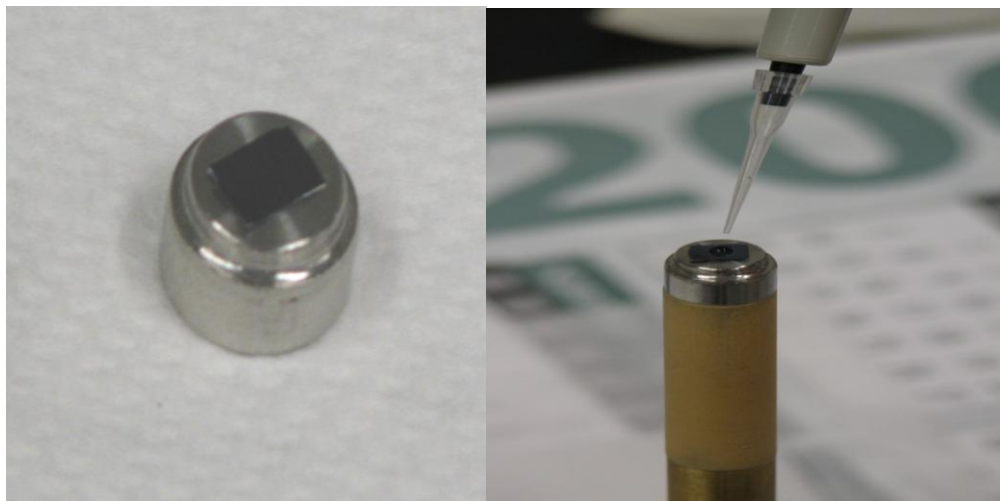


Fig. 2.3: The photo on the left shows a NIMS chip mounted onto the face of an in-house modified MALDI target plate with double-sided adhesive tape. The photo on the right shows the NIMS chip being spotted with analyte solution using a pipette.

**Table 2.2: Mass spectrometer operating settings for NIMS experiments in positive ion mode**

Nebulizer gas pressure (NEB)	1 mTorr
Curtain gas pressure (CUR)	3 mTorr
Collision gas pressure (CAD)	0
Orifice ring voltage (OR)	5.0 V
Quadrupole 2 rod offset voltage (RO2)	-25.0 V
Focusing ring voltage (RNG)	0.0 V
Quadrupole 0 rod offset voltage (Q0)	-6.00 V
Inter-quad 3 lens voltage (IQ3)	-26.5 V
Quadrupole 3 rod offset voltage (RO3)	-27 V
Deflector voltage (DF)	-400.0 V
Channeltron electron multiplier voltage (CEM)	1800.0 V

recorded for MS/MS analysis, for example, a peptide containing a cysteine residue with a relatively intense peak in the mass spectrum, selected from a BSA digest. Operationally, a selected ion is accelerated to a kinetic energy by a potential difference of 30 V between Q0 and Q2 (Fig. 2.2). The collision gas ( $N_2$ ) pressure of approximately  $2.0 \times 10^{-3}$  Torr was then used to obtain the product spectrum of the selected precursor ion,  $[A+H]^+$  over a mass range of  $m/z$  100-1500.

### **2.3.3: Enrichment of cysteine-containing peptides**

A NIMS chip spotted with a fluoruous affinity tag was dosed by aliquots of a peptide mixture containing Pep1 (YAGFLR; 200 fmol), Pep2 (LRRASLGC; 200 fmol) and Pep3 (RPPGFSPFR; 200 fmol), dissolved in a 70 % acetonitrile water solution by volume with 1% Dithiothreitol (DTT). The substrates were kept in a humidified 6-liter water bath chamber at 60 °C for 60 min, washed with 40% methanol and water solution with 0.1% Trifluoroacetic acid (TFA) 3-5 times and then dried under a stream of UHP nitrogen. Note, the capital letters labeling the peptides correspond to the standard 1-letter codes used for amino acid residues in a protein. The abbreviations for the 20 common amino acids are listed in Table 2.3.

A tryptic digestion of BSA was performed by denaturing 1 mg of sample in 1 mL of boiling distilled water for 60 minutes. 1 mL of 2 mM DTT was then added to the BSA solution and maintained at 60 °C for 30 minutes to cleave any disulfide bonds. After cooling to room temperature, 20 µg of sequencing-grade trypsin was added to the BSA solution with a final protease: protein ratio of 1:50. The reaction mixture was then incubated at 37 °C overnight. The digest was quenched by the addition of 10 µL of acetic acid. Subsequently, 1 µL of the BSA tryptic digestion was spotted onto the fluoruous-

affinity NIMS chip to enrich the subset of peptides containing cysteine residues according to the aforementioned method.

**Table 2.3: Abbreviations used for amino acids**

<b>Amino Acid</b>	<b>Three-Letter Abbreviation</b>	<b>One-Letter Abbreviation</b>
Alanine	Ala	A
Arginine	Arg	R
Asparagine	Asn	N
Cysteine	Cys	C
Glutamate	Glu	E
Glutamine	Gln	Q
Glycine	Gly	G
Histidine	His	H
Isoleucine	Ile	I
Leucine	Leu	L
Lysine	Lys	K
Methionine	Met	M
Phenylalanine	Phe	F
Proline	Pro	P
Serine	Ser	S
Threonine	Thr	T
Tryptophan	Trp	W
Tyrosine	Tyr	Y
Valine	Val	V



### 2.3.4: Enzyme activity assay

A substrate (Pep2; 200 fmol) for protein kinase A (PKA) was spotted onto a NIMS chip with the fluororous affinity tag prepared as described above, and then treated with 1  $\mu$ L of enzyme solution. Protein kinase assays were performed according to the manufacturer's protocol for PKA. In brief, reaction mixtures containing 200  $\mu$ M ATP, 10 mM MgCl<sub>2</sub>, and 1 unit/ $\mu$ L PKA in Tris-HCl buffer (pH 7.5) were added to a substrate of the enzyme in a humid chamber at 30 °C for 30 min. The chip surface was then rinsed using 40% methanol water solution and analyzed by NIMS.

For an enzymatic inhibition assay, the inhibitor of staurosporine or imatinib was added to an enzyme reaction mixture and prepared in a series of concentrations using PKA reaction buffer or NEBuffer, respectively. 1  $\mu$ L of each reaction mixture was spotted onto the NIMS chip and incubated at 30 °C for 30 minutes. After the kinase reaction, the chip was rinsed and analyzed according the procedure described above.

### 2.3.5: Measurement of enantiomeric excess by kinetic resolution and NIMS

A solution of 1-phenylethanol (10 nmol in 1  $\mu$ L of CH<sub>2</sub>Cl<sub>2</sub>) was placed on a pSi NIMS substrate covered with BisF<sub>17</sub> initiator. A mixture of (R)-N-acylproline (100 nmol) with a (-C<sub>6</sub>F<sub>13</sub>) fluororous tag and (S)-N-acylproline (100 nmol) with a (-C<sub>8</sub>F<sub>17</sub>) fluororous tag in 10  $\mu$ L of CH<sub>2</sub>Cl<sub>2</sub> was then added, followed by 5  $\mu$ L of a mixture of 4-dimethylaminopyridine (DMAP, 100 nmol) and 1,3-Dicyclohexyl- carbodiimide (DCC, 10  $\mu$ mol). NIMS analyses were performed after evaporating the CH<sub>2</sub>Cl<sub>2</sub> solvent at room temperature.

### 2.3.6: Methodology to fabricate $\text{WO}_3$ and $\text{TiO}_2$ substrates

$\text{WO}_3$  substrates for NIMS were prepared using 0.127 mm thick tungsten foil (99.9% purity). A microstructured surface was generated by irradiating the W foil with the 355 nm output of a tripled Nd:YAG laser (Spectra Physics PRO-250; 4 nsec pulses; 20 Hz repetition rate) for 40 minutes in methanol solvent (intensity = 4–5  $\text{W}/\text{cm}^2$ ), as shown in Fig.2.4. The resultant  $\text{WO}_3$  substrate was subsequently rinsed with methanol solvent three times, and dried under a nitrogen gas flow for 15 minutes. The resultant  $\text{WO}_3$  substrates were activated by heating in an oven for 4 hours at 275 °C. Each  $\text{WO}_3$  substrate could be reused an indefinite number of times. Between runs, a substrate was soaked in methanol solvent for different periods of time depending on the previous analyte concentration prior to re-spotting with analyte. Heat reactivation was only necessary in those instances when the surface becomes damaged due to the use of high incident laser fluencies [75].

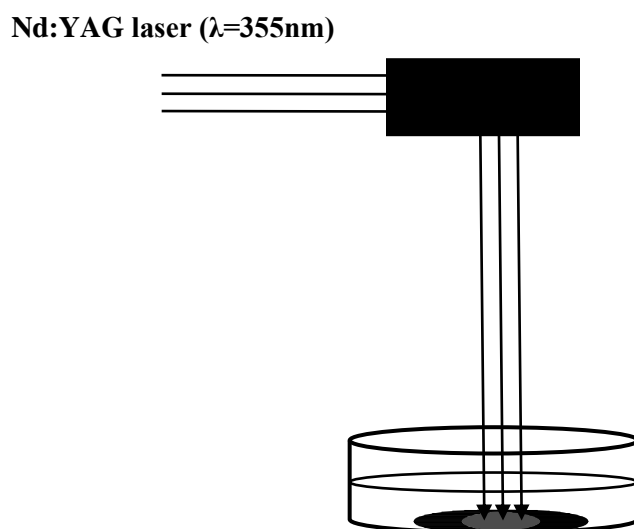


Fig.2.4: Schematic diagram of the experimental arrangement used to fabricate a microstructured  $\text{WO}_3$  NIMS chip by laser irradiation.

TiO<sub>2</sub> chips were made by sonicating pieces of titanium cut from a large foil in isopropanol, ethanol, and deionized water, respectively, and then dried under a nitrogen gas flow. The samples were then immersed into a 1M H<sub>3</sub>PO<sub>4</sub> containing 0.5 wt% HF acid electrolyte solution inside the electrochemical cell described previously in Section 2.2.1. Pt and Ti sheets served as the cathode and anode, respectively. Electrochemical etching was carried out using a potentiostat (VersaSTAT 3, Princeton Applied Research) interfaced to a computer. A potential was ramped from 0 V to 10 V at a sweep rate of 500 mV/s, and then held at 10 V for 500 seconds. After electrochemical treatment, the samples were rinsed thoroughly with deionized water and dried in a nitrogen stream. The resultant microstructured chips were baked in an oven for 20 minutes at 120 °C.

## Chapter 3: Optimization and characterization of NIMS

### 3.1: Optimized conditions for preparing NIMS chip

NIMS sample plates were made by etching a silicon wafer electrochemically in HF/ethanol solution as described in Chapter 2. The resultant matrix-free NIMS substrate can be made reproducibly and are robust, exhibiting a broader analyte mass range and higher analyte ion yield [30]. As NIMS substrates are not commercially available, users must fabricate and characterize their own. It is well-known that different parameters such as the silicon crystal orientation, light intensity, dopant type and level, current density, etching solution concentration, and etching time are able to affect the pSi morphology [76, 77]. In general, the resultant pore diameter for n-type (P-, As-, or Sb-doped) silicon increases with increasing resistivity (decreasing density of dopant atoms), while the reverse is true for p-type (boron-doped) samples. Pore depth is generally proportional to etching time for both n- and p-type materials [78]. Furthermore, a clean silicon wafer surface is essential since the pSi chips produced using silicon wafers which have not been cleaned properly before electrochemical etching leads to a background in the low-mass region of the NIMS mass spectrum [31].

In this work p-type <100> silicon wafers doped with boron were used. The main etching parameters (etching time, current density, and HF concentration), respectively, were varied to optimize the pSi sample pore size, and to maximize the signal-to-noise (S/N) ratio of the NIMS spectra. A hexapeptide Dalargin (YAGFLR) was selected as an analyte to test the NIMS performance. Dalargin is a synthetic analog of the neurotransmitter, Leu-enkephalin consisting of six amino acids. As shown in Fig. 3.1, its

primary structure is Tyr-Ala-Gly-Phe-Leu-Arg. Dalargin has been implicated in various biological activities such as cytoprotection, cardioprotection, and anti-stress activity, and has therapeutic action during alcohol withdrawal [79]. The following discussion describes these experiments.

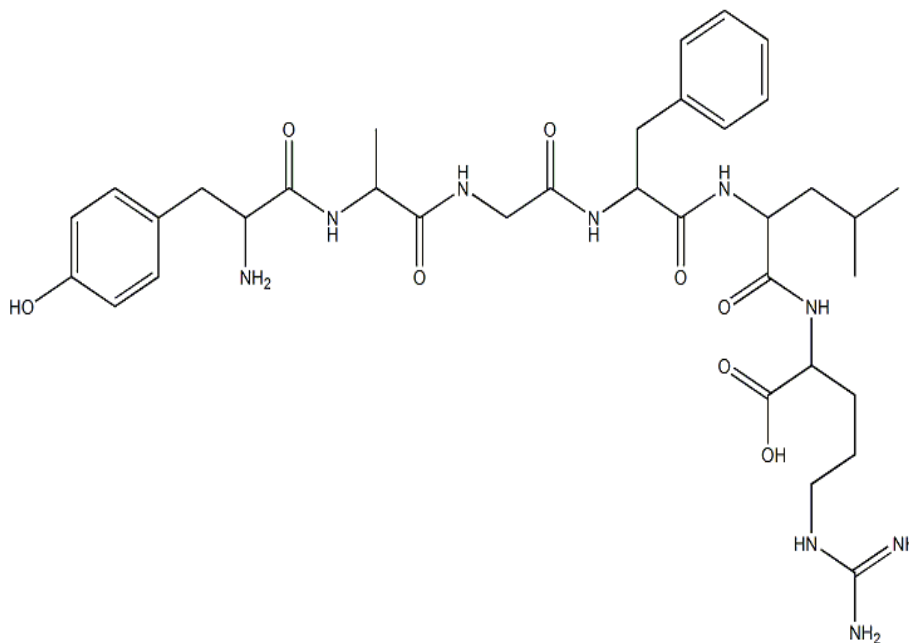


Fig.3.1: The chemical structure of the hexapeptide Dalargin

### 3.1.1: Effect of etching time on the NIMS performance

The effect of etching time on the fabrication procedure on pSi was studied by detecting the peptide Dalargin by NIMS in positive ion mode. The etching time was changed from 10 to 35 minutes at 5-minute intervals. The other etching parameters including current density and hydrofluoric acid/ethanol solution concentration were fixed to 45 mA/cm<sup>2</sup> and 50% (volume ratio), respectively. As shown in the Fig. 3.2, the optimal etching time was found to be 30 minutes. At times < 30 min the analyte ion intensities and signal-to-noise (S/N) ratios were lower while at etching times > 30 min the pSi chip

was found to be more susceptible to breaking. Fig. 3.3 shows two deep grooves that formed in the pSi chip after etching for 35 min. At these longer times the pSi chip would simply collapse due to these structural defects. Fig. 3.4 shows the NIMS spectra of Dalargin obtained for various etching times  $\leq 30$  min.

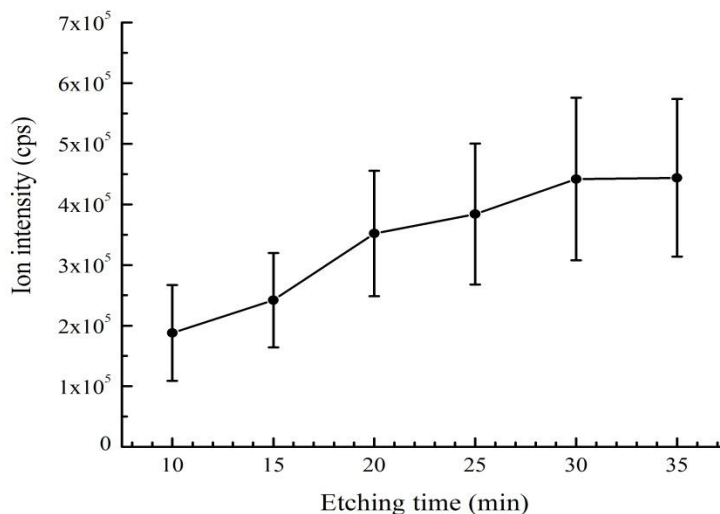


Fig. 3.2: A plot of the NIMS Dalargin ion signal as a function of pSi chip etching time.

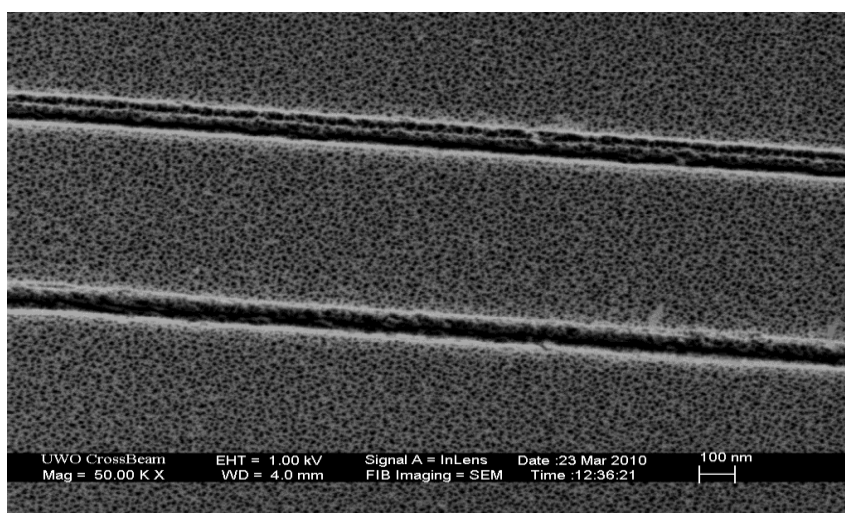


Fig. 3.3: A SEM image of pSi chip produced by electrochemical etching for 35 min at a current density =  $45\text{mA}/\text{cm}^2$  and using 50% (by volume) hydrofluoric acid ethanol solution.

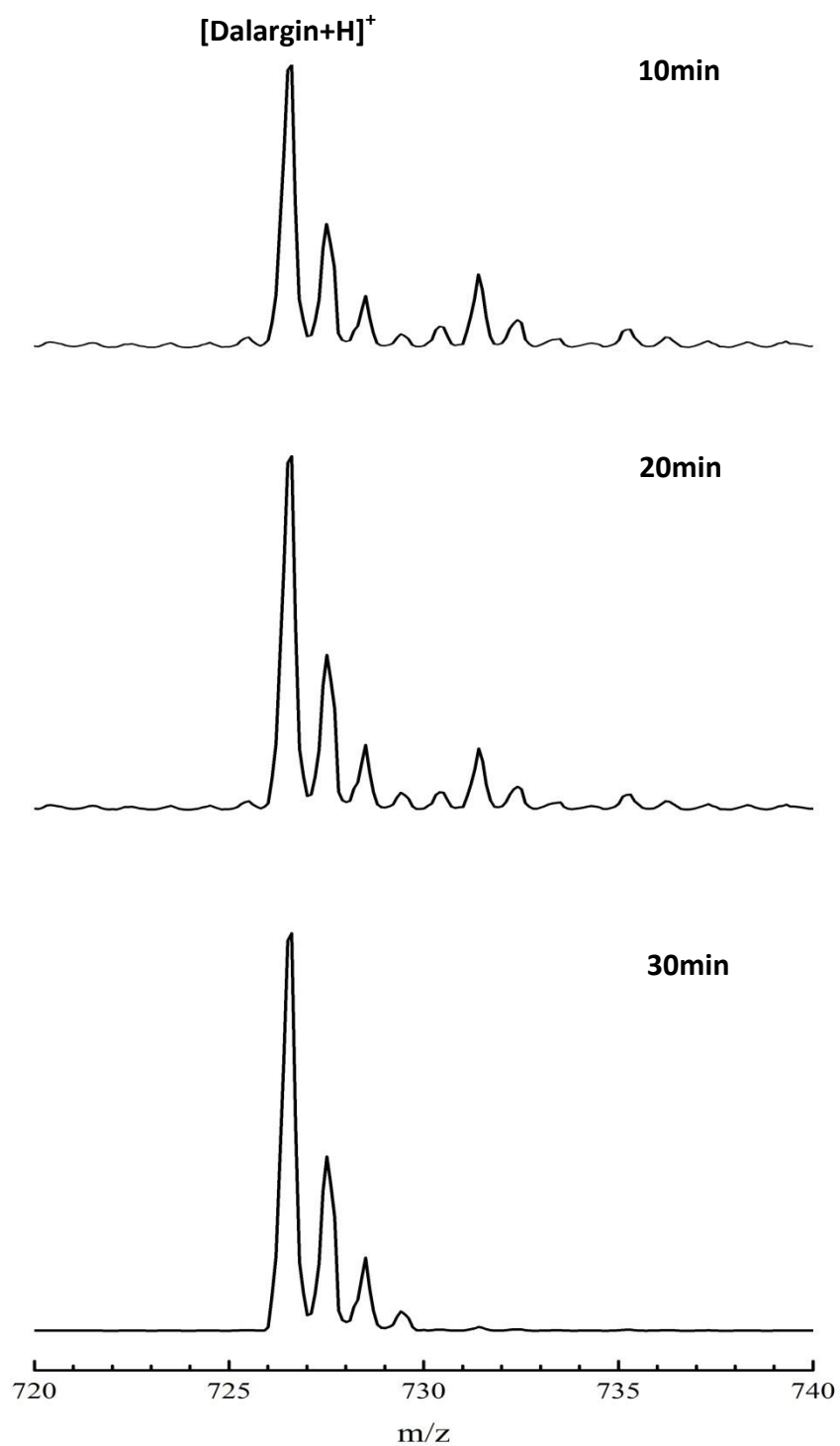


Fig. 3.4: NIMS spectra of protonated Dalargin as a function of pSi etching time using BisF<sub>17</sub> as initiator.

### **3.1.2: Effect of current density on the NIMS performance**

The pSi fabrication and NIMS signals were examined after processing the Si wafer using current densities of 10, 20, 30, 35, 40, 45, 50 mA/cm<sup>2</sup>, respectively, (Fig. 3.5). It should be stressed that the current density at the Si/electrolyte interface has more physical meaning than the absolute current alone. In this study, both the current density and the current for a given cell scale similarly because the area of the Si sample exposed to the electrolyte (1.8 cm<sup>2</sup>) is well defined. pSi formation is dependent on the current density at the Si side of the Si/electrolyte interface which forms holes that move from the bulk towards the interface. However, an overpotential can lead to electropolishing where a surface film is peeled from Si wafer resulting in a morphology that is relatively smooth and planar despite the electrical treatment [80]. The upper picture in Fig.3.6 is a photograph of pSi formed at low potential while the bottom picture shows the smooth Si surface after electropolishing at a high potential. To form pSi, the potential must be controlled between 0 V and an overpotential threshold voltage in the electrochemical etching process. Fig. 3.7 shows that the NIMS signal of protonated Dalargin is strongest when the current density = 45mA/cm<sup>2</sup> with the other parameters fixed (etching time = 30 min and HF acid:ethanol volume ratio = 1:1).

### **3.1.3: Effect of etching solution and pre-etching cleaning on the NIMS performance**

In these experiments the etching solution used was usually a 1:1 mixture by volume of HF acid and absolute ethanol. As shown in the Figs. 3.8 and 3.9 substantial deviations from these “optimum” etching conditions could be tolerated without a significant loss in performance.



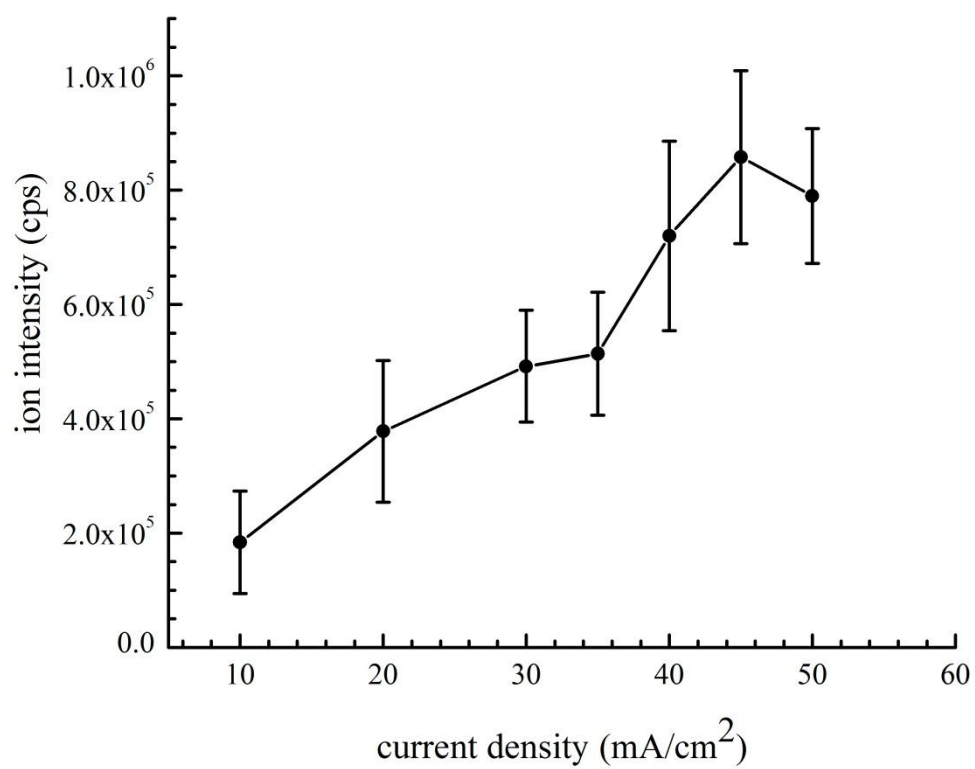


Fig. 3.5: A plot of protonated Dalargin NIMS signal as a function of current density.

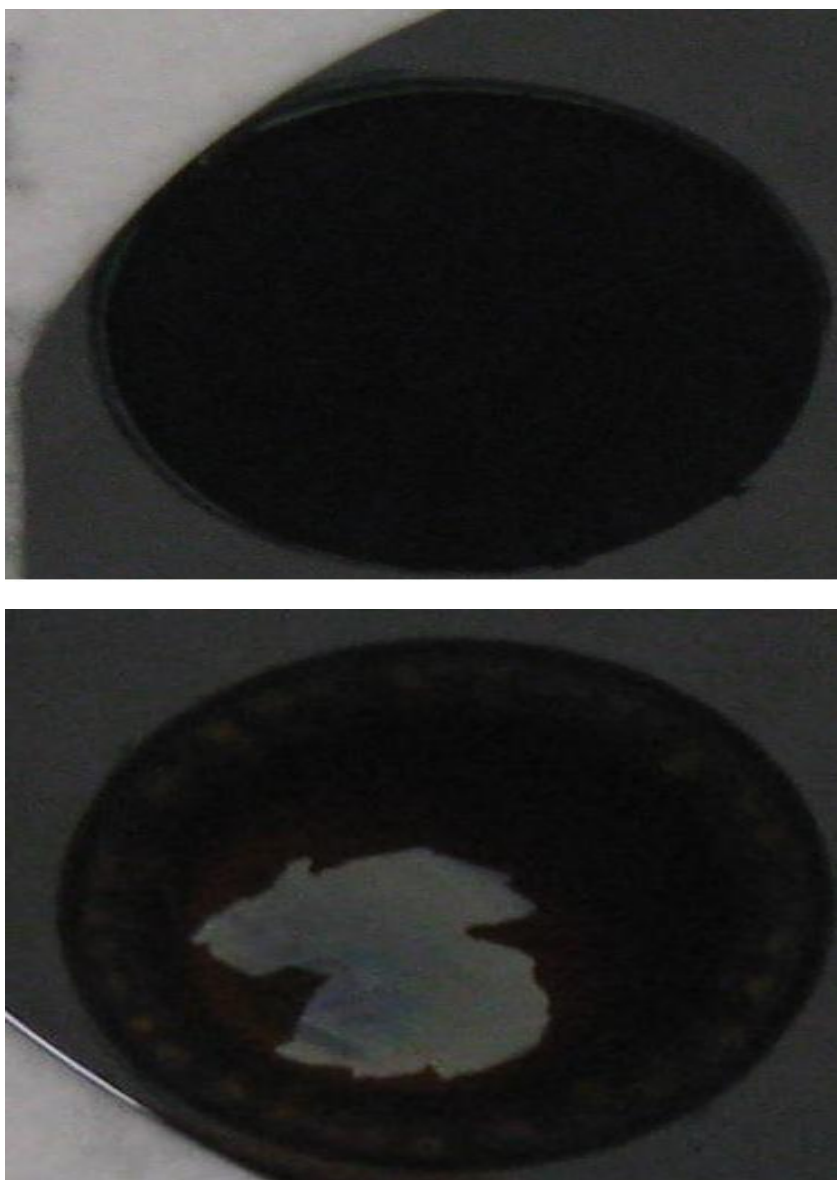


Fig. 3.6: The appearances of pSi etched at a normal electrical potential (<math>< 2.0\text{V}</math>; upper picture) and after electropolishing at an overpotential (> 2.0 V; lower picture).

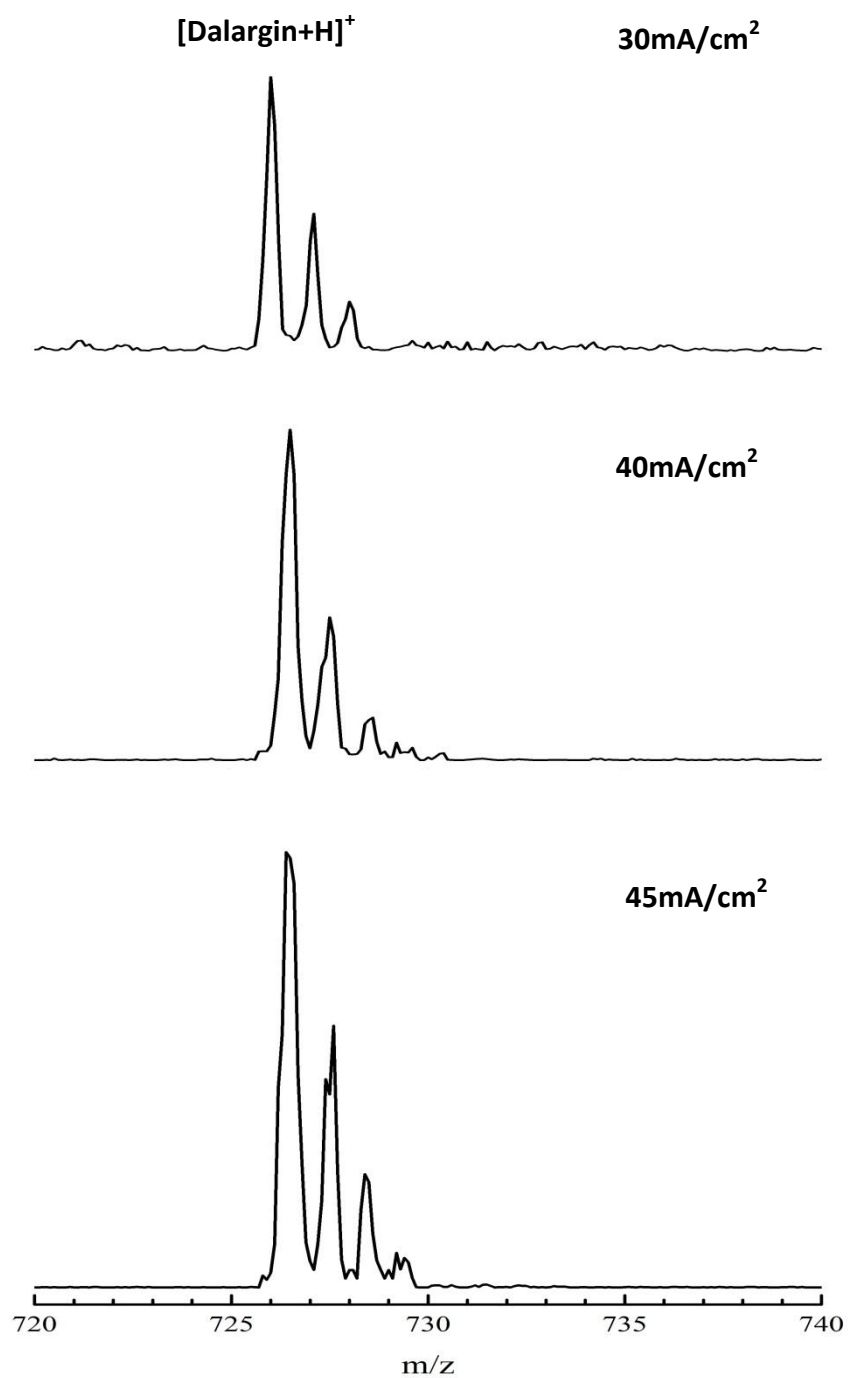


Fig. 3.7: NIMS spectra of protonated Dalargin as a function of current density using BisF<sub>17</sub> as initiator.

A clean silicon surface before electrochemical etching is crucial for obtaining high quality NIMS mass spectra with good S/N ratios. That was demonstrated in this work by comparing NIMS mass spectra of protonated Dalargin using a pSi chip prepared with and without Piranha solution cleaning before electrochemical etching. Fig.3.10 shows that a clean NIMS chip yields a mass spectrum with substantially lower background noise in the low molecular weight mass region than one produced without cleaning. Table 3.1 summarizes the critical parameters and their optimal values deduced in this study for preparing pSi.

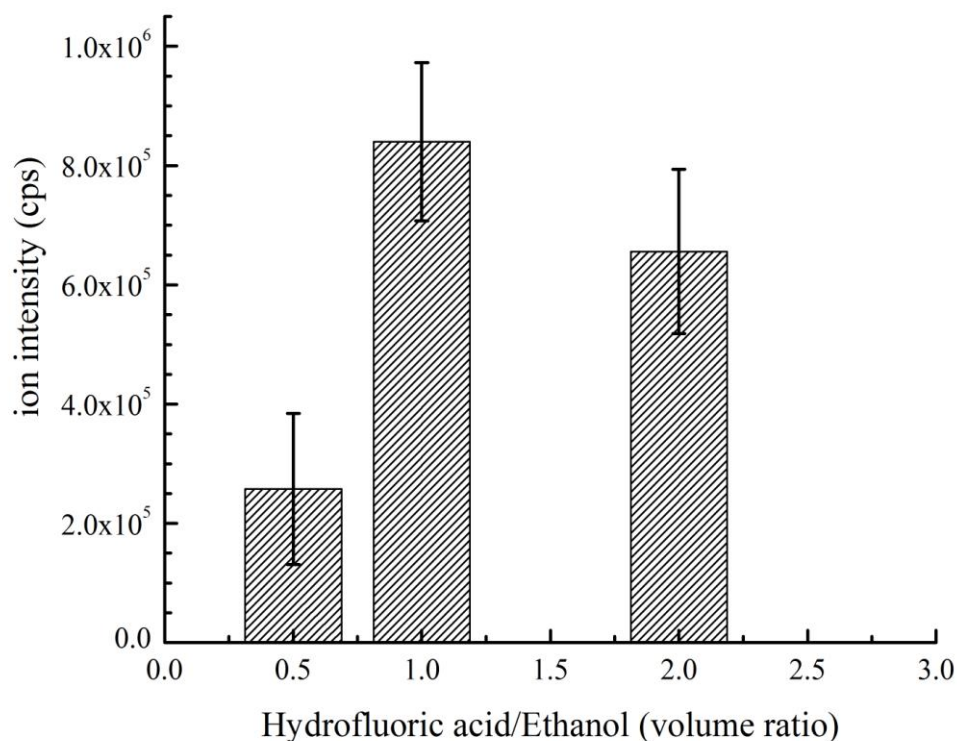


Fig. 3.8: The NIMS ion intensity (ion counts) of protonated Dalargin as a function of the etching solution volume ratio.

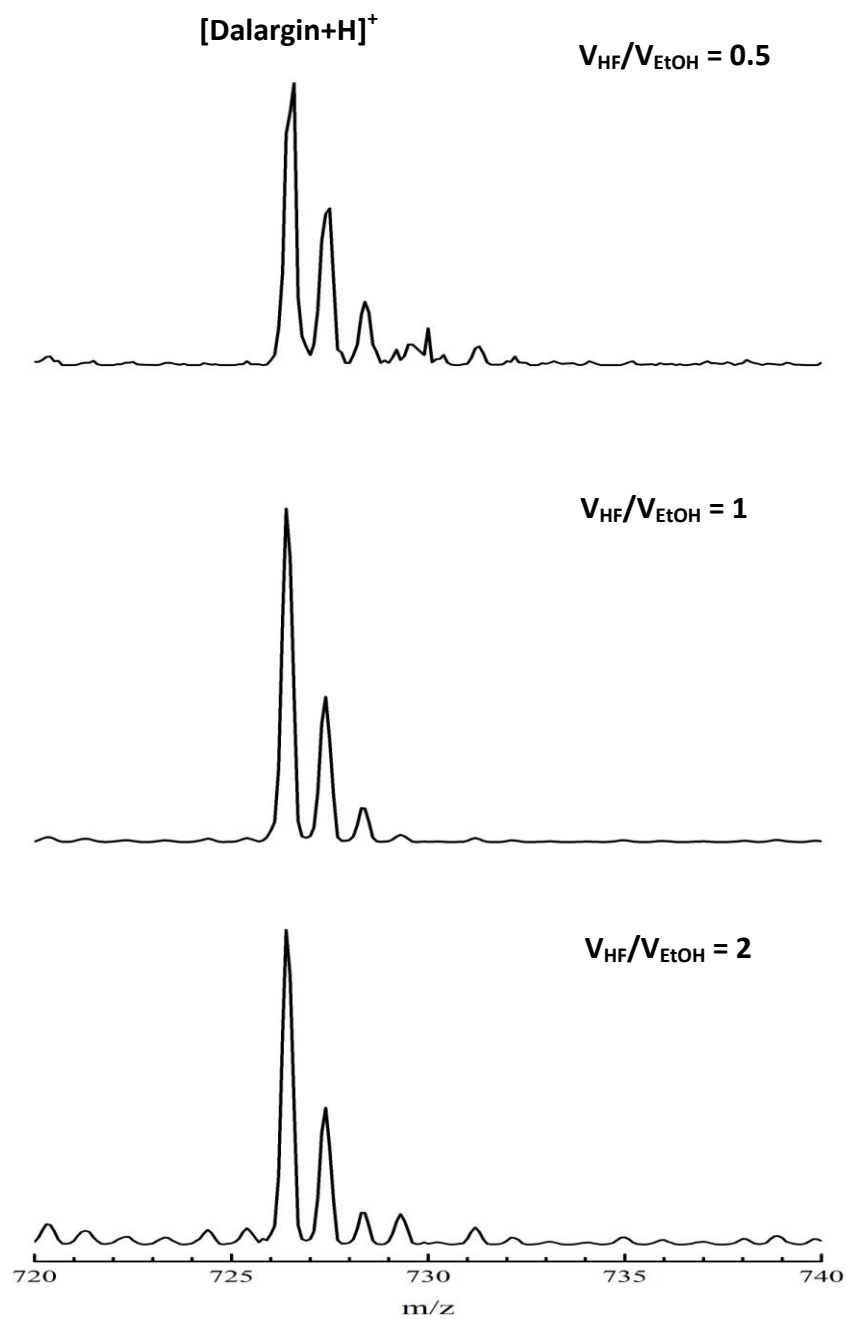


Fig. 3.9: NIMS spectra obtained from pSi substrates formed using different etching solution volume ratios.

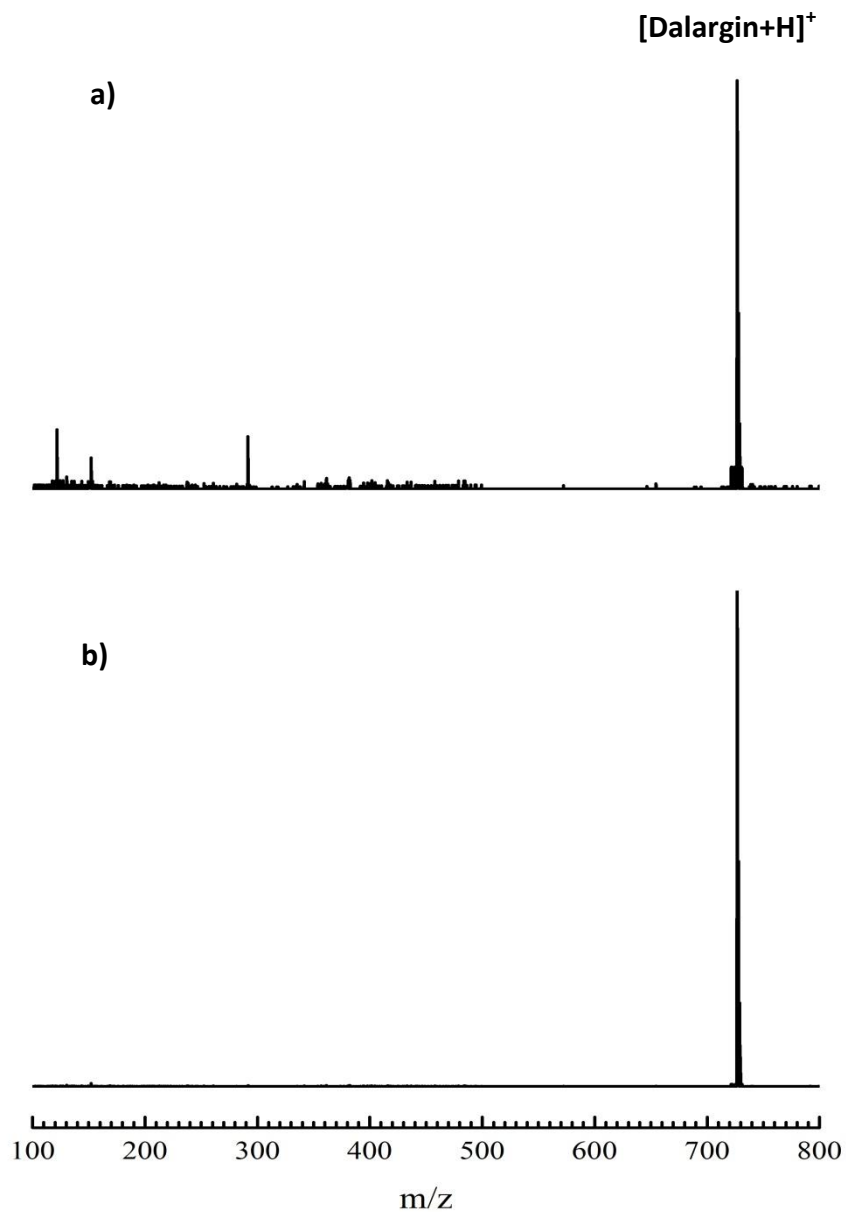


Fig. 3.10: Comparison of the NIMS spectra of Dalargin using pSi prepared with and without Piranha solution cleaning before electrochemical etching. a) NIMS spectrum of Dalargin obtained using a chip that was not cleaned with Piranha solution; b) NIMS spectrum of Dalargin obtained with a chip that was cleaned with Piranha solution. BisF<sub>17</sub> was used as the initiator in both experiments.

**Table 3.1: Critical parameters and their optimum values for making pSi**

<b>Parameter</b>	<b>Optimum value</b>	<b>Unit</b>
HF acid concentration (volume percent)	50	% by volume
Current density	45	mA/cm <sup>2</sup>
Etching time	30	min
Wafer resistivity (p-type)	<0.005	Ω-cm
Pre-etching cleaning with Piranha solution (98% H <sub>2</sub> SO <sub>4</sub> /30% H <sub>2</sub> O <sub>2</sub> )	2:1	Ratio by volume
Potential	<2.0	V

### **3.2: Characterization of NIMS**

#### **3.2.1: SEM imaging of the NIMS chips**

As shown in the upper image of Fig.3.5 pSi is visually black. The SEM image in Fig. 3.11 shows that the pSi surface is composed of 10~20 nm pores which can be filled with an initiator.

#### **3.2.2: Comparison of MALDI, DIOS and NIMS**

In this work, the peptide Dalargin was used as an analyte to test the sensitivity of NIMS and to compare the quality of the mass spectra obtained by NIMS, DIOS and MALDI MS.

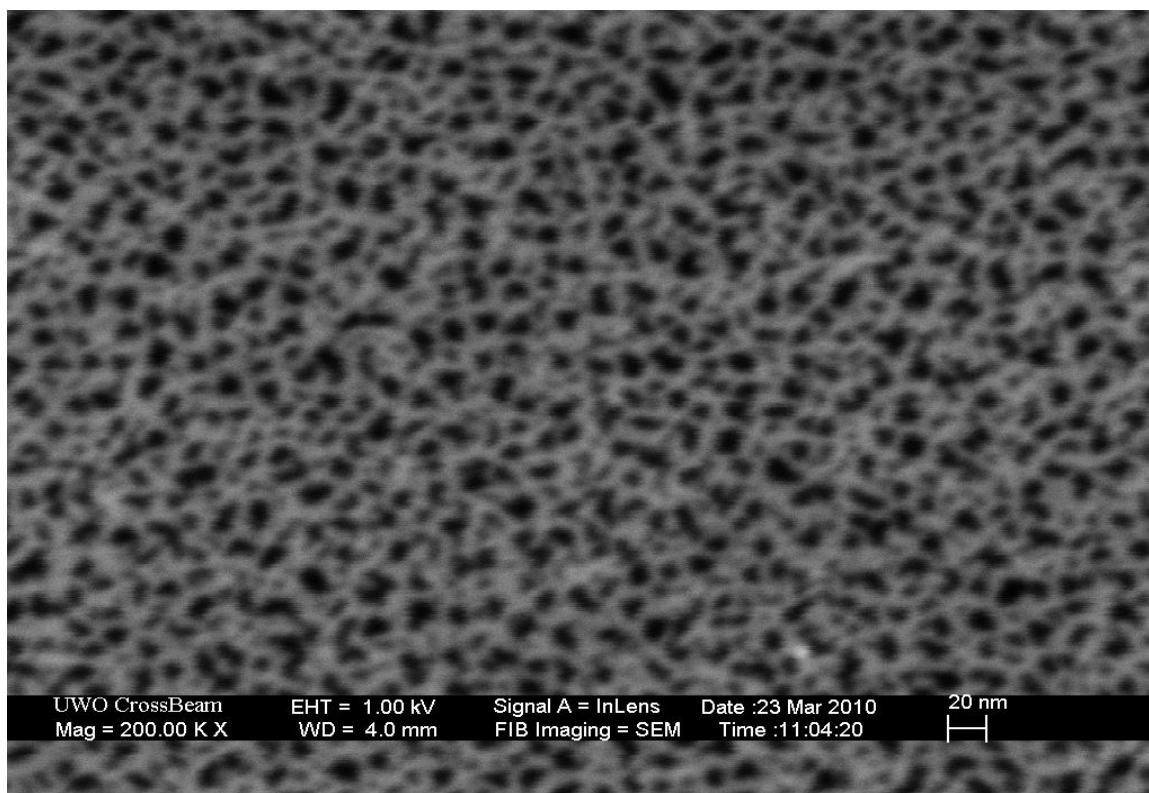


Fig. 3.11: SEM image of the nanostructured surface of a pSi chip obtained using the experimental conditions listed in the Table 3.1.

The  $[\text{Dalargin}+\text{H}]^+$  peak maximum at  $m/z$  726.5 was used to determine the LOD for NIMS. The noise in a S/N evaluation was determined by measuring the average value of the pure noise level between  $m/z$  723 and 725 over  $\sim 1000$  laser shots, each pulse having  $5 \mu\text{J}$  of energy. The average S/N values obtain reflect both the instrumental noise and chemical noise due to the residual contamination on the NIMS surface. The amount of Dalargin in the each spot irradiated by the laser beam was calculated based on the ratio of the laser spot area to the whole sample surface area of the NIMS chip. The laser was repositioned at different locations on the NIMS chip 5 times, and each run at a specific location was repeated 5 times. The resultant ion intensities were then averaged. A S/N



ratio = 3 was considered the minimum value that would allow a peak signal to be clearly differentiated from the noise, thereby giving an indication of the lowest concentration that could be measured reliably.

A standard curve made by plotting the S/N of the NIMS Dalargin ion intensity against number of moles of Dalargin in the spot is shown in Fig. 3.12. A linear regression of the data yielded a  $R^2$  value of 0.9941 and a LOD of  $(0.64 \pm 0.03)$  fmol. This constitutes an improvement of  $\sim 2000$  x in the Dalargin LOD over the value obtained with the same mass spectrometer by DIOS ( $0.32 \pm 0.04$  pmol [83]). It can be concluded that compared to DIOS, NIMS yields spectra with a higher S/N ratio and is a more sensitive analysis technique.

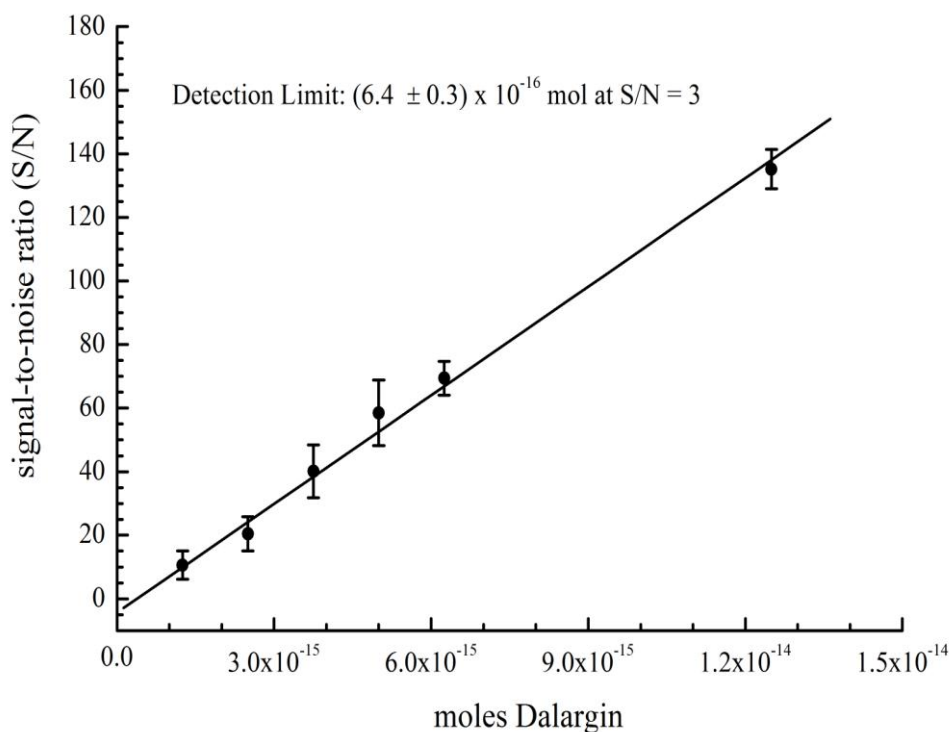


Fig. 3.12: A plot of the S/N ratio of the Dalargin NIMS ion signal versus the number of moles of Dalargin in the sample of the irradiated laser spot.

The NIMS spectrum of Dalargin was compared to that obtained by MALDI MS. CHCA was used as the matrix for the latter technique and the mass spectrum was recorded using the same quadrupole mass spectrometer in positive ion mode. As shown in Fig. 3.13, the NIMS spectrum exhibits strong analyte signals with low background noise. Conversely, there are comparatively more fragment and matrix-related peaks in the MALDI mass spectrum. This confirms that matrix interferences in MALDI MS represent a real limitation that is absent for NIMS.

### **3.2.3: The effect of sample storage time**

The effect of keeping a pSi chip in storage for different lengths of time prior to use for DIOS or NIMS was evaluated by keeping some samples in clean, closed glass containers under one atmosphere at room temperature for 30, 90 and 180 days, respectively. Each pSi surfaces was subsequently dosed with 1  $\mu$ L of 10  $\mu$ M of Dalargin solution before each DIOS or NIMS (initiator, BisF<sub>17</sub>) measurement, and probed with a N<sub>2</sub> laser (337 nm) having 5  $\mu$ J energy per pulse.

The ion intensity in the NIMS spectra changed very little when using a freshly prepared pSi chip or one that was stored for 180 days (Fig.3.14). This shows that keeping a pSi chip in air for months does not significantly influence the NIMS performance. In contrast, the DIOS performance of a pSi chip stored in air for 180 days was very much degraded relative to a freshly made sample. Figs. 3.15 and 3.16 show the NIMS and DIOS spectra obtained from pSi chips stored in air for 0 (freshly prepared), 30 and 180 days, respectively.

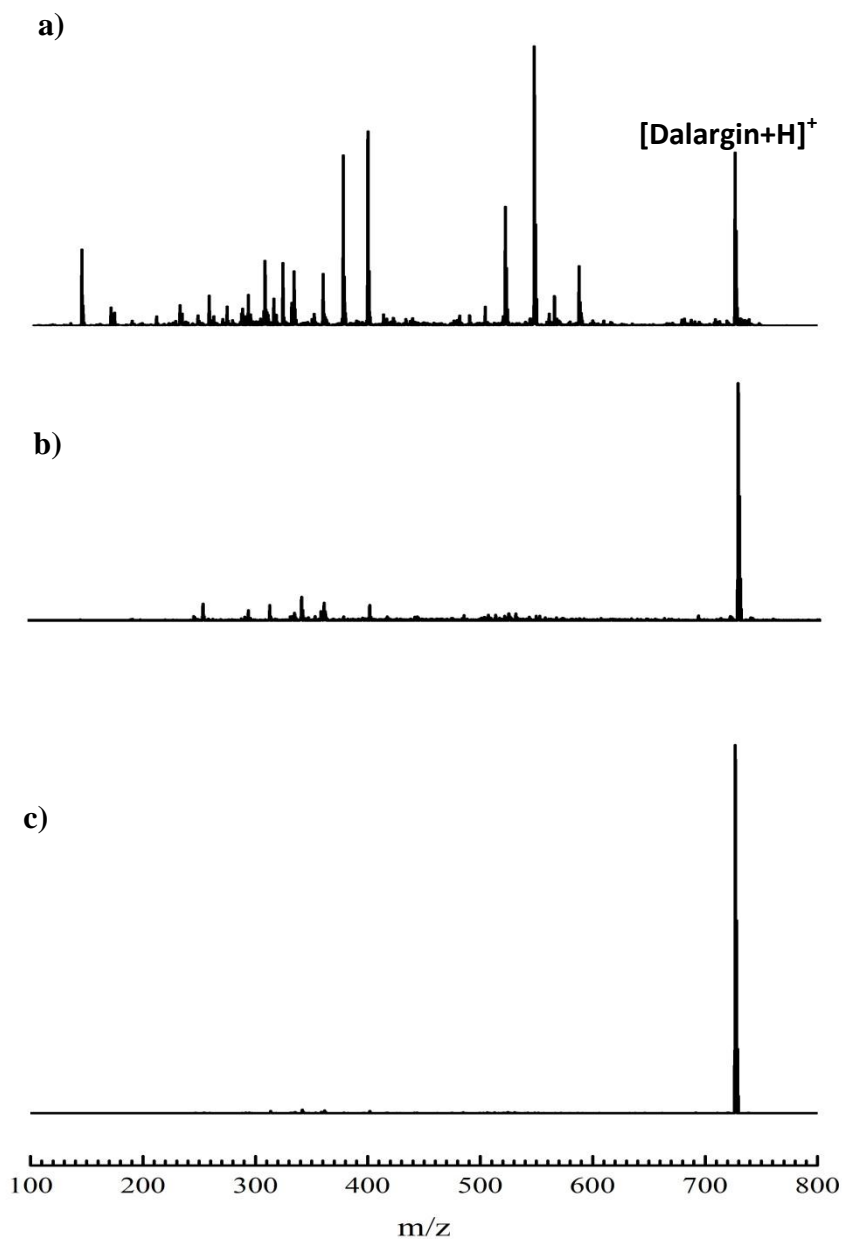


Fig. 3.13: a) MALDI mass spectrum of Dalargin using a CHCA matrix (1 $\mu$ L, 1mM); b) DIOS mass spectrum of Dalargin; c) NIMS spectrum of Dalargin using BisF<sub>17</sub> as initiator. Each sample contained the same amount of Dalargin (1 $\mu$ L, 10 $\mu$ M). The same laser energy per pulse (5 $\mu$ J) was used in each experiments and the mass spectrometer was scanned over the same mass range of 100-800 amu.

One probable reason why the DIOS performance becomes worse after a pSi chip has been stored for a long time in air is that pSi surface groups can become oxidized to silicon oxide (Si–O–Si) and silicon hydroxide (Si–OH) moieties which can dramatically change the surface wetting properties from hydrophobic to hydrophilic. When the surface is hydrophilic the sample droplet is not effectively confined to the porous area [15]. In general, DIOS performance degrades with increasing surface oxidation. Still, it has been noted that some hydrophilic compounds can be detected with better sensitivity using lightly oxidized surfaces or surfaces derivatized with polar functional groups [82]. For NIMS, however, the pSi chip surface is covered with a thin film of fluororous-phase initiator which effectively confines the sample droplet due to its immiscibility with both aqueous and organic phases [83]. Oxidation of surface groups under these conditions therefore has less of an influence on the NIMS performance.

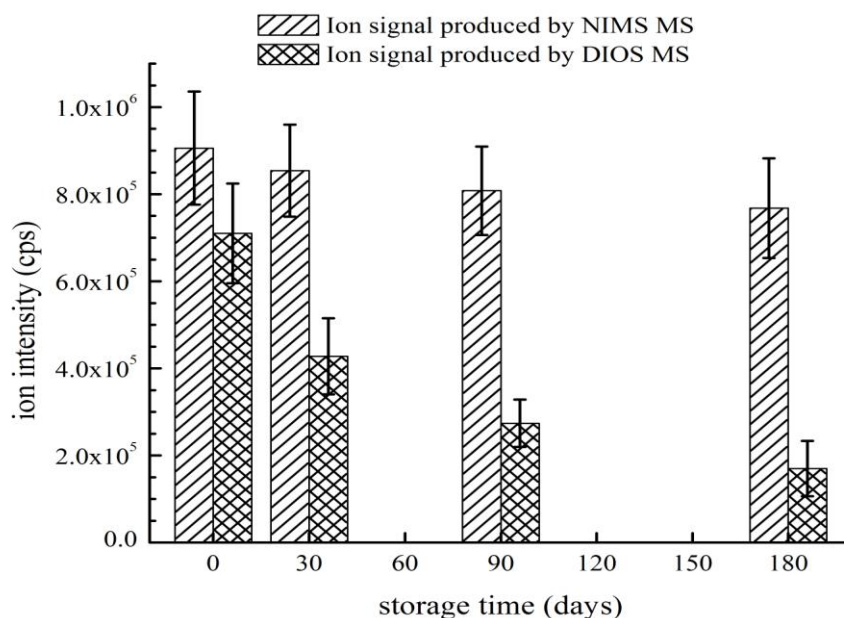


Fig. 3.14: Protonated Dalargin signal intensities obtained by NIMS (initiator, BisF<sub>17</sub>) and DIOS as a function of pSi storage time in air. Note that 0 days implies a freshly prepared pSi chip.

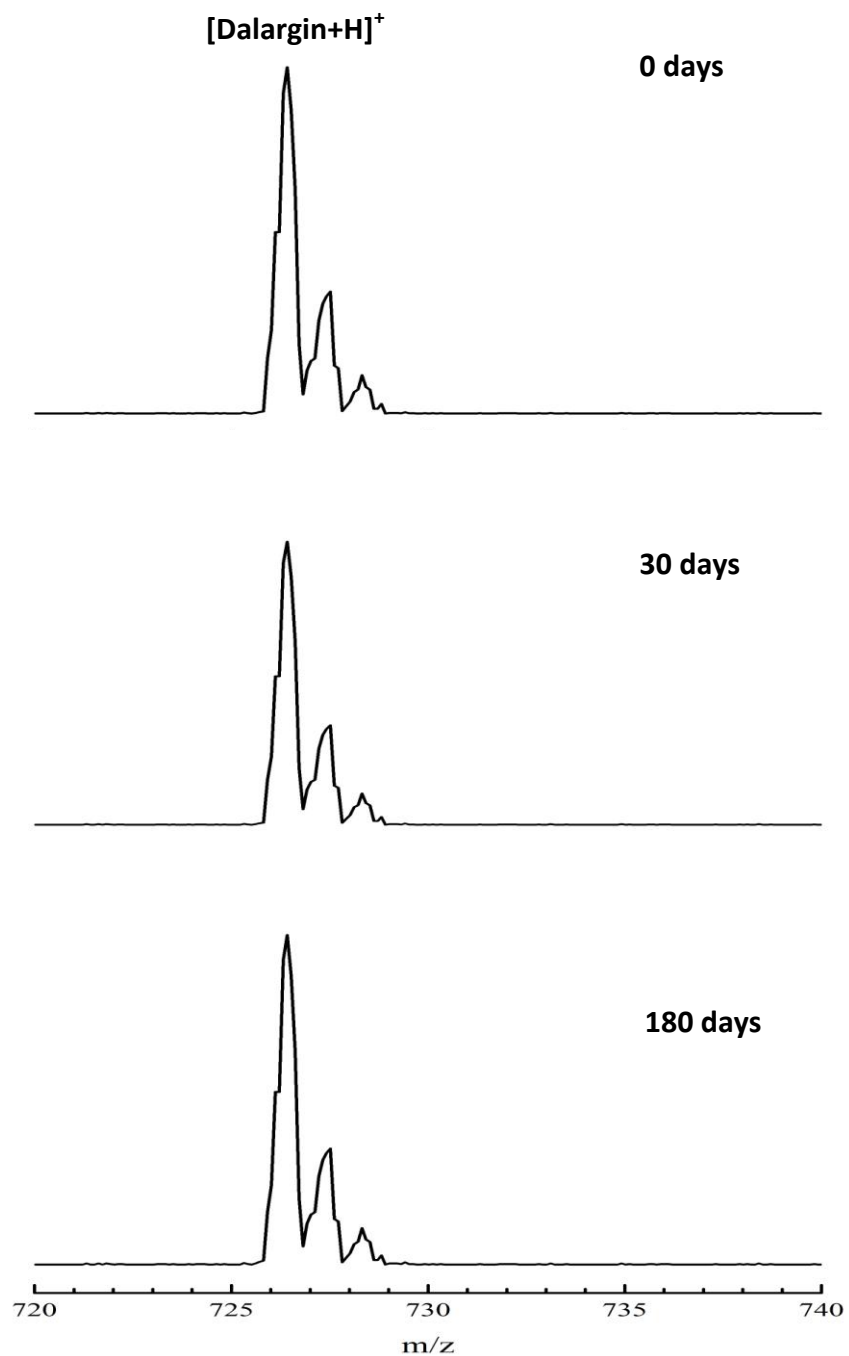


Fig. 3.15: NIMS spectra of Dalargin as a function of storage time in air. Note that 0 days indicates a freshly prepared pSi chip. BisF<sub>17</sub> served as the initiator for each run.

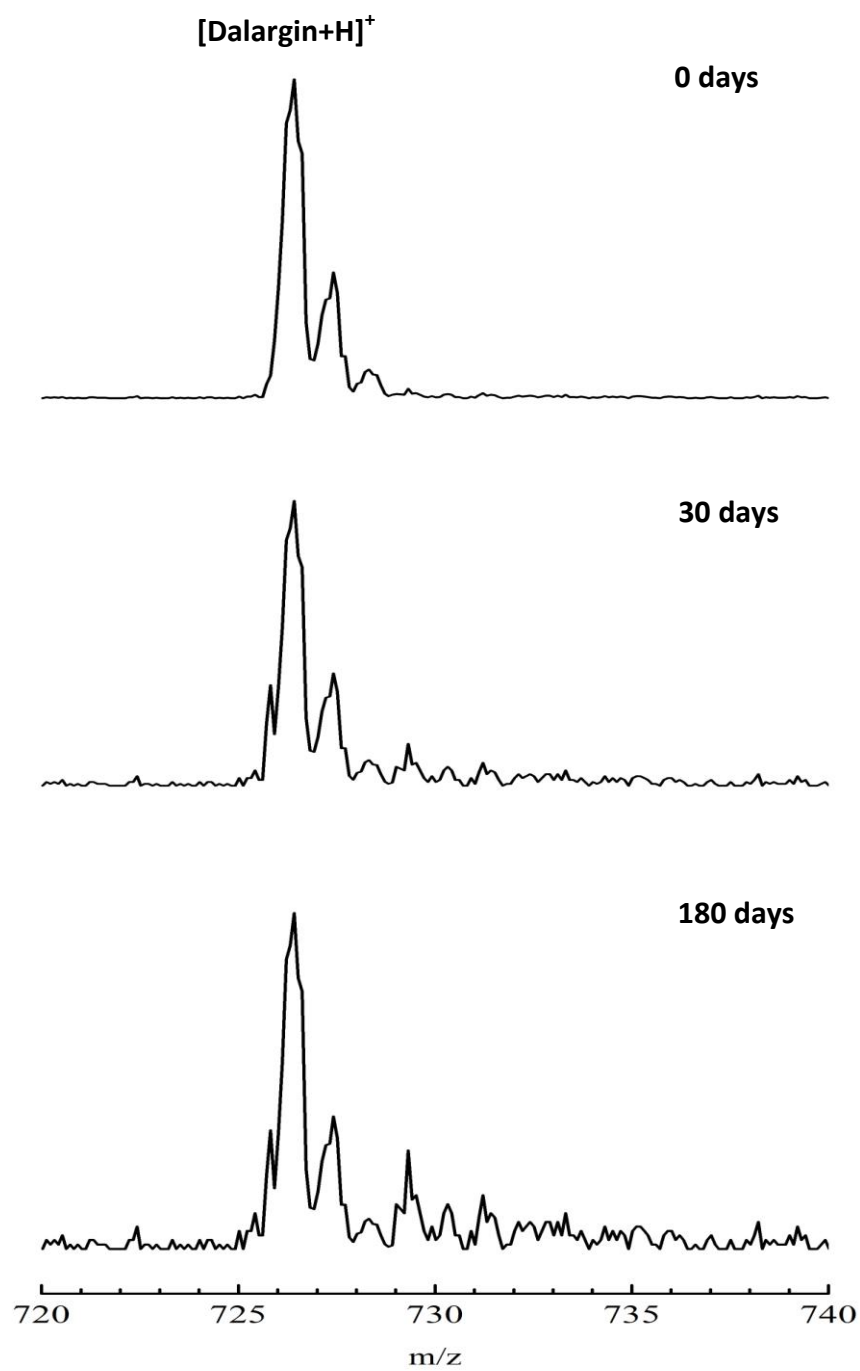


Fig. 3.16: DIOS mass spectra of Dalargin as a function of storage time in air. Note that 0 days indicates a freshly prepared pSi chip.

### 3.3: Analyses of small molecule drugs and peptides using NIMS

Since its introduction in 1980s, MALDI MS has been extensively used to analyze large molecules such as synthetic polymers [84], proteins [1], carbohydrates [85] and nucleic acids [86]. However, its utility is greatly limited in the analysis of small molecules due to background signal interferences from the organic matrix or fragments which can overlap those of the analyte in the mass spectra [87]. NIMS extends the observable mass range to small molecules [30] because these interferences are no longer a factor. The analysis of small molecules such as drugs, metabolites and other biologically important species is therefore one of the potential strengths of this technique. Analyses can be carried out by detecting analytes as radical cations, as protonated ions or as cation adducts depending on the specific compound.

In this section, it is demonstrated that NIMS can be used to detect small molecules that undergo different ionization modes. Five low and moderate molecular weight analytes were selected: the pharmaceutical compounds Fluorouracil (molecular weight, MW = 130 amu) and Quinidine (MW = 324 amu) which ionize to form radical cations; the peptide Bradykinin (MW = 1060 amu) which is readily detected as a protonated species, and the steroid Dexamethasone (MW = 392 amu) and sugar-containing drug Erythromycin (MW = 734 amu) which can be detected as metal cation adducts.

#### 3.3.1: NIMS spectra of molecules that form radical cations

Fluorouracil (or 5-FU, Fig. 3.17) is a chemotherapy agent widely used in the treatment of a range of cancers including colorectal and breast cancers [88]. An aliquot part of 5-FU (2  $\mu$ l, 0.1  $\mu$ M) was spotted directly onto the pSi surface coated with BisF<sub>17</sub> initiator and allowed to dry before NIMS analysis. The mass spectrum in Fig. 3.18 was

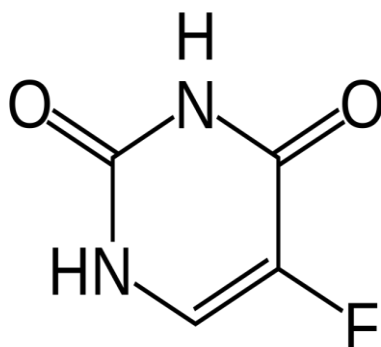


Fig. 3.17: The chemical structure of Fluorouracil

obtained by positioning the focus of the  $N_2$  laser (337 nm; 10  $\mu\text{J}/\text{pulse}$ ) a distance of 0.4 mm above the surface of pSi chip. The dominant feature in the spectrum is the 5-FU's radical cation peak  $[5\text{-FU}]^+$ . The rationale for placing the laser focus 0.4 mm above the substrate surface and a potential mechanism for the generation of radical cations is discussed in detail in Chapter 9 of this thesis.

The LOD for 5-FU was determined by plotting the S/N ratio associated with the mass spectral peak intensity of the cation, ( $m/z$  130), versus the number of moles of 5-FU in the laser spot at the chip surface, which was calculated based on the ratio of the laser spot area to the whole sample surface area of the NIMS chip (Section 3.2.2). The S/N ratio was determined by measuring the average value of the noise level between  $m/z$  119 and 129. As shown in Fig. 3.19, a linear regression of the data yields a  $R^2$  value of 0.9965 and a LOD of  $(4.8 \pm 1) \times 10^{-16}$  mol.



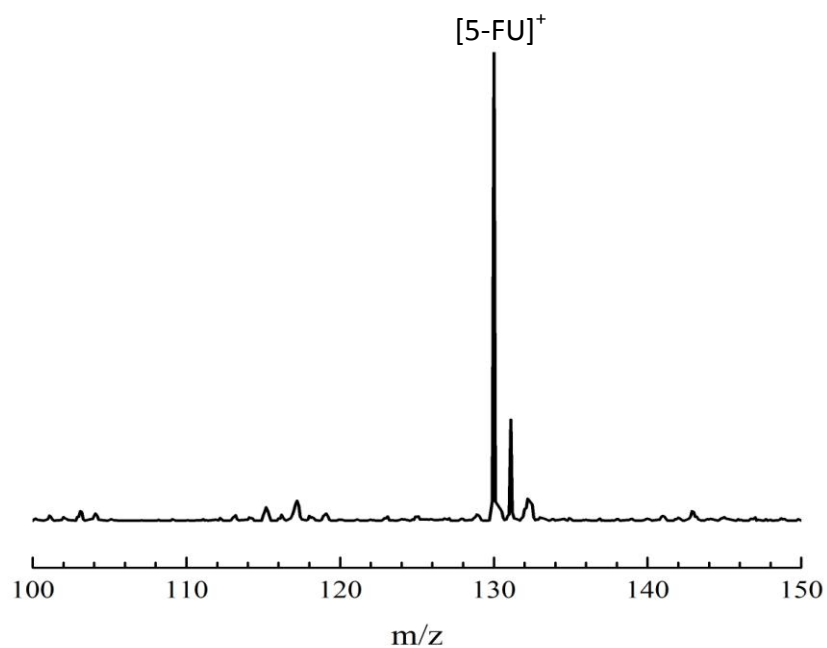


Fig. 3.18: NIMS spectrum of Fluorouracil (200 fmol) obtained by using BisF<sub>17</sub> as the initiator and placing the focus of the N<sub>2</sub> laser (337 nm; 10  $\mu$ J/pulse) a distance of 0.4 mm above the surface of the pSi chip.

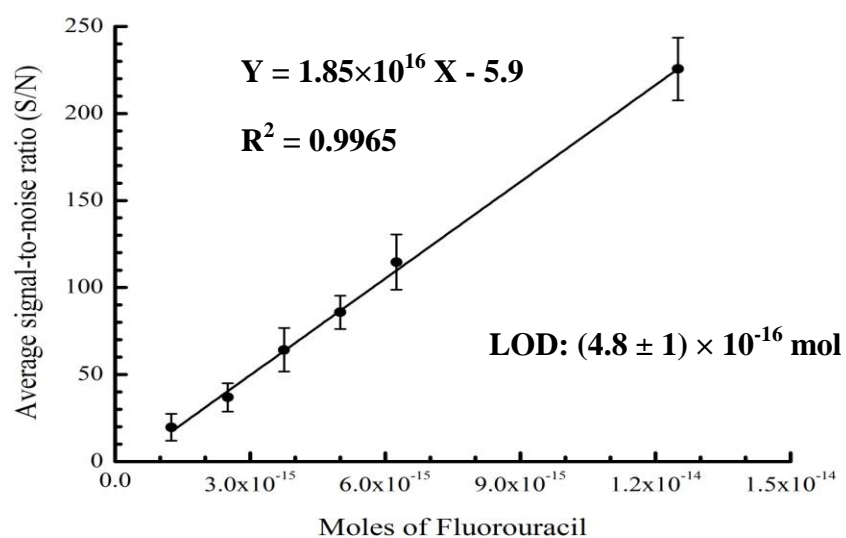


Fig. 3.19: A plot of the S/N ratio of the 5-FU NIMS signal at  $m/z$  130 versus the number of moles of sample within the laser spot.

Quinidine (Fig. 3.20), a stereoisomer of quinine, is a pharmaceutical agent that can act as a class I antiarrhythmic agent for the heart [89]. The NIMS spectrum of Quinidine ( $m/z$  324) using BisF<sub>17</sub> as the initiator and positioning the focus of the N<sub>2</sub> laser (337nm, 10 $\mu$ J/pulse) 0.4 mm (the reason to set up the distance will be discussed in Chapter 9 in detail) above the surface of the pSi chip is shown in the Fig. 3.21.

The LOD for Quinidine was determined in a manner similar for 5-FU and described in Section 3.2.2. The S/N ratio was determined by measuring the average value of the noise level between  $m/z$  318 and 323. As shown in Fig. 3.22, a linear regression of the data yields a R<sup>2</sup> value of 0.9968 and a LOD of  $(1.0 \pm 0.1) \times 10^{-15}$  mol.

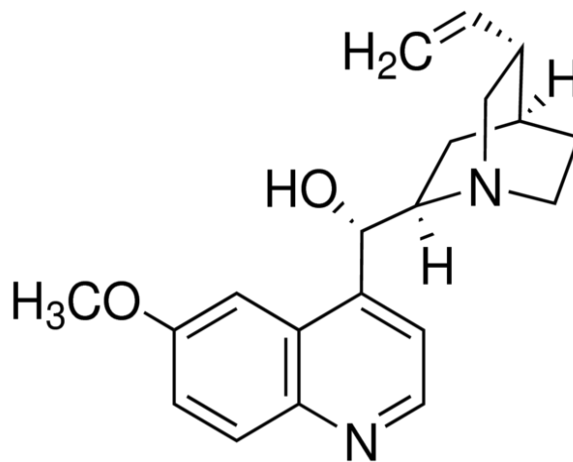


Fig. 3.20: The chemical structure of Quinidine

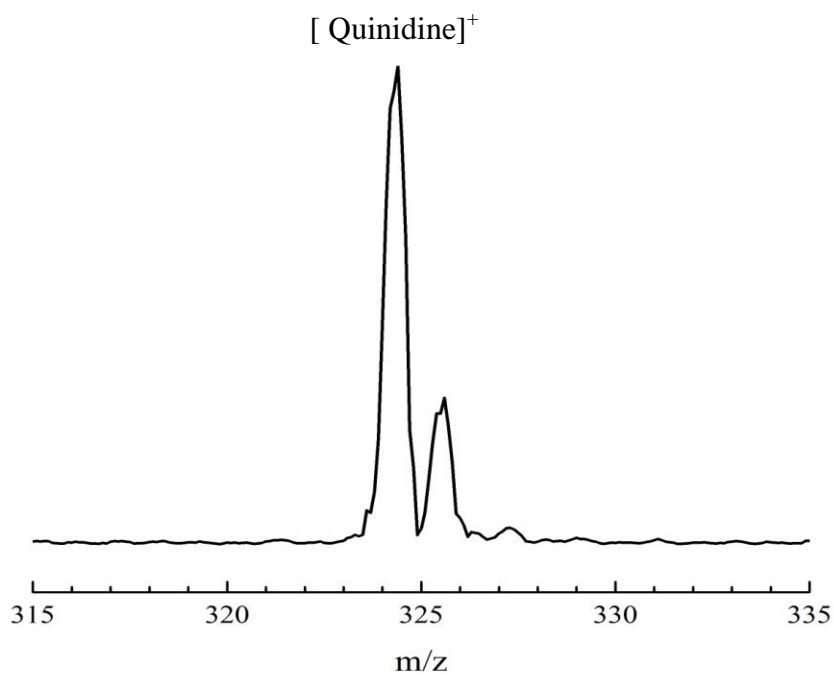


Fig. 3.21: NIMS spectrum of Quinidine (200 fmol) obtained by using BisF<sub>17</sub> as the initiator and placing the focus of the N<sub>2</sub> laser (337 nm; 10  $\mu$ J/pulse) a distance of 0.4 mm above the surface of the pSi chip.

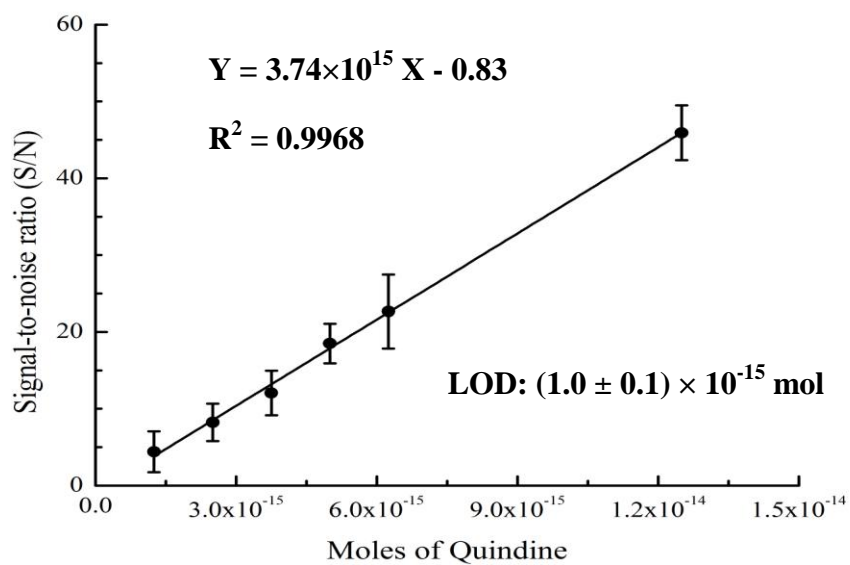


Fig. 3.22: A plot of the S/N ratio of the Quinidine NIMS radical cation signal at  $m/z$  324 versus the number of moles of sample with the laser spot.

### 3.3.2: NIMS spectra of molecules that form protonated cations

Bradykinin is a nine amino acid peptide (Arg-Pro-Phe-Gly-Phe-Ser-Pro-Phe-Arg) with the chemical structure shown in Fig. 3.23. It is formed by cleaving the plasma precursor kininogen with serine proteases known as kininogenases. Bradykinin is known to mediate inflammatory responses, increase vasodilation that in turn reduces blood pressure, and to cause smooth muscles to contract [90].

The NIMS spectrum of Bradykinin using BisF<sub>17</sub> as the initiator is shown in Fig. 3.24. The base peak in the mass spectrum is protonated Bradykinin because the neutral peptide has a strongly basic residue, Arg, which has a large proton affinity (251.2 kcal/mol [91]). The LOD for Bradykinin was determined from the plot shown in Fig. 3.25. The S/N ratio was determined by measuring the average value of the noise level between *m/z* 1052 and 1057. A linear regression of the data in Fig. 3.25 yields a R<sup>2</sup> value of 0.9969 and a LOD of  $(7.1 \pm 1) \times 10^{-16}$  mol.

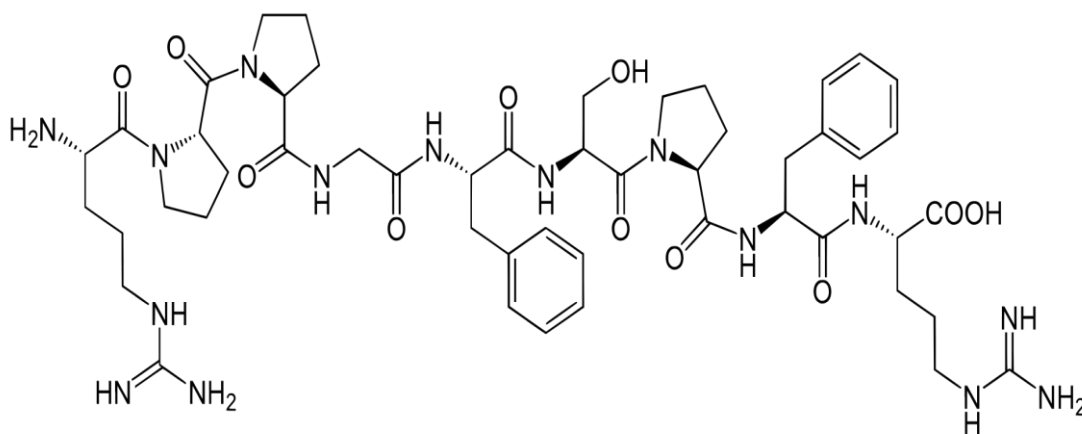


Fig. 3.23: The chemical structure of Bradykinin

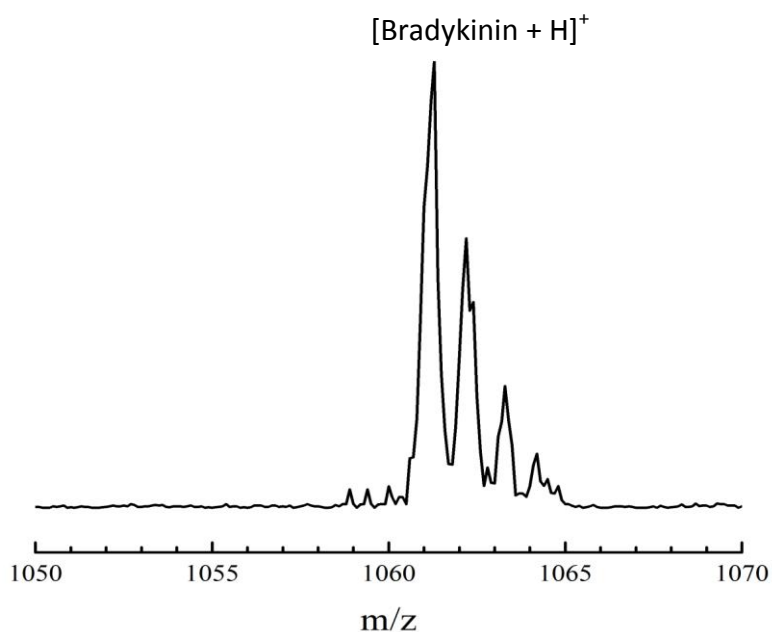


Fig. 3.24: NIMS mass spectrum of Bradykinin (100 fmol) on a pSi substrate using the BisF<sub>17</sub> initiator and a N<sub>2</sub> laser (337 nm) energy of 5 μJ/pulse.

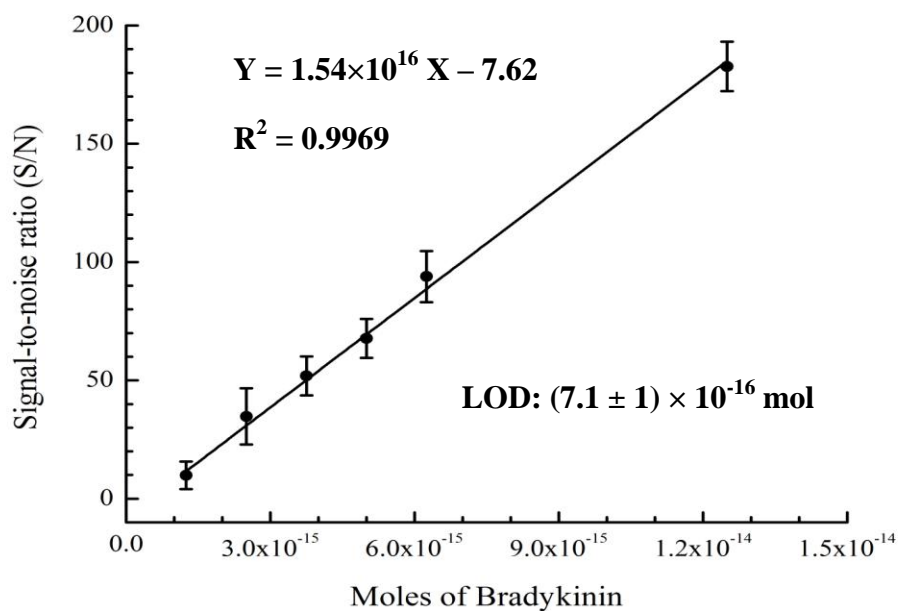


Fig. 3.25: A plot of the S/N ratio of the Bradykinin NIMS signal ( $m/z$  1061) versus the number of moles of sample within the laser spot.

### 3.3.3: NIMS spectra of molecules that form cationized adducts

Carbohydrates and steroids are biologically important classes of pharmaceutical molecules that are difficult to observe by current surface-based MS methods as a result of their poor ionization efficiencies by protonation [4, 43]. However, as shown here, Erythromycin (Fig. 3.26; a carbohydrate-containing antibiotic) and Dexamethasone (Fig. 3.27; a steroid drug) can be detected as metal-cationized adducts using NIMS. In general, carbohydrates readily form sodium adducts ( $\text{ANa}^+$ ) [92] while steroids prefer to form silver adducts ( $\text{AAg}^+$ ) [44].

Erythromycin is an antibiotic used to treat certain infections caused by bacteria and contains a 14-membered lactone ring and two sugars in structure [4]. Given that the ionization efficiency of Erythromycin is generally higher with  $\text{Na}^+$  adducts relative to its protonated form, 5  $\mu\text{L}$  of NaCl solution (1mM) was deposited onto the pSi chip before adding the BisF<sub>17</sub> initiator to provide a source of sodium cations. The NIMS spectrum in Fig.3.28 obtained by depositing 10pmol of Erythromycin and irradiating with 337 nm N<sub>2</sub> laser pulses having 5  $\mu\text{J}$  of energy is dominated by a signal at  $m/z$  757 which corresponds to  $[\text{Erythromycin} + \text{Na}]^+$ .

The LOD for Erythromycin was determined from Fig.3.29 to be  $(1.7 \pm 0.2) \times 10^{-14}$  mol. The S/N ratio here was determined by measuring the average value of the noise level between  $m/z$  745 and 755. The  $R^2$  value from the linear regression of the data = 0.9978.

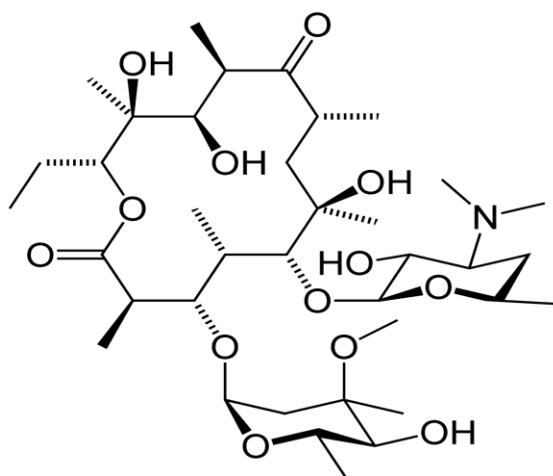


Fig. 3.26: The chemical structure of Erythromycin

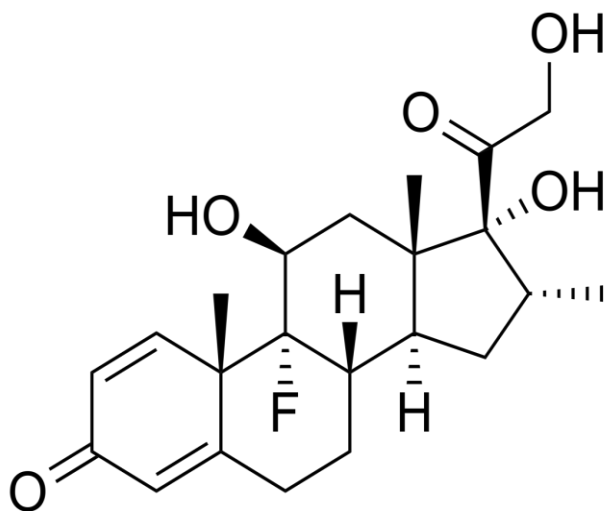


Fig. 3.27: The chemical structure of Dexamethasone.

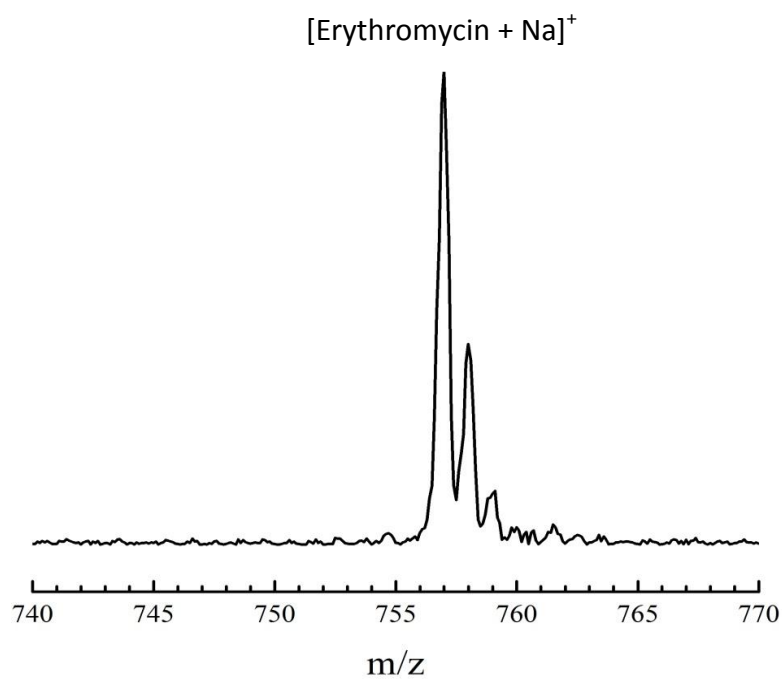


Fig. 3.28: NIMS spectrum of Erythromycin (100 pmol) on a pSi substrate using the BisF<sub>17</sub> initiator and a N<sub>2</sub> laser (337 nm) energy of 5 μJ/pulse.

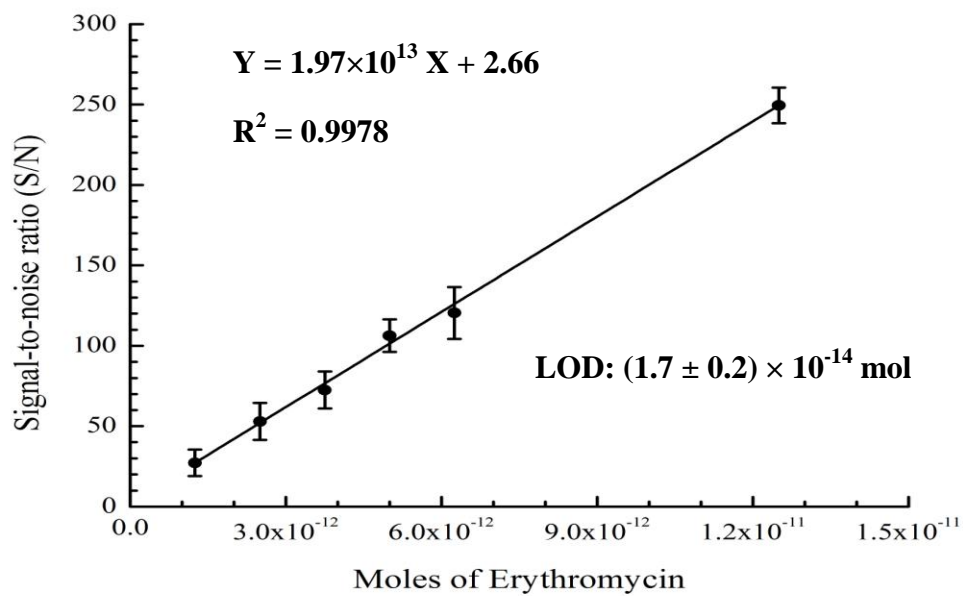


Fig. 3.29: A plot of the S/N ratio of the Erythromycin NIMS signal ( $m/z$  757) versus the number of moles of sample within the laser spot.



Dexamethasone is an anti-inflammatory and immunosuppressant steroid drug [93]. In this work, 5  $\mu\text{L}$  of  $\text{AgNO}_3$  solution (1mM) was spotted onto the pSi substrate to provide a source of cations before adding the  $\text{BisF}_{17}$  initiator. The NIMS spectrum of Dexamethasone (100 pmol) in Fig. 3.30 exhibits two major peaks at  $m/z$  499 and 501 due to  $[\text{Dexamethasone} + \text{Ag}]^+$ . The peak intensities well reflect the natural abundance of the  $^{107}\text{Ag}$  and  $^{109}\text{Ag}$  isotopes; 51.8% and 48.2%, respectively [92].

The LOD for Dexamethasone was determined to be  $(7.5 \pm 0.6) \times 10^{-14}$  mol based on measurement of the  $[\text{Dexamethasone} + ^{107}\text{Ag}]^+$  signal (Fig. 3.30). Here the S/N ratio was determined by measuring the average value of the noise between  $m/z$  492 and 497. The linear regression of the data in Fig. 3.31 yields a  $R^2$  value of 0.9955.

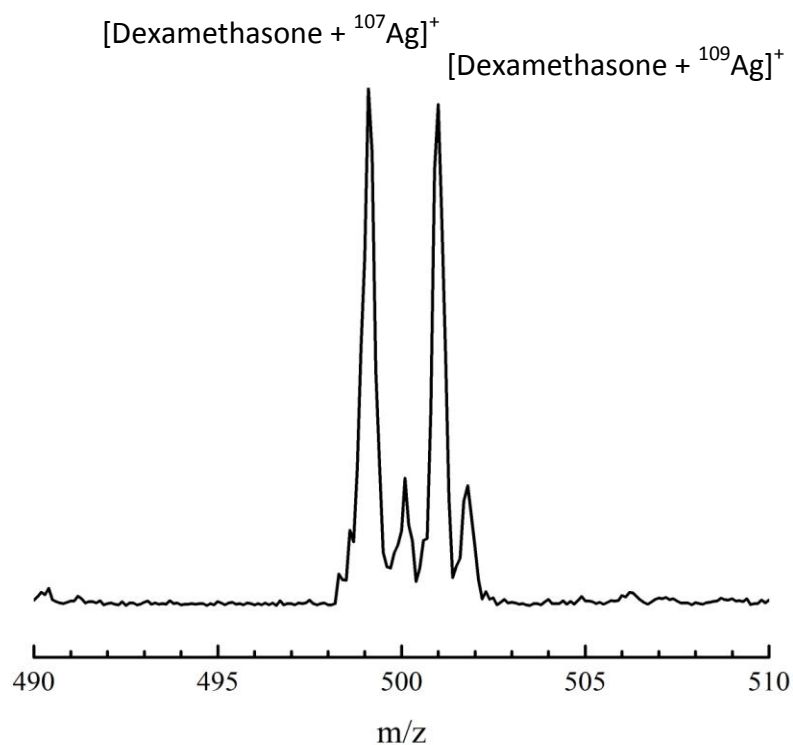


Fig. 3.30: NIMS spectrum of Dexamethasone (100 pmol) on a pSi substrate coated with  $\text{BisF}_{17}$  initiator and  $\text{AgNO}_3$  (5 nmol). The spectrum was obtained using the output of a  $\text{N}_2$  laser (337 nm) having an energy of 5  $\mu\text{J}/\text{pulse}$ .

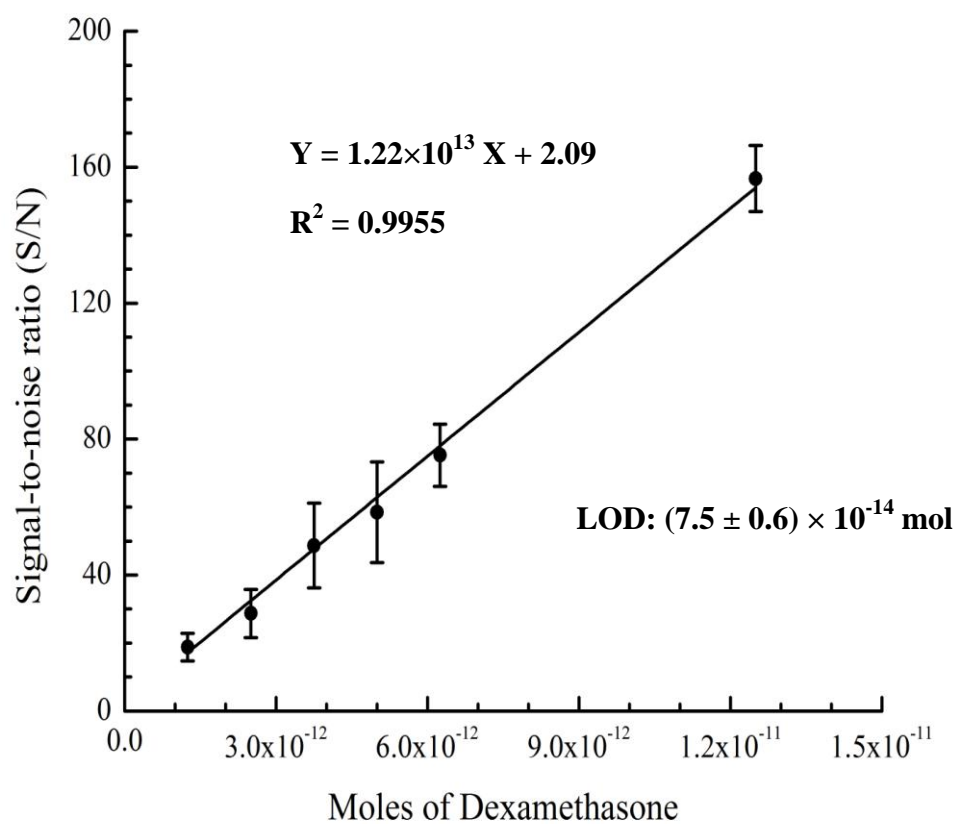


Fig. 3.31: A plot of the S/N ratio of the Dexamethasone NIMS signal ( $m/z$  499) versus the number of moles of sample in the laser spot.

## **Chapter 4: On-chip enrichment and analysis of peptide subsets using maleimide-functionalized fluororous affinity biochip and NIMS**

### **4.1: Background**

To date global analyses of biological samples such as blood, protein digests and cellular metabolite extractions remain a technological challenge due to its complexity in terms of the number of compounds involved and dynamic range of their concentrations; for example, the concentrations of proteins in a plasma can vary by ~10 orders of magnitude [95]. This problem can be solved in part by a “divide and conquer” strategy where biologically or clinically important information is obtained by isolating, enriching and analyzing specific subsets of peptides and proteins [96]. Affinity fractionation and enrichment for the analysis of specific peptide subsets, is based on the specific binding between an immobilized ligand and the analyte. For example, antibody-antigen affinity [97] and biotin-avidin pairing [98] have been widely used in such strategies. Chemically, a thiol resin has been developed for cysteinyl residues [99], lectins for specific glycosylated species [100], and metal affinity-based fractionation involving iron and gallium for phosphorylated peptides [101]. Of them, the biotin-avidin system is arguably one of the most general approaches because it involves using a dual-functional reagent to form a common affinity capture moiety. Typical applications of the biotin-avidin pairing involve binding and enriching targeted analytes by reaction with the biotin group followed by capture of the biotinylated species through affinity interactions using the immobilized avidin. Although this method is very effective, the high affinity between biotin and avidin (with a dissociation constant approaching  $10^{-15}$  M [72]) often make it difficult for target

analytes to fully elute from the capture resin [102]. In addition, the biotinylated peptide can complicate the interpretation of MS/MS spectral data [103]. Lastly, these custom biological reagents are relatively expensive.

Recently a novel separation and enrichment method based on fluororous-affinity interactions was introduced [104]. This field has grown since the introduction of fluororous biphasic catalytic techniques [62]. In general, fluororous-affinity tags for separation and enrichment participate in one of two modes. The first is based on the use of a F-SPE column which uses perfluoroalkyl chains as bonded phase instead of a resin to facilitate analyte separation [105]. Here a sample in solution is selectively labeled with a fluororous tag containing an appropriate functional group and then loaded onto the fluororous solid-phase media for separation. The unbound species and contaminants are subsequently washed away using a suitable organic solution. Finally, the desired bound species are eluted from the affinity column for MS analysis [106]. This column chromatography-based method, however, is prone to sample loss due to analyte adsorption onto the solid phase and is susceptible to sample contaminant during transfer to the mass spectrometer.

The second strategy is based on a biochip where the analytes of interest are captured by a fluororous tag immobilized on a fluororous-silylated surface by fluorine-fluorine interactions. This approach should provide a more rapid and sensitive analysis of targeted species due to on-site enrichment and washing followed by direct MS analysis [107]. Fluororous-affinity immobilization has been shown to be useful for small molecule microarrays that can be used to analyze carbohydrates [61] or screen for inhibitors [55].

In this work, a fluororous affinity tag of 3-(perfluorooctyl)-propyl-1-maleimide (RF<sub>17</sub>, Fig. 4.1), which combines a long perfluororous carbon chain(-C<sub>8</sub>F<sub>17</sub>) with a

chemically active functional alkene group, is used for the first time on a NIMS chip to enrich peptides containing cysteine residues, and to improve their detection sensitivity by mass spectrometry. Initiators such as perfluorinated siloxanes trapped in the nanostructure pores not only greatly increase the desorption efficiency of MS based on the DIOS, but also exhibit an ability to immobilize fluororous-affinity tags via fluorine-fluorine interactions.

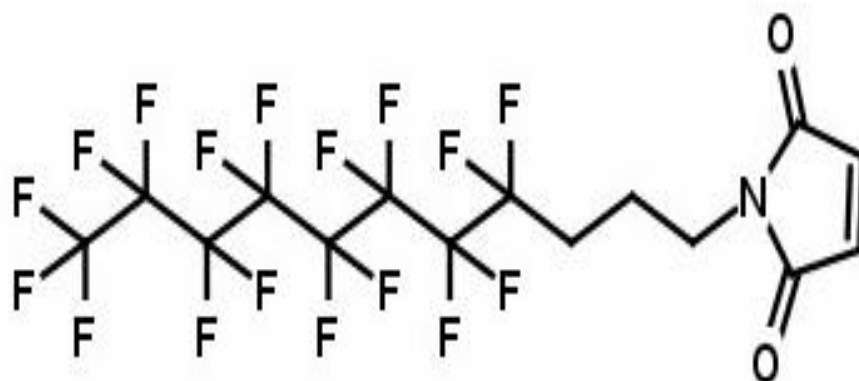


Fig. 4.1: The chemical structure of fluororous-affinity tag, 3-(perfluorooctyl)-propyl-1-maleimide (RF<sub>17</sub>).

In this work the utility of our methodology is first demonstrated by determining the optimal binding and washing conditions for a mixture of three peptides, and then by separating and enriching cysteine-containing peptides from a Bovine Serum Albumin (BSA) digest. Finally the compatibility of such fluororous tagged peptides with MS/MS sequencing strategies is evaluated.

#### 4.2: Results and discussions

The ability to isolate and enrich a desired subset of analytes from extremely complex mixtures is an indispensable tool for any viable methodology designed to totally

analyze biosamples such as a protein digest, blood or urine. The workflow designed for the experiments carried out in this work is shown in the Fig. 4.2. As shown in the Fig. 4.3 the fluoros-affinity tag used in this work was synthesized by a simple and highly selective Michael addition reaction between the thiol and maleimide groups [108].

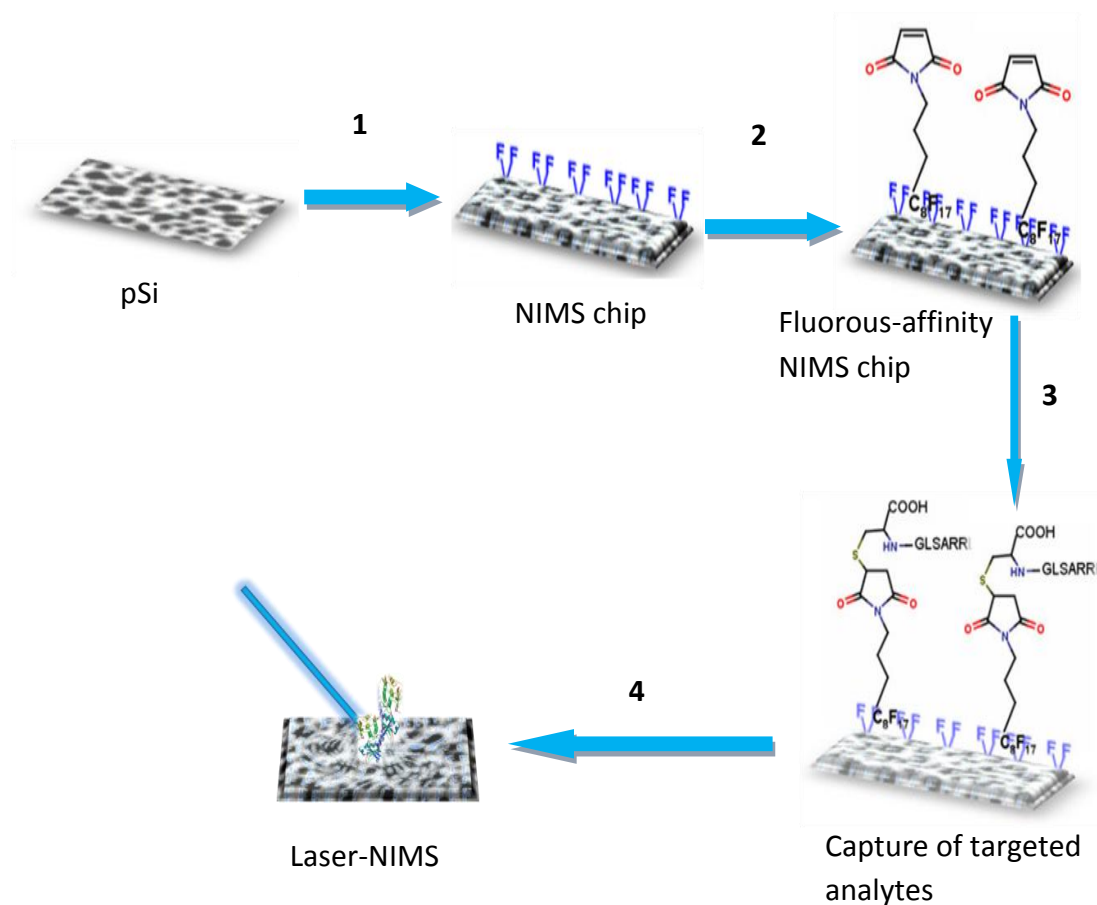


Fig. 4.2: Schematic diagram for the methodology: **1.** a thin film of initiator is coated in the surface of porous Si produced by electrochemical etching; **2.** a fluoros affinity tag is immobilized on the NIMS chip by fluorine-fluorine interactions; **3.** a specific peptide is captured by the affinity tag; **4.** mass analysis by NIMS.

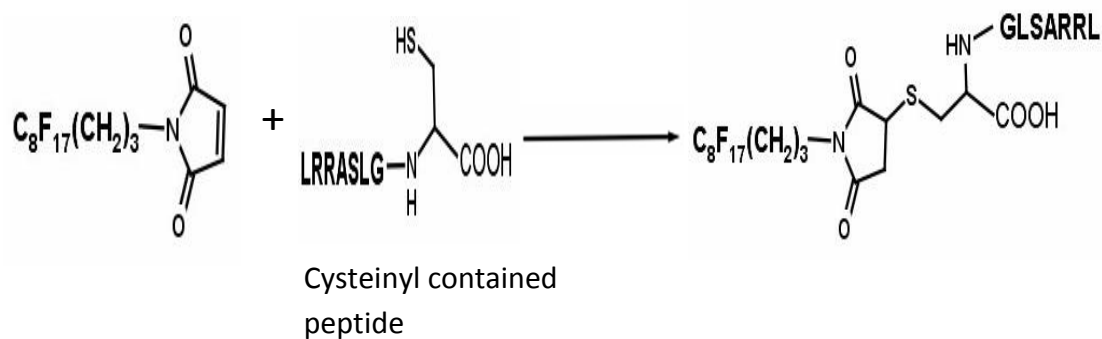


Fig. 4.3: The binding chemical reaction occurring between RF<sub>17</sub> and Pep2.

Typically, a crude mixture is loaded onto a NIMS chip containing some specific fluororous affinity tags. The chip is then eluted with a fluorophobic solvent such as 40% methanol water solution with 0.1% TFA to remove any unbound nonfluorous compounds, salts and contaminants. The sample was then subjected to NIMS analysis. To demonstrate the feasibility of this methodology, a mixture of peptides composed of Pep1 (YAGFLR, Fig. 3.1), Pep2 (LRRASLGC, Fig. 4.4) and Pep3 (RPPGFSPFR, Fig. 3.23), where only Pep2 contained a cysteine residue, was tested according to the method described above.

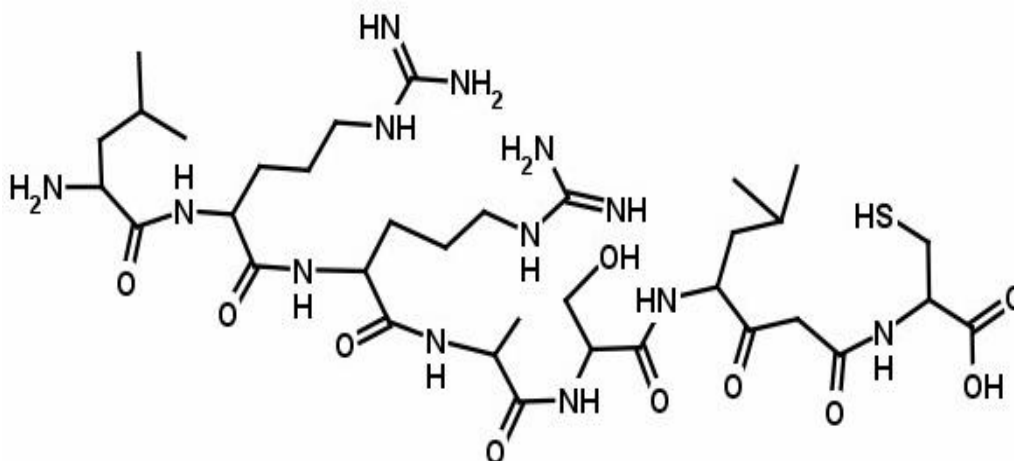


Fig. 4.4: The chemical structure of Pep2 (LRRASLGC).

#### 4.2.1: Characterization of the binding reaction and washing conditions

Prior to selectively enriching the cysteine-containing peptides using a fluorosulfate affinity NIMS chip, the conditions required for effective binding between the cysteine residue (-SH) and maleimide functional group (-C=C-) need to be optimized, as well as the composition of the methanol / water solution for washing off any unbound species. A plot of log (ion intensity) for Pep2 (Fig. 4.5) versus reaction time was used to estimate the rate of the binding reaction at room temperature. The graph shows that the reaction proceeds quickly for ~the first 90 minutes, then slowly thereafter. The reaction is still ongoing after three hours at room temperature. The binding reaction temperature was varied by keeping the NIMS chip in a water bath chamber maintained at different temperatures. Fig. 4.6 is a plot of the ion intensities of tagged and untagged Pep2 as a function of temperature for a fixed reaction time of 60 minutes. Together, these plots show that the near optimum conditions for immobilizing the tagged analyte is 60 °C for 60 minutes.

The effect of the percentage concentration of methanol in the washing solution on enrichment efficiency was also investigated. As shown in the Fig. 4.7, the signal intensity for unbound Pep3 in the NIMS chip decreased rapidly with increasing % methanol while that for the Pep2 bound to the NIMS chip did not significantly change. Although Pep3 appeared to be washed off completely when the amount of methanol in solution reached 60%, at that composition Pep2 was also observed to decrease. It was determined that a 40% methanol in water solution with 0.1% TFA was the most effective composition for separating the two species.



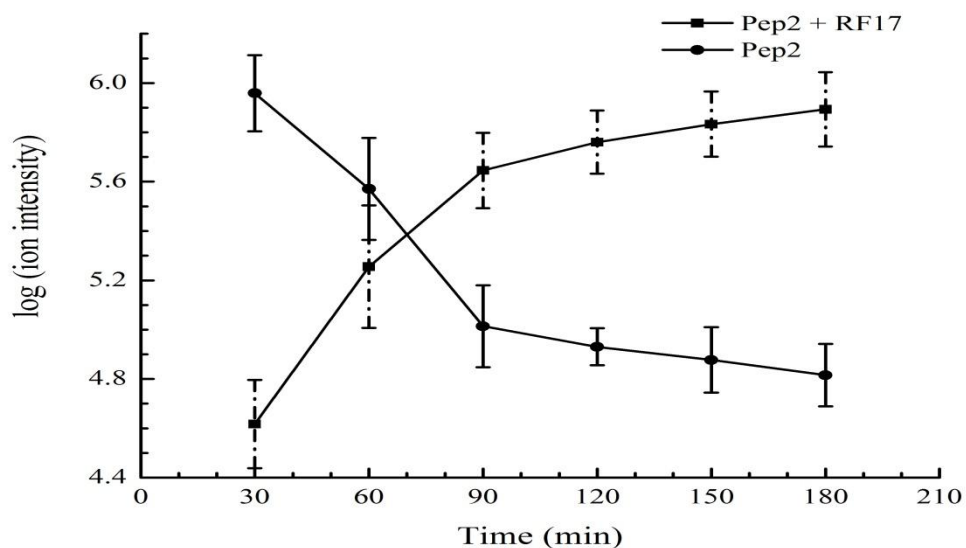


Fig. 4.5: The effect of reaction time on cysteine residue binding efficiency. The square and circle dots show the ion intensities produced by NIMS of Pep2 plus 3-(perfluoroalkyl) propyl-1-maleimide and untagged Pep2, respectively, with different reaction time.

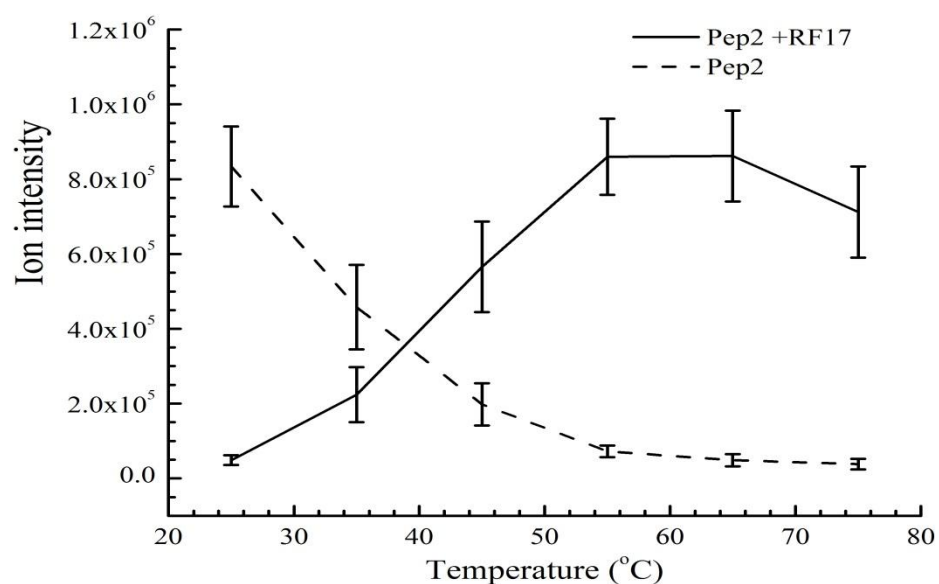


Fig. 4.6: The effect of temperature on cysteine residue binding efficiency. The solid and dash lines show the ion intensities produced by NIMS of Pep2 plus 3-(perfluoroalkyl) propyl-1-maleimide and untagged Pep2, respectively, with different reaction temperature.

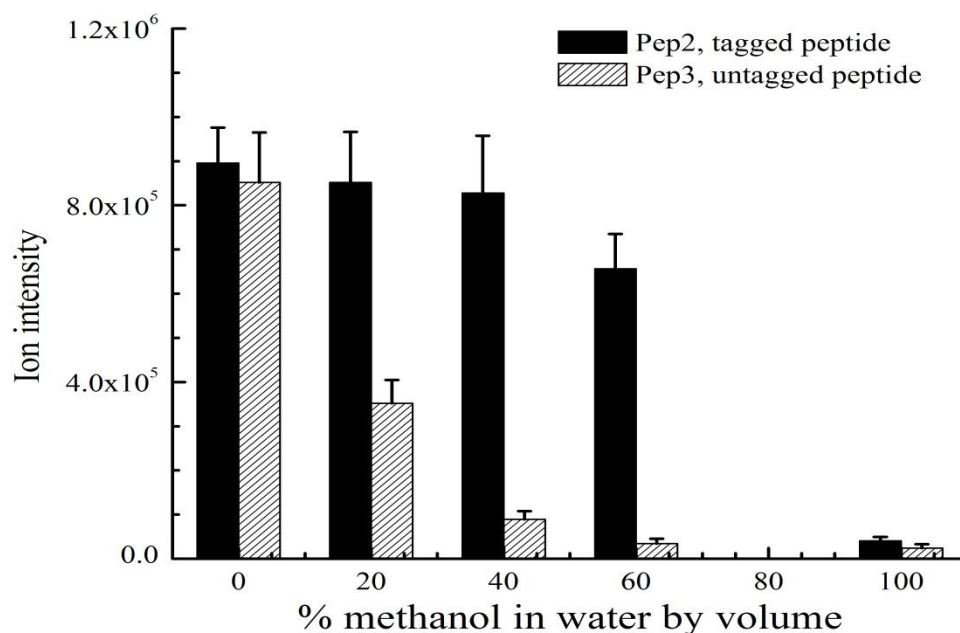


Fig. 4.7: Optimization of the washing solvent composition for cysteine residue enrichment on a fluoros-affinity NIMS chip determined by plotting the ion intensity of the tagged and untagged peptides as a function of the percentage of methanol used.

#### 4.2.2: Comparison of the NIMS mass spectra without fluoros affinity tags, before washing and after washing

First, a mixture of three peptides, Pep1 (YAGFLR,  $m/z$  726.5), Pep2 (LRRASLGC,  $m/z$  876.1) and Pep3 (RPPGFSPFR,  $m/z$  1061.2) was analyzed by a NIMS chip without using the RF<sub>17</sub> immobilizing fluoros-affinity tag. As shown in Fig. 4.8a, all three peptides exhibit strong protonated parent signals in the mass spectrum, regardless of whether they contain a cysteine residue or not. When the mixture was incubated with the immobilized fluoros tag at 60 °C for 60 minutes (Fig. 4.8b) but not washed before analysis, the protonated peak of Pep2 shifted to  $m/z$  1433.3, which corresponds to the mass of protonated Pep2 plus RF<sub>17</sub>. The mass signals for the other two peptides were

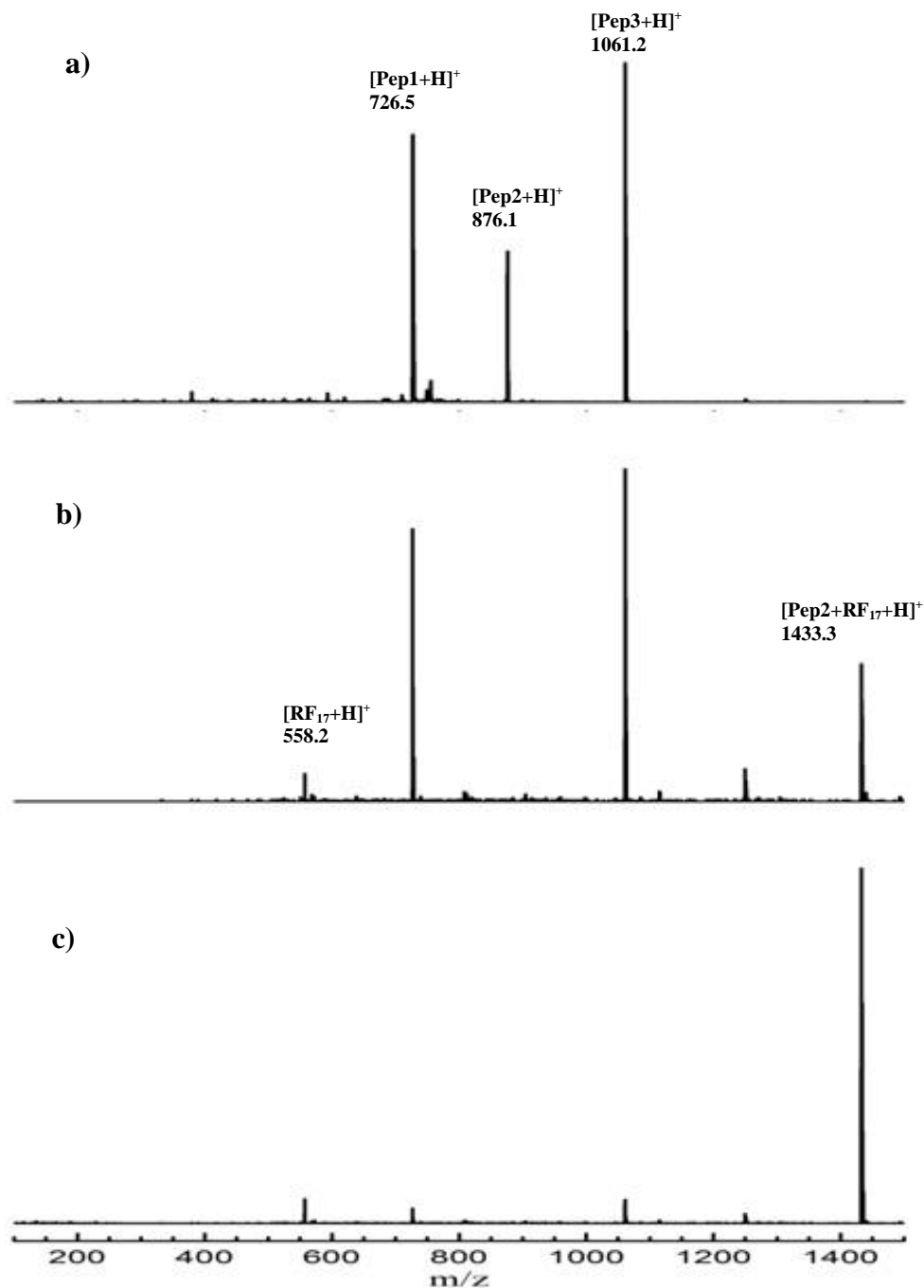


Fig. 4.8a): NIMS spectrum of the mixture Pep1, Pep2 and Pep3; b): NIMS spectrum of the mixture Pep1, Pep2 and Pep3 which has been incubated with the fluoros-affinity NIMS chip before washing; c): NIMS spectrum of the mixture Pep1, Pep2 and Pep3 which has been incubated with the fluoros-affinity NIMS chip after washing with a 40% methanol water solution containing TFA.

unchanged. In addition, a weaker intensity peak corresponding to protonated immobilizing fluororous tag (protonated 3-(perfluoroalkyl)propyl-1-maleimide,  $[\text{RF}_{17}+\text{H}]^+$ ,  $m/z$  558.2) also appears. This demonstrates that the tag only affected the peptide containing the cysteine residue. Finally, the mixture on the fluororous-affinity NIMS chip was analyzed after the unbound peptides had been removed from the chip surface using the optimized washing solution (Fig. 4.8c). Here, the protonated peaks of Pep1 and Pep3 have almost completely disappeared while the protonated peak of Pep 2 plus immobilizing fluororous-affinity tag remains. This shows that only the cysteine-containing peptide was selectively captured by the functionalized NIMS chip and therefore, effectively enriched.

#### **4.2.3: Enrichment of a cysteine-containing peptide residue from a BSA digest**

To further demonstrate the effective utility of fluororous-affinity NIMS chips for the analysis of complex biological samples, a group of peptides from BSA tryptic digest was fractionated, enriched and subsequently detected by NIMS. BSA contains 35 cysteine residues and therefore, produces a relatively complex cysteine-containing peptide residue mixture after reduction of double bond of S=S and tryptic digestion. Table 4.1 shows all peptide sequences with mass range from 500 to 3000 Da detected by such a fluororous-affinity NIMS biochip before and after washing using 40% methanol water solution with 0.1% TFA.

**Table 4.1: Assignments of peptides from a BSA tryptic digest using  
fluorous-affinity NIMS**

Position	Peptide sequence	[A+H] <sup>+</sup>	[A+RF <sub>17</sub> +H] <sup>+</sup>	Before washing	After washing
101-105	VASLR	545.3		✓	
223-228	CASIQK	649.3	1206.5	✓	✓
236-241	AWSVAR	689.4		✓	
198-204	GACLLPK	701.4	1258.6		✓
29-34	SEIAHR	712.4		✓	
581-587	CCAADDK	725.3	1282.5		✓
483-489	LCVLHEK	841.5	1398.7		✓
161-167	YLYEIAR	927.5		✓	✓
123-130	NECFLSHK	977.5	1534.7	✓	✓
413-420	QNCDQFEK	1011.4	1568.6		✓
499-507	CCTESLVNR	1024.5	1581.7		✓
588-597	EACFAVEGPK	1050.5	1607.7	✓	✓
66-75	LVNELTEFAK	1163.6		✓	
300-309	ECCDKPLLEK	1177.6	1734.8		✓
361-371	HPEYAVSVLLR	1283.7		✓	
402-412	HLVDEPQNLIK	1305.7		✓	
76-88	TCVADESHAGCEK	1349.5	1986.7 <sup>(1)</sup>		✓
76-88	TCVADESHAGCEK	1349.5	2543.9 <sup>(2)</sup>		✓
375-386	EYEATLEECCA	1388.6	1945.8		✓
569-580	TVMENFVAFVDK	1399.7		✓	
421-433	LGEYGFQNALIVR	1479.8		✓	✓

387-399	DDPHACYSTVFDK	1497.6	2054.8		✓
139-151	LKPDPNTLCDEFK	1519.7	2076.9	✓	✓
347-359	DAFLGSFLYEYSR	1567.7		✓	
267-280	ECCHGDLLECADDR	1578.6	2135.8	✓	✓
184-197	YNGVFQECCQAEDK	1633.7	2190.9		✓
469-482	MPCTEDYLSLILNR	1667.8	2225.0	✓	✓
508-523	RPCFSALTPDETYVPK	1823.9	2381.1		✓
529-544	LFTFHADICTLPDT EK	1850.9	2408.1		✓
319-336	DAIPENLPPLTADFAE DK	1956.0		✓	
45-65	GLVLIAFSQYLQQCPF DEHVK	2435.2	2992.4	✓	✓

Note: (1). There is a phosphorylation group at position 82 (Serine residue, S); (2). There are two fluoruous-labeled cysteine residues (C) in different positions which are separated by eight other residues.

Assignments were made by matching the masses of the observed residues with those calculated using the UniPortKB-Swiss-Prot PeptideMass software. Only seven peptide fragments containing cysteine residues are seen before washing (Fig. 4.9a), presumably because of signal suppression and background noises due to the presence of salts [109]. After washing, the number of cysteine-containing peptides increased to 19 from 7, while the other peptides which did not contain cysteine effectively disappeared, (Fig. 4.9b). At the same time, the background noise significantly decreased to produce a mass spectrum with a better signal-to-noise ratio. These results confirm that the enrichment strategy for cysteine containing fragments with a washing step can effectively

simplify the resultant mass spectrum of a complex mixture, and increase the detect sensitivity for a peptide subset of interest.

Interestingly doubly-labeled peptides were seldom observed for peptides with adjacent cysteines. The sole example observed of a peptide with two fluorouracil-affinity tags is TCVADESHAGCEK, where the two cysteines are separated by other eight residues. This is different from when fluorouracil labelling takes place in solution; there doubly- and even triply-labeled cysteine-containing peptides are observed [72]. It is proposed that interfacial reactions are subject to more steric hindrance and orientational effects. This hypothesis agrees with a study that reported that an interfacial reaction can differ dramatically from the corresponding solution-phase reaction [110].

#### **4.2.4: Compatibility of fluorouracil-affinity enrichment methodology with MS/MS sequencing**

An ideal approach for the analysis of complex biosamples would necessarily involve effective separation and enrichment of the analytes of interest, followed by qualitative identification of the targeted analytes using methodologies such as MS/MS protein sequencing. Typically, the classic biochemical affinity method involving biotin-streptavidin pairs can complicate MS/MS spectra that make the results difficult to interpret [103]. In this work a cysteine-containing peptide with a fluorouracil-affinity tag,  $C^{RF17}$ ASIQK, was subjected to collision-induced dissociation (CID) in the triple quadrupole (QqQ) mass spectrometer to establish if fluorouracil-affinity NIMS can lead to proper MS/MS sequencing and yield simpler spectra that can be readily interpreted.

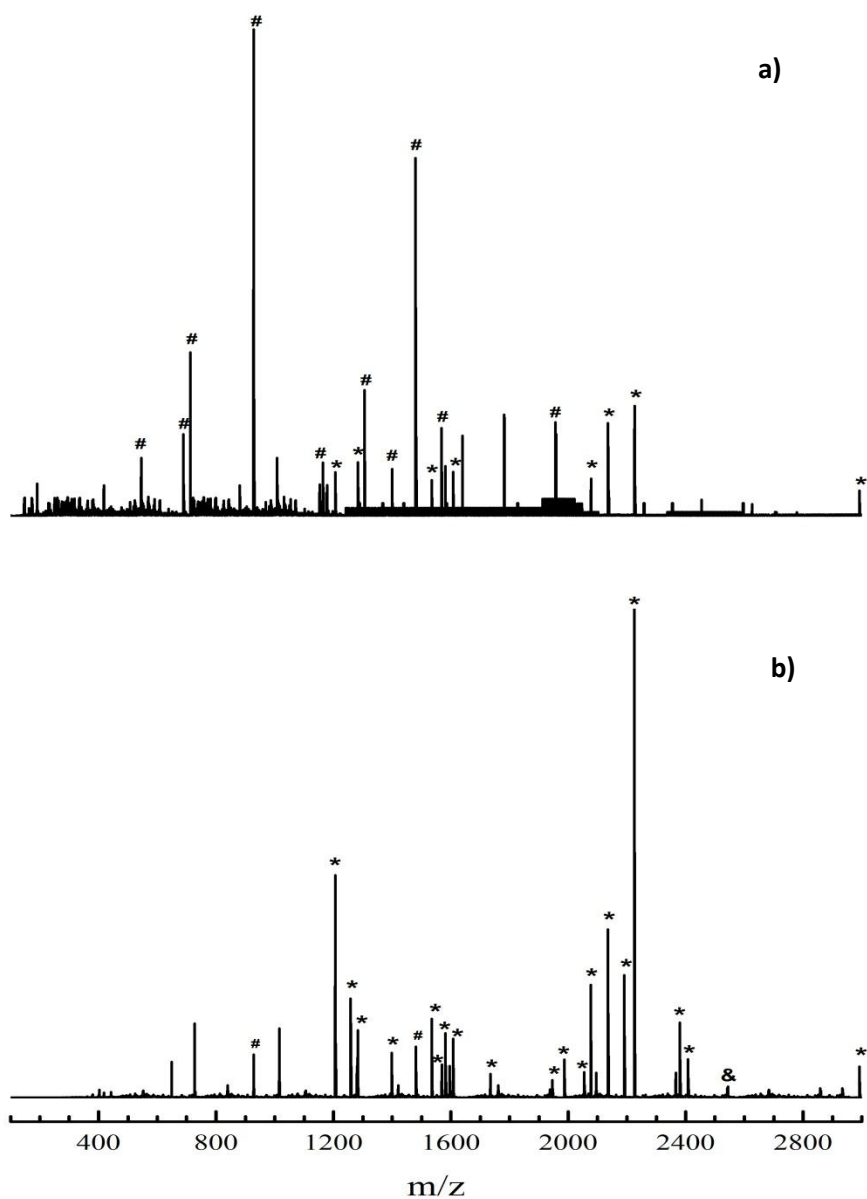


Fig. 4.9a): NIMS spectrum of a group of residues from a 200 fmol BSA tryptic digest before washing. 4.9b): NIMS spectrum produced at the same condition as 4.9a), but recorded after washing the chip with 40% methanol in water solution containing 0.1% TFA. # corresponds to peptide peaks detected by NIMS not containing cysteine residues; \* corresponds to peptide peaks containing cysteine residues; & corresponds to one peptide fragment containing two cysteine residues.



The MS/MS spectrum of the analyte shown in Fig.4.10 is composed of multiple b and y ion series. In general, y and b ions result from the cleavage of the CO-NH bond, which is the most common one among three possible cleavage points in the formation of peptide fragment ions. The numbering of y and b indicates which peptide bond is cleaved based on counting from C- or N- terminus, respectively. No fragment ions from perfluorinated tag are observed. In most MS/MS spectra immonium ions,  $[\text{H}_2\text{N}=\text{CH}-\text{R}_1]^+$  (where  $\text{R}_1$  represents side chain group in amino acid residue), are often observed and provide information on the types of amino acids present in the sequence.

Interestingly, the MS/MS spectrum of the cysteine residue containing a fluorinated tag in Fig. 4.10 exhibits a unique immonium ion of  $m/z$  633, which is attributed to the characteristic mass (76) of the cysteinyl immonium ion plus the mass of fluorinated tag (557). This characteristic ion can serve as a marker to confirm if any given species is indeed labeled. These results are in good agreement with those observed by Brittain *et al.* [106] and confirm that a fluorinated-affinity tag does not complicate the MS/MS spectrum. Instead, the presence of the tag makes the spectral interpretation simpler by providing a distinctive marker for the tagged cysteine residues.

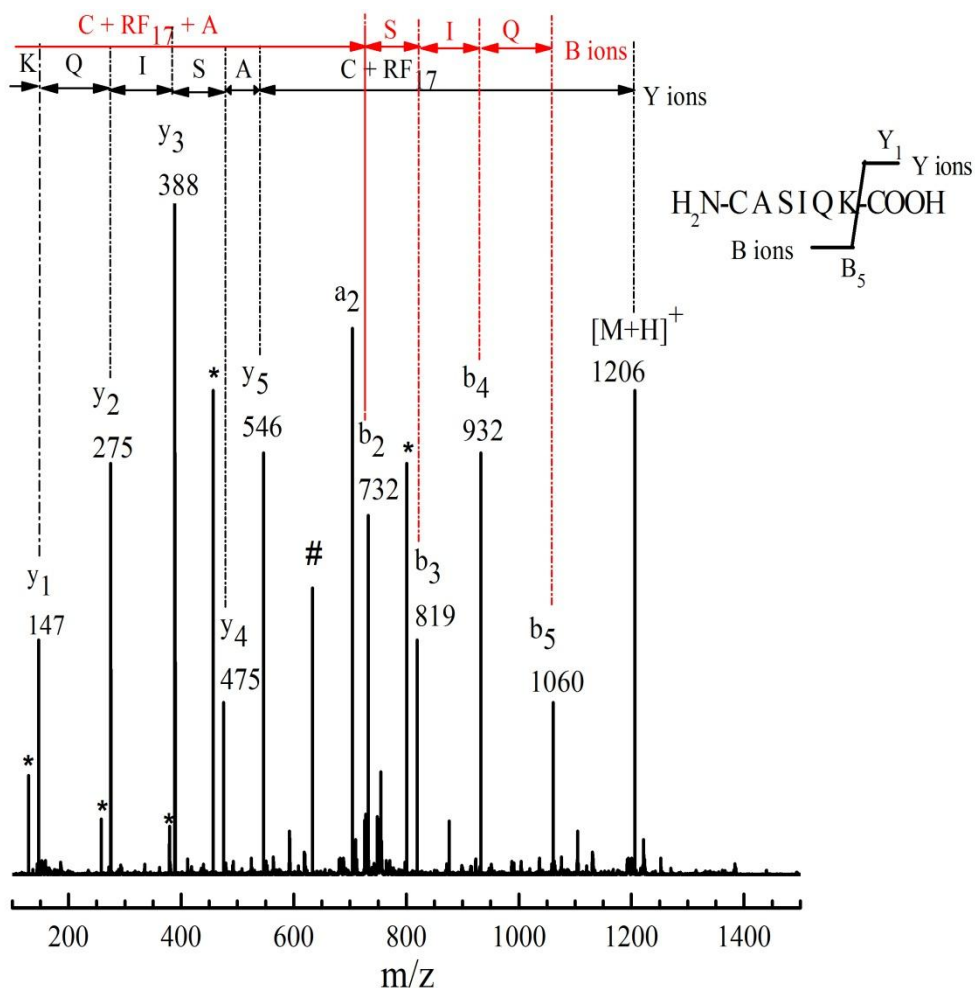


Fig. 4.10: A MS/MS spectrum of fluoros-affinity labeled peptide,  $C^{RF17}ASIQK$ , produced by CID using  $[M+H]^+$  as precursor. The top shows the complete peptide sequence of Y and B ions which were assigned from mass differences corresponding to the mass of amino acid residues. The graphic in the top right corner exhibits how Y and B ions are cleaved. The  $a_2$  ion, which is obtained by loss CO(28) from a  $b_2$  ion, is often observed as a diagnostic for  $b_2$ . # is an immonium ion peak of fluoros-tagged cysteine residue at  $m/z = 633$  with a structure  $[H_2N=CH-C^{RF17}]^+$ , where  $C^{RF17}$  is fluoros-tagged cystenyl. \* correspond to ions which have lost water or ammonia.

## **Chapter 5: Label-free kinase activity assay and inhibitor screening using a fluoros-affinity NIMS chip**

### **5.1: Background**

Enzymes play a crucial role in regulating a wide range of life processes such as cell growth, migration, differentiation and death [111, 112]. They are also widely used in industry to screen for drug targets [113] and as biocatalysts in the manufacturing of biofuels [114]. It is therefore important to develop rapid and sensitive methods to elucidate enzyme catalytic mechanisms, characterize enzymatic activities, and to rapidly screen for inhibitory compounds [115]. Most current enzyme assays make use of the differences in spectroscopic properties between a substrate and a product during conversion. Typical analytical technologies include the fluorescence and UV-Vis absorption spectroscopy [116, 117]. Although these methods are rapid, simple and suitable when using high-throughput microtiter plates and microarrays [118-120], they can suffer from limitations which include faulty outcomes caused by the introduction of a fluorescence group into the substrate to overcome the fact that most naturally occurring substrates do not readily exhibit any absorption or emission properties in the optical regime [121, 122]. Derivatization can also change the kinetic properties of the substrate and perturb the absorption and fluorescence spectra of enzymes, cofactors and/or buffers in the reaction mixtures [123].

Radioactivity assays of enzyme-catalyzed reactions rely on substrate radioactive labels. Although the use of radioactively-labelled substrates preserves the chemical integrity of the substrate, the synthesis of radioactive-labelled compounds can be quite

laborious, and the handling and ultimately disposal of radioactively “hot” materials requires strict safety protocols [115].

MS is a technique that is ideally suited for enzymatic activity assays and inhibitor potency screening because mass detection is a direct measurement, and product formation can be readily established by simply measuring the reactant-product mass differences resulting from the enzyme reaction [124]. One of earliest techniques developed was GC-MS to monitor volatile by-products of enzyme reactions [125, 126]. Subsequent development of ionization techniques such as thermospray MS and fast atom bombardment (FAB) MS allowed polar substrates and products in aqueous solutions to be measured [127-130]. Protein kinase assays were also developed obtained imaging peptide-conjugated gold nanoparticles using SIMS [131].

The attractiveness of MS over UV-Visible absorption spectrometry, fluorescence and radioactivity detection stems from its ability to perform enzyme assay using label-free substrates, thereby circumventing the often laborious and costly protocols associated with substrate labelling. Unlike fluorescence-based assays, mass detection avoids sample autofluorescence and/or light scattering, thereby reducing the number of false positives and negatives during high-throughput screening for enzymatic inhibitors [132]. Furthermore, unlike label-based detection, mass detection can be used to simultaneously monitor the concentrations of a range of compounds during an enzyme-catalyzed reaction including those of substrate, product, possible cofactors, coenzyme, and any internal standards [133, 134].

Today, MALDI and ESI MS have emerged as powerful methodologies capable of directly measuring substrates and reaction products [112, 135-137]. Recently, the

capabilities of MALDI MS have been extended to include imaging (MALDI IMS) [131, 138]. DIOS MS has also been used to measure enzyme substrate kinetics by analyzing the residue of a reacting enzyme and substrate droplet as it travels down the length of a porous silicon microfluidic channel [138].

Despite the power of MALDI MS it possesses a number of inherent limitations including the presence of “sweet spots”, areas on the solid solution surface where MALDI ion signal intensities are particularly intense. These are due to the heterogeneity of the solid solution formed when the matrix and analyte are co-crystallized. Quantitative analyses are therefore extremely challenging because of the resultant shot-to-shot variability [5]. Furthermore, low molecular weight substrates and products can be readily masked by strong matrix signals. Similarly, a difficulty associated with high throughput enzyme inhibitor screening based on ESI MS, is the need to desalt the sample which significantly slows down the analysis and increases its cost [124].

The new desorption/ionization technique of NIMS, which uses ‘initiator’ molecules trapped within a nanostructured material to assist the release and ionization of intact molecules adsorbed on that material's surface upon laser or ion irradiation, has a number of features which can overcome the limitation noted above for MALDI MS and ESI MS [30]. The advantages of NIMS over MALDI MS and other surface desorption/ionization techniques include higher analyte sensitivity and simpler sample preparation; the latter is due to the fact that NIMS is "matrix-free" in that the analyte is not co-crystallized with the initiator.

The sensitivity and throughput of enzyme assays can be markedly improved by transforming conventional solution-based approaches to those involving an immobilized

phase [139]. For example, the evaluation of ligand–receptor interactions and enzymatic activities using peptide chips [140-144], is seen as an attractive option. Many enzyme processes, including kinase [145] and protease[146, 147] activities, can be readily studied using peptides as model substrates.

Recently the use of biochips based on fluororous-affinity interactions has emerged as a new technique for studying biological systems [104]. This approach takes advantage of a fluororous tag immobilized on the surface of a biochip to capture analytes of interest by fluorine-fluorine interactions. When combined with mass spectrometry, it can through on-site enrichment provide rapid and sensitive analyses of targeted species [107]. As a proof-of-principle experiment, a NIMS enzymatic assay, or "Nimzyme", was developed to detect both addition and cleavage reactions by enzymatic catalysis of sialyltransferase and galactosidase with extremely high sensitivity (subpicogram level) [71]. In this way the enzyme activity of crude cell lysates from thermophilic bacteria could be directly characterized. In addition, fluororous-affinity immobilization has been used to construct small molecule microarrays for the analysis of carbohydrates [61] and for high-throughput enzyme inhibitor screening for drug discovery [55].

In this work, substrates containing cysteine residues were anchored to a NIMS chip and used to detect kinase activities for the first time by employing a fluororous affinity tag of 3-(perfluorooctyl)-propyl-1-maleimide. This “soft” immobilization, which is accomplished by non-covalent fluorine-fluorine interactions, allows enzyme substrates and reaction products to be efficiently desorbed and subsequently ionized in a mass spectrometer. This methodology was first demonstrated by our group for a rapid screening protein kinase A (PKA, Fig. 5.1 [148]) activity assay for different peptide

substrates. A multi-kinase activity assay was also demonstrated using such fluoros-  
affinity NIMS chip which incorporated a mixture of kinase-specific peptide substrates.  
The enzymatic inhibition potency was characterized by an  $IC_{50}$  value obtained by directly  
measuring the ratio of substrate-to-product concentrations against known inhibitors for  
PKA and Abl protein tyrosine kinase (Abl, Fig.5.2, [149]).

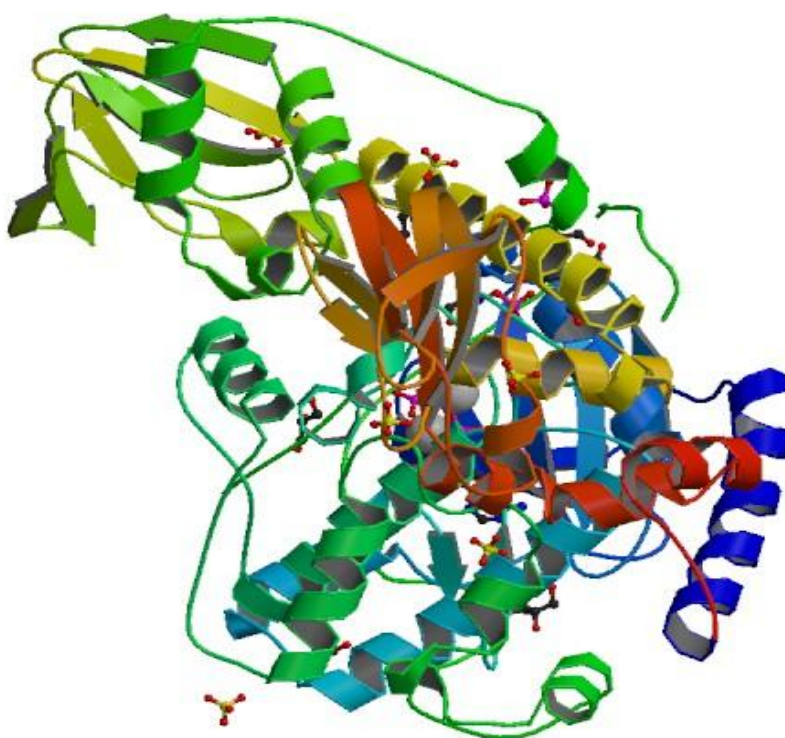


Fig. 5.1: The crystal structure of protein kinase A (PKA) [148].

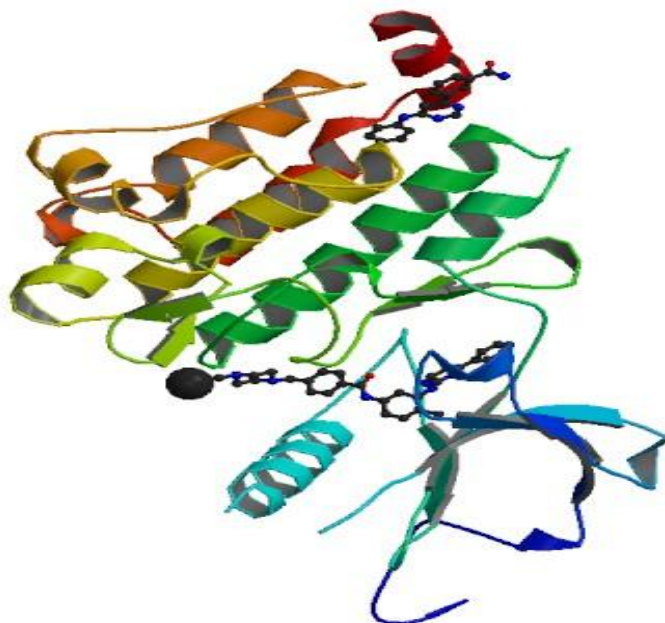


Fig. 5.2: The crystal structure of Abl protein tyrosine kinase (Abl) [149].

## 5.2: Results and discussion

Previous experiments using fluoros-affinity NIMS chips have demonstrated that a desired subset of analytes (e.g. peptides containing cysteine residue) can be efficiently isolated and enriched from extremely complex samples such as a BSA protein digest, as described in chapter 4. There, a cysteine-containing peptide substrate was anchored to the surface of a fluoros-affinity NIMS chip by a simple and highly selective Michael addition reaction between thiol and maleimide groups [108]. In this work, the strategy takes advantage of surface-immobilized substrates to perform an enzyme activity assay to provide a quantitative evaluation of enzyme inhibition to demonstrate that inhibitor screening can be done rapidly. The workflow designed for this experiment is shown in the Fig. 5.3. First, a crude mixture containing a particular substrate, or a substrate mixture



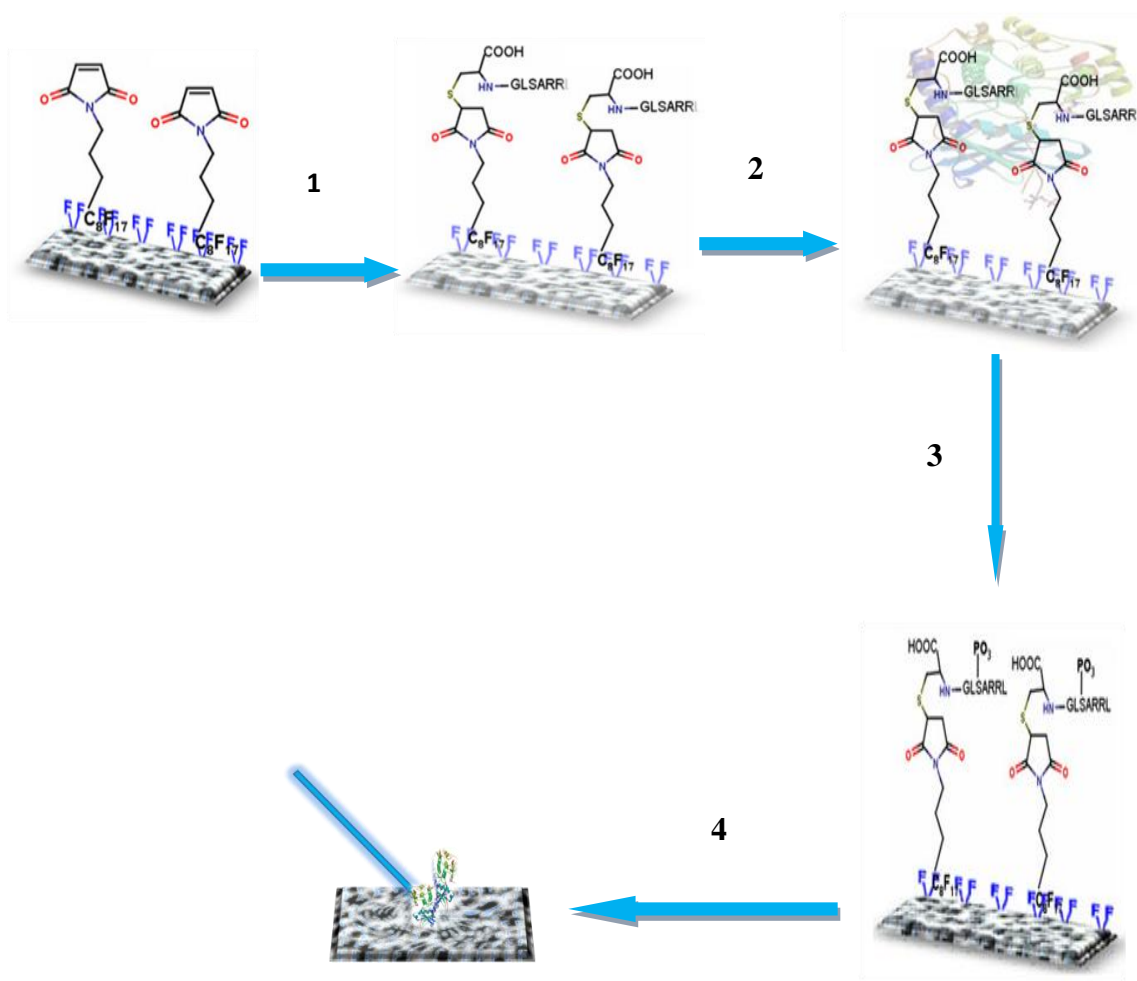


Fig. 5.3: Schematic diagram for NIMS-based assays: 1. A specific class of substrate peptides is captured by fluororous phase interactions with a fluororous affinity tag immobilized on a NIMS chip. 2. An enzyme such as protein kinase A (PKA) is added onto the NIMS chip; 3. A product such as phosphorylated peptide is produced by the enzyme reaction. 4. The substrate and product are detected by NIMS.

containing many types of species is loaded onto a NIMS chip with a specific fluororous affinity tag. Next, an enzyme in a reaction buffer solution is added onto the loaded fluororous-affinity NIMS chip allowing the dissolved enzyme molecules to diffuse to the sites at which the substrates are bound. After the enzyme catalytic reactions are completed the chip is eluted with a fluorophobic solvent such as 40% methanol water solution with 0.1% TFA to remove any residual nonfluorous compounds that are not

bound to the fluororous affinity tag, salts and other contaminants. This step does not affect the bound substrates or products with fluororous tags. Finally, the NIMS chip is subjected to mass spectrometry analysis. The feasibility of a kinase PKA assay using this methodology is demonstrated here by analyzing a mixture of three peptides (Pep1, Pep2 and Pep3), where only substrate Pep2 contains a cysteine residue.

### **5.2.1: Enzymatic activity assay of PKA with fluororous-affinity NIMS chip**

Protein kinases are enzymes that catalyze the transfer of a phosphate group to tyrosine, serine or threonine residue of a substrate protein [142]. They play a crucial role in regulatory functions of all cellular processes including cell growth, migration, differentiation and death [111]. Hence, kinase activities assays are extreme important for developing lead compounds for drug discovery.

In this work fluororous-affinity NIMS chips were developed as an assay for protein kinase A (PKA) activity. The substrate chosen for study was a peptide (Pep2, LRRASLGC) containing both cysteine and serine residues. This allows it to be both easily immobilized by the fluororous-affinity NIMS chip and to be phosphorylated by the PKA enzyme. Fig. 5.4a shows a single major peak at  $m/z$  1433 corresponding to the protonated product of Pep2 having the fluororous affinity tag. After treatment with PKA using the procedure described above the original peak corresponding to the substrate peptide disappeared, and a new peak was observed at  $m/z$  1513 (Fig. 5.4b) which corresponds to the peptide having been phosphorylated. The expected mass change of 80 confirms the addition of the phosphate group to the peptide substrate by PKA, as shown in Fig. 5.5. The peak intensities also suggest that fluororous affinity immobilization does not significantly interfere with the reactivity of either the enzyme or the substrate.

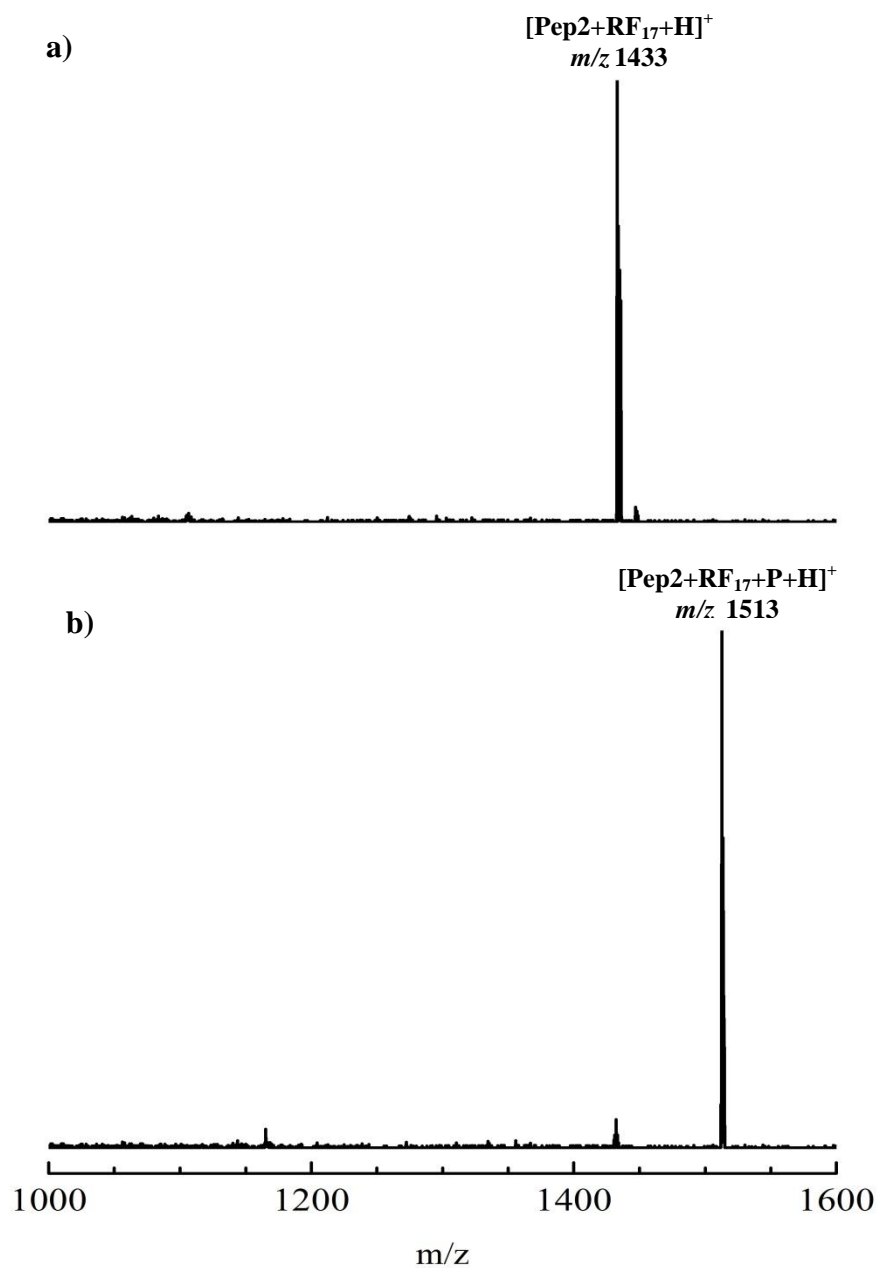


Fig. 5.4a) The mass spectrum of a substrate (Pep2) with fluoros tag before adding the PKA enzyme. b) The mass spectrum after adding PKA. The major peak corresponds to phosphorylated Pep2 resulting from the reaction of the substrate with PKA.

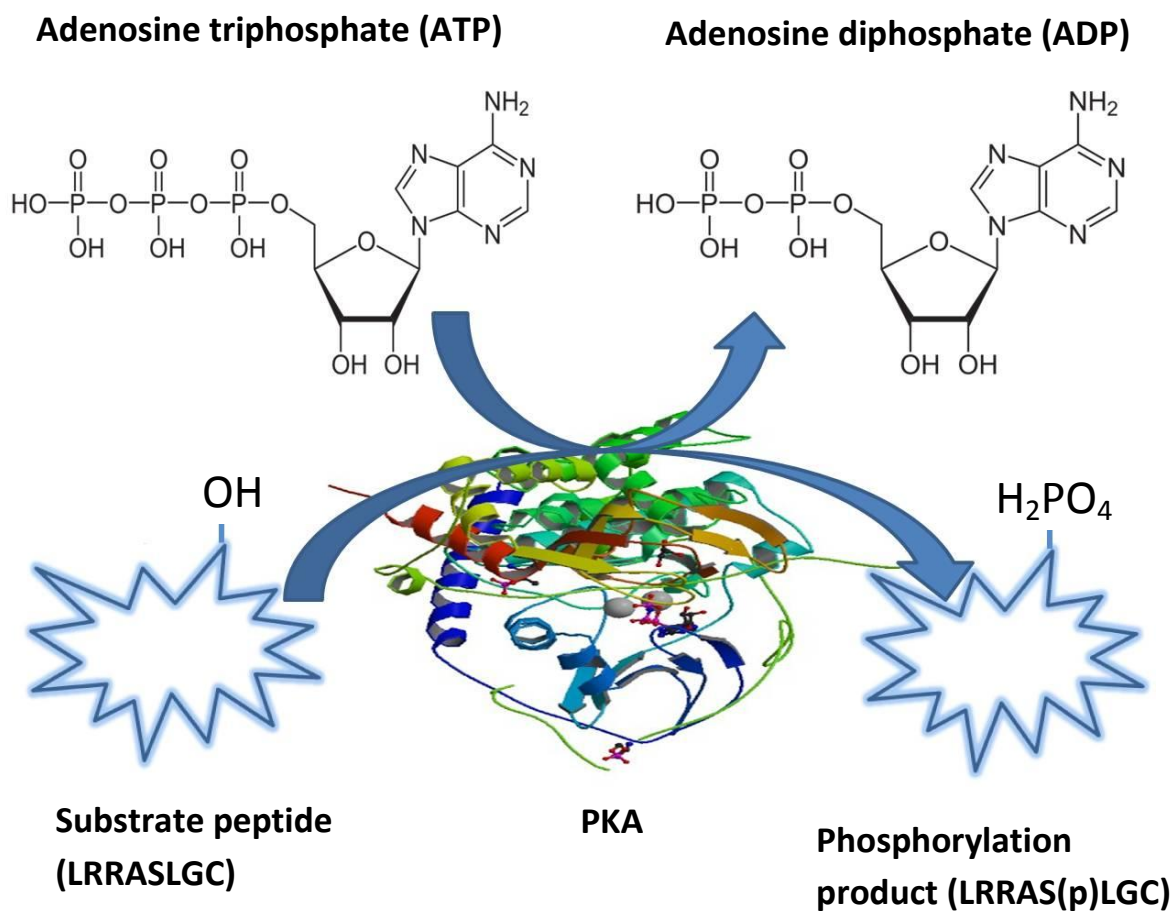


Fig. 5.5: Schematic diagram of phosphorylation reaction under assistance of protein kinase A (PKA), which can catalyse the transfer of ATP terminal phosphate to peptide or protein substrates at serine or threonine residues.

A substrate mixture composed of three peptides: Pep1, Pep2 and Pep3 was next spotted into the chip surface as a model system to evaluate the utility of fluoros-affinity NIMS chips as an enzymatic activity assay for complex biological samples. The phosphorylation reaction was allowed to proceed at 30°C in a water bath chamber for 30 min. The chip was then rinsed 3-5 times using a 40% methanol water solution and places in the mass spectrometer for NIMS analysis. As expected (Fig. 5.6), only the Pep2 substrate was phosphorylated. This shows that the methodology developed here is suitable for the direct analysis of complex mixtures.

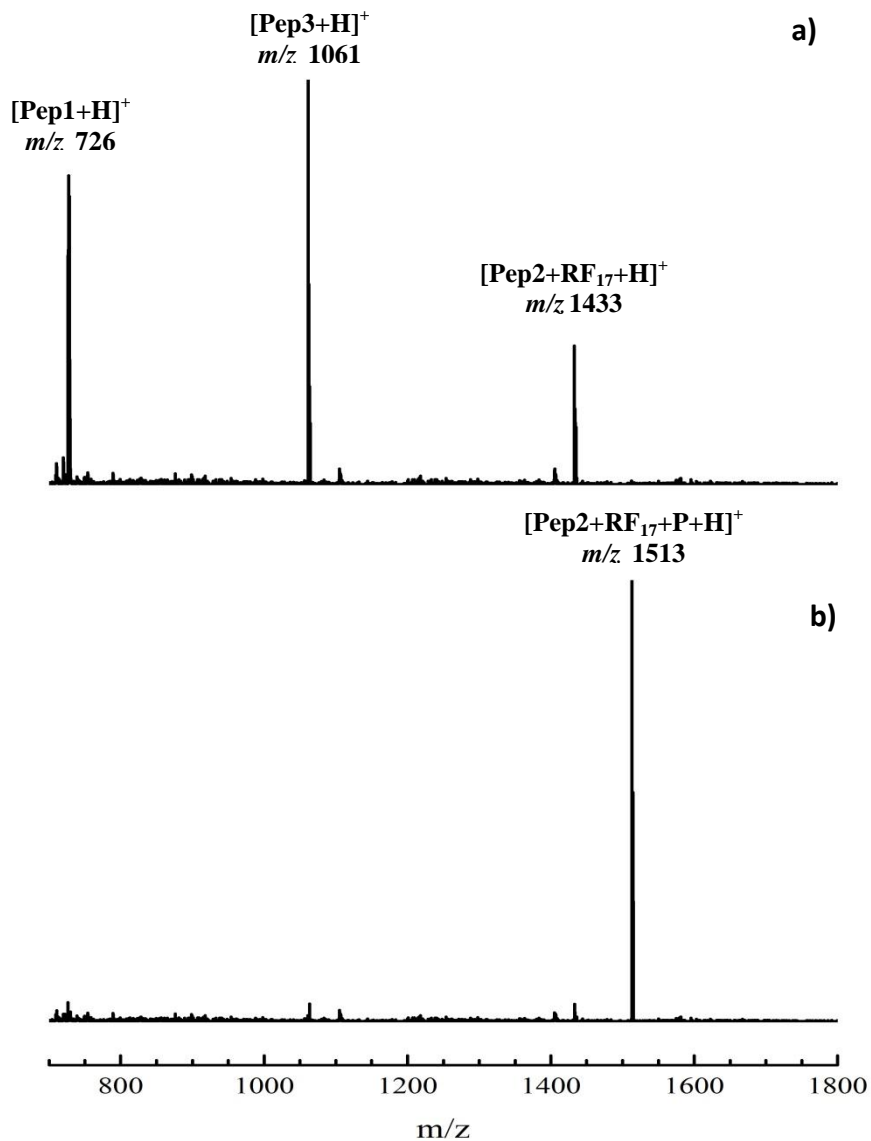


Fig. 5.6a) Mass spectrum of a mixture of peptides (Pep1, Pep2 and Pep3) obtained using a fluoros-affinity NIMS MS chip before adding kinase PKA. b) Mass spectrum of the products formed from the mixture in a) after the addition of PKA and rinse using a 40% methanol water solution.

### 5.2.2: NIMS chips for multiple kinase activity assays

Mass spectrometric techniques can provide information on both the extent of a reaction (percent conversion of substrates) and help to identify the products. These attributes provide an advantage over other enzyme activity assays (e.g. fluorescence and radioactivity assays) that typically provide information only on the extent of a reaction. Here we demonstrate that fluoros-affinity NIMS chips are capable of simultaneously measuring the PKA activity of multiple substrates. Specifically, a mixture of two peptides (Pep2 and Pep4, IYAAPKKKC, Fig. 5.7) was anchored to the maleimide-terminated surface of a fluoros-affinity NIMS chip. The resultant NIMS mass spectrum exhibits two well resolved peaks corresponding to the protonated tagged peptides:  $[\text{Pep2}+\text{RF}_{17}+\text{H}]^+$  and  $[\text{Pep4}+\text{RF}_{17}+\text{H}]^+$  (Fig. 5.8a).

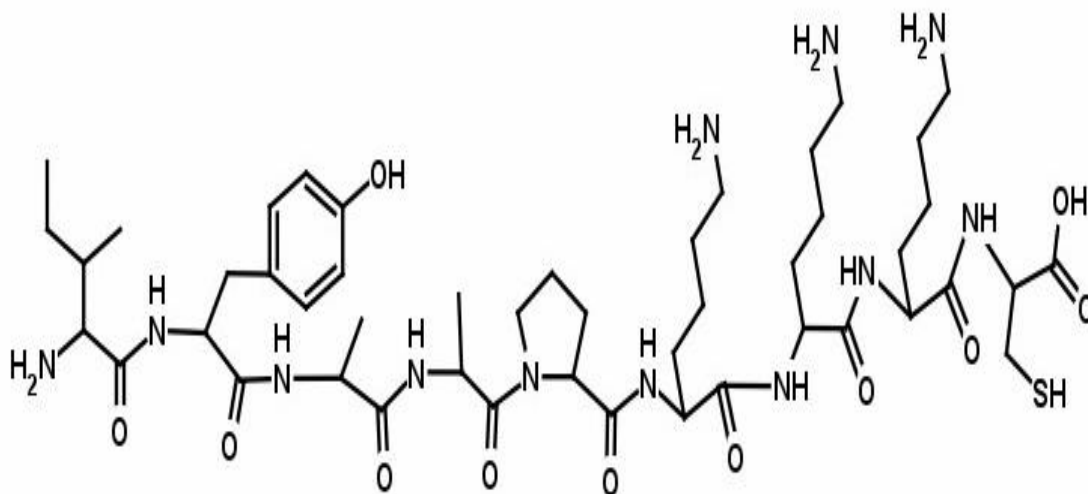


Fig. 5.7: The chemical structure of Pep4 (IYAAPKKKC).

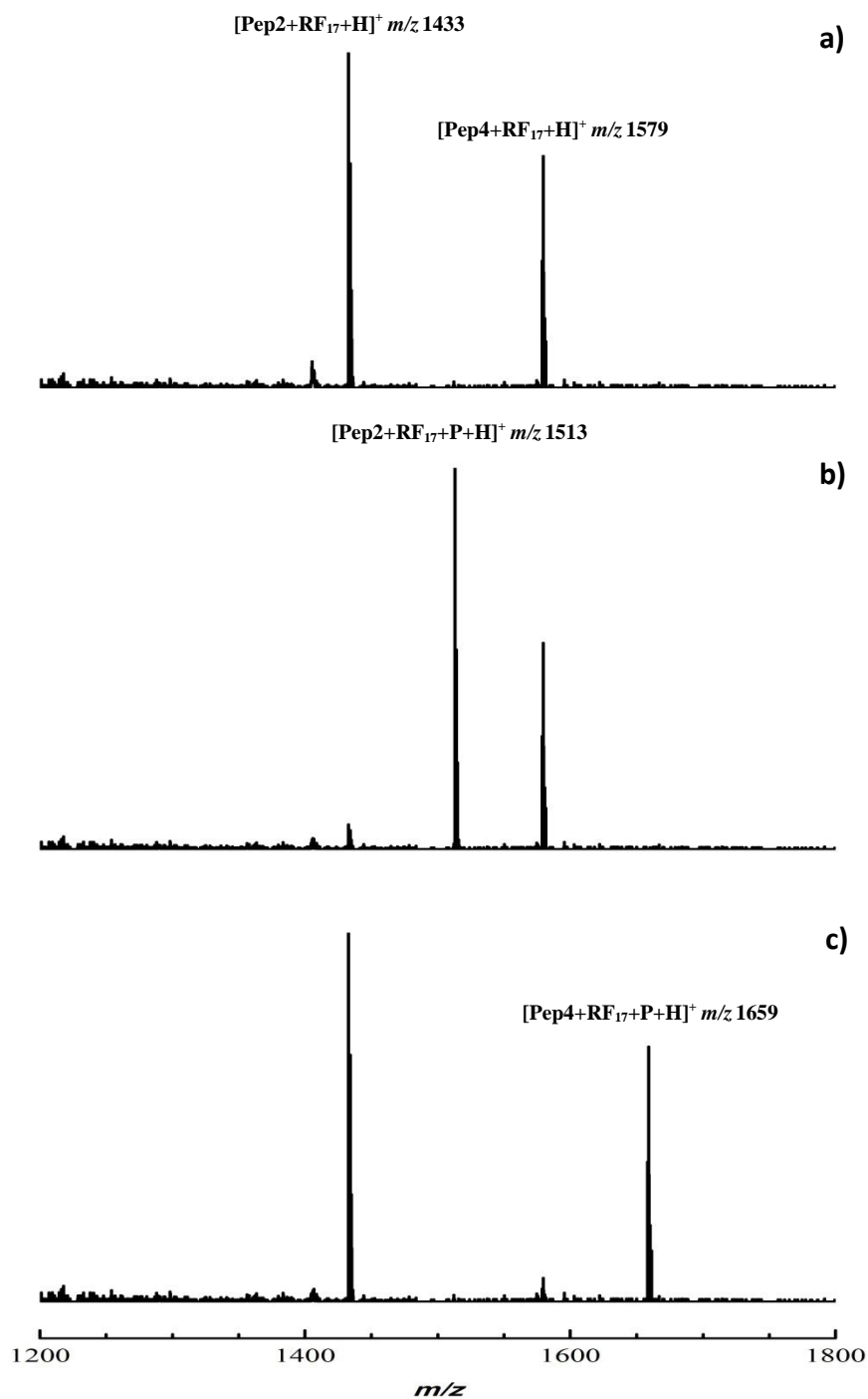


Fig. 5.8: NIMS spectra of obtained for the simultaneous measurement of multiple kinase activities. a) the NIMS spectrum of substrate peptides of LRRASLGC (Pep2) for PKA and IYAAPKKKC (Pep4) for Abl. b) the NIMS spectrum obtained after adding PKA. Only Pep2 has been phosphorylated. c) the NIMS spectrum obtained after the addition of Abl. Only Pep4 has been phosphorylated.

For comparison, PKA was added into a completely identical fluoruous-affinity NIMS chip where only Pep2 was expected to be phosphorylated. This can be confirmed by examining Fig. 5.8b). Here the mass peak corresponding to the phosphorylated Pep2 is observed while Pep4 is unaffected. In a separate experiment, an identically-prepared NIMS chip was treated with kinase Abl which was expected to react specifically with Pep4. As shown in Fig. 5.8c), Pep4 is phosphorylated while Pep2 was unaffected. These results show that a single fluoruous-affinity NIMS chips can be used to rapidly and easily characterize different enzyme reactions for substrate mixtures.

### **5.2.3: Quantitative analysis of enzyme inhibition by product/substrate ratio measurements**

It is well-known that MALDI MS sample inhomogeneity results in poor sample-to-sample and shot-to-shot reproducibility. Although various strategies have been developed to minimize these problems [123], these methods increase the complexity of sample preparation, decrease detection sensitivity or require extra clean-up steps to reduce ion suppression caused by contaminating salts.

A near ideal quantitative analysis strategy would involve monitoring the relative ratio of the substrate/product intensities by MS. This ratio is a direct measure of enzyme activity and inhibition without internal standards [150-152]. In such methods, ion intensities for the substrates and products of each enzyme reaction are used to calculate the percent conversion (% C) of a substrate to product, and subsequently, the percent maximal activity (% MA) in a manner similar to previous reports [150, 153, 154]. % C is defined as the product ion intensity ( $I_p$ ) divided by the sum of the substrate ion intensity ( $I_s$ ) and  $I_p$  multiplied by 100% [150]:



$$\% C = [I_p / (I_p + I_s)] \times 100\% \quad (5.1)$$

% MA is defined as the degree of enzyme inhibition to which the % C from the control reaction (no inhibitor) has been diminished in reactions that contain an inhibitor based on Eq 5.2 [153]:

$$\% MA = (\% C \text{ with inhibitor} / \% C \text{ without inhibitor}) \times 100\% \quad (5.2)$$

The average background signal, which is taken as any product signals in the absence of the enzyme, was routinely subtracted from all % C measurements prior to calculating % MA [153]. IC<sub>50</sub> values are calculated from a 10-point sigmoidal dose response curve, which is a plot of log [inhibitor] against % MA.

Greis and colleagues [124] investigated the validity of the assumption that simple products/substrates for enzyme ratios retain a linear relationship thereby allowing for accurate and quantitative measurement using known molar ratios of products and substrates for PKA spotted onto a MALDI probe for analysis. The plot of the percent product from MALDI-TOF MS against the known molar ratios showed that the phosphorylated products had a slight under-estimation compared to the known molar ratios in positive ion mode while a slight over-estimation in negative ion mode, as shown in the Fig. 5.9 [124]. One could expect that the negative ion mode favor the ionization and detection of the phosphorylated product due to its increased acidity in contrast to the substrate peptides. Whatever the case, what is the most important is that the product/substrate ratios produce a good linear relationship with their molar ratios in both cases and can be used to directly compare relative enzymatic activity for inhibition measurement.

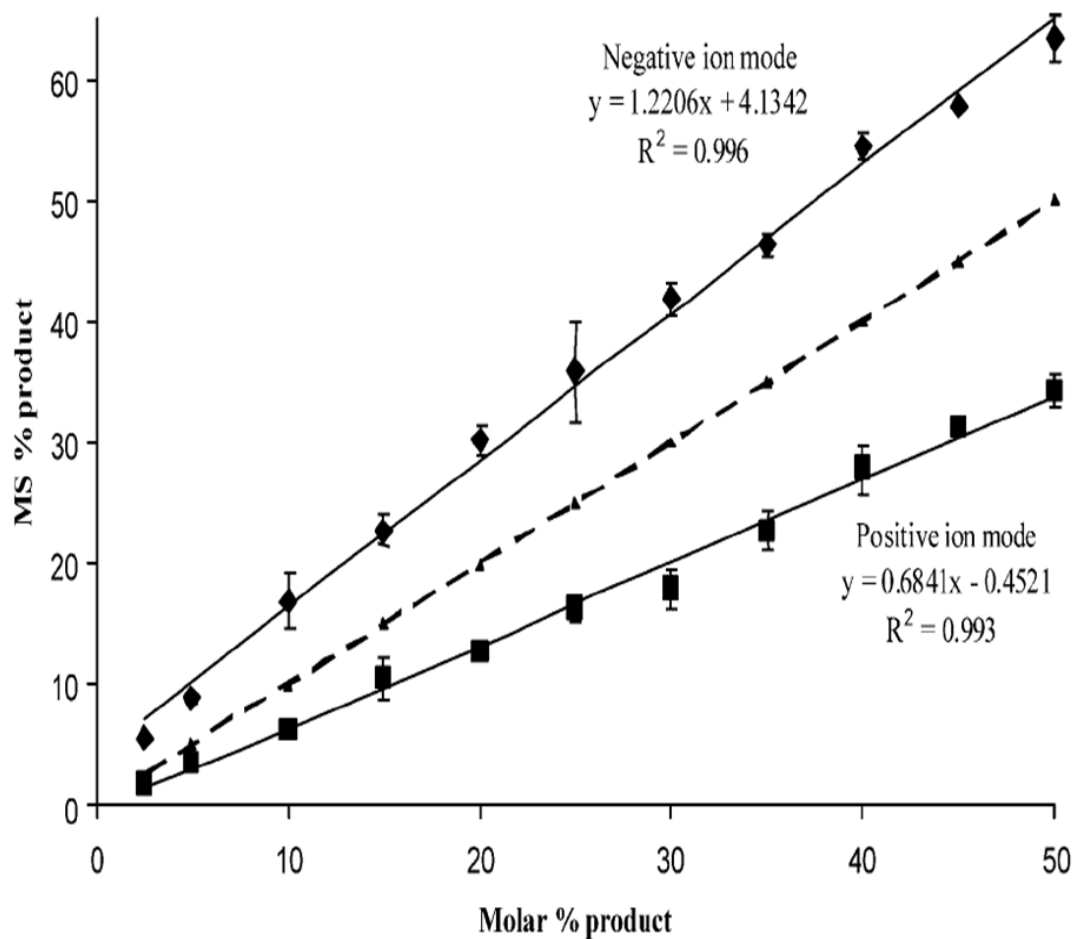


Fig. 5.9: Plots of the percent product measured by MALDI-TOF MS using CHCA as matrix versus the indicated molar ratios onto the MALDI target plate demonstrated validation of product/substrate for enzyme ratios served as a quantitative enzyme assay without internal standards. The dashed line represents the theoretical linear relationship if the MS readout matched the molar ratios (i.e., the substrate and product had equal ionization and detection efficiencies) [124].

The quantitative nature of the enzyme assay without internal standards developed was validated in this work by NIMS detection using a standard substrate peptide, LRRASLGC, for kinase PKA and its phosphorylated product, LRRAS(p)LGC. Fig. 5.10 shows a plot of the percent product peptide positive ion NIMS intensity normalized by the sum of the intensities of substrate and product peptide signals versus the percent number of moles of phosphorylated peptide in a 200 fmol peptide mixture. The correlation is excellent ( $R^2 = 0.9959$ ) and the slope (0.738) is closer to the theoretical value (1) than that (0.684) [124] from MALDI MS detection Greis and colleagues did, presumably because the sample distribution is more homogeneous on a NIMS plate than in a MALDI matrix.

The validation of the NIMS detection as a feasible alternative to enzymatic inhibition assay was also evaluated by determining the half maximal inhibitory concentration ( $IC_{50}$ ) values, which is a measure of the effectiveness of a compound in habiting biological or biochemical function, for two known inhibitors: staurosporine (Stsp; Fig. 5.11) and Imatinib(originally STI571; Fig. 5.12). Stsp is a non-selective potent inhibitor against a variety of protein kinases including PKA [155]. The  $IC_{50}$  value of 20 nM was obtained from a 10-point dose-dependent inhibition assay plot of log [Stsp] against %MA (Fig. 5.13a). This agrees well with the  $IC_{50}$  values of 25-50 nM from MALDI MS studies and 20-60 nM using fluorescence detection [154].

Imatinib is an inhibitor of Abl, a drug used to treat certain types of cancer [156]. An  $IC_{50}$  value of 79 nM for Imatinib against Abl was obtained from Fig. 5.13b, which also agrees with previous reports [142, 157-159]. These results demonstrated that fluoruous-affinity NIMS can be effectively used for quantitative assays of kinase activities and its inhibition.

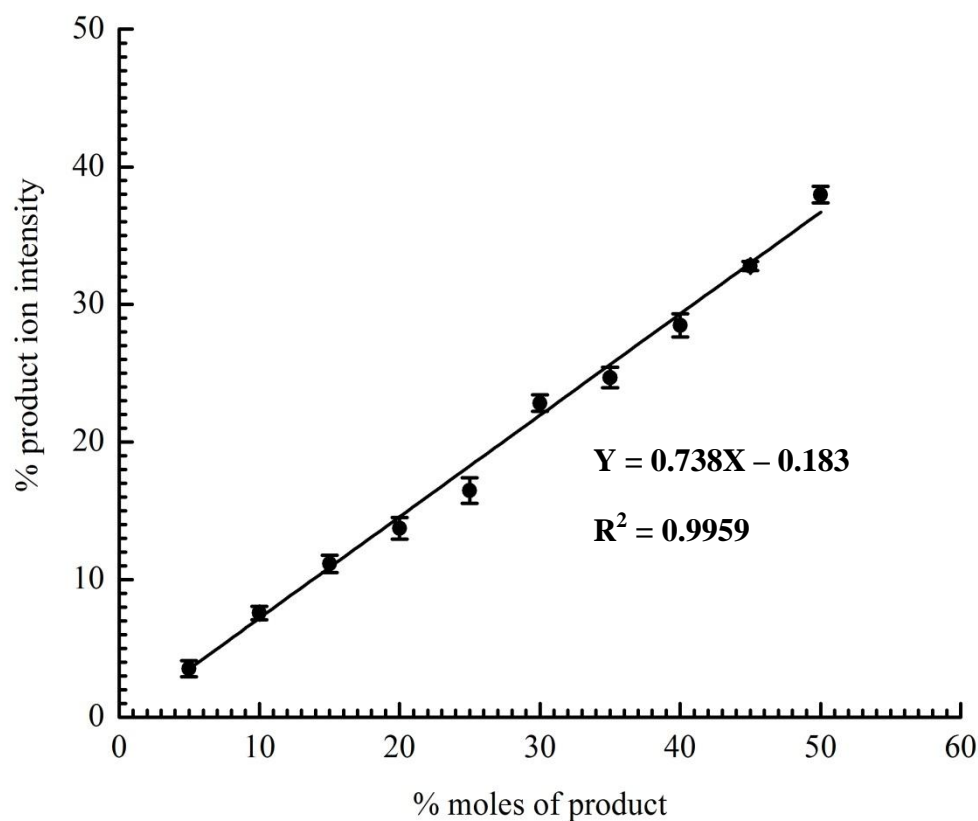


Fig. 5.10: Validation of the simple quantitative kinase PKA enzyme assay without internal standards by NIMS detection. In this experiment a standard substrate peptide, LRRASLGC, was used which was phosphorylated by the enzyme to produce the product peptide, LRRAS(p)LGC. The percent product peptide ion intensity over the intensity sum of substrate and product peptide from NIMS detection in positive ion mode is plotted against the percent number of moles of phosphorylated peptide in the 5 replicates with 200 fmol peptide mixture each.

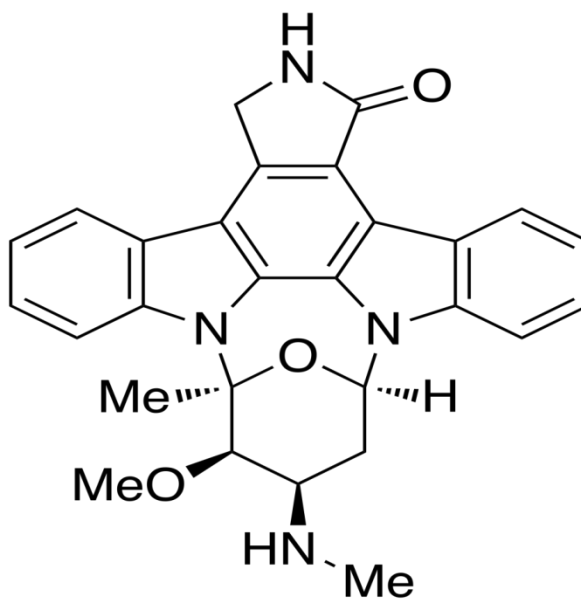


Fig. 5.11: The chemical structure of the PKA inhibitor staurosporine.

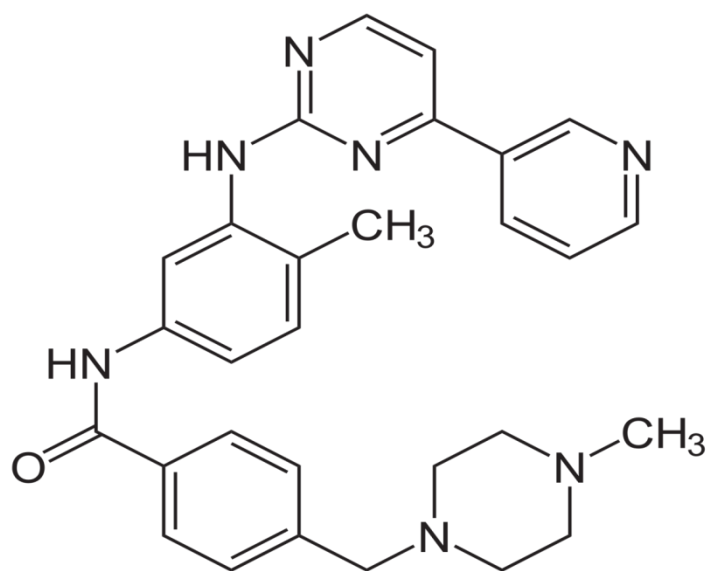


Fig. 5.12: The chemical structure of the Abl inhibitor imatinib.

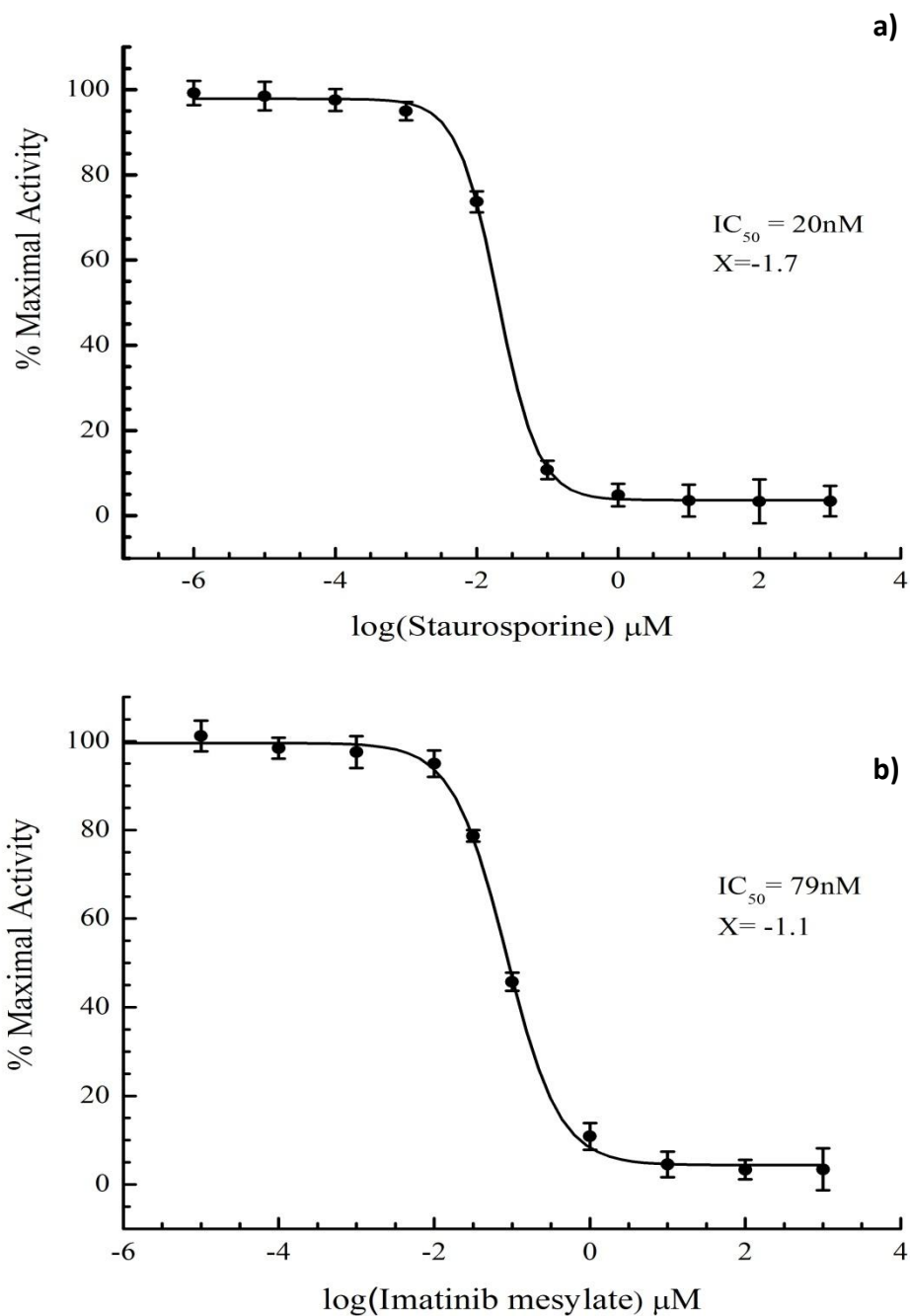


Fig. 5.13a) a 10-point dose-dependent inhibition assay curve obtained by plotting the log [Stsp] against degree of enzyme inhibition, %MA. b) a similar assay curve of the Abl inhibitor imatinib. Note that X means the log inhibition concentration.

#### **5.2.4: A potential platform for enzyme inhibitor screening**

Rapid compound screening for enzyme inhibition was next investigated using a fluoros-affinity NIMS chip. As shown in Fig. 5.14 Stsp and two classes of compounds, A (chemical structure shown in Fig. 5.15) and B (chemical structure shown in Fig. 5.16) as examples randomly chosen from chemicals library in our lab, were evaluated as inhibitor of kinase PKA using a NIMS chip having four dot array format. One of the dots contained no compound and was used as a control. A comparison of the mass spectra of the three classes of compounds with that of the control dot (Fig. 5.17) shows immediately that Stsp is the most potent inhibitor (as expected) while compound A was the least. Given that fluoros-affinity immobilization has been successfully used to construct small molecular microarray [61] and that NIMS has been shown to be effective at characterizing a peptide microarray [30], it is expected that the fluoros-affinity NIMS methodology will find applications as high throughput enzyme inhibitor screening methodology for drug discovery.

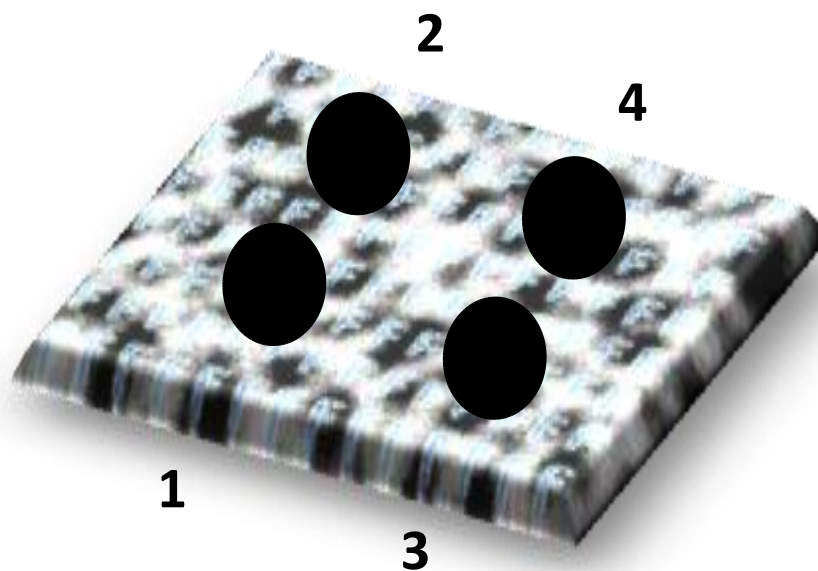


Fig. 5.14: A cartoon of a 2 x 2 NIMS chip array. Dot 1 is a control region of the chip where an enzyme and substrate have been added but not an inhibitor. Dot 2 is a region of the NIMS chip where the enzyme, the substrate in Dot 1, and a known inhibitor have been added. Dot 3 corresponds to a region of the NIMS chip where the enzyme, substrate, and potential inhibitor calix[4]arene have been added. Dot 4 corresponds to a region of the NIMS chip where the enzyme, substrate, and potential inhibitor C-methylcalix[4]resorcinarene have been added. Note that the area of each dot is  $\sim 3.14 \text{ mm}^2$ , and here the dots are not drawn to scale.



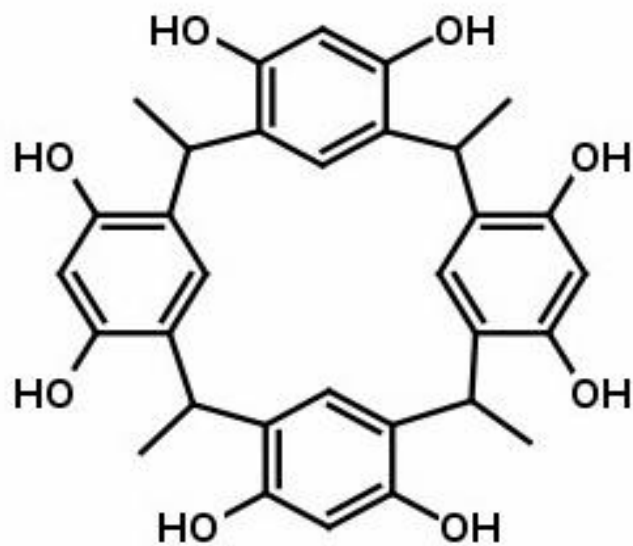


Fig. 5.15: The chemical structure of compound C-Methylcalix[4]resorcinarene.

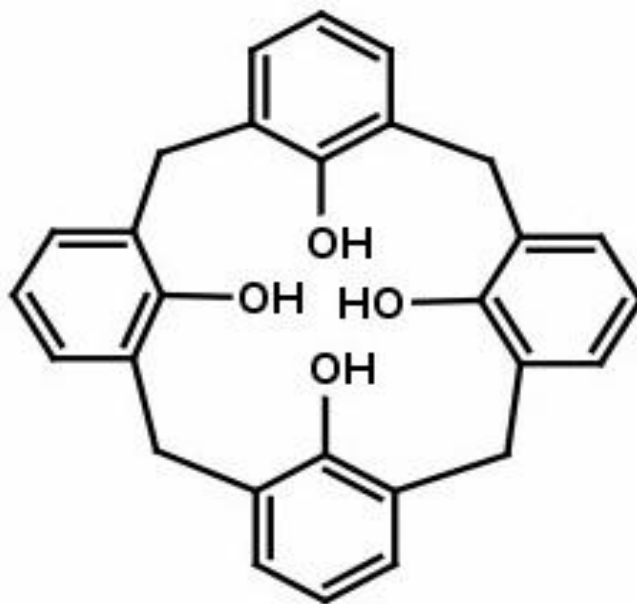


Fig. 5.16: The chemical structure of compound Calix[4]arene.

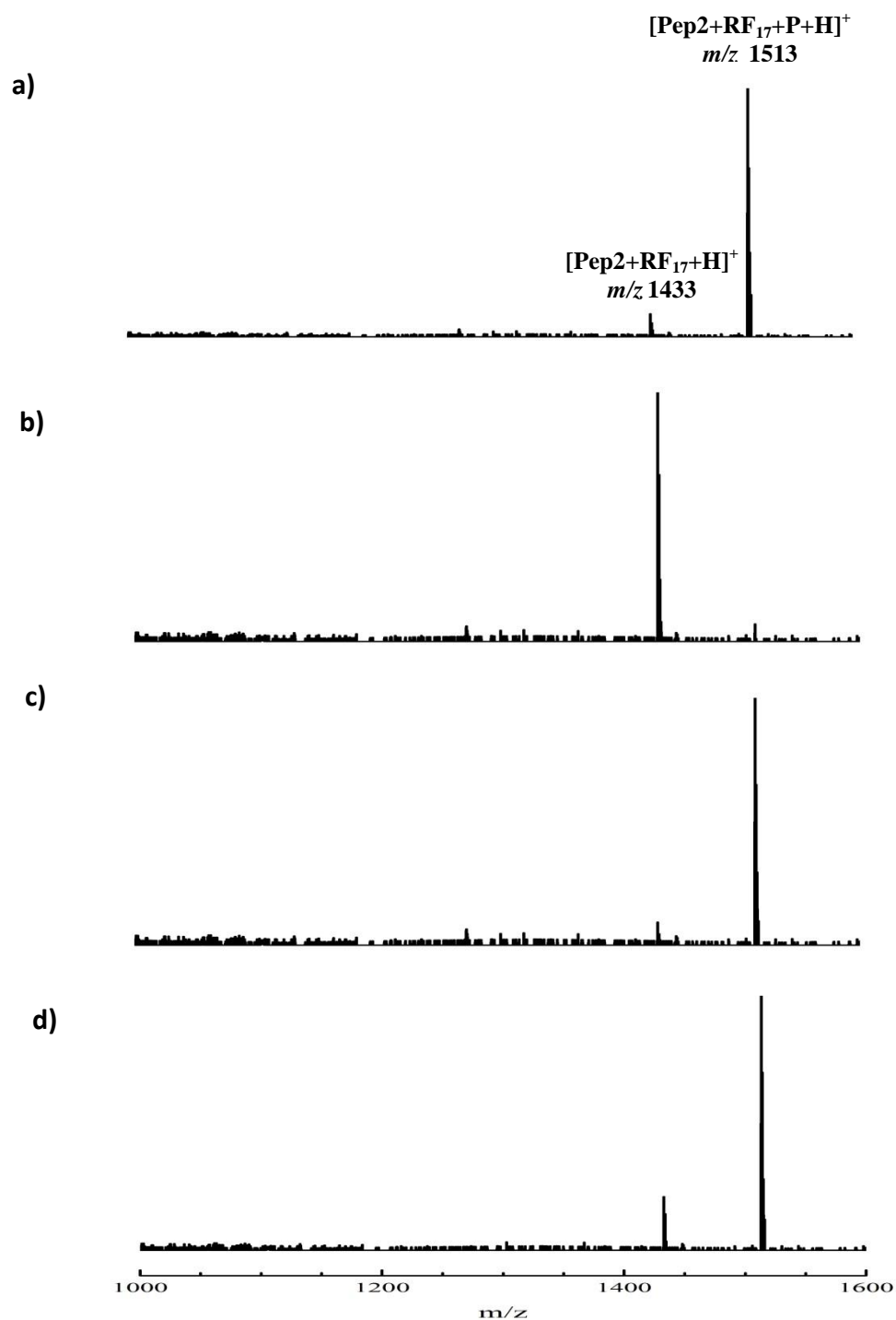


Fig. 5.17: The fluoros-affinity NIMS chip was used to perform enzymatic inhibitor screening in 4-dot format. a): NIMS spectrum of phosphorylation of substrate Pep2 for PKA without inhibitor and other compounds (Control); b): NIMS spectrum after adding a known inhibitor, staurosporine; c): NIMS spectrum after adding compound A, Calix[4]arene; d): NIMS spectrum after adding compound B, C-Methylcalix[4]resorcinarene.

## Chapter 6: Measurement of enantiomeric excess by kinetic resolution and NIMS

### 6.1: Overview

The term: enantiomeric excess (ee) was originally defined to describe enantiomeric composition of an optically active substance, as shown in Eq. (6.1) [160].

$$ee = |F_+ - F_-| \quad (6.1)$$

where  $F$  is the mole fraction of each enantiomer and  $F_+ + F_- = 1$ . In practice, it can be determined using the equation (6.2) [161] as a percent ee if the amount of each enantiomer produced was known.

$$ee = \frac{R-S}{R+S} \times 100 \quad (6.2)$$

where  $R$  and  $S$  are the respective fractions of enantiomers in a mixture such that  $R + S = 1$ .

Recently, ee values have been used to quantitate stereoselectivity; that is, the ee value is taken as a measure of how optically pure a substance is or alternatively, the degree of contamination by the “opposite-handed” enantiomer of a chiral compound [161]. An intriguing reason to measure the ee of organic molecules is to discover new enantioselective catalytic processes by testing a great number of catalyst candidates [162].

The simplest strategy to rapidly determine the ee of a chiral molecule is to use circular dichroism (CD) to directly measure the angle through which plane polarized light is rotated after passing through a sample. However, this approach has two problems that make it difficult to utilize in a practical manner. First, the sensitivity of this approach is relatively low and second, the results are susceptible to impurities, particularly if they are

chiral [28]. In general, the most widely used strategy for determining ee is to first physically separate enantiomers by HPLC or GC using a chiral stationary phase, followed by detection of the purified enantiomers using UV-visible spectroscopy [163, 164]. However, this method is often slow, expensive, tediously complex and may require labeling with a chromophore [27].

MS as a chiral detection technology was firstly developed by Fales and Wright in 1977 [165]. Since then, many other MS methods have been developed to rapidly measure ee values [27, 166, 167]. For example, Tao and Cooks used ESI-MS to determine low ee values from the difference in rates of dissociation of chiral ligands from gas-phase copper complexes generated in situ with the analyte of interest [166]. Siuzdak, Finn and others employed automated quantitative ESI-MS [167] and chip-based DIOS MS [27], respectively, to perform measurement of ee by kinetic resolution. This approach relies on the principles of double asymmetric induction to resolve enantiomers by selectively reacting one enantiomer of a racemic mixture with a chiral reagent, catalyst, or enzyme [161]. The advantages of MS detection are that many different types of molecules can be detected with high sensitivity without the need of a chromophore, it is tolerant of impurities (mass peaks other than those for the compounds of interest can be ignored), and potentially it is amenable to high-throughput applications [28].

In this work, a strategy was developed to measure the ee of analyte of interest based on kinetic resolution and NIMS. It involves fluororous-phase diastereoselective derivatization of the analyte, 1-phenylethanol (compound a) in Fig. 6.1), with chiral reagents having fluororous tags of different mass (compounds b) and c) in Fig.6.1). The compound is spotted on the surface of a NIMS chip covered with a thin film of initiator

(the perfluorinated siloxane, BisF<sub>17</sub>). As shown in Fig. 6.1 this approach provides kinetic resolution, followed by direct product NIMS detection. Compared to other methods based on MS, the strategy here requires less sample preparation, is more tolerant to buffers, impurities and other potential contaminants, and is highly sensitive.

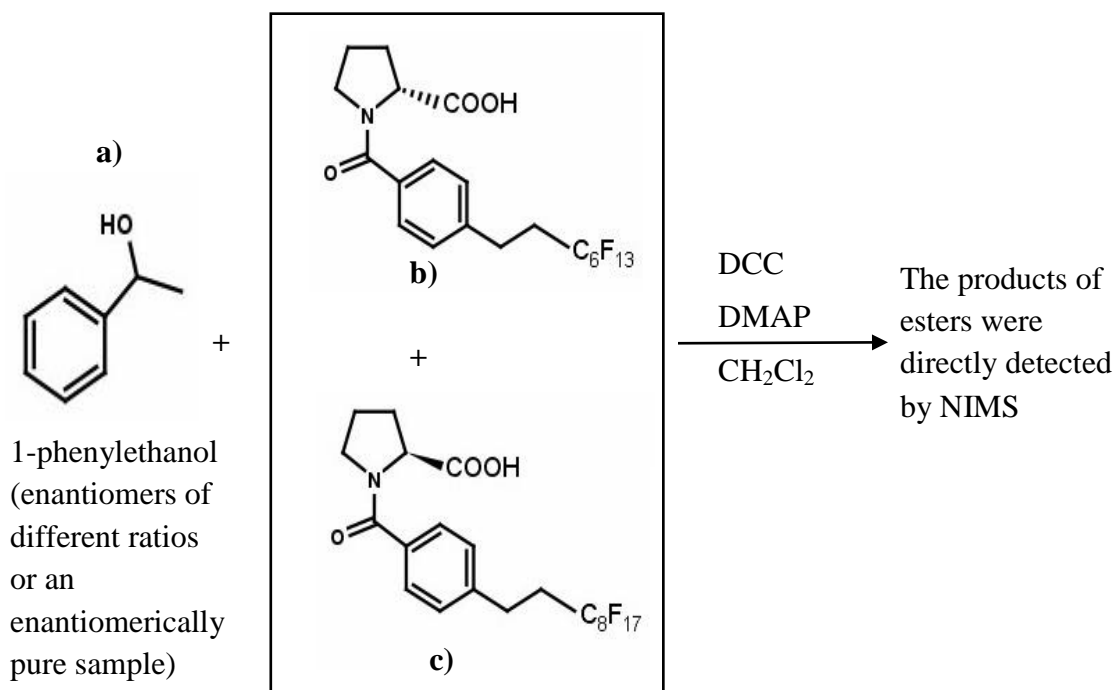


Fig. 6.1: A scheme showing the reaction of 1-phenylethanol (enantiomers of different ratios or an enantiomerically pure sample) with equivalent fluorinated-mass tagged chiral acids.

## 6.2: Determination of ee based on kinetic resolution and NIMS

Enantiomeric excess is defined as the absolute difference between the mole fractions of an enantiomer pair. In practice, it is most often expressed as a percent enantiomeric excess (% ee) [161]. The % ee of an analyte can be determined based on the ability of a chiral reagent or catalyst to selectively derivatize one enantiomer of the analyte in the presence of the other. As a general rule, an enantiomeric mixture of alcohols, R-OH (R configuration) and S-OH (S configuration) will react with chiral mass-tagged acids A-CO<sub>2</sub>H (R configuration) and B-CO<sub>2</sub>H (S configuration), as shown in the Fig.6.2.

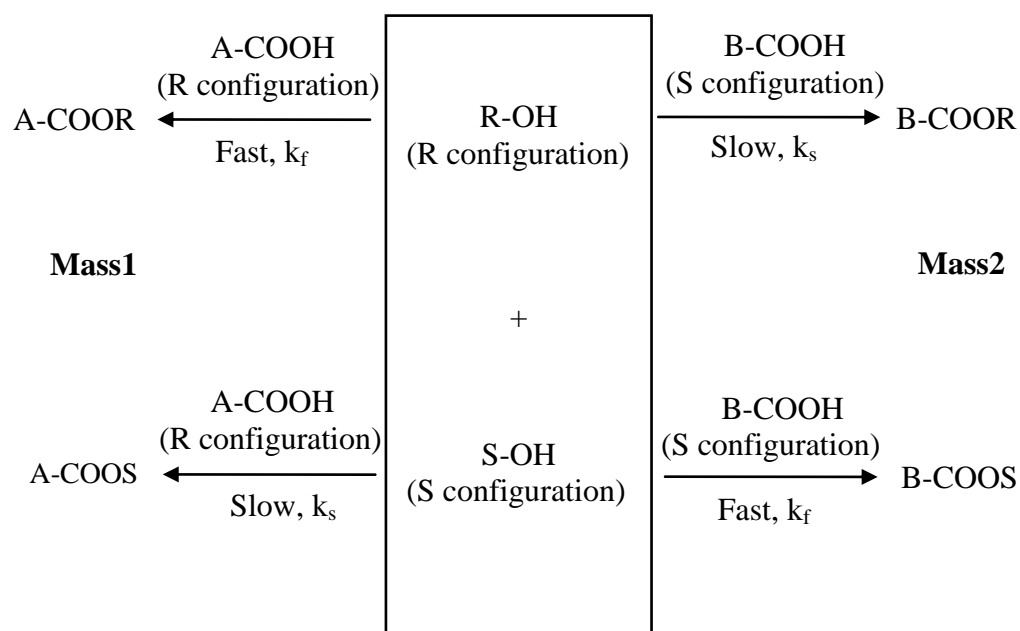


Fig. 6.2: A schematic diagram of the generalized reactions of chiral alcohols with mass-tagged chiral acids in a kinetic resolution process.

In general, the reactions of the enantiomers of any pair of chiral reagents will proceed with non-equal rate constants ( $k_f > k_s$ ; f: fast, s: slow). Specifically, a reaction will be fast for “matched” sets of reagents; for example, an R-alcohol reacting with an R-acylating agent. On the other hand, the reaction rate of an S-alcohol reacting with an R-acylating agent will be small ( $k_s$ ) [28]. If the kinetic resolution selectivity ( $p$ ) is known, where  $p$  is defined as the relative rates of the competing fast and slow processes, the relative amounts of the product esters produced using the scheme in Fig. 6.2, measured in this work by mass spectrometry, can be used to determine the enantiomeric composition of the analyte using Eq. 6.3.

$$\% ee = \left[ \frac{(y - 1)(p + 1)}{(y + 1)(p - 1)} \right] \times 100 \quad (6.3)$$

where  $p = \frac{k_f}{k_s}$ ,  $y = \frac{I_{\text{mass } 1}}{I_{\text{mass } 2}}$  (product signal intensity ratio).

### 6.3: Results and discussions

In this work an equimolar mixture of pseudoenantiomeric fluororous mass-tagged chiral acylating agents (b), R configuration and c), S configuration) were used that differ in a substituent remote to the chiral center, bearing  $C_6F_{13}$  and  $C_8F_{17}$ , respectively, such that the mass of the molecule is correlated to its absolute configuration (R configuration acylating agent is 565 Da and S is 665 Da). As shown in the Fig. 6.1, first, 1-phenyl-ethanol was reacted with a 20-fold excess of an equimolar mixture of acids b) and c) in the presence of 1,3-dicyclohexylcarbodiimide (DCC) and the catalyst 4-Dimethylaminopyridine (DMAP) on the surface of a fluororous phase NIMS chip according to the experimental methodology described in Chapter 2.3.5. The products were detected

directly by NIMS using a nitrogen laser (337 nm) putting out 4 ns 5  $\mu$ J pulses at a repetition rate of 10 Hz.

The kinetic resolution selectivity factor ( $p$ ) was obtained by the known %  $ee$  of 1-phenylethanol and the relative amounts of the acylated products using Eq. 6.4 which was derived from Eq. 6.3.

$$p = \frac{\% ee(y + 1) + 100(y - 1)}{\% ee(y + 1) - 100(y - 1)} \quad (6.4)$$

For the enantiomerically pure compound (100%  $ee$ ), a value of  $p =$

$$\frac{100(y+1)+100(y-1)}{100(y+1)-100(y-1)} = y = 2.4 \pm 0.3$$

was established by averaging the ratio of signal intensity for ester sodium adducts from three NIMS spectra because the peak signal intensity of the protonated products is less than that of sodium adducts. Fig. 6.3 showed a representative NIMS spectrum of a crude acylation reaction mixture obtained using a pure R configuration alcohol (Fig. 6.4).

With the  $p$  value obtained from an optically pure sample, 1-phenylethanol was then prepared in 80%, 60%, 40% and 20% enantiomeric excess ((R-S)/(R+S)), performed chemical reaction according to the scheme shown in the Fig. 6.1, and the %  $ee$  determined by measuring the relative amounts of the esters from mass-tagged acids b) and c) using NIMS (BisF<sub>17</sub> as the initiator). The results shown in Table 6.1 were obtained by averaging three NIMS spectra for each sample and the observed values are well within the  $\pm 10\%$  error range characteristic of MS enantiomeric excess determination (MSEED) method devised here [28].



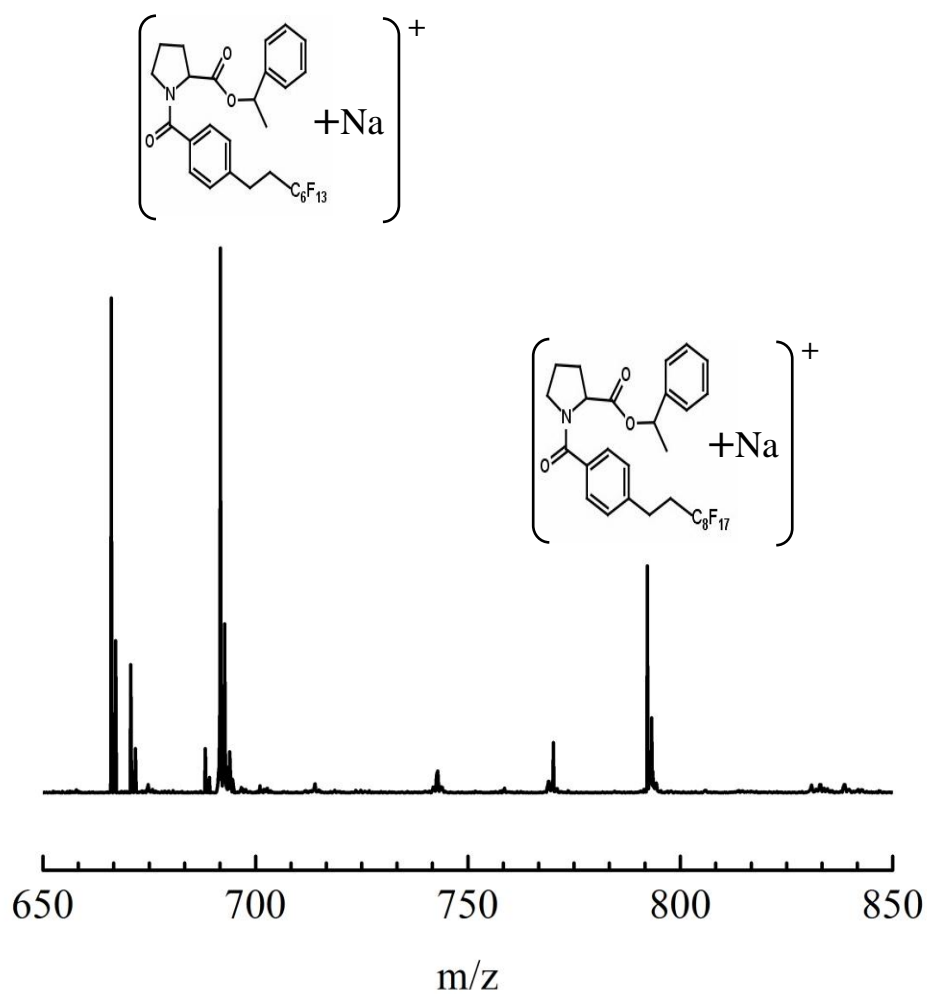


Fig. 6.3: A typical 337 nm NIMS spectrum of the products from the reaction of pure R-1-phenylethanol with equimolar mixture of pseudoenantiomeric fluorinated mass-tagged chiral acylating agents (b and c)). The initiator used was BisF<sub>17</sub>.

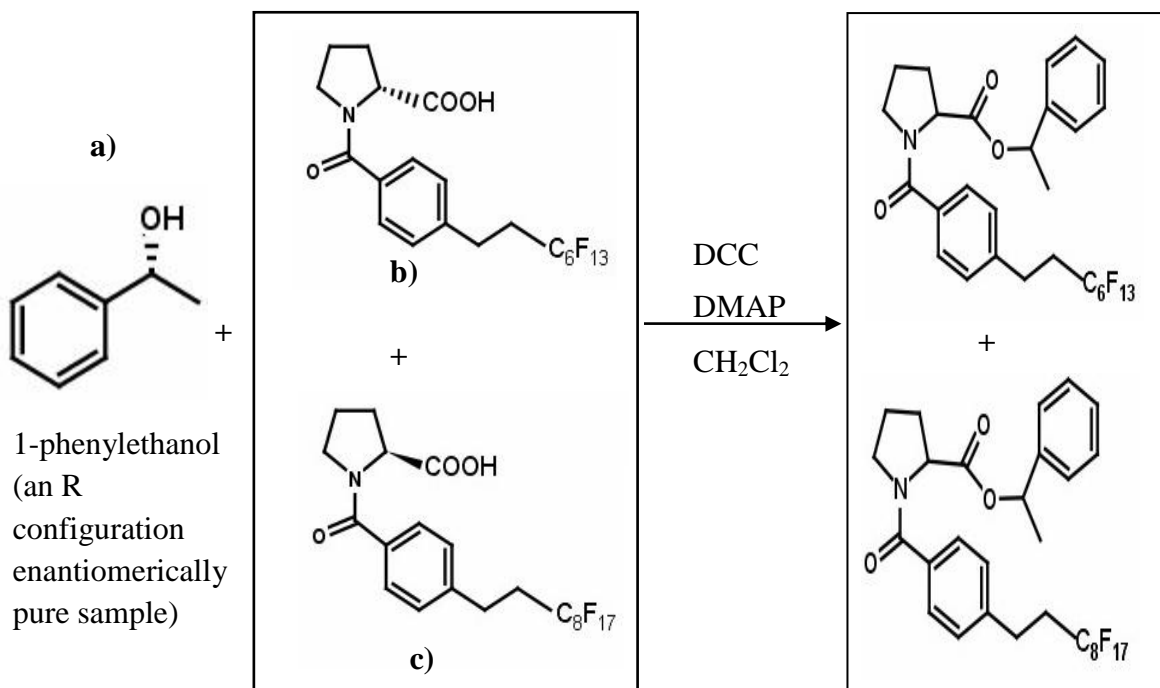


Fig. 6.4: A scheme of 1-phenylethanol (an R configuration enantiomerically pure sample) reacting with equivalent fluororous-mass tagged chiral acids.

**Table 6.1: NIMS analysis of 1-phenylethanol enantiomeric excess using fluororous mass tags b and c**

Actual % ee	80	60	40	20
Measured % ee	86 ± 7	63 ± 5	38 ± 3	22 ± 2

## Chapter 7: An exploration of visible-NIMS and NIMS using WO<sub>3</sub> and TiO<sub>2</sub> substrates

### 7.1: Visible laser NIMS

#### 7.1.1: Overview of visible MALDI and SALDI

The vast majority of MALDI mass spectra and almost all SALDI mass spectra have been acquired using either UV [84, 168] or IR [169] lasers as irradiation sources for desorption and ionization. Relatively few studies have been carried out using visible lasers (400 nm - 750 nm) due to scarcity of known suitable organic matrix molecules that can absorb visible light. Yet despite this MALDI MS using visible wavelength lasers is expected to exhibit several advantages over UV-MALDI and IR-MALDI. For example, many macromolecules of interest have UV light absorbing chromophores but are transparent at visible wavelengths making them more stable against fragmentation under visible irradiation [170, 171]. Furthermore, coherent radiation in the green portion of the visible spectrum at 532 nm can be readily generated by frequency-doubling the IR output of a Nd: YAG laser. Nd: YAG lasers are relatively inexpensive solid state devices that have intense outputs and can be operated for long periods of time compared to the laser most commonly used for UV-MALDI; namely, the N<sub>2</sub> gas laser (337 nm) [172]. There have been a few reports published where compounds such as Rhodamine dyes (RB, R6G) [171, 173], neutral red [174] and 2-amino-3-nitrophenol [175] have been used as matrixes for 532 nm-MALDI MS.

The Lipson group has explored the suitability of number of organic laser dyes as visible-MALDI matrices including Coumarin 480 which absorbs near 480 nm [176], and Rhodamine dyes (R575, R610) which under specific conditions proved to be viable media

for small molecular weight analyte detection by 532 nm irradiation [177, 178]. Despite these successes none of compounds appear to be as effective as the standard UV MALDI matrices CHCA and DHB. Recently, Au-assisted visible-MALDI [179] and visible-SALDI using gold nanorods [180] as well as graphite substrates [181] have emerged as more promising approaches for the development of visible laser MS.

NIMS based on pSi can be initiated using a nitrogen laser or various ion sources ( $\text{Au}^+$ ,  $\text{Ga}^+$ ,  $\text{Bi}^+$  and  $\text{Bi}_3^+$ ) [30]. One might expect that a visible wavelength laser could also be used as a NIMS irradiation source because pSi absorbs strongly throughout the UV-visible spectrum [182]. In this work, we demonstrate that ions can be generated by NIMS on pSi using the 532 nm output of a frequency-doubled Nd-YAG laser. The hexapeptide Dalargin was used as a test analyte to assess the viability of visible-NIMS.

### 7.1.2: Results and Discussion

NIMS substrates were made by etching a silicon wafer electrochemically in HF/ethanol solution. Coherent radiation at 532 nm was generated by frequency doubling the output of a Q-switched Nd: YAG laser (Quanta-Ray GCR-4;  $\lambda = 1064$  nm; 10 Hz repetition rate) in a KDP nonlinear crystal, as described in Chapter 2. The 532 nm laser beam was introduced into a 100  $\mu\text{m}$  diameter optical fiber using a 5 cm focal length lens and directed towards the sample plate of the mass spectrometer. Fig. 7.1 shows that the visible laser NIMS mass spectrum of Dalargin (2 pmol) using  $\text{BisF}_{17}$  as the initiator molecule exhibits strong analyte signals with low background noise. The peaks at  $m/z$  726 and 748 correspond to protonated Dalargin ( $[\text{Dalargin} + \text{H}]^+$ ) and the sodium ion adduct of the Dalargin ( $[\text{Dalargin} + \text{Na}]^+$ ), respectively.

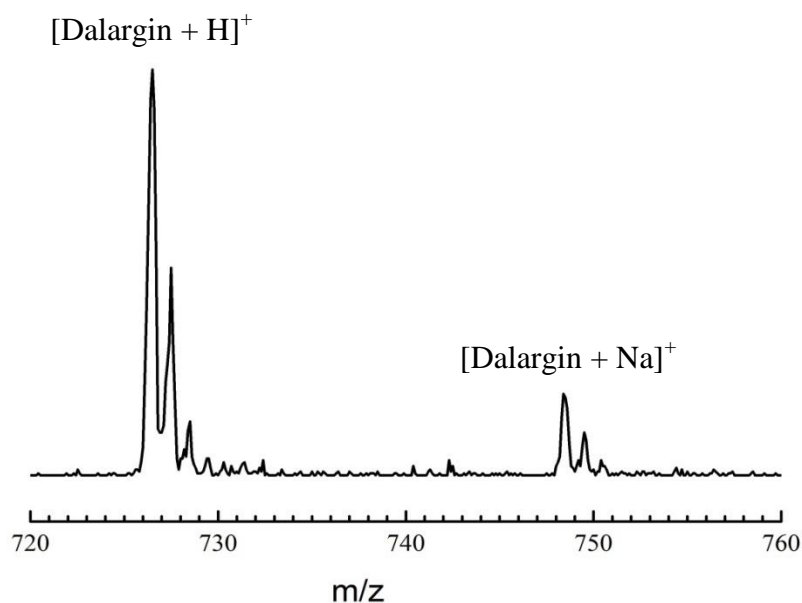


Fig. 7.1: Visible NIMS spectrum of Dalargin (2 pmol) using BisF<sub>17</sub> as initiator and the 532 nm output of a Nd-YAG laser operating at a 10 Hz repetition rate.

The  $[\text{Dalargin} + \text{H}]^+$  NIMS peak maximum at  $m/z$  726 was used to determine the LOD. The noise in a S/N evaluation was determined by measuring the average value of the pure noise level between  $m/z$  723 and 725 over  $\sim 1000$  laser shots, each pulse having 20  $\mu\text{J}$  of energy. The average S/N values obtained reflect both the instrumental and chemical noise due to the residual contamination on the NIMS surface. The amount of Dalargin irradiated by the laser beam was calculated based on the ratio of the laser spot area to the whole sample surface area of the NIMS chip. The laser was repositioned 5 times to different locations on the NIMS chip, and each run at a specific location was repeated 5 times and the ion intensities averaged. A S/N ratio = 3 was considered the minimum value that would allow the peak signal to be clearly differentiated from the

noise, thereby giving an indication of the lowest concentration that could be measured reliably.

A standard curve made by plotting the S/N of the visible laser NIMS intensity measurement for Dalargin against number of moles of Dalargin in the spot as shown in Fig. 7.2. A linear regression of the data yielded a  $R^2$  value of 0.9963 and a LOD of  $(3.1 \pm 0.7) \times 10^{-14}$  mol. This result shows that visible-NIMS is  $\sim 50 \times$  less sensitive than UV-NIMS ( $(6.4 \pm 0.3) \times 10^{-16}$  mol; Chapter 3), and requires higher pulse energies. However, this constitutes a 15 x improvement in the LOD for Dalargin by visible-MALDI MS ( $(2 \pm 1) \times 10^{-13}$  mol) using the best visible binary matrix (R575 + HCl) and the same mass spectrometer [177].

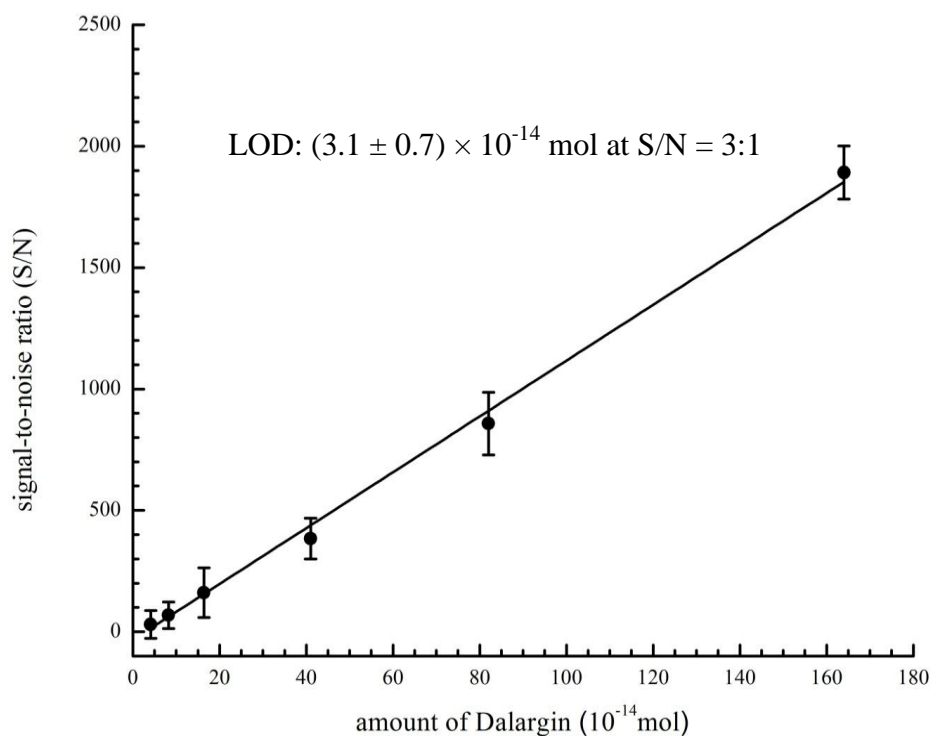


Fig. 7.2: A plot of the S/N ratio of the protonated Dalargin visible-NIMS signal versus the number of moles of Dalargin in the sample.

Since the home-made MALDI source employed in this work is typically about one order of magnitude less sensitive than a commercial MALDI-TOF instrument under similar fluencies (but different energies and spot sizes) [177], it is believed that the analyte detection limit can be improved using a modern MALDI-TOF mass spectrometer with a better ion transmission efficiency and a laser operating at 532 nm.

## **7.2: New NIMS substrates: microstructured WO<sub>3</sub> and porous TiO<sub>2</sub>**

As described in Chapter 1, NIMS is very similar to DIOS except that it uses a liquid initiator such as fluorinated or perfluorinated siloxane propellant to facilitate desorption of intact analyte. NIMS takes advantage of both the basic principles of DIOS but because a liquid initiator is involved it also has some features which are similar to MALDI. Some of the benefits of NIMS include a much better sensitivity than DIOS: only 700 yocto-mol ( $10^{-24}$  mol) for calcium antagonist erapamil (~ 420 molecules), and a relatively simple sample preparation. NIMS works well under both laser and ion beam ( $\text{Au}^+$ ,  $\text{Ga}^+$ ,  $\text{Bi}^+$  and  $\text{Bi}_3^+$ ) irradiation [30].

DIOS (the forerunner of NIMS) was introduced in 1999 and was the first SALDI method that used a specific substrate such as pSi to assist in the desorption and ionization of the sample molecules [9]. Since then, a variety of nanomaterials have been explored as possible substrates for SALDI MS. They include carbon nanotubes [183], microstructured tungsten oxide [75], porous alumina [184], silver nanoparticles [185], platinum nanoflowers [186], gold nanomaterials [187, 188], nanotitania [189], and so on. To the best of our knowledge, only pSi to date has been utilized as a substrate for NIMS.

This thesis focuses on two particularly promising candidates: microstructured WO<sub>3</sub> and porous TiO<sub>2</sub> as possible NIMS substrates. The WO<sub>3</sub> chip, which was developed

in the Lipson group, is an excellent substrate for SALDI MS because it has been shown to be effective in detecting low-molecular weight compounds in both positive- and negative-ion modes, as well as radical cations of compounds which are difficult to protonate and/or deprotonate [75]. In the latter case,  $\text{WO}_3$  chip should be useful for charactering non-polar or conducting polymers and functional dendrimers.  $\text{TiO}_2$  semiconducting nanoparticles are widely used in the field of photocatalysis and as a component of dye-sensitized solar cells [190]. Like pSi,  $\text{WO}_3$  and  $\text{TiO}_2$  have many properties such as high melting points, low heat capacities ( $C_p$ ) and relatively low thermal conductivities ( $k$ ), which make them excellent substrates for SALDI MS. In this study,  $\text{WO}_3$  and  $\text{TiO}_2$  were tested as potential NIMS substrates using  $\text{BisF}_{17}$  as the initiator. The hexapeptide Dalargin was used as the test analyte.

### 7.2.1: $\text{WO}_3$ chip as a NIMS substrate

The experimental details for making microstructured  $\text{WO}_3$  are presented in Chapter 2. Briefly, a  $\text{WO}_3$  chip for NIMS analysis was produced by irradiating tungsten foil for 40 minutes in methanol with the 355 nm output of a frequency-tripled Nd-YAG laser (intensity  $\sim 4\text{-}5 \text{ W/cm}^2$ ). The resultant chip was then heat activated by placing it in an oven for 4 hours at  $275^\circ\text{C}$ . As shown in Fig. 7.3, The SEM image of a typical  $\text{WO}_3$  substrate exhibits a mixture of pores, crevices and protrusions with dimensions ranging from nanometers to micrometers in size.

The NIMS process was initiated by a 337 nm  $\text{N}_2$  laser operating at a 10 Hz repetition rate. Each pulse had an energy of 10  $\mu\text{J}$ . Fig. 7.4 shows the NIMS mass spectrum of Dalargin (0.5 pmol). The peaks at  $m/z$  726 and 748 correspond to  $[\text{Dalargin} + \text{H}]^+$  and  $[\text{Dalargin} + \text{Na}]^+$ , respectively.



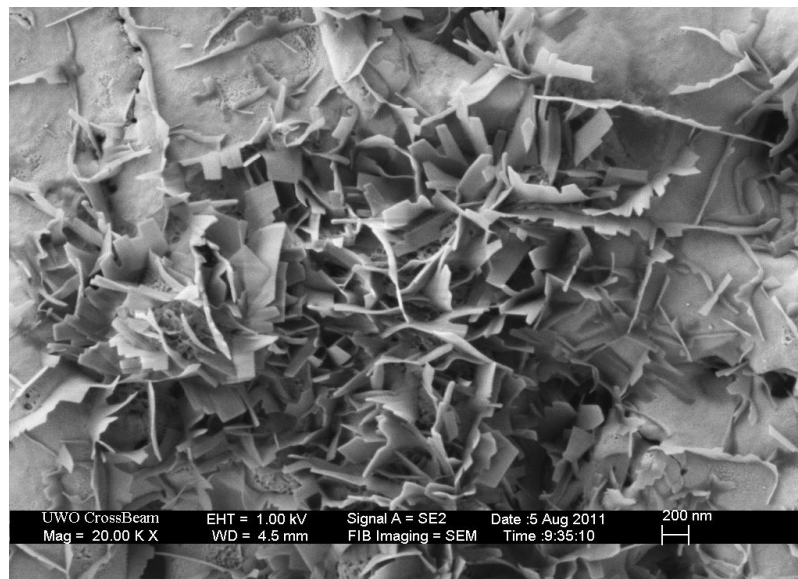


Fig. 7.3: SEM image of a microstructured  $\text{WO}_3$  substrate for NIMS produced by irradiating W foil for 40 minutes in methanol with the 355 nm output of a frequency-tripled Nd-YAG laser at an intensity of  $\sim 4\text{-}5 \text{ W/cm}^2$ , followed by heat activation.

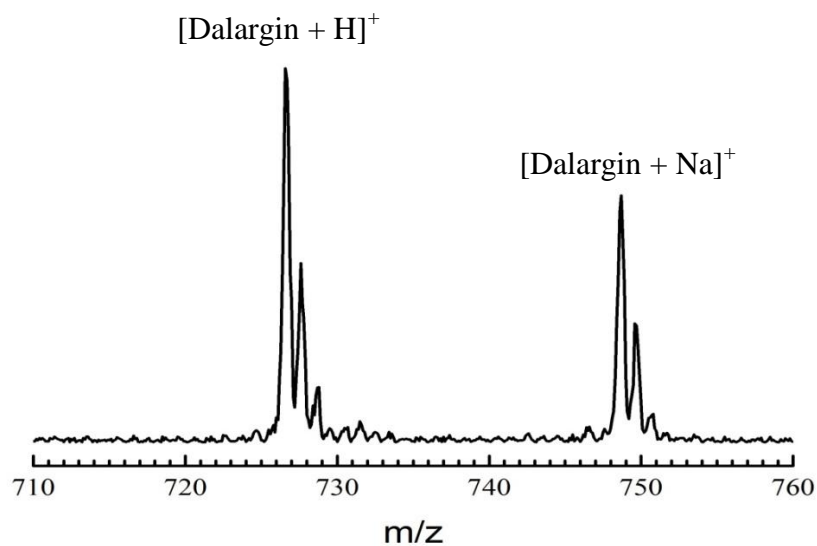


Fig. 7.4: NIMS spectrum of Dalargin (0.5 pmol) from a microstructured  $\text{WO}_3$  substrate using  $\text{BisF}_{17}$  as an initiator. The NIMS process was initiated using 337 nm output of a  $\text{N}_2$  laser operating at a 10 Hz repetition rate and having an energy of  $10 \mu\text{J/pulse}$ .

### 7.2.2: TiO<sub>2</sub> chip used for NIMS substrate

Fig. 7.5 shows SEM images of the resulting TiO<sub>2</sub> substrate produced by an electrochemical etching process in 1 M H<sub>3</sub>PO<sub>4</sub> containing 0.5 wt% HF acid in which a potential was ramped from 0 V to 10 V at a sweep rate of 500 mV/s followed by holding the potential at 10 V for 500 seconds (Chapter 2). Under these conditions the TiO<sub>2</sub> chip surface consists of pores with diameters of approximately a few tens of nanometer.

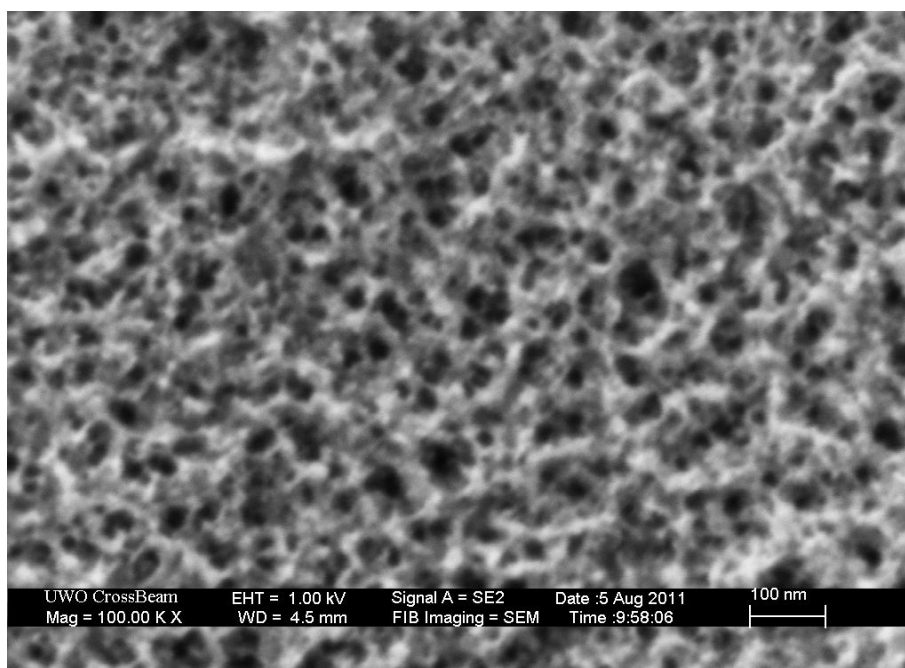


Fig. 7.5: SEM image of porous TiO<sub>2</sub> substrate for NIMS produced by electrochemical etching in 1 M H<sub>3</sub>PO<sub>4</sub> containing 0.5 wt% HF acid. Here the potential was ramped from 0 V to 10 V at a sweep rate of 500 mV/s followed by holding the potential at 10 V for 500 seconds.

Fig. 7.6 shows the NIMS spectrum of Dalargin (1 pmol) obtained from porous TiO<sub>2</sub> substrate using BisF<sub>17</sub> as the initiator and 15  $\mu$ J pulses of a 337 nm N<sub>2</sub> laser at a repetition rate of 10 Hz. While the resultant mass spectrum using TiO<sub>2</sub> is similar to that obtained using WO<sub>3</sub>, higher laser energies are needed to obtain the same degree of

analyte sensitivity as that obtained with a  $\text{WO}_3$  substrate.

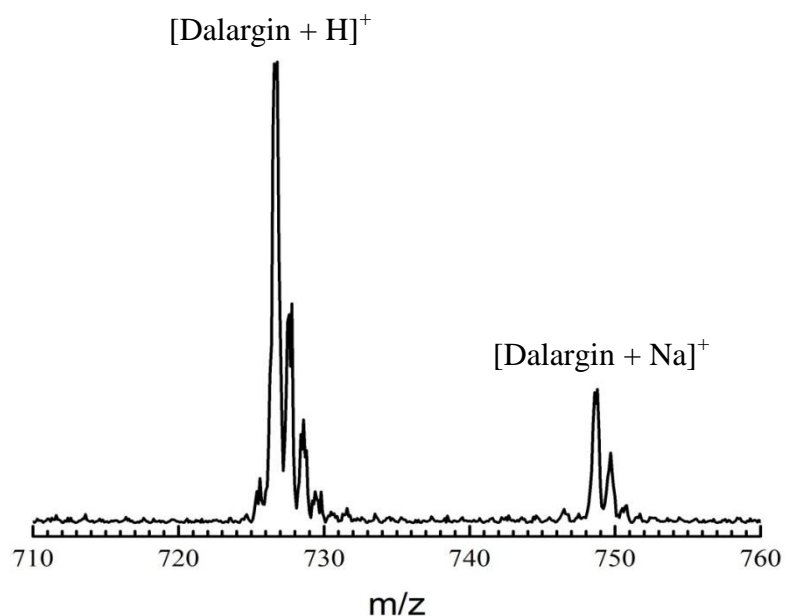


Fig. 7.6: NIMS spectrum of Dalargin (1 pmol) from a porous  $\text{TiO}_2$  substrate using  $\text{BisF}_{17}$  as an initiator. The NIMS process was initiated using the 337 nm output of a  $\text{N}_2$  laser operating at a 10 Hz repetition rate and having an energy of 15  $\mu\text{J}/\text{pulse}$ .

Overall, both  $\text{WO}_3$  and  $\text{TiO}_2$  appear to be less effective than pSi as NIMS substrates. However, the NIMS performance could be further improved by refining the fabrication of the  $\text{WO}_3$  and  $\text{TiO}_2$  chips. Metal-based materials can also possibly overcome the fragility found for pSi.

## **Chapter 8: Mechanisms of laser desorption/ionization by MALDI and NIMS**

### **8.1: MALDI**

MALDI is an extremely complicated “event” involving optical, mechanical, thermodynamic and physicochemical processes related to phase transitions and ionization phenomena [3]. There is an on-going debate about the MALDI desorption/ionization mechanism at the molecular level. Its resolution has been complicated by the large number of critical parameters involved including the incident laser wavelength and pulse duration, laser fluence, the structure of the solid solution made by co-crystallizing an analyte and matrix, the sample preparation protocol, and so on.

Despite the complexity of the problem, a “two-step” model which first involves the formation of primary ions followed by secondary ion generation within the desorption plume expansion is now widely accepted [191]. As shown in the Fig. 8.1[191], the “two-step” model differentiates the time scales of the decay of the optically excited primary ions (on the order of nanoseconds) [192] and the expansion of the MALDI plume (on the order of microseconds) [8]. Three aspects of the MALDI mechanism will be discussed here in more details: the primary laser desorption and ionization steps, secondary ion formation, and some of the key parameters influencing the MALDI process.

#### **8.1.1: Desorption in MALDI**

The first step in the MALDI mechanism involves the laser excitation of the matrix molecules in the solid solution containing the analyte of interest [3]. A large portion of the incident laser energy is rapidly converted to heat resulting in an explosive

formation of a gaseous material plume. In general, a high-quality MALDI mass spectrum is linearly correlated with the degree of matrix optical absorption [193]. The population of the first excited singlet state (generally  $S_1$ ) obtained by resonant optical absorption is considered the primary excitation step [194]. Apart from some energy loss caused by fluorescence, intersystem crossing and photochemical reactions, most of the laser energy that is stored in the excited states of the matrix is subsequently converted by nonradiative relaxation into intramolecular lattice vibrations (i.e. heat) on a time scale of nanoseconds or faster [192, 195].

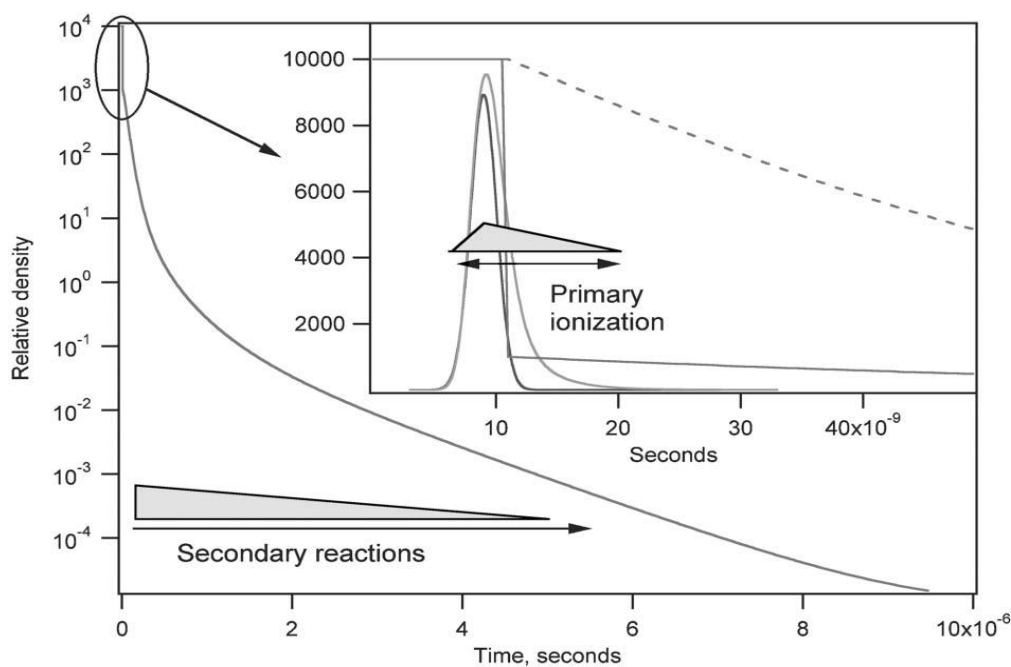


Fig. 8.1: Density changes with time during plume expansion in a MALDI process. The inset shows the initial behaviour in which the lower and upper curves represent a typical laser pulse and an average lifetime of matrix excited state, respectively; the dashed line is for a phase explosion while the solid line is for desorption [191].

A number of models have been proposed to explain the phase transition that occurs during the MALDI desorption step. For example, it has been suggested that

thermal desorption takes place by sublimating or evaporating individual molecules layer-by-layer from the surface inward [196-198]. In another, molecules and clusters of molecules are ejected by volume ablation [199]. For IR-MALDI the ejection of bulk material could result from a laser-induced photoacoustic stress pulse generated within the matrix made possible by the relatively larger laser penetration depths at those wavelengths [3].

Generally, sublimation/evaporation-like processes occur at low laser fluences below or close to the ion detection threshold. Although a small number of clusters may be generated at low laser fluences, individual molecules are the predominant species ejected in the plume [3, 194]. Assuming that yield of ejected molecules is proportional to the desorption rate which in turn is dictated by the temperature increase generated by the incident laser, the overall yield can be expressed as [200]:

$$Y \sim P(A) \exp\left(\frac{-E_a}{k_B(T_0 + \eta F)}\right) \quad (8.1)$$

where  $Y$  is the yield (amount) of the ejected molecules,  $P(A)$  is a pre-exponential factor which is an entropy-related term with a weak temperature dependence,  $E_a$  is the activation energy of the desorption process;  $k_B$  is the Boltzmann constant;  $T_0$  is the initial sample temperature;  $\eta$  is a conversion factor that is designated to the transformation of laser pulse energy into (lattice) temperature of the sample, and  $F$  is the laser fluence.

At higher laser fluences, molecule desorption is governed by volume photoablation. This corresponds to an explosive phase change where the desorption rate is less than the rate of laser energy deposition into the matrix, resulting in an overheated sample [201]. In this case, the overall material yield,  $Y$ , which includes molecular clusters, is better fitted by an equation of the form: [199]

$$Y \sim \delta \ln \left[ \frac{F}{\delta(E_v^* - cT_0)} \right]^n \quad (8.2)$$

where  $\delta$  is the penetration depth of the laser irradiation,  $E_v^*$  is a critical energy density,  $c$  is the specific heat of the material;  $n$  is an integer = 1 for a flat-top beam profile and 2 for a Gaussian beam profile. Note that Eq. 8.2 is only valid for fluences  $F > \delta(E_v^* - cT_0)$  [3].

The actual desorption process depends substantially on the properties of the laser (wavelength, fluence, pulse duration, etc.) and the matrix material used in a MALDI experiment, making a detailed understanding challenging [199]. The initial plume densities are also very large which means that the ejected material undergoes a large number of intermolecular collisions upon desorption. These collisions are expected to have a significant effect on the expansion characteristics and inevitably lead to considerable dynamical changes during the material expansion [194].

## 8.1.2: Ionization in MALDI

### 8.1.2.1: Primary ion formation

The mechanism of primary ion formation which occurs during or shortly after the laser pulse has irradiated the solid solution remains controversial. Two competing models have emerged as front runners to explain this phenomenon: energy pooling [191] and cluster ionization [202].

**The energy pooling model:** Energy pooling is a phenomenon which occurs in the gas phase between neighbouring excited molecules [203, 204]. Upon photoexcitation to their first excited singlet state ( $S_1$ ) neighbouring molecules either collisionally and/or electronically undergo singlet-singlet ( $S_1$ - $S_1$ ) annihilation promoting one of the partners into their second excited state ( $S_2$ ) while relaxing the other to ground state ( $S_0$ ) [192].

This process can carry on between  $S_1$  and  $S_{n \geq 2}$  partners until finally ionization takes place.

Pooling would be of the limited importance for MALDI if only excited analyte pairs were involved. However, energy pooling is possible by interactions between analyte and matrix molecules [205]. The excitation within matrix clusters can "hop" between cluster components relatively easily (excitonic behaviour). This and energy pooling can substantially increase the ionization efficiency because there is less dependence on where the excitation in the cluster "sits". The intermolecular pooling and hopping processes involving neighbouring matrix molecules are sketched in Fig.8.2 [191]. Evidence for  $S_1$ - $S_1$  pooling has been deduced by fluorescence quenching studies, while energy pooling of a  $S_1$  molecule with a higher excited state,  $S_n$  was demonstrated by a 2-pulse time-delayed (between 2-3 nano-second) MALDI experiment [195].

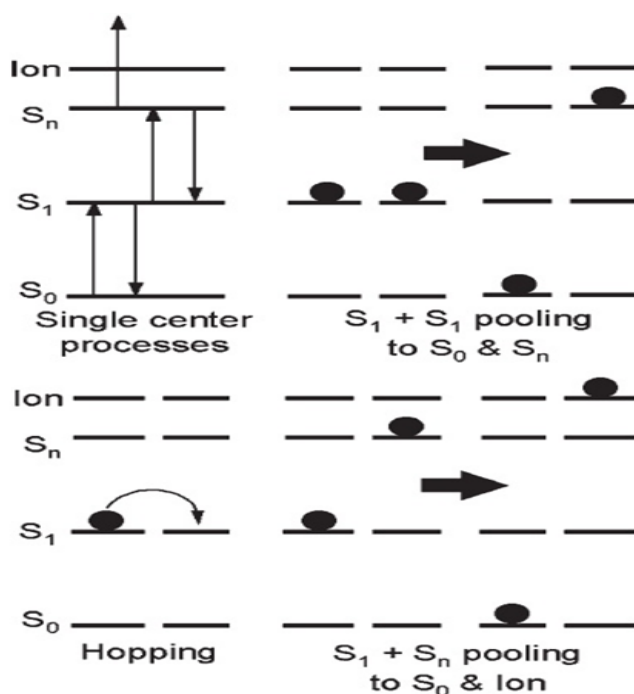


Fig. 8.2: Schematic of the pooling and hopping processes involving neighbouring matrix molecules.  $S_0$  is the electronic ground state,  $S_1$  the first singlet excited state, and  $S_n$  an excited state above  $S_1$  [191].



**The cluster ionization mechanism:** Typical MALDI analytes such as peptides, proteins, nucleotides and so on are believed to be pre-charged in the solid matrix solution. Thus, the primary ions can be formed by separating preformed analyte ions from their counter ions or by neutralizing their counter ions [202]. In general, there are two main pathways which can generate charged species. The most straightforward ionization route is by charge separation in clusters having a deficit/excess of ions [206]. The other is cluster photoionization, in which charge separations are achieved by performing photoionization and losing the resultant electrons from the materials [207, 208].

The energy required to overcome ion-pair interactions is expected to be supplied by the energy released from cluster dissociation. This energy requirement may be reduced by residual solvent, that is, partial solvation via a dielectric screening effect, and by any hydrogen-bonding with matrix molecules [202]. Once charged clusters are produced, the final ions formed result from desolvation of matrix and/or residual solvent. The efficiency of ionization by charge separation is dependent on the acid-base properties of the analyte, matrix and additives, their solvation properties, and how they are incorporated into the solid matrix solution [209].

In addition to these two models, other mechanisms have been proposed for primary ion formation, including multiphoton ionization, Excited State Proton Transfer (ESPT), and a polar fluid scenario. Direct multiphoton ionization of matrix or matrix-analyte complexes comes about by the coherent nonlinear optical absorption of two or more photons. While feasible, the incident fluence must be high; usually higher than the typical fluence values used in MALDI experiments [194].

ESPT is an attractive ionization mechanism in that it is a one-photon event at UV

excitation wavelengths which can occur in the  $S_1$  excited state. However, an ESPT pathway is not generally expected to dominate in MALDI mass spectrometry because molecules capable of proton transfers require an environment that efficiently stabilizes charge separation [204]. For example, known ESPT systems are often only active in water or amine environments. Direct evidence of ESPT involving matrix molecules such as DHB has not been found in either solution or in gas-phase clusters of DHB and analytes [210].

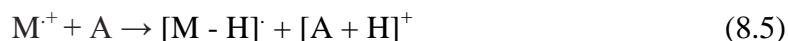
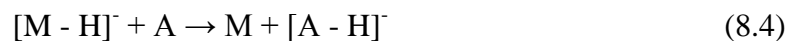
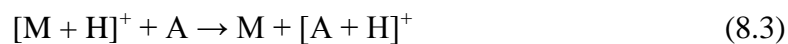
In the polar fluid model, the vaporized matrix behaves like a warm dense polar fluid solvent that allow free ions to be stabilized. Since the interactions between the polar fluid and analyte are energetic enough to ionize organic acids, it promotes the separation of previously associated ions, resulting in free, mobile solvated protons and alkali ions [211]. While the polar fluid picture continues to be incorporated as a part of molecular dynamics (MD) simulations of the MALDI picture, it is not considered to be the fundamental basis for ion separation [191].

#### **8.1.2.2: Secondary ion formation**

Understanding the secondary reactions that take place in the MALDI plume is important because these reactions have a major, even definitive impact on the observed mass spectrum. Secondary reactions lead to essentially the same observed mass spectra regardless of the mechanism involved in primary ion formation [191]. The matrix is the dominant neutral partner in secondary ion formation reactions because it is nearly always present in substantial excess; the ion-to-neutral ratio in MALDI is typically  $10^{-4}$ - $10^{-7}$  [212, 213]. The following are some of the possible ion-molecule reactions leading to secondary ion formation:

**Proton transfer:** Proton transfers between either a protonated, deprotonated or radical matrix molecule and a neutral analyte molecule are probably the most important secondary reactions in MALDI since energetically they tend to be highly exothermic.

The reactions can be written as:



where M is a matrix molecule or cluster; M<sup>•</sup>: is a radical matrix, A is an analyte and H is a proton.

Neutral analytes such as peptides and proteins tend to have somewhat higher proton affinities (PAs typically  $\geq 900$  kJ/mol [214, 215]) than typical matrix molecules (between 850 and 900kJ/mol) [216-218]. In negative ion detection mode, the difference in the gas-phase basicities (GPBs) of the deprotonated analytes and the matrix anions determines whether proton detachment from a neutral analyte molecule is energetically feasible [194].

**Cation Transfer:** Adducts of an analyte with various cations can be unwelcome in a MALDI mass spectrum if the signals for the protonated species are already intense. However, it can be very useful for some analyte molecules such as oligosaccharides and synthetic polymers which have low PAs relative to that of the matrix. In these cases, such analytes can be preferentially detected as cationized species. The species are generally detected as  $[A + Na]^+$  or  $[A + K]^+$  because these alkali cations are ubiquitous in most experimental apparatus [219].

**Electron transfer:** Electron transfer from either the analyte to matrix cations or

from neutral matrix molecules to analyte ions is the simplest type of matrix-analyte secondary ion-molecule reaction [220-222]. The former is represented by:



The reaction is efficient only when ionization potential (IP) of the matrix is greater than that of the analyte; otherwise the analyte is not ionized [8].

**Electron Capture:** Electron capture reactions are thought to play an important role in producing the singly charged ions that are prevalent in MALDI mass spectra [206]. Photoelectric emission from any metal surface in the MALDI instrument exposed to the incident laser beam can produce substantial quantities of free electrons, especially since the presence of matrix or contaminants in small amounts on the metal can reduce the work function of the metal [223]. Electron capture mass spectra of a series of typical MALDI matrixes have been investigated [36]. The results suggest that the process of free low-energy electron capture by matrix molecules is one origin of negative ions.

Secondary ion-molecule reactions not only explain which ions are observed in the final mass spectrum, they also help to understand another feature of MALDI; namely, the matrix suppression effect (MSE) [8]. MSE is a rather general phenomena in MALDI, in which matrix ions can be completely suppressed at certain analyte concentrations [224]. However, the phenomenon was not fully understood until it was placed in the context of the two-step picture and interpreted as a consequence of secondary reactions [191]. When the reactions of primary matrix ions with analytes are thermodynamically favourable as secondary reaction processes, they can proceed to completion. The degree of matrix suppression depends on the matrix/analyte (M/A) concentration ratio [7]. In MALDI MS of caffeine using CHCA as matrix, for example, the matrix suppression is nearly

completed in mass spectrum when the M/A ratio is  $\sim 3$  (large amount of analyte), while more matrix signals appear in the spectrum when the amount of analyte is less (M/A = 27) [8].

### **8.1.3: Some key parameters influencing desorption/ionization process**

In general, MALDI is strongly dependent on the laser irradiation conditions including the laser wavelength and laser fluence. MALDI also depends on the materials making up the matrix.

#### **8.1.3.1: Laser wavelength and matrix absorption**

It has been recognized since the early days of MALDI that the matrix must absorb at the incident laser wavelength to obtain a high-quality mass spectrum [168, 225].

Typically the intensity of the features in the mass spectrum is dependent on a matrix's molar absorption coefficient at the incident wavelength and increases with increasing matrix absorption. The best mass spectra are obtained using a laser wavelength that corresponds to the absorption maximum of the matrix [193, 211]. A matrix with a lower absorption coefficient can be used however by irradiating the sample with a higher fluence at the appropriate wavelength. However, analyte ions will not be produced if the absorption approaches some critically low value [211].

The spectral absorption spectrum of a solid matrix can differ considerably from its solution spectra. Solid-state absorption spectra tend to broaden toward longer wavelengths, that is, to the red [226, 227]. One potential benefit of the broadened solid phase absorption profile is that MALDI laser wavelengths can be used that lay outside their solution absorption bands [3].

### **8.1.3.2: The effect of laser fluence on MALDI ion signal intensity**

Laser fluence is defined as the pulse energy per unit area. This metric strongly influences the observed ion signal intensities in a MALDI mass spectrum [3]. In general, the ion signal intensities increase steeply with laser fluence above a threshold value where MALDI ions are first detected [228, 229]. However, it is also observed that at fluence levels 2-3 times the threshold value the ion signal intensities do not increase appreciably [200]. This is attributed to the side effects such as fragmentation reactions or absorption saturation [3]. Indeed, these factors can reduce the MALDI ion signals [229].

Often the MALDI ion signal,  $I$ , dependence as a function of incident laser fluence,  $F$ , is represented by an equation of the form  $I \sim F^n$  [230, 231]. The exponent  $n$  is dependent on the matrix and the instrumental configuration used in a MALDI process, as well as the laser spot size [200, 229]. Typically values of  $n$  have been determined between 5 and 10 from MALDI spectra obtained using laser spot sizes of 50-200  $\mu\text{m}$  in diameter [3].

### **8.1.3.3: Sample preparation protocols**

It is well-known that the protocols used to make a matrix-analyte sample play a key role in a successful MALDI MS analysis. For example, a proper M/A ratio is indispensable for obtaining a MALDI mass spectrum with a good signal-to-noise ratio in that the quality of the mass spectra deteriorate significantly if the ratio is too high or too low [232]. Generally, the critical value of the M/A ratio increases with the molecular weight of analyte. The solvent, buffers and other detergents used in sample preparation process can also affect the MALDI MS performance [233-235]. A comparison of dry and wet depositions of analyte on matrix crystals reveals that it is crucial to sufficiently rewet

the matrix surface layers with analyte solvent to optimize the MALDI performance [236]. In contrast to ESI, however, MALDI is relatively more tolerant toward impurities such as salts.

There are many approaches to making solid matrix-analyte solutions. Two of them: the “dried-droplet” and “thin-layer” protocols are widely used for MALDI MS analyses. In the dried-droplet method, matrix and analyte are co-crystallized by simply mixing their solutions together and slowly air-drying. For the thin-layer protocol volatile solvents such as acetone or acetonitrile facilitate a fast evaporation of solvent and the formation of homogeneous microcrystalline “films” [3]. Interestingly, both yield very different sample morphologies but similar MALDI mass spectra. This suggests that sample morphology is less important for a successful MALDI analysis [233].

## **8.2: DIOS**

Although the DIOS mechanism is currently not well understood, many operational aspects of MALDI also apply to DIOS. Both, for example, use a laser pulse to excite and desorb the analyte, and both involve a thermal desorption process, and ion formation by intermolecular reactions such as proton transfers. Thus, insight into the DIOS mechanism is helped by first understanding the MALDI desorption/ionization process described above. At the same time there are some significant differences between the two methods.

### **8.2.1: The desorption process in DIOS**

In general, the desorption process involves the absorption of laser irradiation by a solid substrate and subsequent transfer of that energy to the analyte, resulting in its movement from the solid substrate to the gas phase. It has been demonstrated that photoactive and photo-luminescent pSi efficiently absorbs UV-visible light [237]. At the

N<sub>2</sub> laser wavelength of 337 nm, for example, pSi can have an effective absorption coefficient of up to  $10^5 \text{ cm}^{-1}$  [238].

Another very useful property of pSi is its ability to use the absorbed laser energy to form energetic electron–hole pairs or excitons [78]. Electron–hole pairs separate within the space-charge layer located in the surface of pSi, thereby creating an electric field, and when they relax via nonradiative recombination of electrons and holes or carrier–phonon scattering, surface adsorbates can become vibrationally excited [239]. It has been calculated that the band gap at the surface of pSi is reduced to 0.65–0.25 eV which is similar to the band gap energies of nanosized Si clusters such as Si<sub>11</sub>, Si<sub>14</sub>, Si<sub>17</sub>, Si<sub>18</sub>, Si<sub>30</sub> and Si<sub>33</sub>, (0.4–0.6 eV) [240].

One mechanism proposed to explain the analyte desorption in DIOS is the high peak temperatures obtained by laser irradiating the strongly absorbing pSi which results in part from its poor thermal contact with the underlying bulk material [241, 242]. Similar to MALDI, the analyte phase change is a thermal vaporization process which is induced by the heating of the substrate surface by the incident laser. The laser-induced temperature increase in the surface is determined by two effects: heat conduction and laser light absorption. For example, when a pSi substrate is irradiated by a 337 nm N<sub>2</sub> laser the surface temperature is estimated to reach as high as 600 K [243]. Unlike the MALDI plume which expands in three dimensions, the DIOS expansion is one-dimensional due to the confinement imposed by the porous structure. Since the resulting plume cannot expand freely, the plume density remains elevated for a longer period relative to a free expansion [244]. In addition, solvent remains trapped in the nanopores by capillary forces which can lead to very large long-range density fluctuations and may



induce a transition from bulk liquid to a two-dimensional adsorbate phase [245]. This gives rise to a high-density solvent plume containing the adsorbate.

Desorption in DIOS is determined in part by the interaction between the pSi surface and the analyte. This surface interaction energy is expected to influence the energy transfer during the desorption event. In general, the activation energy barrier to release the analyte from the surface,  $E_a^{des}$ , controls the rate of desorption. The desorption rate,  $k_{des}$ , can be expressed by an Arrhenius-type equation:

$$k_{des} = A \exp\left(-\frac{E_a^{des}}{RT}\right) \quad (8.7)$$

where  $A$  is a pre-exponential factor related to the frequency of attempts to cross the barrier.  $E_a^{des}$  is dependent on the interactions between the pSi surface and the adsorbate molecules as well as the surface coverage because of possible interactions between the adsorbates [241].

## 8.2.2: Ion formation in DIOS

### 8.2.2.1 Primary and secondary ionization

The effects of some fundamental and experimental parameters (for example, pSi preparation method, pore size, laser wavelength, sample composition, pH, and so on [15, 25, 243]) on the performance of DIOS have been studied. However, it is still not completely understood how ionization occurs under DIOS conditions. One thought is that the optical absorption and thermal conductivity properties of pSi provide enough energy to promote analyte desorption and ionization. The two-step framework, which is emerging as a viable model to explain MALDI [191] may also apply to DIOS; that is, primary ions are first generated within the time scale of the laser irradiation pulse while

secondary ions are formed by ion-molecule reactions in the expanding plume.

Primary ion formation is an extremely complicated process and may involve several possible pathways. Photoexcitation and energy pooling is thought to be a possible mechanism because electronic structure of a pSi surface can support exciton formation [239]. As described in 8.1.2.1, exciting the analyte in its  $S_1$  state can lead a higher excited  $S_n$  state by exciton migration and pooling. Subsequently, energy pooling by species in their  $S_1$  and  $S_n$  states produces the primary ions. In some cases, pre-existing ions or ion pairs can be present in the nanopores. These ions can be separated and released from the surface by the accelerating voltage of the mass spectrometer and/or the electric field of the incident laser beam [77].

Ion-molecule reactions similar to those described above for MALDI may also be important in the DIOS plume. These include excited-state proton transfers from the excited Si-H groups to the analyte, electron transfers to and from the surface, as well as cationization. For organic compounds with high aqueous basicities, proton transfer reactions to form protonated molecules  $[A+H]^+$  may take place via a Si-O $\cdots$ H-A complex. The adsorbed water plays an important role here because water dissociates upon adsorption and becomes incorporated into the pSi surface as Si-OH. In general, only basic analytes with the aqueous pKa values  $> 4$  can be effectively ionized according to this model [246]. In some cases, cationization by  $Na^+$  and  $K^+$  is the dominant process in positive ion detection [247, 248], especially when the proton affinity of the analyte is small [8].

A complete understanding of MALDI and DIOS involves not only the desorption and ionization process, but also any chemical reaction that the analytes undergo within

the gas phase plume [249]; for example, analyte reduction [250]. Studies of various organic dyes with different reduction potentials by DIOS/MALDI MS have shown that reductions were more obvious for the DIOS process compared to MALDI. When Cu(II) ions were added as an electron scavenger the reduction processes were suppressed for MALDI and not for DIOS. These observations were rationalized as follows: in MALDI with thick sample layer where Photoelectric emission from any metal surface seldom comes about, only a small number of electrons responsible for analyte reduction are supplied by matrix molecules, which are effectively scavenged by the Cu(II) ions. In DIOS however, the silicon substrate supplies a large number of electrons to the analytes, making the Cu(II)-doping ineffective.

#### **8.2.2.2: Proton source**

In MALDI, the matrix is one of the major proton sources. It has been shown through deuteration studies that proton exchange between the excited matrix and any residual solvent in the matrix is unimportant [251]. In DIOS, it has been suggested that the pSi surface can serve as a proton source. The hydrogen-rich pSi surface SiH<sub>x</sub> (x, ~1–3) is a result of the anodic etching process in HF used to make the porous silicon [80]. One possible chemical reaction that describes the anodization is:



Surface heating [252] and photochemical processes [253] are known to cause loss of surface hydrogen from porous silicon, and this process does not fit a second order rate equation. This suggests that hydrogen loss is not strictly in the form of molecular hydrogen [254].

It is also important to note that solvent, water or residual hydrofluoric acid (HF)

can provide protons for DIOS, and/or the trapped solvent and residual gas accumulated in the pores can serve as photochemical ionization agents [241]. For example, an ion yield enhancement of 10 to 40 times was found upon introduction of residual acetic acid or water vapors, demonstrating that gas-phase species can also play a significant role in ionization [243].

In general, the native pSi surface is terminated by Si-H bonds that are hydrophobic. This surface, however, is not stable in air and it is gradually oxidized to form surface Si-OH. It has been proposed that the hydroxyl surface terminations are an important proton source for analytes with high PA. It was also found that fluorinated pSi surface are advantageous because fluorine increases the acidity of the Si-OH moieties [241].

### **8.2.3: Some pSi properties influencing DIOS performance**

#### **8.2.3.1: Porosity and surface structure of the pSi**

The porosity and surface structure of porous silicon used in DIOS are known to play important roles in desorption and ionization processes. Typical n-type DIOS surfaces having porosities of 30-40% can have surface areas a million times greater than that of a planar surface ( $\sim 100 \text{ m}^2/\text{cm}^2$  of etched material). This high surface area significantly lowers the melting point of silicon: pore coalescence and structural collapse were observed at  $900 \text{ }^\circ\text{C}$  [258] in contrast to the melting point of bulk Si ( $1410 \text{ }^\circ\text{C}$ ) [256]. The driving force for this melting process is an increase in the surface energy of pSi ( $0.2 \text{ J}/\text{cm}^2$ ) relative to bulk Si ( $0.0001 \text{ J}/\text{cm}^2$ ). This suggests that the pSi surface energy can be decreased by surface diffusion of silicon atoms upon heating resulting in pore coalescence; that is, larger pore radii and a smaller surface area [255]. For example, pSi

will melt using typical nitrogen laser energies ( $\sim 15 \text{ mJ/cm}^2$ ) because the surface temperature can rise as high as 600 K [257]. As a result, lower laser intensities are required for DIOS experiments involving Si nanowire features [244].

The DIOS process is affected by the pSi surface structure. The correlation between the DIOS performance and surface structure is determined by several factors including the surface area, the nanoscale morphology leading to higher optical absorptions, and the low resultant thermal conductivities [258]. Heat conduction, for example, is inversely correlated with morphology; fine microcolumns lose heat radially at a lower rate than the bulk material due to phonon confinement and boundary scattering [259]. Furthermore, the morphological features of the pSi provide a framework in which solvent and analyte molecules become trapped. Therefore, the combination of large optical absorption coefficient (a  $\sim 10^5 \text{ cm}^{-1}$  [260]) and low thermal conductivities promotes efficient energy transfer from the substrate to adsorbed analyte molecules which desorb intact upon irradiation with a pulsed laser [25].

### **8.2.3.2: Chemical properties of pSi surface**

The chemical properties of pSi surfaces such as wettability, pH, and so on, are also important for optimizing the performance of DIOS MS. The wettability of the surface determines the distribution of the analyte inside the nanopores. Generally higher wettability allows the analyte solution to penetrate deeper into the pore structure [241]. As noted previously, pSi freshly prepared by electrochemical etching is chemically unstable because its Si-H terminated surface is susceptible to oxidization, resulting in the change of surface wettability. This Si-H surface leads readily to a characteristic chemical background in the DIOS mass spectra as it tends to trap hydrocarbons from the ambient

environment [239]. Fortunately, both the wettability and the stability of the pSi surface can be altered by surface derivatization [261].

The pH value of the sample also has a significant impact on the quality of the DIOS mass spectrum. For example, peptide ion signals in negative-ion mode are insignificant relative to the background noise using a low pH buffer solution. However, the analyte signal improves greatly at a buffer solution of higher pH values with a corresponding decrease in the background noise [25]. In some cases the gas-phase analyte proton affinity turns out to be more important for enhancing its DIOS MS sensitivity than its pKa value in solution [246].

### **8.2.3.3: Other influencing factors**

In addition to the physical and chemical properties of the pSi substrate and analyte, the characteristics of the irradiating laser pulse and other environmental factors also affect the DIOS performance. For example, as noted above the laser fluence thresholds for desorption and ionization are lower in DIOS than those in conventional MALDI MS [18]. Similarly, the choice of laser wavelength is also important in this regard. In general, fluence levels are lowest for UV lasers (for example, the 337 nm N<sub>2</sub> laser output) and much higher using visible photons (for example, the 532 nm output of a doubled Nd:YAG laser). Interestingly, the fluences required when using IR wavelengths (for example the fundamental output of a Nd:YAG laser at 1.064 $\mu$ m) lie between the UV and visible wavelength values. Like MALDI, above threshold, DIOS ion signal intensities increase rapidly with increasing laser fluence, ultimately saturating at high fluence levels [246].

The mass spectra generated by DIOS are less dependent on the wavelength of the

laser because pSi can absorb at any photon energy exceeding the band gap of crystalline silicon (1.1 eV). For example, the laser-induced microcolumn arrays on a silicon surface exhibit a close-to-unity absorbance between the near UV (> 250 nm) and near-IR (< 2.5  $\mu\text{m}$ ) [262, 263]. This differs from MALDI, where a matrix's ability to absorb the energy of the laser and absorption efficiency are highly dependent on its molecular and electronic structure [249].

Investigations have also shown that increasing the ion source pressure in the mass spectrometer reduces the number of desorbed ions in a DIOS experiment. The amount of water adsorbed on the pSi surface is also affected by the ion source pressure. Given that the experimental conditions within the mass spectrometer are important, it should probably not be surprising that there are inconsistent reports for the same type of experiments in the literature [239].

### **8.3: NIMS**

NIMS is related to DIOS but makes use of some of the advantages associated with MALDI; specifically, the use of initiator molecules to facilitate desorption/ionization of analytes from a nanostructure surface [32]. It is expected therefore, that many aspects of the desorption/ionization mechanism in DIOS or MALDI will also apply to NIMS. For example, NIMS takes advantage of the large optical absorptions of pSi to absorb laser irradiation and effectively convert that energy into heat, resulting in an explosive expulsion of the initiator molecules into the gas-phase facilitating the desorption of adsorbed analytes [30]. It has been logically suggested that ion formation in NIMS also take place by the two-step mechanism which has been used to explain the ionization steps in MALDI and DIOS, (Sections 8.1 and 8.2). However, some features of NIMS are not

well understood. For example, ion beams have been used instead of photons to form intact analyte ions by NIMS. However, SEM images of the ion-radiated surfaces do not reveal any obvious changes in nanostructure surfaces before and after a NIMS event. As well, unlike conventional MALDI and DIOS, laser-NIMS can produce multi-charged proteins similar to ESI [30].

Usually molecules such as fluorinated siloxanes serve as the initiators in NIMS desorption and ionization. SEM imaging has shown that after laser irradiation, the pSi surface used in NIMS is degraded. This is attributed to rapid surface heating which causes the initiator adsorbed to the substrate to explosively enter the gas-phase [30]. The initiator molecules however, are not ionized in the process because they are chosen to be transparent to incident UV light [31]. Furthermore, because the initiator molecules are not co-crystallized or incorporated with analyte molecules they are not really matrix molecules. In this regard NIMS is fundamentally different from MALDI [32].

Although NIMS is a newly developed matrix-free desorption/ionization technique, it has already proven to be useful for the analysis of complex biofluids and metabolites, and for tissue imaging.



## Chapter 9: The SALDI ionization mechanism

### 9.1: Introduction

Surface techniques such as DIOS and NIMS have been successfully applied in the analyses of small drug molecules, peptides, synthetic polymers and enzymes [9, 30, 83, 264]. As discussed in Chapter 8 however, the elucidation of the SALDI ionization mechanism is controversial and elusive [239].

It is well-known that the ion signal intensity ( $I$ ) of a particular analyte in both MALDI and DIOS depends strongly on the laser influence ( $F$ ) [18, 229]. Experimentally, ion signals in a mass spectrum appear above a threshold fluence value, rise rapidly and then saturate at high laser fluence. The signals can even decline at higher fluence values due to the onset of side reactions resulting in fragmentation and substrate surface deformation. That said, there is still a debate as to whether the threshold fluence is a genuine physical attribute of the process versus an experimental limitation.

The ion signal intensities are observed to increase with a power-law of  $I \sim F^n$  in the range between threshold and saturation [176]. In the case of non-resonant multiphoton ionization (MPI), the slope of the  $\ln$ - $\ln$  plot of  $I$  versus  $F$ ,  $n$ , indicates the number of photons involved in the nonlinear absorption process [265]. For organic molecules with ionization potentials around 9 eV the number of photons involved tends to be  $\sim 2$ -3 (assuming that UV photons with energies of  $\sim 3.7$  eV (337 nm) are used). The slopes of the  $\ln$ - $\ln$  plots in MALDI MS and DIOS however, tend to be very large ( $n$  between 4 and 10). In such cases equating the slope of these  $\ln$ - $\ln$  plots with the number of photons does not make physical sense.

## 9.2: Small molecule ionization experiments using a pSi substrate

Caffeine ( $C_8H_{10}N_4O_2$ ; molar mass =  $194.2 \text{ gmol}^{-1}$ ) is one of the most widely consumed biologically-active substances and a well-known stimulant due to its action as an antagonist to adenosine receptors in the central nervous system [266]. Its chemical structure is shown in Fig. 9.1. Caffeine was used as an analyte to investigate the physical processes taking place when using pSi for DIOS and NIMS because surprisingly its mass spectrum exhibited two peaks; one corresponding to the radical cation as well as the expected feature corresponding to the protonated species. The former are rarely observed in MALDI, DIOS or NIMS. Furthermore, the relative intensities of these features were found to depend critically on the location of the laser focus relative to the substrate surface (Fig. 9.2). The two configurations (laser focus at the surface and above the surface) are shown schematically in Fig. 9.3. Similar observations were subsequently found in this work using other SALDI substrates such as microstructured tungsten oxide ( $WO_3$ ) [75] and titanium dioxide ( $TiO_2$ ) [267] indicating that the mechanisms involved are specific to the analyte but general with respect to the substrate provided the material is porous and a semiconductor.

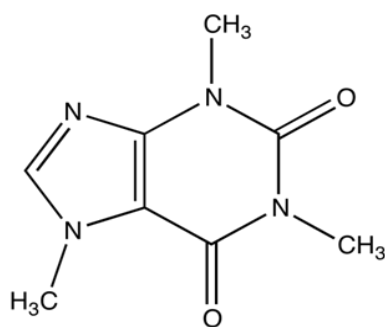


Fig. 9.1: Chemical structure of caffeine;  $C_8H_{10}N_4O_2$ ; molar mass =  $194.2 \text{ gmol}^{-1}$

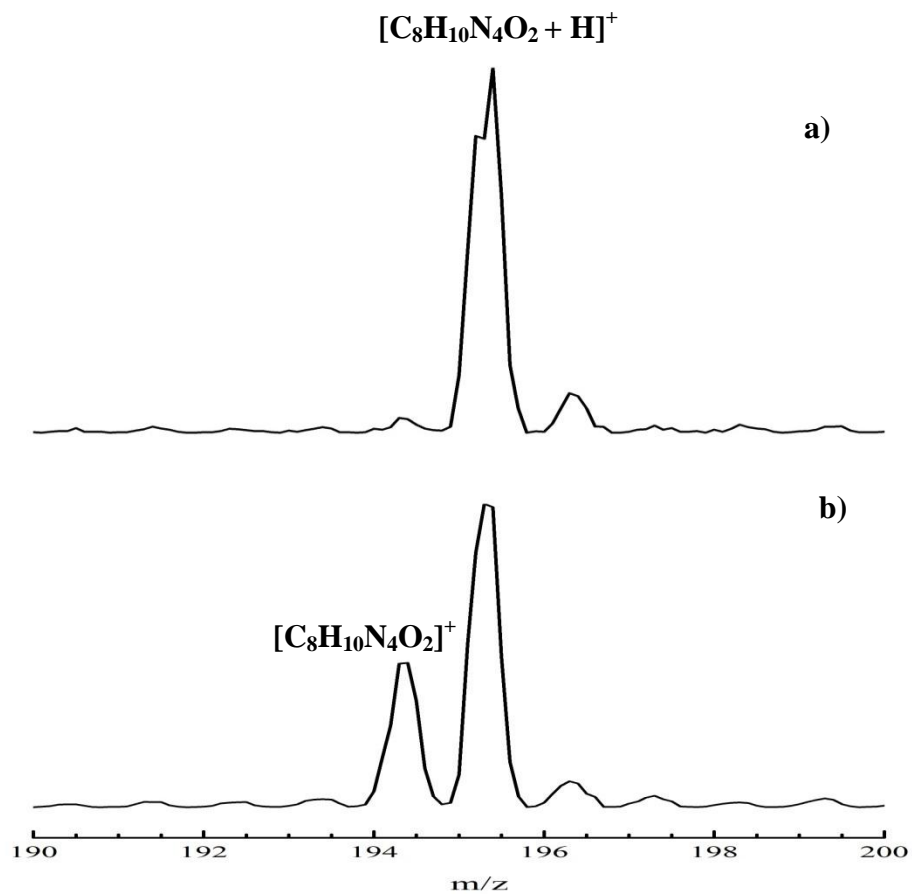


Fig. 9.2: DIOS mass spectra of caffeine obtained a) when the incident laser was focussed at the surface of the pSi chip and b) when the laser was focussed above the surface of the pSi chip.

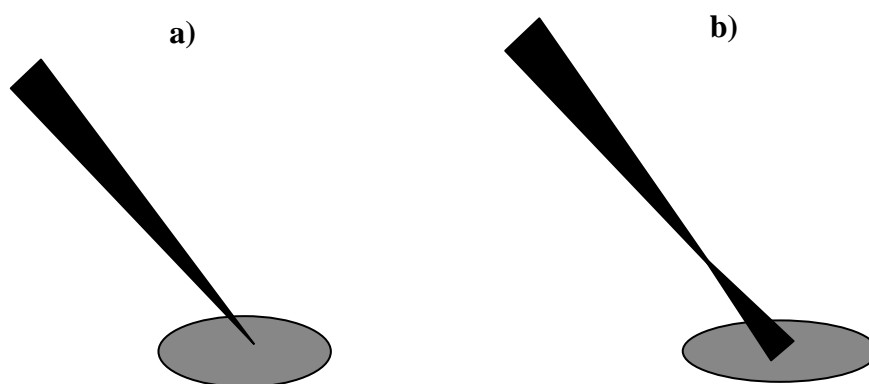


Fig. 9.3: Schematic diagram illustrating a) the incident laser focussed at the surface of pSi chip and b) the laser focussed above the surface of the pSi chip.

### **9.2.1 Ionization when the output of the laser is focussed at the surface of the pSi chip**

The effect of laser fluence on the DIOS protonated caffeine signal (2 $\mu$ L, 1mM), was studied by focusing the spot size of the output of a N<sub>2</sub> laser to  $7.85 \times 10^{-4}$  cm<sup>2</sup> at the surface of a pSi chip and varying the pulse energy from 4  $\mu$ J to 25  $\mu$ J. As shown in Fig. 9.4 the slope of the ln-ln plot of analyte signal intensity versus laser fluence in this region is  $\sim 4.6$ . The physical meaning of the slope in DIOS is obscured by the fact that intermolecular reactions likely play a key role in determining the magnitude of the analyte signals. As noted above it is highly unlikely that the slope in Fig. 9.4 corresponds to the number of photons absorbed in the primary ionization step since the laser intensities used were not particularly high, and the total energy corresponding to four or more photons, if deposited into the analyte during the absorption step, would leave the molecule well above its ionization potential ( $\sim 7.91$  eV [268]).

### **9.2.2: Ionization when the output of the laser is focussed above the surface of the pSi chip**

The dependence of the radical ion DIOS signal intensity of caffeine on the position of the laser focus above the substrate surface was investigated (Fig. 9.5). As the laser focus is moved above the surface the higher fluence in the focal volume is sampling the plume above the surface rather than being deposited into the substrate. In this work the distance was changed from 0.1 mm to 1 mm in intervals of 0.1 mm. The highest radical cation signal intensity was obtained when  $d = 0.4$  mm.

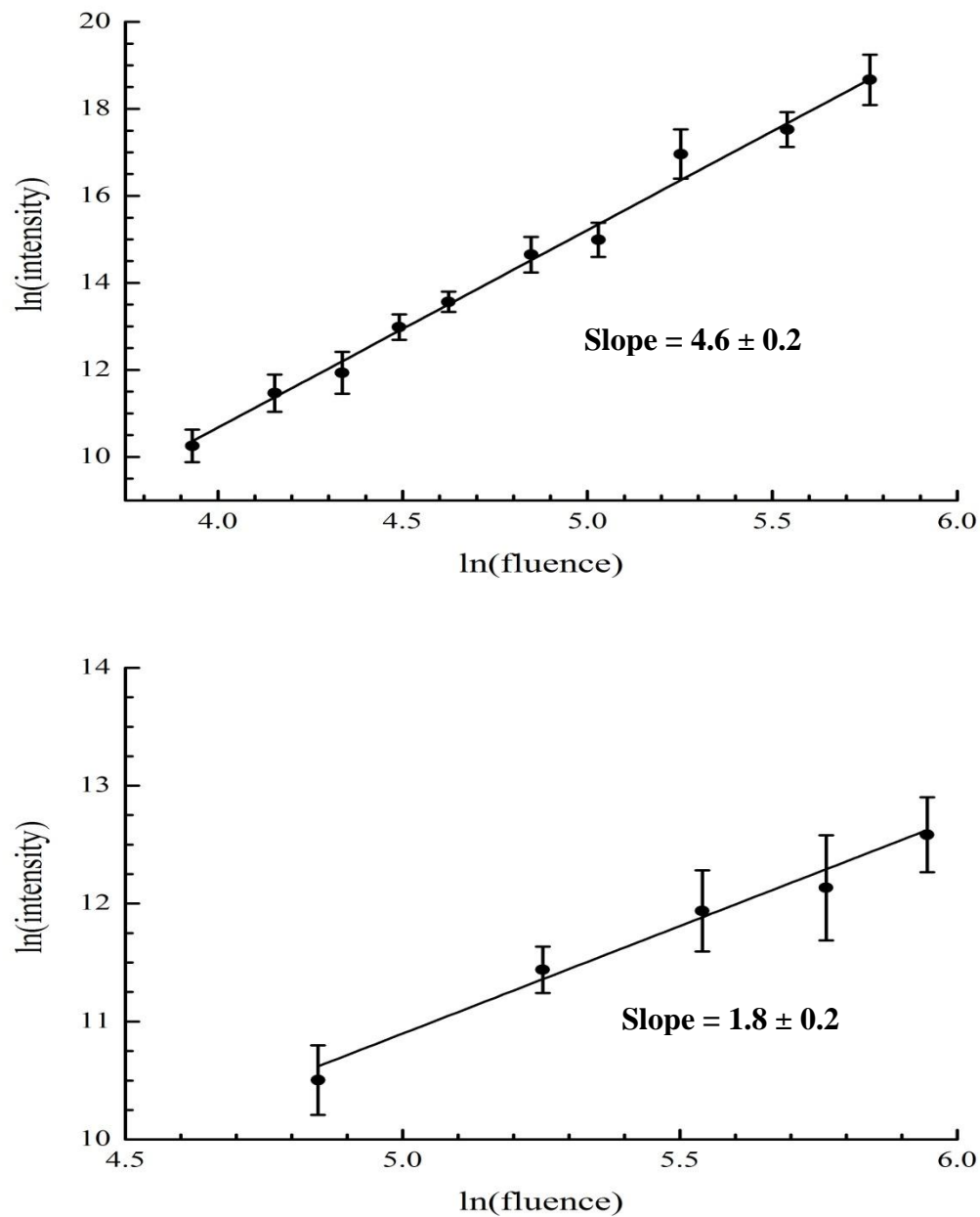


Fig. 9.4: The  $\ln$ - $\ln$  plots of the DIOS signal intensity of the protonated caffeine ion (upper plot) and radical caffeine ion (bottom plot) versus laser fluence when the output of the  $N_2$  laser (337 nm) was focussed at the surface of the pSi substrate.

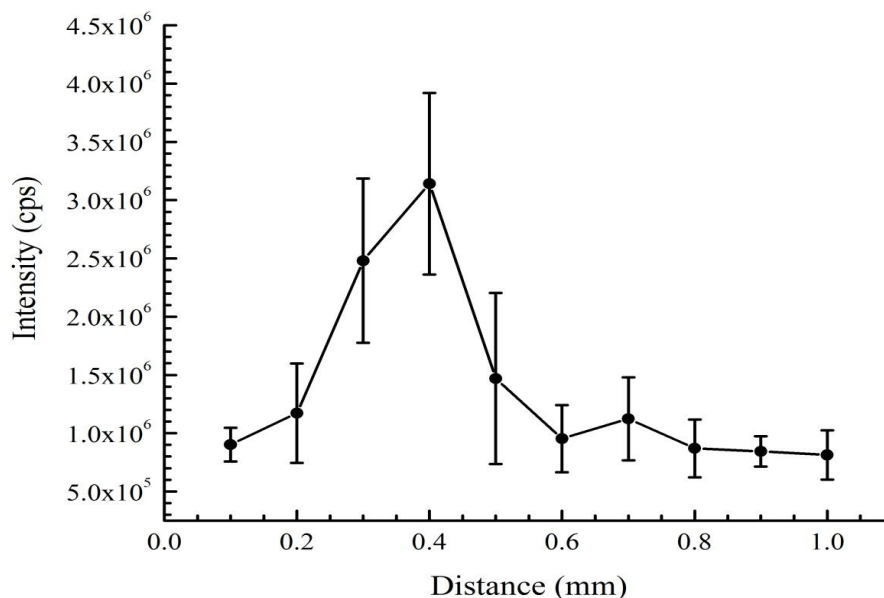


Fig. 9.5: The DIOS-MS signal intensity of the radical caffeine ion as a function of the distance between the laser focus and the surface of the pSi chip.

Fig. 9.6 shows that the ln-ln plot of the radical cation signal intensity versus laser fluence has a slope of  $\sim 2.4$  when the incident laser was focused 0.4 mm above the pSi surface. This value strongly infers that a different mechanism is at play relative to that suggested by the bottom trace of Fig. 9.4. Indeed, the slopes, which are derived from the ln-ln plot of the radical cation signal intensity versus laser fluence, are what one might expect for a multiphoton ionization process.

The effect of laser fluence on the NIMS spectrum of caffeine was also investigated using compound BisF<sub>17</sub> as an initiator and by placing the incident laser focus 0.4 mm above the substrate surface. Fig. 9.7 shows that the slope of the ln-ln plot of the signal intensity of the radical cation versus laser fluence was  $\sim 1.9$ ; again strongly suggestive of a multiphoton ionization process. The signal intensity of radical cation is dramatically increased relative to that of the protonated ion (Fig. 9.8) since the initiator

(BisF<sub>17</sub>) is able to carry more caffeine molecules into the gas phase due to its volatility under laser irradiation.

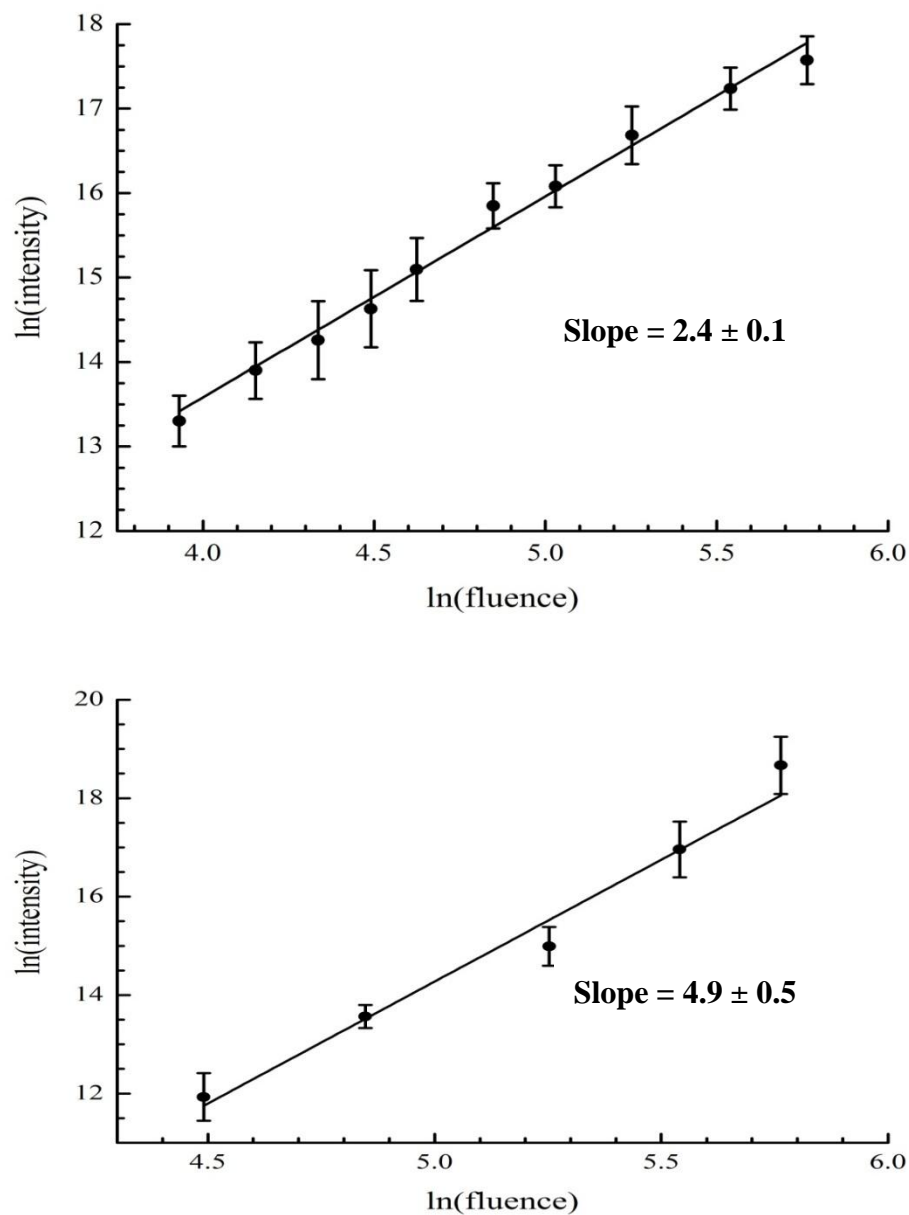


Fig. 9.6: The  $\ln$ - $\ln$  plots of the DIOS-MS signal intensity of caffeine versus laser fluence for the radical cation (upper plot) and the protonated ion (bottom plot) when the output of the N<sub>2</sub> laser (337 nm) is focussed 0.4 mm above the surface of the pSi substrate.

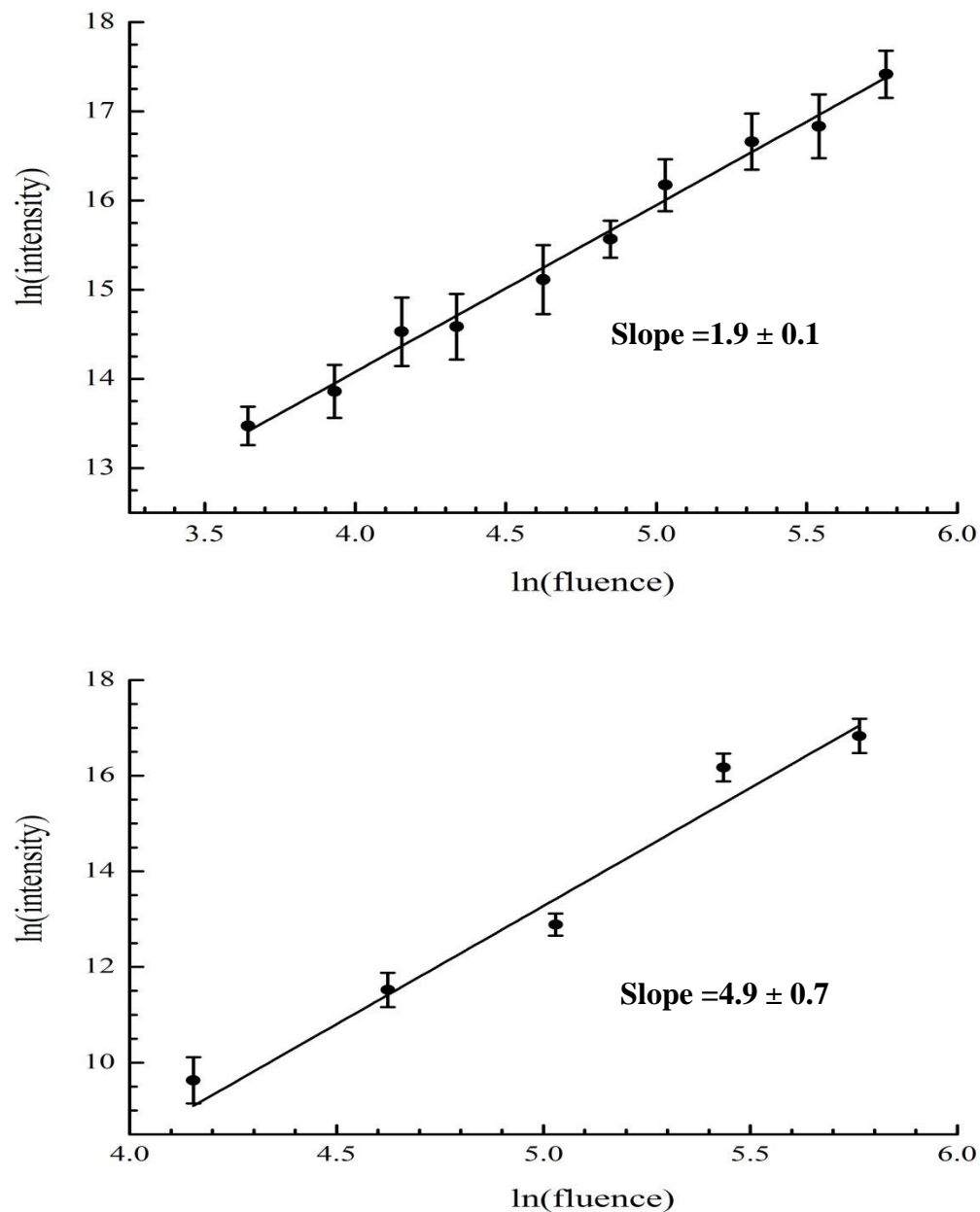


Fig. 9.7: The ln-ln plots of the NIMS signal intensity of caffeine versus laser fluence, for the radical cation (upper plot) and protonated caffeine ion (bottom trace), using BisF<sub>17</sub> as an initiator and placing the focus of incident N<sub>2</sub> laser beam (337 nm) 0.4 mm above the surface of the pSi chip.



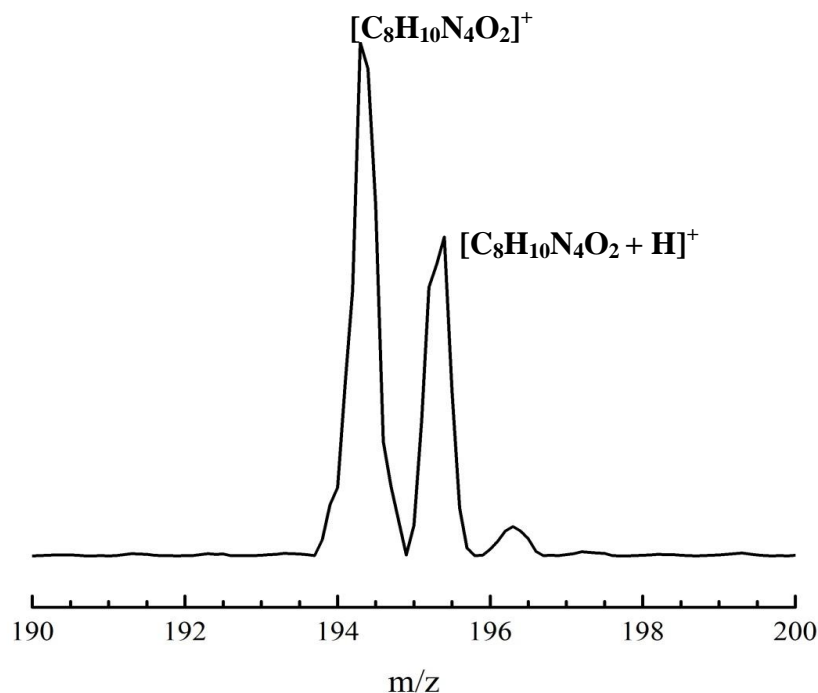


Fig. 9.8: NIMS spectrum of caffeine obtained using BisF<sub>17</sub> as the initiator and placing the focus of the incident N<sub>2</sub> laser (337 nm) 0.4mm above the surface of the pSi chip.

### 9.2.3: Improving the ionization efficiency using two lasers

Timing plays an important role when post-ionizing neutrals in a two-laser experiment because the distribution of laser-desorbed molecules at a given point in the resultant gas expansion is itself time-dependent. In this work two lasers were used; a doubled Nd:YAG laser (532 nm) to initiate desorption and a N<sub>2</sub> laser (337 nm) to probe the resultant gas plume. As shown in Fig. 9.9 the timing sequence begins by triggering the Nd:YAG laser and an oscilloscope at the same time, which correspond to  $t = 0$ . The N<sub>2</sub> laser was then fired after 191  $\mu$ s when the Nd:YAG laser pulse comes out, with a variable relative delay between 1 to 10  $\mu$ s. The UV output emerged  $\sim 0.8 \mu$ s after the second

trigger. In this way, the DIOS plume containing the analyte plume could be probed by the  $N_2$  laser output at different stages of its development as it expanded away from the surface.

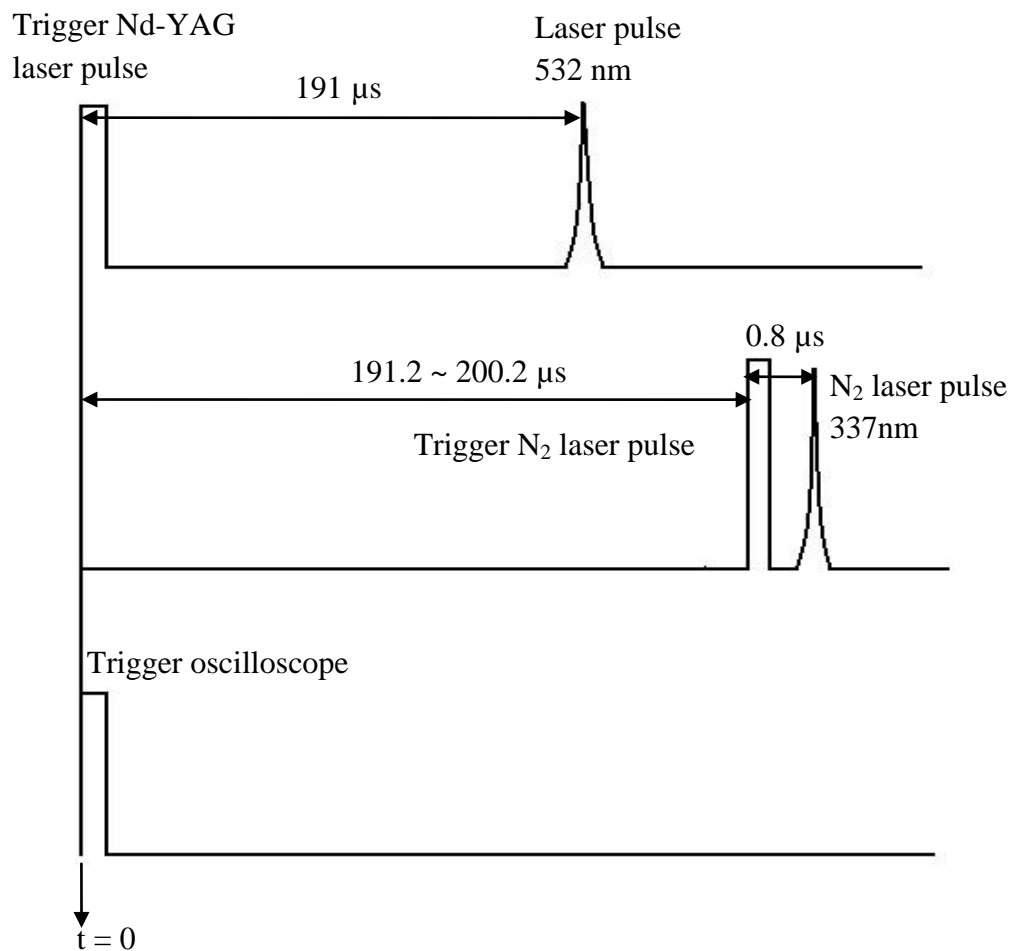


Fig. 9.9: Time delay sequence for a two-laser post-ionization DIOS experiment. The time axis as shown is not drawn to scale.

The energy of the 532 nm Nd:YAG laser used for desorption was held at 25  $\mu\text{J}$ /pulse, while the  $\text{N}_2$  laser energy was held at 5  $\mu\text{J}$ /pulse. The latter value is a little higher than the threshold value needed to observe a DIOS signal with the experimental instrumentation in the lab. This energy level was chosen to ensure that any signal enhancement due to a two-laser DIOS experiment was more evident when comparing the signals obtained by a single-laser DIOS run.

The enhancement for caffeine as a function of delay time using two lasers is shown in Fig. 9.10. Each data point represents an average value of the ion signal intensity of radical caffeine cation (2 $\mu\text{L}$ , 1mM) at  $m/z$  194.2 acquired over 1000 scans between  $m/z$  = 190 and 200. Figure 9.10 shows that the caffeine radical cation signal intensity is enhanced by 337 nm UV post-ionization relative to that observed using nitrogen laser alone, maximizing by ~80% at a time delay of ~ 5  $\mu\text{sec}$ . The overall profile of the plot is a measure of the time evolution of the plume, and shows that species are released slowly (on the microsecond time scale) relative to the duration of the incident desorbing laser pulse (nanosecond time scale).

Experiments were then carried out with the roles of the lasers reversed; that is, the DIOS plume was generated by the UV output of the  $\text{N}_2$  laser (337nm) followed by post-ionization using the visible Nd-YAG laser output (532 nm) with the same pulse energy as the  $\text{N}_2$  laser at a time delay of ~ 5  $\mu\text{sec}$ . As show in Fig. 9.11, the radical cation peak ( $[\text{C}_8\text{H}_{10}\text{N}_4\text{O}_2]^+$ ) decreased significantly compared to observed with the original configuration. This is attributed to the fact that it takes at least 4 photons of 532 nm light (photon energy, 2.33 eV) to ionize caffeine (IP, ~7.91 eV [271]) compared to only 3 photons of 337 nm light (3.68 eV).

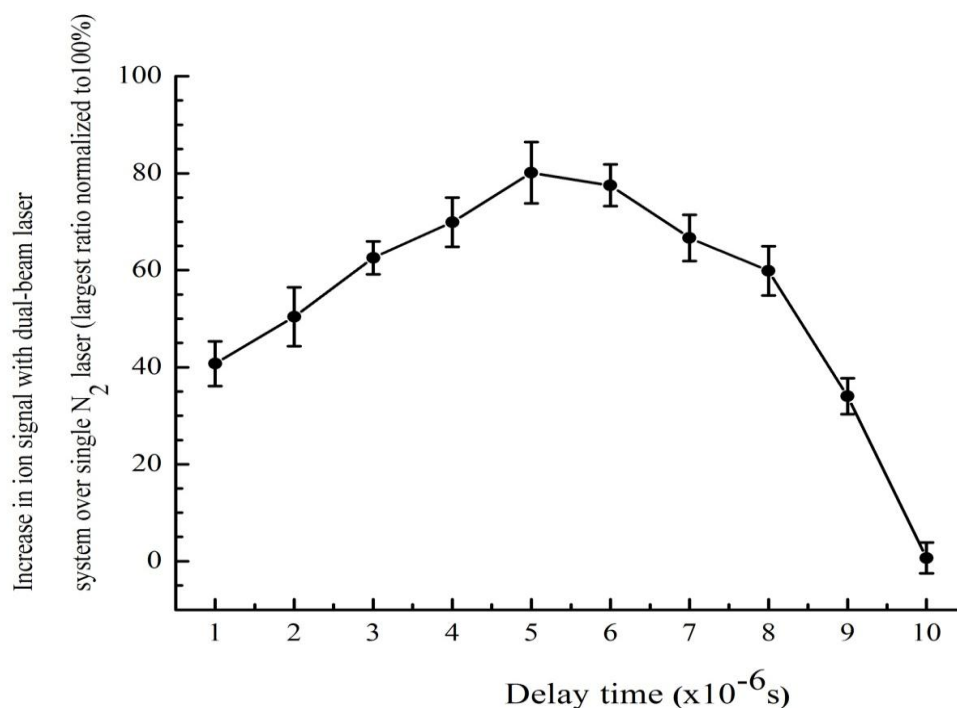


Fig. 9.10: A plot showing the enhancement of the radical caffeine cation signal intensity at  $m/z$  194.2 produced by two-laser DIOS over a DIOS experiment performed with a single laser, as a function of delay time.

These results indicate that the incident laser desorbs neutrals as well as ions and that the neutral analyte molecules can be post-ionized after an appropriate delay relative to the desorption laser. The time evolution of the analyte plume reflects the time scale on which the substrate is heated by the incident laser pulses, which in turn is determined by the heat capacity and thermal conductivity of the substrate material. At short delay time, most of the desorbed neutrals have not yet reached the focal volume of the second post-ionization laser. At the longest delay time most of the neutrals have already passed through the focal volume of the second laser pulse, and fewer molecules are being desorbed. Therefore, the optimum delay corresponds to the time when the UV pulse intersects the plume with the maximum number density of desorbed material. This occurs after  $\sim 5$   $\mu$ sec for caffeine. This result indicates that on average the caffeine molecules are

moving very slowly (assuming  $d = 0.4$  mm,  $v = d/t \sim 80$  ms<sup>-1</sup>) and therefore the expansion is probably more effusive than supersonic in nature. The experiments here show that compared to a single laser experiment the efficiency of radical cation formation during DIOS can be increased by directly ionizing the expanding plume with a second laser after an appropriate time delay. This implies that the approach described in this thesis may be used to deliver biomolecules into the gas-phase for spectroscopic characterization.

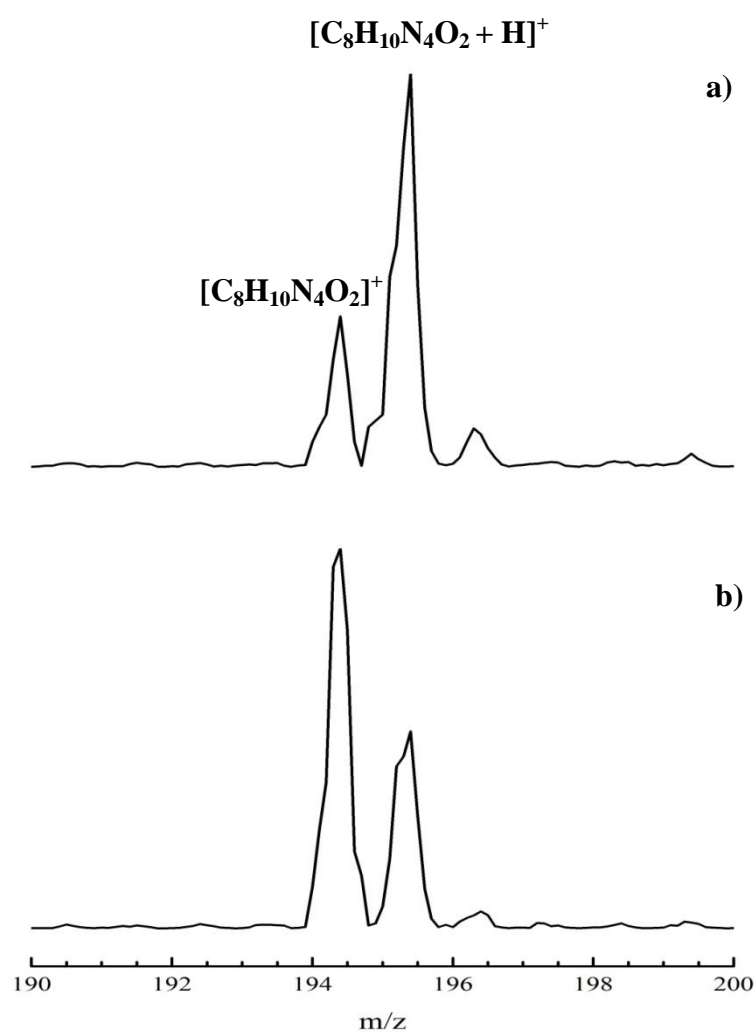


Fig. 9.11: DIOS spectra of caffeine obtained in a two-laser experiment where a) DIOS was initiated with a N<sub>2</sub> laser (337 nm) while the visible output of a doubled Nd-YAG laser (532nm) was used for post-ionization and b) DIOS was initiated with a double Nd:YAG laser (532 nm) while the UV output of a N<sub>2</sub> laser (337 nm) was used for post-ionization.

### 9.3: Peptide ionization using a pSi substrate

The dependence of peptide analyte ion signal intensity on laser fluence by DIOS was investigated using the hexapeptide Dalargin. First, a ln-ln plot of the protonated Dalargin ion signal intensity versus laser fluence was made for the case where the incident laser was focused at the surface of the pSi chip (Fig. 9.12a). The slope of the line of best fit is  $\sim 5$ , a value which is very similar to that observed from MALDI (5~10) depending on matrix and mass spectrometer used [200, 229].

Next, the ln-ln plot of the protonated Dalargin signal intensity formed by DIOS versus laser fluence was measured when the laser focus was positioned 0.4 mm above the surface of the pSi chip (Fig. 9.12b). The slope in this case is  $\sim 4$ , but unlike caffeine, a radical cation peak ( $[\text{Dalargin}]^+$ ) is not observed in mass spectra while the peak due to  $[\text{Dalargin} + \text{H}]^+$  is substantially decreased. Lastly, a ln-ln plot was made of the NIMS protonated Dalargin signal intensity versus laser fluence using  $\text{BisF}_{17}$  as an initiator. Slopes of  $n \sim 3.9$  and  $\sim 4.5$  were found when the laser was focused 0.4 mm above the surface and at the surface, respectively (Fig. 9.13). Although the NIMS  $[\text{Dalargin} + \text{H}]^+$  peak signal intensity was significantly larger than that obtained by DIOS the radical cation  $[\text{Dalargin}]^+$  was still not observed. This may be because the proton affinity of the polypeptide is so large that any radical cations formed efficiently react with the substrate or other molecules in the plume to form the protonated species. More experiments are required however to confirm this hypothesis.

As explained below these results suggest that peptide desorption is initiated by a thermal mechanism.

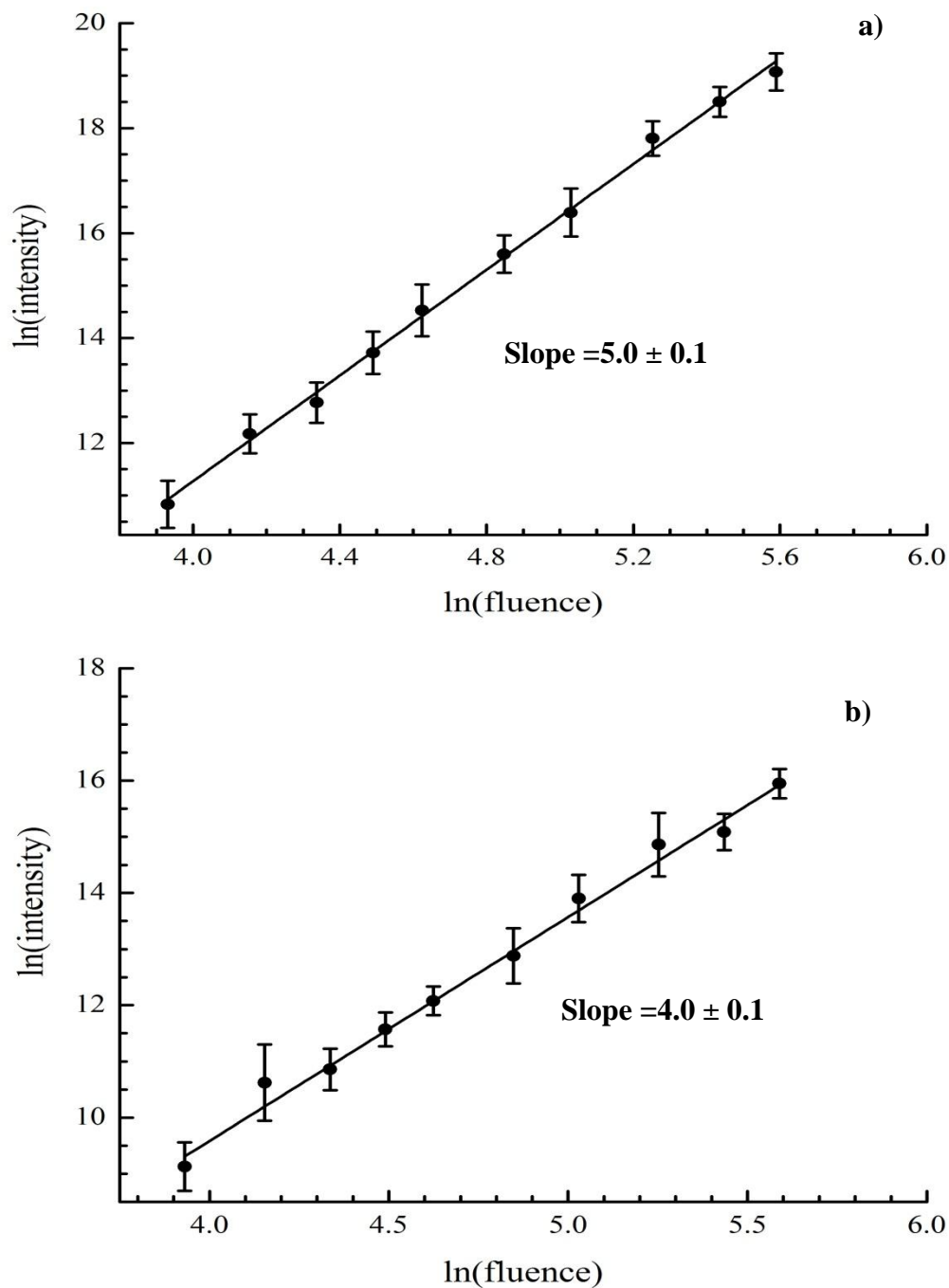


Fig. 9.12:  $\ln$ - $\ln$  plots of the protonated Dalargin ion intensity formed by DIOS versus laser fluence when a) the focus of  $N_2$  laser (337nm) was placed at the surface of the pSi chip, and b) when the output of the incident  $N_2$  laser (337 nm) was focused 0.4 mm above the surface of the pSi chip.

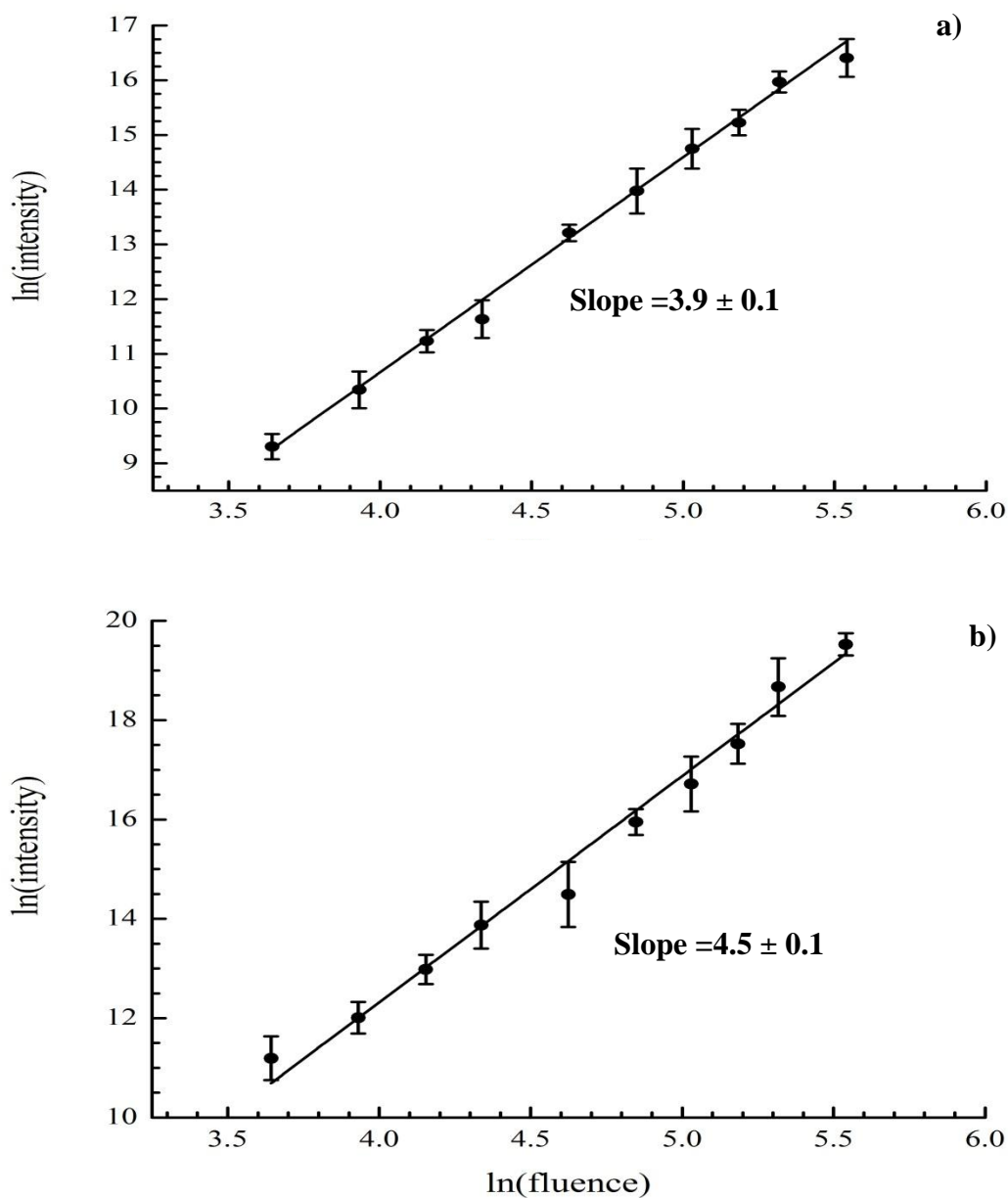


Fig. 9.13: ln-ln plots of the protonated Dalargin NIMS signal intensity versus laser fluence using BisF<sub>17</sub> as an initiator a) when the focus of N<sub>2</sub> laser (337 nm) was placed 0.4 mm above the surface of the pSi chip and b) when the focus of N<sub>2</sub> laser (337 nm) was placed at the surface of the pSi chip.



#### 9.4 Ionization process using different substrates

Recently microstructured tungsten oxide ( $\text{WO}_3$ ) and titanium dioxide ( $\text{TiO}_2$ ) were developed as effective SALDI substrates and used to detect a variety of small drug molecules and peptides [75, 267, 270]. Similar to the experiments described above, the desorption ionization mechanisms using  $\text{WO}_3$  and  $\text{TiO}_2$  chips as SALDI substrates were investigated by constructing  $\ln$ - $\ln$  plots of the analyte ion peak signal intensity versus laser fluence. Fig. 9.14 shows the results for caffeine ( $5\mu\text{L}$ ,  $1\text{mM}$ ) obtained by using a  $\text{N}_2$  laser ( $337\text{ nm}$ ) to initiate the SALDI process on a  $\text{WO}_3$  chip. The slope obtained from the plot when the incident laser was focused at the surface of the chip is  $\sim 4.2$  (the upper trace in Fig.9.14) when detecting the protonated species, and  $\sim 2.4$  (the bottom trace in the Fig.9.14) when detecting radical molecular ion. The slopes obtained for the radical cation and protonated species when the incident laser focus was placed  $0.4\text{ mm}$  above the substrate surface (the bottom trace in Fig.9.15) and at the surface (the upper trace in Fig.9.15), are  $\sim 2.2$  and  $\sim 4.9$ , respectively.

Similarly, the slopes obtained for protonated caffeine and the radical cation using a porous  $\text{TiO}_2$  chip as the SALDI substrate are  $\sim 4.6$  and  $\sim 3.0$ , respectively (Fig. 9.16) when the focus of the  $\text{N}_2$  laser ( $337\text{ nm}$ ) was located at the chip surface. Similar slopes of  $\sim 3.9$  and  $\sim 2.0$ , (Fig. 9.17) were obtained when the focus of  $\text{N}_2$  laser was located  $d = 0.4\text{ mm}$  above the  $\text{TiO}_2$  chip surface for the protonated species and the radical cation, respectively. These results are similar to those obtained using pSi, and show that while the substrate must be porous the “chemical” identity of the substrate material appears to be less important. All slopes derived from plots of  $\ln(I)$  versus  $\ln(F)$  for the formation of protonated and radical cations from Caffeine and Dalargin are listed in Table 9.1.

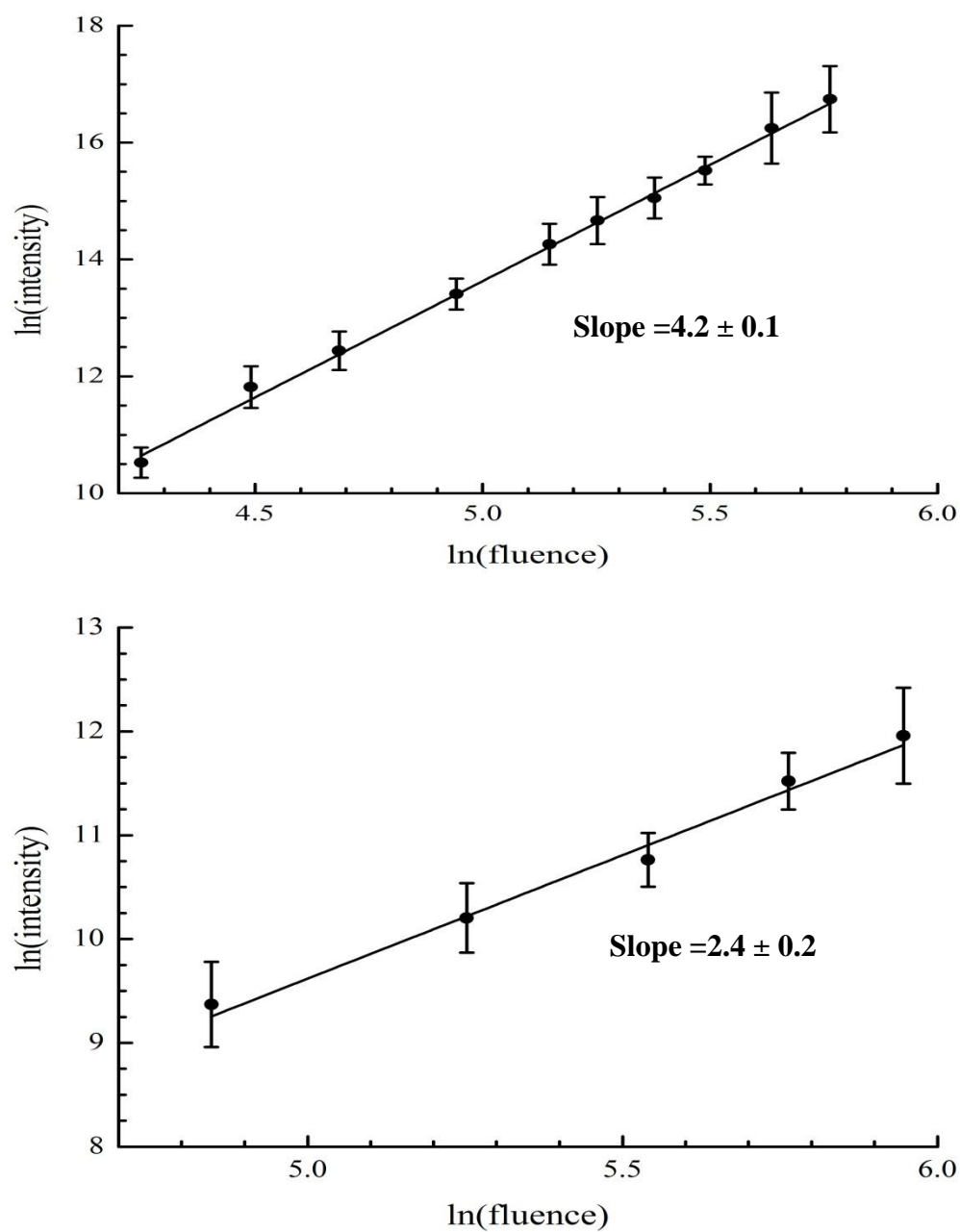


Fig. 9.14:  $\ln$ - $\ln$  plots of the SALDI ion signal intensity of protonated caffeine (upper plot) and the radical cation (bottom plot) versus laser fluence using  $\text{WO}_3$  as a substrate when the focus of the  $\text{N}_2$  laser (337 nm) was placed at the surface of the chip.

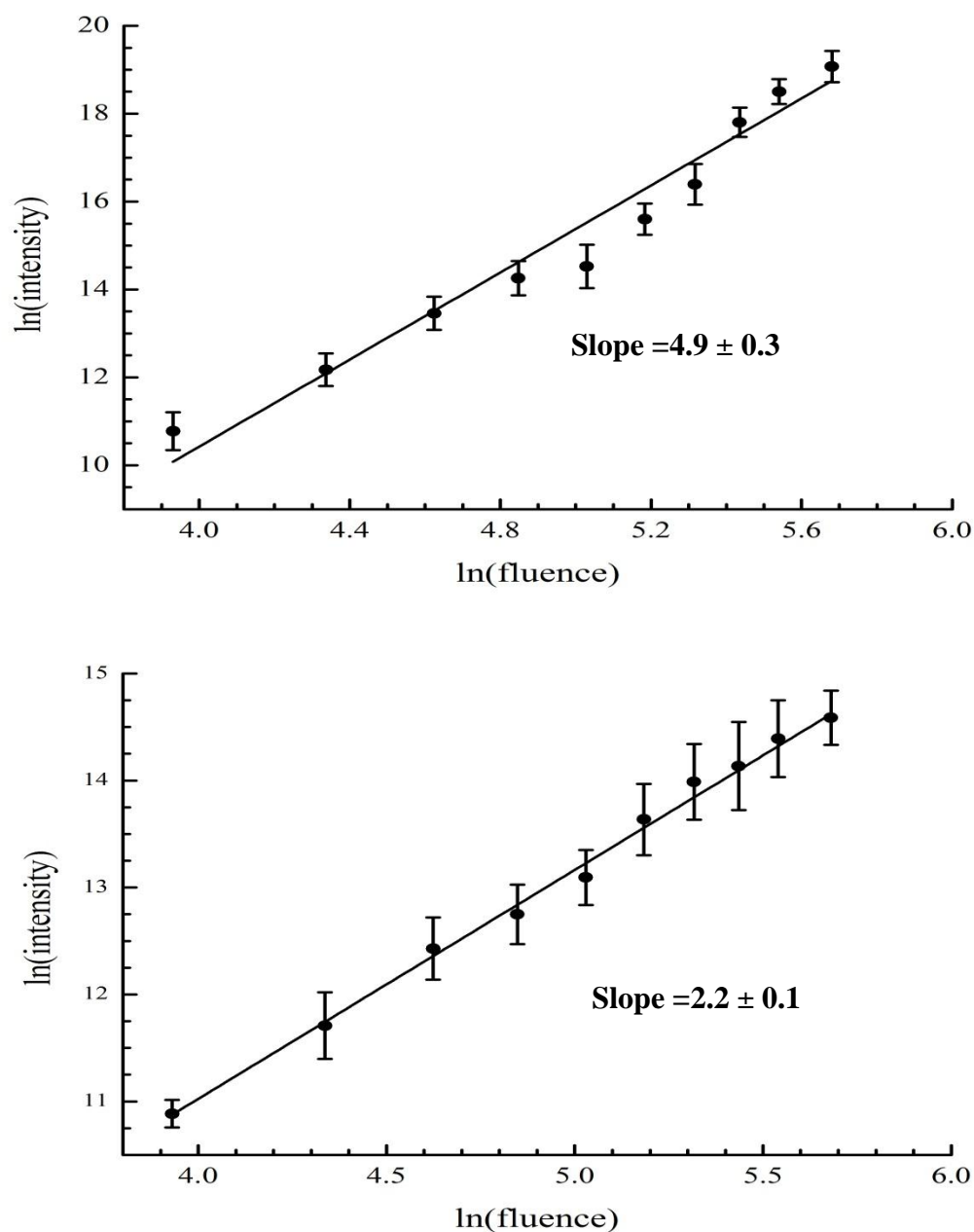


Fig. 9.15:  $\ln$ - $\ln$  plots of the SALDI ion signal intensity of protonated caffeine (upper plot) and the radical cation (bottom plot) versus laser fluence using  $\text{WO}_3$  as a substrate when the focus of the  $\text{N}_2$  laser (337 nm) was located  $d = 0.4$  mm above the surface of the chip.

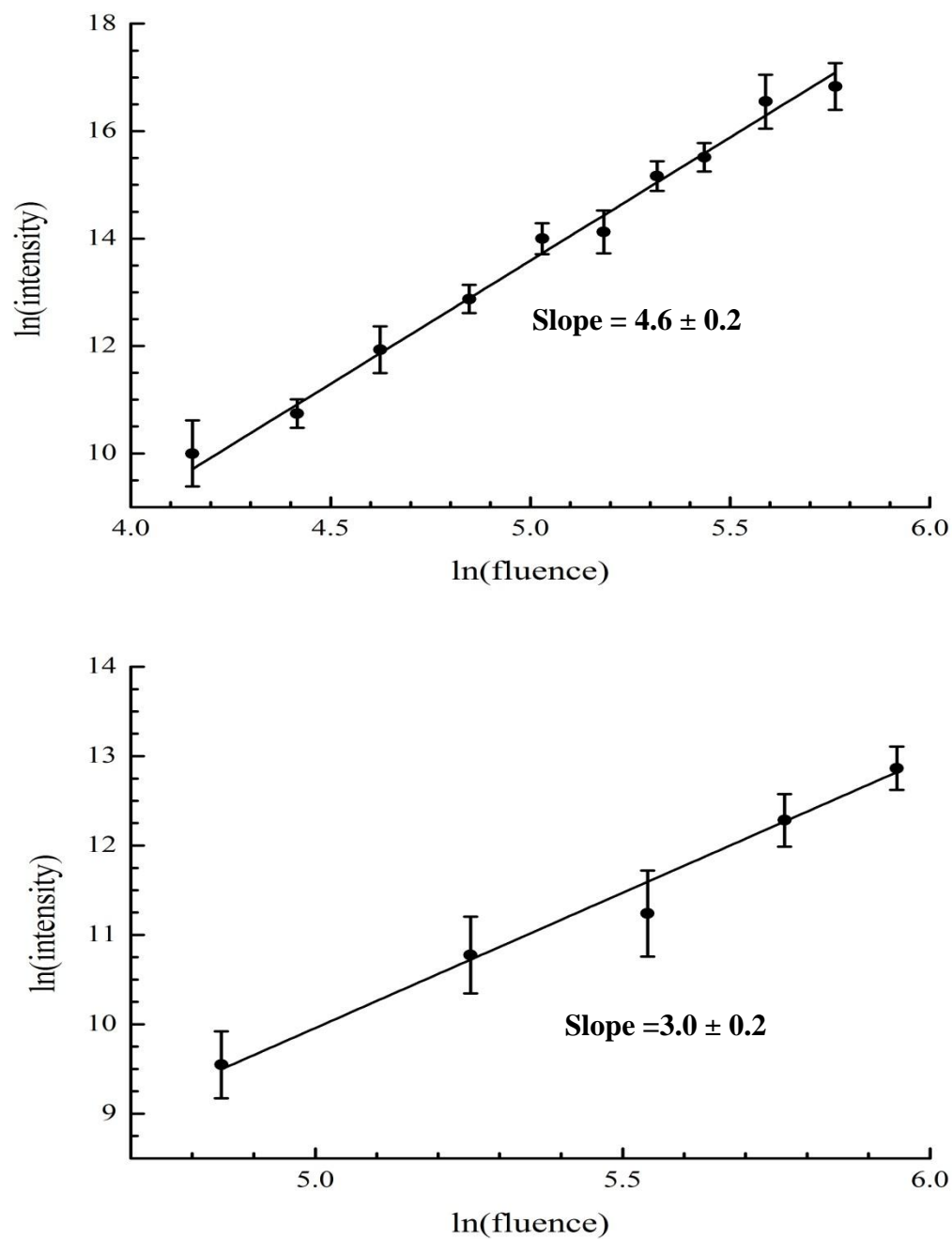


Fig. 9.16:  $\ln$ - $\ln$  plots of the SALDI ion signal intensity of protonated caffeine (upper plot) and the radical cation (bottom plot) versus laser fluence using  $\text{TiO}_2$  as a substrate when the focus of  $\text{N}_2$  laser (337 nm) was placed at the surface of the chip.

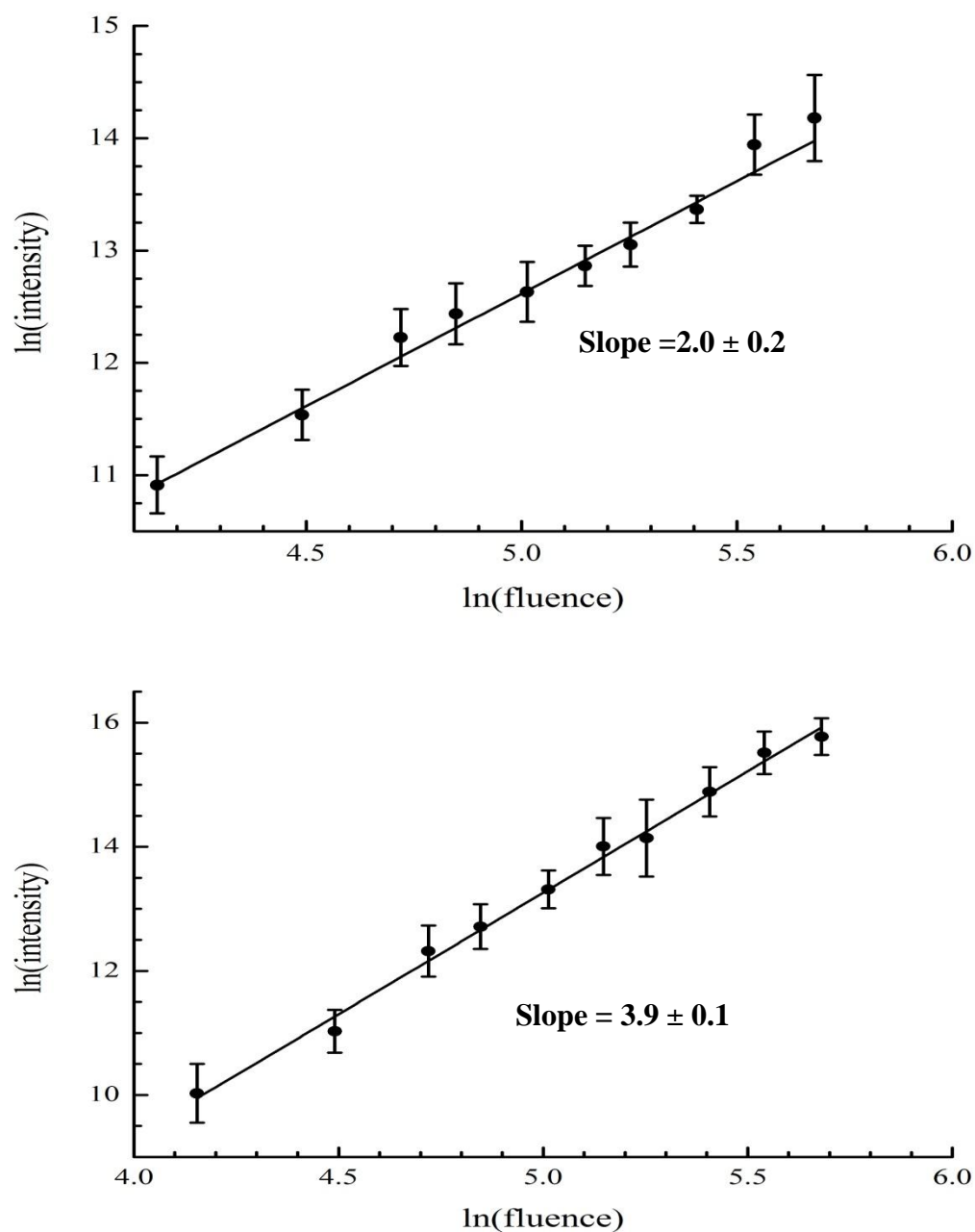


Fig. 9.17:  $\ln$ - $\ln$  plots of the SALDI ion signal intensity of the caffeine radical cation (upper plot) and the protonated species (bottom plot) versus laser fluence using  $\text{TiO}_2$  as a substrate and placing the focus of  $\text{N}_2$  laser  $d = 0.4$  mm above the surface of the chip.

**Table 9.1: Slopes derived from plots of  $\ln(I)$  versus  $\ln(F)$  for protonated and radical cations formed using pSi,  $\text{WO}_3$  and  $\text{TiO}_2$  as SALDI substrates**

Substrates	Analyte ions	Slope from focus of laser located at the surface of substrate	Slope from focus of laser located above the surface of substrate (d=0.4mm)
pSi	Protonated Dalargin ion	$5.0 \pm 0.1$	$4.0 \pm 0.1$
	Protonated Caffeine ion	$4.6 \pm 0.2$	$4.9 \pm 0.5$
	Radical Caffeine cation	$1.8 \pm 0.2$	$2.4 \pm 0.1$
$\text{WO}_3$	Protonated Caffeine ion	$4.2 \pm 0.1$	$4.9 \pm 0.3$
	Radical Caffeine cation	$2.4 \pm 0.2$	$2.2 \pm 0.1$
$\text{TiO}_2$	Protonated Caffeine ion	$4.6 \pm 0.2$	$3.9 \pm 0.1$
	Radical Caffeine cation	$3.0 \pm 0.2$	$2.0 \pm 0.2$

## 9.5: Discussion

The ln-ln plots of the SALDI analyte ion signal intensity,  $I$ , versus laser fluence,  $F$ , are based on an ion signal fluence dependence of the form:

$$I \sim F^n \quad 9.1$$

If the desorption/ionization mechanism involves a multiphoton process then “ $n$ ” would be identified as the number of photons absorbed by analyte. A 337 nm photon from a  $N_2$  laser has  $\sim 3.67$  eV of energy. If the IP of a typical organic molecule is  $\sim 9.5$  eV  $n$  would be  $\sim 3$ . Therefore, an  $n \geq$  four-photon process is considered to be highly improbable.

Conversely, if the ionization process is initiated by thermal desorption, the process is expected to be governed by an Arrhenius equation of the form, as described in Chapter 8 [200]:

$$I \sim A \exp \left( -E_a / k_B T \right) \quad 9.2$$

where  $E_a$  is the desorption activation energy,  $k_B$  is the Boltzmann constant,  $T$  is the effective temperature at the substrate determined by the fluence of the incident laser fluence:

$$T = T_0 + \eta F \quad 9.3$$

and  $T_0$  is room temperature (298.15 K). Substituting Eq. 9.3 into Eq. 9.2 yields:

$$I \sim A \exp \left[ \frac{-E_a}{k_B (T_0 + \eta F)} \right] \quad 9.4$$

The constant  $\eta$  is a function of the physical properties of the substrate and determines the conversion of the deposited energy into a temperature increase within the substrate material. Assuming that complete thermal equilibrium is achieved, then [200]:

$$\eta = \frac{(1-R)\alpha}{\rho c} \quad 9.5$$

where  $R$  are the reflection losses,  $a$  is the absorption coefficient,  $\rho$  is the density and  $C$  is the specific heat capacity. The physical parameters for the SALDI substrates studied in this thesis are listed in Table 9.2.

**Table 9.2: Physical parameters for the SALDI substrates used in this thesis.**

	pSi	WO <sub>3</sub>	TiO <sub>2</sub>
Band gap energy (eV)	2.2 [271]	2.75 [272]	3.2 [273]
R	0.22 [78]	0.18 [274]	0.12 [275]
$a$ (m <sup>-1</sup> )	10 <sup>7</sup> [260]	2 × 10 <sup>6</sup> [276]	2.5 × 10 <sup>6</sup> [277]
$\rho$ (kg m <sup>-3</sup> )	-	-	3.89 × 10 <sup>3</sup> [278]
$k$ (W m <sup>-1</sup> K <sup>-1</sup> )	1 [279]	1.63 [280]	1.3~5.6 [281]
$C$ (J K <sup>-1</sup> kg <sup>-1</sup> ), or $C_v$ (J K <sup>-1</sup> m <sup>-3</sup> )*	0.7 × 10 <sup>6</sup> by $C_v$ [279]	2.28 × 10 <sup>6</sup> by $C_v$ [280]	688.64 by $C$ [282]
$\eta$ (K m <sup>2</sup> J <sup>-1</sup> )	11.14	0.72	0.82

\*  $C_v$  is the specific heat capacity per unit volume and equal to  $\rho C$ . The number in the brackets are references.

In general, heating leading to a temperature increase within the substrate ( $\Delta T_s$ ) is determined by two effects: heat conduction and laser light absorption [243]. If the laser penetration depth  $\delta_d = 1/a$  where  $a$  is absorption coefficient, is much larger than the thermal conduction depth  $\delta_c = (\frac{kt}{C\pi})^{1/2}$ , where  $k$  is the thermal conductivity,  $C$  is the specific capacity, and  $t$  is the length of the laser pulse, the substrate heating will be determined essentially by direct local laser energy absorption. In this case, the substrate temperature rise can be estimated using the following equation [243]:

$$\Delta T_s = \frac{aF}{C} \quad 9.6$$

where  $a$ ,  $F$  and  $C$  have the same physical meaning as defined for equations 9.4 and 9.5.



On the other hand, if  $\delta_c > \delta_d$ , the local temperature rise  $\Delta T_s$  will be limited by heat conduction. In this case  $\Delta T_s$  can be calculated using [243]:

$$\Delta T_s = \left( \frac{2F}{kt} \right) \times \delta_c \quad 9.7$$

In this work for example, if caffeine is desorbed and ionized by focusing 6  $\mu\text{J}$  of 337 nm  $\text{N}_2$  laser light (a typical laser energy used for DIOS; laser pulse duration  $t = 4$  ns) at the surface of pSi substrate, then  $\delta_d = 1/a = 1/(10^7 \text{ m}^{-1}) = 0.1 \mu\text{m} > \delta_c = \left( \frac{kt}{c\pi} \right)^{1/2} = 0.042 \mu\text{m}$ . Under these conditions  $\Delta T_s = \frac{aF}{c} = 1091\text{K}$ ; a value that is close to the value obtained using Eqs. 9.3 and 9.5 ( $\Delta T = T - T_0 = 1149 - 298 = 851$  K). Therefore, it appears that the heating process leading to desorption in pSi is determined mainly by direct laser light absorption. It is predicted that over the range of laser energies used in this thesis (4  $\mu\text{J}$  to 25  $\mu\text{J}$ ), the substrate temperatures ranged from 866 K to 3841 K under 337 nm irradiation. At the higher incident laser fluences heat conduction effects are expected to be important in preventing the substrate from melting.

Fig. 9.18 shows plots of  $\ln(I)$  for the protonated caffeine ion versus  $1/(T_0 + \eta F)$  using pSi,  $\text{WO}_3$  and  $\text{TiO}_2$  as substrates when the focus of  $\text{N}_2$  laser (337 nm) is located at the chip surfaces. If Eq. 9.4 is valid then the slope of the  $\ln$ - $\ln$  plot is given by  $-E_a/k_B$ . The values of desorption activation energy ( $E_a$ ) derived from the lines of the best fits range between 0.54 and 0.77 eV (Table 9.3). These SALDI desorption energies are lower than those derived from MALDI experiments (0.7 ~ 1 eV for typical matrix compounds [200]) which suggests that analytes are more readily desorbed from the condensed phase by SALDI than by MALDI.

Different results are obtained for the caffeine radical cations. The plots of  $\ln(I)$

versus  $1/(T_0 + \eta F)$  when the focus of the  $N_2$  laser was located  $d = 0.4$  mm above the surface of the chip are shown in Fig. 9.19. The desorption activation energies  $E_a$  (0.26 ~ 0.42 eV; Table 9.4) are smaller than those derived for the protonated species. Still overall, the high quality of the fits in Figs. 9.18 and 9.19 strongly suggests that a thermal mechanism is important in the formation of both protonated analyte and radical cations.

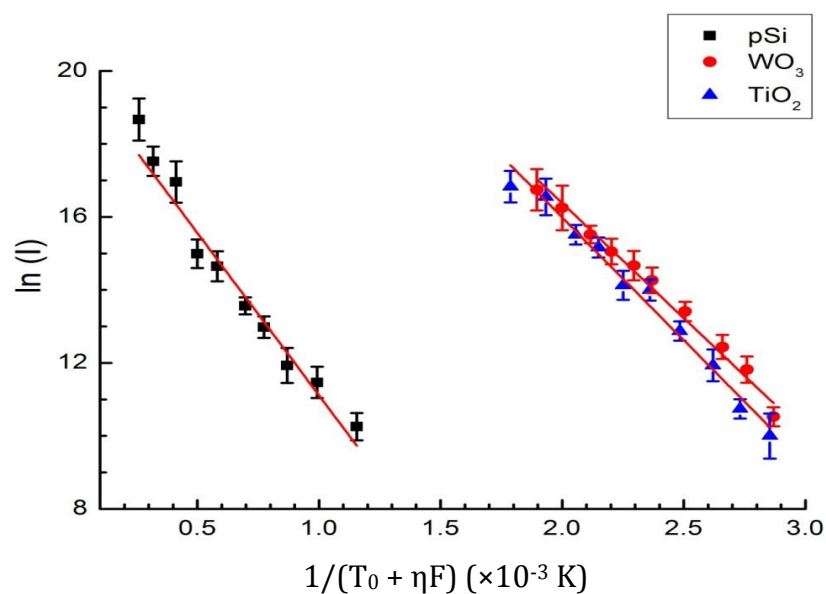


Fig.9.18: Plots of  $\ln(I)$  for the protonated caffeine ion versus  $1/(T_0 + \eta F)$  using pSi,  $WO_3$  and  $TiO_2$  as substrates when the focus of  $N_2$  laser was located at the chip surfaces.

Table 9.3: The slope and  $E_a$  values from plots of  $\ln(I)$  for protonated Caffeine ion versus  $1/(T_0 + \eta F)$  when the focus of the  $N_2$  laser was placed at the surface of the chip

	pSi	$WO_3$	$TiO_2$
Slope (K)	$-8898.7 \pm 577$	$-6311.4 \pm 273$	$-6729.5 \pm 339$
$E_a$ (kJ mol <sup>-1</sup> )	$73.9 \pm 5$	$52.4 \pm 2$	$55.9 \pm 3$
$E_a$ (eV)	$0.77 \pm 0.05$	$0.54 \pm 0.02$	$0.58 \pm 0.03$

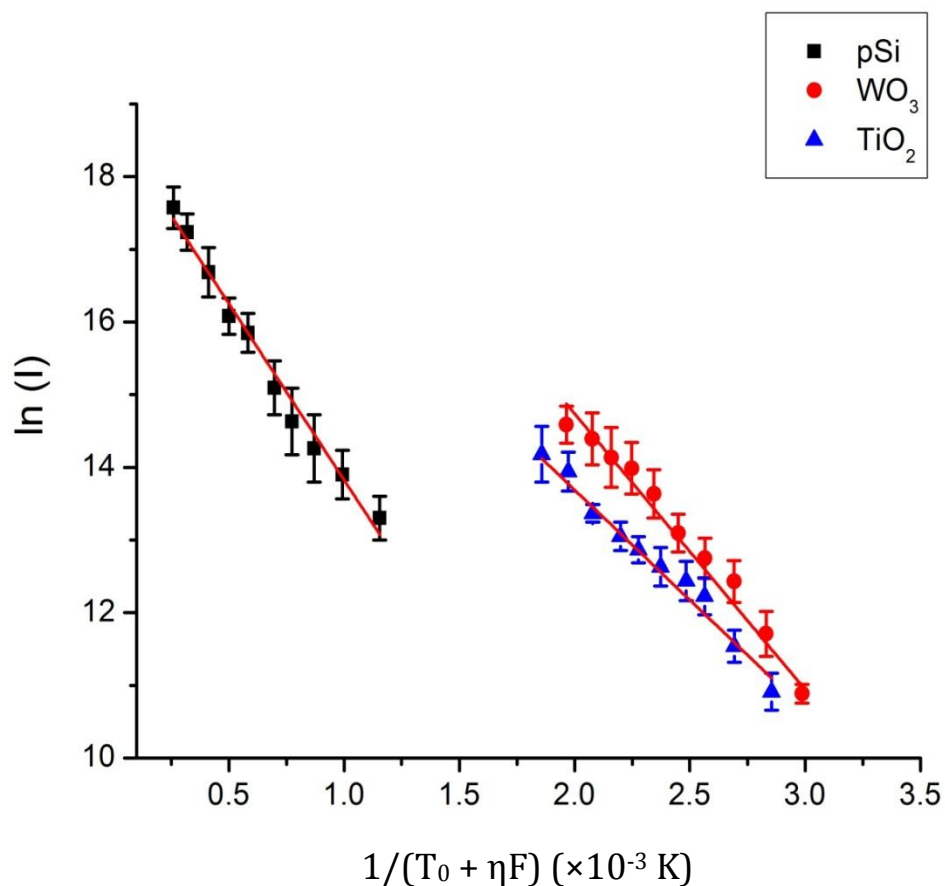


Fig. 9.19: Plots of  $\ln(I)$  for the caffeine radical cation versus  $1/(T_0 + \eta F)$  using pSi,  $\text{WO}_3$  and  $\text{TiO}_2$  as substrates when the focus of  $\text{N}_2$  laser was located  $d = 0.4$  mm above the chip surfaces.

Table 9.4: The slope and  $E_a$  values from plots of  $\ln(I)$  for Caffeine radical cation versus  $1/(T_0 + \eta F)$  when the focus of the  $\text{N}_2$  laser was located  $d = 0.4$  mm above the surface of the chip

	pSi	$\text{WO}_3$	$\text{TiO}_2$
Slope (K)	$-4848.95 \pm 188$	$-3795.62 \pm 161$	$-3032.44 \pm 158$
$E_a$ ( $\text{kJ mol}^{-1}$ )	$40.3 \pm 2$	$31.5 \pm 2$	$25.2 \pm 1$
$E_a$ (eV)	$0.42 \pm 0.02$	$0.33 \pm 0.02$	$0.26 \pm 0.01$

As noted, the desorption activation energies derived from Fig. 9.18 for the protonated species are larger than those derived from Fig. 9.19 for the radical cations. One possible explanation for this is that the form of the analyte within the porous substrate leading to a protonated analyte is more tightly bound than the form of the analyte leading to radical cation formation. Specifically, these results could be understood if the protonated species are pre-formed in the solvent trapped within the pores and are held tightly to the substrate via hydrogen bonding. On the other hand, the radical cations are associated with the release of neutral molecules prior to ionization, which are held to the substrate primarily through weaker van der Waals interactions. The source of the proton leading to pre-formed protonated ions is not completely understood but there is work that suggests the proton transfer in etched silicon is facilitated by the formation of electrons and holes during laser irradiation [246].

The slopes of the  $\ln(I)$  versus  $\ln(F)$  plots ( $\sim 4-5$  when the laser focus is for protonated ion and  $\sim 2-3$  for molecular radical ion no matter where the laser focus is, as shown in the Table 9.1) also suggest that the ionization mechanisms are different for the protonated species and the radical cations. As shown in Fig. 9.2, the strongest radical cation signals were observed when the incident laser was focused  $\sim 0.4$  mm above the surface of the substrate. In general, radical cations are seldom observed by MALDI or SALDI. In this thesis a new ionization mode is therefore postulated to explain the observation of radical cations and the strong dependence of the ion signal on the position of laser focus relative to the substrate surface. The new process shown schematically in Fig. 9.20 is called Surface Assisted Multiphoton Ionization (SAMPI), and appears to be generic for every nanostructured semiconducting substrate examined to date.

At the surface the SALDI spectra are dominated by the formation of protonated species. Although the desorption process also yields neutrals the weak radical cation signals suggest that most of the laser energy is absorbed by the substrate. However, as the laser focus is moved above the surface the fluence at the surface decreases because of an increase in the laser spot area. If the laser focus is too far away the fluence will be too low at the surface to initiate desorption. Furthermore, the number of neutrals entering the laser focal volume will be less as the density of plume decreases (due to the expansion). Under the experimental conditions in this thesis placing the laser focus  $d = 0.4$  mm above the substrate corresponds to the optimum distance where there is still a relatively large fluence at the surface for desorption and a large number of neutrals entering the laser focal volume to be ionized by multiphoton ionization.

The electronic structure of caffeine (IP,  $\sim 7.9$  eV [268]) has been studied. The molecule has a strong  $\pi - \pi^*$  transition at  $35246 \text{ cm}^{-1}$  (4.34 eV) which lies higher in energy than the photon energy of the  $\text{N}_2$  laser. At the two photon level Rydberg states are expected to be present which can facilitate (2+1) resonance enhanced multiphoton ionization [269]. The cations are not expected to be cold because as described above the plume is probably at best a weak adiabatic expansion. Hence, hot band transitions within the focal volume could also contribute to the ion signal. Both effects could be operative. Regardless, one would expect that the  $\ln$ - $\ln$  plots of caffeine radical cation signal intensity versus fluence to have a slope of  $\sim 2$  as observed.

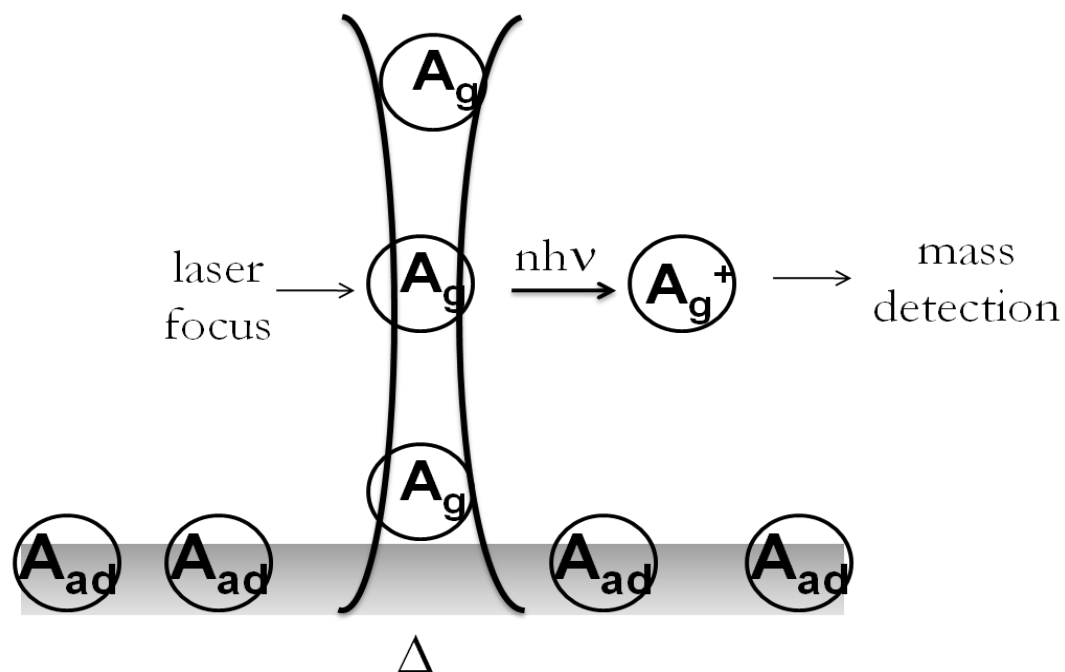


Fig. 9.20: A schematic diagram showing the Surface Assisted Multiphoton Ionization (SAMPI) process.  $A_{ad}$  and  $A_g$  correspond to adsorbed and gas-phase analyte molecules, respectively.

## Chapter 10: Conclusions and future work

### 10.1: Conclusions

The proceeding chapters have described the progress made in development and applications of NIMS. This work involves four essential directions: (1) the fabrication and characterization of pSi substrates for NIMS, (2) the development of functional fluorinated affinity NIMS chips for biological/biomedical applications, (3) an exploration of new micro/nanostructured substrates and laser sources for NIMS, and (4) an investigation of the relationship between laser fluence and the desorption ionization mechanism,

The thesis was presented as follows:

(1) In Chapters 2 and 3, a home-made apparatus, constructed to produce pSi for NIMS applications, was described. The electrochemical etching parameters for fabricating pSi were optimized at room temperature to obtain the best possible NIMS ion signals. The best values of the current density, etching solution concentration and etching time were found to be  $45 \text{ mA/cm}^2$ , 50% HF acid concentration in ethanol by volume, and 30 minutes, respectively.

The performance of pSi-based NIMS using BisF<sub>17</sub> as initiator was evaluated by detecting the protonated polypeptide Dalargin, and comparing those results with the signals obtained by DIOS MS. The LOD of  $(0.64 \pm 0.03) \text{ fmol}$  for Dalargin by NIMS represents an improvement of  $\sim 2000 \times$  over the DIOS value measured with the same mass spectrometer. Experiments showed that compared to DIOS MS, NIMS yields spectra with a higher S/N ratio, is a more sensitive analysis technique and exhibits better

reproducibility because the pSi substrate surface is more stable with the initiator coating under ambient conditions.

A wide range of biological and pharmaceutical compounds were also analyzed in order to determine the versatility of this method. It was demonstrated that NIMS can be used to detect small molecules that exhibit different ionization modes. For example, Fluorouracil (LOD:  $(4.8 \pm 1) \times 10^{-16}$  mol) and Quinidine (LOD:  $(1.0 \pm 0.1) \times 10^{-15}$  mol) were detected as radical cations. The peptide Bradykinin (LOD:  $(7.1 \pm 1) \times 10^{-16}$  mol) was readily detected as a protonated species. The steroid Dexamethasone (LOD:  $(1.7 \pm 0.2) \times 10^{-14}$  mol) and sugar-containing drug Erythromycin (LOD:  $(7.5 \pm 0.6) \times 10^{-14}$  mol) were detected as metal cation adducts.

(2) In Chapter 4, fluororous-affinity NIMS chips were used to effectively separate and enrich on-chip cysteine-containing peptides from mixtures. Specifically, the fluororous affinity tag 3-(perfluoroalkyl) propyl-1-maleimide was used to bind a peptide containing a cysteine residue from mixture of three peptides to a NIMS chip. The mass spectra obtained after washing could be readily interpreted, and unlike rigid covalent surface attachment strategies, fluororous-phase non-covalent immobilization may enhance enzymatic activity by providing conformational flexibility.

The signal intensity of the tagged peptide was examined as a function of binding reaction time, temperature and the washing solution composition. The best conditions were found to be a binding reaction time of 60 minutes at 60 °C followed by a washing step using 40% methanol in water solution. The utility of NIMS chips for the analysis of complex biological samples was further demonstrated by enriching and subsequently analysing cysteine-containing peptides from a BSA tryptic digest. Unlike classic



bioaffinity reagents, the methodology in this work provided mass spectral results which were relatively easy to interpret.

Chapter 5 examined the capability of fluoros-affinity NIMS chips on enzyme assays. Specifically, the products formed by the reaction of peptide substrates with kinase PKA, could be directly determined by mass spectrometry. It was also shown that PKA enzymatic inhibition could be quantitatively screened in a combinatorial fashion. The validity of using fluoros-affinity NIMS to quantitatively analyse enzymatic inhibition was confirmed by deriving the  $IC_{50}$  values of two inhibitors and comparing them with those obtained by other methods. A NIMS approach in this regard is more reproducible than MALDI MS because the sample is evenly distributed on the chip surface, and the mass spectra are clear of any interfering matrix ions and adduct ions.

Chapter 6 describes a new NIMS technique to determine the enantiomeric excess of stereoisomers by kinetic resolution. The experimental results showed that the enantiomeric excess could be determined within  $\pm 10\%$  which may be sufficient to meet the requirement for screening asymmetric catalysts. Compared to GC/HPLC-ESI-MS over a chiral stationary phase, the chip-based NIMS strategy takes less time, is more tolerant to buffer components, impurities and other potential contaminants, needs less reagents, and involves an easier sample preparation.

(3) Chapter 7 demonstrates that the NIMS spectrum of peptide (Dalargin) using  $BisF_{17}$  as initiator can be obtained by irradiating pSi with the 532 nm output of a frequency-doubled Nd-YAG laser. Compared to visible-MALDI MS, visible-NIMS yields mass spectra with higher S/N ratios and is a more sensitive analysis technique with the LOD of  $(31+7)$  fmol. The results suggest that visible-NIMS can be carried out reliably

using robust and increasingly inexpensive lasers such as the frequency-doubled output of a Nd-YAG laser at 532 nm.

It was also demonstrated that good NIMS mass spectra could be obtained using microstructured  $\text{WO}_3$  and porous  $\text{TiO}_2$  substrates although the results were not as good as those obtained using pSi. However, metallic materials may be able to compensate for the known mechanical and chemical fragility of pSi.

(4) Chapter 8 summarizes some recent advances in our understanding of the desorption/ionization mechanism of MALDI, DIOS and NIMS. Models have been proposed to explain both the desorption process, and a two-step ionization mode where primary ions are formed during or shortly after the laser pulse which then undergo secondary gas-phase reactions in the expanding plume of desorbed material. Some key parameters influencing the desorption and ionization processes are described including the effect of the laser wavelength, the role of the matrix/substrate in absorbing the incident laser energy, the dependence of desorption/ionization on laser fluence, and sample preparation protocols.

In Chapter 9, the SALDI mechanism was investigated for several substrates by measuring the ion signal,  $I$ , as a function of laser fluence,  $F$ . Plots of  $\ln(I)$  versus  $1/(T_0 + \eta F)$  were constructed for pSi,  $\text{WO}_3$  and  $\text{TiO}_2$  for the case when the incident laser focus was located at the surface of substrate, and when the laser focus was located  $d = 0.4$  mm above the substrate surface. The plots support the premise that desorption is driven by a thermal process. Desorption activation energies were derived from the plots.

The slopes derived from ln-ln plots of the protonated ion signals assuming an  $I \sim F^n$  dependence were  $\geq 4$  when the laser focus was placed at the surface of substrate,

which also supports a thermal desorption mechanism. However the surprising observation of radical cations when laser focus was located above the surface ( $d = 0.4$  mm) suggests a new ionization mechanism is operative which in this work is called Surface Assisted Multiphoton Ionization (SAMPI). The SAMPI mechanism which appears to be generic for all the porous SALDI substrates studied in this thesis and may prove to be useful for delivering biomolecules into the gas-phase for spectroscopy.

## 10.2: Future work

Two future directions should be considered. The versatility of NIMS can be enhanced by developing new fluoruous affinity tags which are highly selective for specific chemical functionalities. For example, hydrazine-containing fluoruous affinity tags can be used to separate and enrich glycopeptides or carbohydrates in biofluids, which serve as biomarkers for a variety of important biological functions, including cell communication, immune response, tumor metastasis, and so on [283].

The Lipson research group has expertise in the generation and use of coherent VUV light at 118.2 nm (the third harmonic obtained by tripling the 355 nm output of a Nd:YAG laser in Xe gas) extensively to soft-ionize a variety of volatile species such as xanthate ester mixtures [284] and a selection of organic compounds with different functional groups [285, 286]. In almost every case, the resultant soft ionization of a neutral species results in parent ion formation with minimal fragmentation. Recently, attempts were made in the Lipson lab to combine the high sensitivity of VUV laser single photon ionization (SPI) with of MALDI and DIOS, and some satisfactory results for gas-phase molecules were obtained. One could expect that combining laser SPI with the excellent desorption capabilities of SAMPI could significantly enhance the efficiency of

radical cation formation for non-volatile species by directly ionizing the expanding plume with a second laser after an appropriate time delay.

A similar two-laser pump probe experiment using tunable UV or VUV laser sources could also open up a powerful means of recording high resolution molecular spectra of non-volatile biomolecules. If these species could themselves be ionized by resonance ionization methods, the sensitivity of analyte detection should be significantly improved. The one drawback would be that the desorbed molecules from SALDI substrates may be hot leading to more congested spectra than one would anticipate using supersonic jets. However, the routes to gas-phase biomolecules are limited and so the SALDI methods described in this thesis would represent a significant advance.

**REFERENCES**

1. Karas, M. and Hillenkamp, F., Laser desorption ionization of proteins with molecular masses exceeding 10000 daltons. (1988). *ANAL CHEM*, **60**, 2299-2301.
2. Tanaka, K., Waki, H., Ido, Y., Akita, S., Yoshida, Y. and Yohida, T., Protein and polymer analyses up to m/z 100,000 by laser ionization time-of-flight mass spectrometry. (1988). *RAPID COMMUN MASS SP*, **2**, 151-153.
3. Dreisewerd, K., The desorption process in MALDI. (2003). *CHEM REV*, **103**, 395-425.
4. Harvey, D., Analysis of carbohydrates and glycoconjugates by matrix-assisted laser desorption/ionization mass spectrometry: An update covering the period 2003-2004. (2008). *MASS SPECTROM REV*, **27**, 125-201..
5. Strupat, K., Karas, M. and Hillenkamp, F., 2,5-Dihydroxybenzoic acid: a new matrix for laser desorption—ionization mass spectrometry. (1991). *INT J MASS SPECTROM*, **12**, 89-102.
6. Weickhardt, C., Moritz, F. and Grottemeyer, J., Time-of-flight mass spectrometry: State-of-the-art in chemical analysis and molecular science. (1996). *MASS SPECTROM REV*, **15**, 139-162.
7. Knochenmuss, R., Stortelder, A., Breuker, K. and Zenobi, R., Secondary ion-molecule reactions in matrix-assisted laser desorption/ionization. (2000). *J MASS SPECTROM*, **35**, 1237-1245.
8. Knochenmuss, R. and Zenobi, R., MALDI ionization: The role of in-plume processes. (2003). *CHEM REV*, **103**, 441-452.
9. Wei, J., Buriak, J. and Siuzdak, G., Desorption-ionization mass spectrometry on porous silicon. (1999). *NATURE*, **399**, 243-246.
10. Lin, Y. and Chen, Y., Laser desorption/ionization time-of-flight mass spectrometry on sol-gel-derived 2,5-dihydroxybenzoic acid film. (2002). *ANAL CHEM*, **74**, 5793-5798.
11. Ren, S. and Guo, Y., Oxidized carbon nanotubes as matrix for matrix-assisted laser desorption/ionization time-of-flight mass spectrometric analysis of biomolecules. (2005). *RAPID COMMUN MASS SP*, **19**, 255-260.
12. Cha, S. and Yeung, E., Colloidal graphite-assisted laser desorption/ionization mass spectrometry and MSn of small molecules. 1. Imaging of cerebrosides directly from rat brain tissue. (2007). *ANAL CHEM*, **79**, 2373-2385.

13. Su, C. and Tseng, W., Gold nanoparticles as assisted matrix for determining neutral small carbohydrates through laser desorption/ionization time-of-flight mass spectrometry. (2007). *ANAL CHEM*, **79**, 1626-1633.
14. Thomas, J., Shen, Z., Blackledge, R., and Siuzdak, G., Desorption-ionization on silicon mass spectrometry: an application in forensics. (2001). *ANAL CHIM ACTA*, **442**, 183-190.
15. Shen, Z., Thomas, J., Averbuj, C., Broo, K., Engelhard, M., Crowell, J., Finn, M. and Siuzdak, G., Porous silicon as a versatile platform for laser desorption/ionization mass spectrometry. (2001). *ANAL CHEM*, **73**, 612-619.
16. Laiko, V., Taranenko, N., Berkout, V., Musselman, B. and Doroshenko, V., Atmospheric pressure laser desorption/ionization on porous silicon. (2002). *RAPID COMMUN MASS SP*, **16**, 1737-1742.
17. Go, E., Apon, J., Luo, G., Saghatelian, A., Daniels, R., Sahi, V., Dubrow, R., Cravatt, B., Vertes, A. and Siuzdak, G., Desorption/ionization on silicon nanowires. (2005). *ANAL CHEM*, **77**, 1641-1646.
18. Li, J., Lu, C., Hu, XK., Yang, XJ., Loboda, AV. and Lipson, RH., Nanostructured porous silicon by laser assisted electrochemical etching. (2009). *INT J MASS SPECTROM*, **285**, 137-142.
19. Tuomikoski, S., Huikko, K., Grigoras, K., Ostman, P., Kostianen, R., Baumann, M., Abian, J., Kotiaho, T. and Franssila, S., Preparation of porous n-type silicon sample plates for desorption/ionization on silicon mass spectrometry (DIOS-MS). (2002). *LAB CHIP*, **2**, 247-253.
20. Pedraza, A., Fowlkes, J. and Lowndes, D., Silicon microcolumn arrays grown by nanosecond pulsed-excimer laser irradiation. (1999). *APPL PHYS LETT*, **74**, 2322-2324.
21. Cuiffi, J., Hayes, D., Fonash, S., Brown, K. and Jones, A., Desorption-ionization mass spectrometry using deposited nanostructured silicon films. (2001). *ANAL CHEM*, **73**, 1292-1295.
22. Choi, D., Yu, H., Jang, S. and Yang, S., Colloidal lithographic nanopatterning via reactive ion etching. (2004). *J AM CHEM SOC*, **126**, 7019-7025.
23. Barla, K., Bomchil, G., Herino, R., Pfister, J. and Baruchel, J., X-ray topographic characterization of porous silicon layers. (1984). *J CRYST GROWTH*, **68**, 721-726.
24. Finkel, N., Prevo, B., Velez, O. and He, L., Ordered silicon nanocavity arrays in surface-assisted desorption/ionization mass spectrometry. (2005). *ANAL CHEM*, **77**, 1088-1095.

25. Kruse, R., Li, X., Bohn, P. and Sweedler, J., Experimental factors controlling analyte ion generation in laser desorption/ionization mass spectrometry on porous silicon. (2001). *ANAL CHEM*, **73**, 3639-3645.
26. Thomas, J., Shen, Z., Crowell, J., Finn, M. and Siuzdak, G., Desorption/ionization on silicon (DIOS): A diverse mass spectrometry platform for protein characterization. (2001). *P NATL ACAD SCI USA*, **98**, 4932-4937.
27. Shen, Z., Yao, S., Crowell, J., Siuzdak, G. and Finn, M., DIOS-MSEED: A chip-based method for measurement of enantiomeric excess by kinetic resolution/mass spectrometry. (2001). *ISRAEL J CHEM*, **4**, 313-316.
28. Finn, M., Emerging methods for the rapid determination of enantiomeric excess. (2002). *CHIRALITY*, **7**, 534-540.
29. Kruse, R., Rubakhin, S., Romanova, E., Bohn, P. and Sweedler, J., Direct assay of *Aplysia* tissues and cells with laser desorption/ionization mass spectrometry on porous silicon. (2001). *J MASS SPECTROM*, **36**, 1317-1322.
30. Northen, TR., Yanes, O., Northen, MT., Marrinucci, D., Uritboonthai, W., Apon, J., Golledge, SL., Nordstrom, A. and Siuzdak, G., Clathrate nanostructures for mass spectrometry. (2007). *NATURE*, **449**, 1033-U3.
31. Woo, HK., Northen, TR., Yanes, O. and Siuzdak, G., Nanostructure-initiator mass spectrometry: a protocol for preparing and applying NIMS surfaces for high-sensitivity mass analysis. (2008). *NAT PROTOC*, **3**, 1341-1349.
32. Greving, MP., Patti, GJ. and Siuzdak, G., Nanostructure-initiator mass spectrometry metabolite analysis and imaging. (2011). *ANAL CHEM*, **83**, 2-7.
33. Patti, GJ., Woo, HK., Yanes, O., Shriver, L., Thomas, D., Uritboonthai, W., Apon, JV., Steenwyk, R., Manchester, M. and Siuzdak, G., Detection of carbohydrates and steroids by cation-enhanced nanostructure-initiator mass spectrometry (NIMS) for biofluid analysis and tissue imaging. (2010). *ANAL CHEM*, **82**, 121-128.
34. Northen, TR., Yanes, O., Northen, MT., Marrinucci, D., Uritboonthai, W., Apon, J., Golledge, SL., Nordstrom, A. and Siuzdak, G., Clathrate nanostructures for mass spectrometry. (2007). *NATURE*, **449**, 1033-U3 (supplementary).
35. Amantonico, A., Flamigni, L., Glaus, R. and Zenobi, R., Negative mode nanostructure-initiator mass spectrometry for detection of phosphorylated metabolites. (2009). *METABOLOMICS*, **5**, 346-353.
36. Woo, H., Northen, TR., Yanes, O. and Siuzdak, G., Nanostructure-initiator mass spectrometry: a protocol for preparing and applying NIMS surfaces for high-sensitivity mass analysis. (2008). *NAT PROTOC*, **3**, 1341-1349.

37. Yanes, O., Woo, HK., Northen, TR., Oppenheimer, SR., Shriver, L., Apon, J., Estrada, MN., Potchoiba, MJ., Steenwyk, R., Manchester, M. and Siuzdak, G., Nanostructure Initiator Mass Spectrometry: Tissue Imaging and Direct Biofluid Analysis. (2009). *ANAL CHEM*, **81**, 2969-2975.
38. Patti, GJ., Shriver, LP., Wassif, CA., Woo, HK., Uritboonthai, W., Apon, J., Manchester, M., Porter, FD. and Siuzdak, G., Nanostructure-initiator mass spectrometry (NIMS) imaging of brain cholesterol metabolites in Smith-Lemli-Opitz syndrome. (2010). *NEUROSCIENCE*, **170**, 858-864.
39. Liotta, L., Ferrari, M. and Petricoin, E., Written in blood. (2003). *NATURE*, **425**, 905-905.
40. Vinayavekhin, N., Homan, E. and Saghatelian, A., Exploring Disease through Metabolomics. (2010). *ACS CHEM BIOL*, **5**, 91-103.
41. Halket, JM., Waterman, D., Przyborowska, AM., Patel, RKP., Fraser, PD. and Bramley, PM., Chemical derivatization and mass spectral libraries in metabolic profiling by GC/MS and LC/MS/MS. (2005). *J EXP BOT*, **56**, 219-243.
42. Marko-Varga, G., Lindberg, H., Lofdahl, CG., Jonsson, P., Hansson, L., Dahlback, M., Lindquist, E., Johansson, L., Foster, M. and Fehniger, TE., Discovery of biomarker candidates within disease by protein profiling: Principles and concepts. (2005). *J PROTEOME RES*, **4**, 1200-1212.
43. Kauppila, TJ., Talaty, N., Jackson, AU., Kotiaho, T., Kostianen, R. and Cooks, RG., Carbohydrate and steroid analysis by desorption electrospray ionization mass spectrometry. (2008). *CHEM COMMUN*, **23**, 2674-2676.
44. Chiu, T., Chang, LC., Chiang, CK. and Chang, HT., Determining estrogens using surface-assisted laser desorption/ionization mass spectrometry with silver nanoparticles as the matrix. (2008). *J AM SOC MASS SPECTR*, **19**, 1343-1346.
45. Hanash, S., Disease proteomics. (2003). *NATURE*, **422**, 226-232.
46. Merchant, TE., Kasimos, JN., Vroom, T., de Bree, E., Iwata, JL., de Graaf, PW. and Glonek, T., Malignant breast tumor phospholipid profiles using P-31 magnetic resonance. (2002). *CANCER LETT*, **176**, 159-167.
47. Ran, S., Downes, A. and Thorpe, P., Increased exposure of anionic phospholipids on the surface of tumor blood vessels. (2002). *CANCER RES*, **62**, 6132-6140.
48. Chaurand, P., Norris, JL., Cornett, DS., Mobley, JA. and Caprioli, RM., New developments in profiling and imaging of proteins from tissue sections by MALDI mass spectrometry. (2006). *J PROTEOME RES*, **5**, 2889-2900.
49. Hutchens, T. and Yip, T., New desorption strategies for the mass-spectrometric analysis of macromolecules. (1993). *RAPID COMMUN MASS SP*, **7**, 576-580.



50. Gurard-Levin, Z.A. and Mrksich, M., Combining self-assembled monolayers and mass spectrometry for applications in biochips. (2008). *ANNU REV ANAL CHEM*, **1**, 767-800.
51. MacBeath, G., Koehler, AN. and Schreiber, SL., Printing small molecules as microarrays and detecting protein-ligand interactions en masse. (1999). *J AM CHEM SOC*, **121**, 7967-7968.
52. Kuruvilla, FG., Shamji, AF., Sternson, SM., Hergenrother, PJ. and Schreiber, SL., Dissecting glucose signalling with diversity-oriented synthesis and small-molecule microarrays. (2002). *NATURE*, **416**, 653-657.
53. Vegas, AJ., Fuller, JH. and Koehler, AN., Small-molecule microarrays as tools in ligand discovery. (2008). *CHEM SOC REV*, **37**, 1385-1394.
54. Urbina, HD., Debaene, F., Jost, B., Bole-Feysot, C., Mason, DE., Kuzmic, P., Harris, JL. and Winssinger, N., Self-assembled small-molecule microarrays for protease screening and profiling. (2006). *CHEMBIOCHEM*, **7**, 1790-1797.
55. Vegas, AJ., Bradner, JE., Tang, W., McPherson, OM., Greenberg, EF., Koehler, AN. and Schreiber, SL., Fluorous-based small-molecule microarrays for the discovery of histone deacetylase inhibitors. (2007). *ANGEW CHEM INT EDIT*, **4**, 7960-7964.
56. Winssinger, N., Pianowski, Z. and Debaene, F., Probing biology with small molecule microarrays (SMM). (2007). *TOP CURR CHEM*, **278**, 311-342.
57. Hergenrother, P., Depew, K. and Schreiber, S., Small-molecule microarrays: Covalent attachment and screening of alcohol-containing small molecules on glass slides. (2000). *J AM CHEM SOC*, **122**, 7849-7850.
58. Lee, M. and Shin, I., Fabrication of chemical microarrays by efficient immobilization of hydrazide-linked substances on epoxide-coated glass surfaces. (2005). *ANGEW CHEM INT EDIT*, **44**, 2881-2884.
59. Barnes-Seeman, D., Park, SB., Koehler, AN. and Schreiber, SL., Expanding the functional group compatibility of small-molecule microarrays: Discovery of novel calmodulin ligands. (2003). *ANGEW CHEM INT EDIT*, **42**, 2376-2379.
60. Bryan, MC., Plettenburg, O., Sears, P., Rabuka, D., Wacowich-Sgarbi, S. and Wong, CH., Saccharide display on microtiter plates. (2002). *CHEM BIOL*, **9**, 713-720.
61. Ko, KS., Jaipuri, FA. and Pohl, NL., Fluorous-based carbohydrate microarrays. (2005). *J AM CHEM SOC*, **127**, 13162-13163.
62. Horváth, IT. and Rábai, J., Facile catalyst separation without water: fluoruous biphasic hydroformylation of olefins. (1994). *SCIENCE*, **266**, 72-75.

63. Studer, A., Hadida, S., Ferritto, R., Kim, SY., Jeger, P., Wipf, P., Curran, DP., Fluorous synthesis: A fluorous-phase strategy for improving separation efficiency in organic synthesis. (1997). *SCIENCE*, **275**, 823-826.
64. Zhang, W. and Curran, DP., Synthetic applications of fluorous solid-phase extraction (F-SPE). (2006). *TETRAHEDRON*, **62**, 11837-11865.
65. Curran, DP., Chemistry. Fluorous tags unstick messy chemical biology problems. (2008). *SCIENCE*, **321**, 1645-1646.
66. Yoder, NC., Yuksel, D., Dafik, L. and Kumar, K., Bioorthogonal noncovalent chemistry: fluorous phases in chemical biology. (2006). *CURR OPIN CHEM BIOL*, **10**, 576-583.
67. Zhang, W., Fluorous synthesis of heterocyclic systems. (2004). *CHEM REV*, **104**, 2531-2556.
68. Zhang, W., Fluorous Linker-Facilitated Chemical Synthesis. (2009). *CHEM REV*, **109**, 749-795.
69. Kusnezow, W. and Hoheisel, JD., Solid supports for microarray immunoassays. (2003). *J MOL RECOGNIT*, **16**, 165-176.
70. Brittain, SM., Ficarro, SB., Brock, A. and Peters, EC., Enrichment and analysis of peptide subsets using fluorous affinity tags and mass spectrometry. (2005). *NAT BIOTECHNOL*, **23**, 463-468.
71. Northen, TR., Lee, JC., Hoang, L., Raymond, J., Hwang, DR., Yannone, SM., Wong, CH. and Siuzdak, G., A nanostructure-initiator mass spectrometry-based enzyme activity assay. (2008). *P NATL ACAD SCI USA*, **10**, 3678-3683.
72. Ying, WT., Perlman, DH., Li, L., Théberge, R., Costello, CE. and McComb, ME., Highly efficient and selective enrichment of peptide subsets combining fluorous chemistry with reversed-phase chromatography. (2009). *RAPID COMMUN MASS SP*, **23**, 4019-4030.
73. Jaipuri, FA., Collet, BYM. and Pohl, NL., Synthesis and quantitative evaluation of Glycero-D-manno-heptose binding to concanavalin a by fluorous-tag assistance. (2008). *ANGEW CHEM INT EDIT*, **47**, 1707-1710.
74. Lacey, D., Experiments in VUV and visible wavelength MALDI using a triple quadrupole mass spectrometer. (2006), London, Ont.: Faculty of Graduate Studies, University of Western Ontario.
75. Yang, X., Hu, XK., Loboda, AV. and Lipson, RH., Microstructured Tungsten Oxide: A Generic Desorption/Ionization Substrate for Mass Spectrometry. (2010). *ADV MATER*, **22**, 4520-4523.

76. Janshoff, A., Dancil, K., Steinem, C., Greiner, D., Lin, V., Gurtner, C., Motesharei, K., Sailor, M. and Ghadiri, M., Macroporous p-type silicon Fabry-Perot layers: fabrication, characterization, and applications in biosensing. (1998). *J AM CHEM SOC*, **120**, 12108-12116.
77. Collins, R., Tischler, M. and Stathis, J., Photoinduced hydrogen loss from porous silicon. (1992). *APPL PHYS LETT*, **61**, 1649-1651.
78. Cullis, A., Canham, L. and Calcott, P., The structural and luminescence properties of porous silicon. (1997). *J APPL PHYS*, **82**, 909-965.
79. Pencheva, N., Pospisek, J., Hauzerova, L., Barth, T. and Milanov, P., Activity profiles of dalargin and its analogues in mu-,delta- and kappa-opioid receptor selective bioassays. (1999). *BRIT J PHARMACOL*, **128**, 569-576.
80. Smith, R. and Collins, S., Porous silicon formation mechanisms. (1992). *J APPL PHYS*, **71**, R1-R22..
81. Li, J., The preparation of porous microcolumn arrays of silicon, and post-ionization of neutral particles from DIOS-MS, in Faculty of Graduate Studies. (2008). University of Western Ontario.
82. Jacobson, L. and Estler, R., Investigation of optimum surface modification in porous silicon for negative ion DIOS (Desorption Ionization on Silicon) mass spectrometry. (2003). *ABSTR PAP AM CHEM S*, **225**, U437-U437.
83. Northen, TR., Lee, JC., Hoang, L., Raymond, J., Hwang, DR., Yannone, SM., Wong, CH. and Siuzdak, G., A nanostructure-initiator mass spectrometry-based enzyme activity assay. (2008). *P NATL ACAD SCI USA*, **10**, 3678-3683.
84. Tanaka, K., Waki, H., Ido, Y., Akita, S., Yoshida, Y. and Yohida, T., Protein and polymer analyses up to m/z 100,000 by laser ionization time-of-flight mass spectrometry. (1988). *RAPID COMMUN MASS SP*, **2**, 151-153.
85. Stahl, B., Linos, A., Karas, M., Hillenkamp, F. and Steup, M., Analysis of fructans from higher plants by matrix-assisted laser desorption/ionization mass spectrometry. (1997). *ANAL BIOCHEM*, **246**, 195-204.
86. Tang, K., Taranenko, N., Allman, S., Chang, L. and Chen, C., Detection of 500-nucleotide DNA by laser-desorption mass-spectrometry. (1994). *RAPID COMMUN MASS SP*, **8**, 727-730.

87. McCombie, G. and Knochennuss, R., Small-molecule MALDI using the matrix suppression effect to reduce or eliminate matrix background interferences. (2004). *ANAL CHEM*, **76**, 4990-4997.
88. Longley, D.B., D.P. Harkin, and P.G. Johnston, 5-fluorouracil: mechanisms of action and clinical strategies. (2003). *NAT REV CANCER*, **3**, 330-338.
89. Furner, R.L., Brown, G.B. and Scott, J.W., A method for differentiation and analysis of quinine and quinidine by gas chromatography/mass spectrometry.(1981). *J ANAL TOXICOL*, **5**, 275-278.
90. Abraham, W.M., Scuri, M. and Farmer, S.G., Peptide and non-peptide bradykinin receptor antagonists: Role in allergic airway disease. (2006). *EUR J PHARMACOL*, **533**, 215-221.
91. Hoaglund-Hyzer, C., Counterman, A. and Clemmer, D., Anhydrous protein ions. (1999). **99**, *CHEM REV*, 3037-3079.
92. Patti, G.J., Woo, H. K., Yanes, O., Shriver, L., Thomas, D., Uritboonthai, W., Apon, J. V., Steenwyk, R., Manchester, M. and Siuzdak, G., Detection of carbohydrates and steroids by cation-enhanced nanostructure-initiator mass spectrometry (NIMS) for biofluid analysis and tissue imaging. (2010). *ANAL CHEM*, **82**, 121-128.
93. Arthur, K.E., Wolff, J.C. and Carrier, D.J., Analysis of betamethasone, dexamethasone and related compounds by liquid chromatography/electrospray mass spectrometry. (2004). *RAPID COMMUN MASS SP*, **18**, 678-684.
94. Shields, W., Craig, D. and Dibeler, V., Absolute isotopic abundance ratio and the atomic weight of silver. (1960). *J AM CHEM SOC*, **82**, 5033-5036.
95. Anderson, N.L. and Anderson, N.G., The human plasma proteome: history, character, and diagnostic prospects. ( 2002). *MOL CELL PROTEOMICS*,**1**, 845-867.
96. Zhang, H., Li, XJ., Martin, DB. and Aebersold, R., Identification and quantification of N-linked glycoproteins using hydrazide chemistry, stable isotope labeling and mass spectrometry. (2003). *NAT BIOTECHNOL*, **21**, 660-666.
97. Liu, T., Qian, WJ., Mottaz, HM., Gritsenko, MA., Norbeck, AD., Moore, RJ., Purvine, SO., Camp, DG. and Smith, RD., Evaluation of multiprotein immunoaffinity subtraction for plasma proteomics and candidate biomarker discovery using mass spectrometry. (2006). *MOL CELL PROTEOMICS*, **5**, 2167-2174.

98. Mirzaei, H., Baena, B., Barbas, C. and Regnier, F., Identification of oxidized proteins in rat plasma using avidin chromatography and tandem mass spectrometry. (2008). *PROTEOMICS*, **8**, 1516-1527.
99. Liu, T., Qian, WJ., Strittmatter, EF., Camp, DG., Anderson, GA., Thrall, BD. and Smith, R. D., High-throughput comparative proteome analysis using a quantitative cysteinyl-peptide enrichment technology. (2004). *ANAL CHEM*, **76**, 5345-5353.
100. Plavina, T., Wakshull, E., Hancock, WS. and Hincapie, M., Combination of abundant protein depletion and multi-lectin affinity chromatography (M-LAC) for plasma protein biomarker discovery. (2007). *J PROTEOME RES*, **6**, 662-671.
101. Posewitz, MC. and Tempst, P., Immobilized gallium(III) affinity chromatography of phosphopeptides.(1999). *ANAL CHEM*, **71**, 2883-2892.
102. Steen, H. and Mann, M., A new derivatization strategy for the analysis of phosphopeptides by precursor ion scanning in positive ion mode. (2002). *J AM SOC MASS SPECTR*, **13**, 996-1003.
103. Oda, Y., Nagasu, T. and Chait, BT., Enrichment analysis of phosphorylated proteins as a tool for probing the phosphoproteome. (2001). *NAT BIOTECHNOL*, **19**, 379-382.
104. Curran, D.P., Chemistry - Fluorous tags unstick messy chemical biology problems. (2008). *SCIENCE*, **321**, 1645-1646.
105. Zhang, W., Fluorous synthesis of heterocyclic systems. ( 2004). *CHEM REV*, **104**, 2531-2556.
106. Brittain, S.M., Ficarro, SB., Brock, A. and Peters, EC., Enrichment and analysis of peptide subsets using fluorous affinity tags and mass spectrometry. (2005). *NAT BIOTECHNOL*, **23**, 463-468.
107. Go, EP., Uritboonthai, W., Apon, JV., Trauger, SA., Nordstrom, A., O'Maille, G., Brittain, SM., Peters, EC. and Siuzdak, G., Selective metabolite and peptide capture/mass detection using fluorous affinity tags. (2007). *J PROTEOME RES*, **6**, 1492-1499.
108. Su, J. and Mrksich, M., Using mass spectrometry to characterize self-assembled monolayers presenting peptides, proteins, and carbohydrates. (2002). *ANGEW CHEM INT EDIT*, **41**, 4715-4718.
109. Duan, J., Wang, H. and Cheng, Q., On-plate desalting and SALDI-MS analysis of peptides with hydrophobic silicate nanofilms on a gold substrate. (2010). *ANAL CHEM*, **82**, 9211-9220.

110. Kwon, Y. and Mrksich, M., Dependence of the rate of an interfacial Diels-Alder reaction on the steric environment of the immobilized dienophile: an example of enthalpy-entropy compensation. (2002). *J AM CHEM SOC*, **124**, 806-812.
111. Hunter, T., Signaling--2000 and beyond. (2000). *CELL*, **1**, 113-127.
112. Cutillas, PR., Khwaja, A., Graupera, M., Pearce, W., Gharbi, S., Waterfield, M. and Vanhaesebroeck, B., Ultrasensitive and absolute quantification of the phosphoinositide 3-kinase/Akt signal transduction pathway by mass spectrometry. (2006). *P NATL ACAD SCI USA*, **24**, 8959-8964.
113. Drews, J., Drug discovery: A historical perspective. (2000). *SCIENCE*, **287**, 1960-1964.
114. Zhang, YHP., Himmel, ME. and Mielenz, JR., Outlook for cellulase improvement: screening and selection strategies. (2006). *BIOTECHNOL ADV*, **5**, 452-481.
115. Liesener, A. and Karst, U., Monitoring enzymatic conversions by mass spectrometry: a critical review. (2005). *ANAL BIOANAL CHEM*, **7**, 1451-1464.
116. Tholey, A. and Heinzle, E., Methods for biocatalyst screening. (2002). *ADV BIOCHEM ENG BIOT*, **74**, 1-19.
117. Morís-Varas, F., Shah, A., Aikens, J., Nadkarni, NP., Rozzell, JD. and Demirjian, DC., Visualization of enzyme-catalyzed reactions using pH indicators: rapid screening of hydrolase libraries and estimation of the enantioselectivity. (1999). *BIOORGAN MED CHEM*, **10**, 2183-2188.
118. Goddard, JP. and Reymond, JL., Enzyme assays for high-throughput screening. (2004). *CURR OPIN BIOTECH*, **4**, 314-322.
119. Sun, H., Chattopadhyaya, S., Wang, J. and Yao, SQ., Recent developments in microarray-based enzyme assays: from functional annotation to substrate/inhibitor fingerprinting. (2006). *ANAL BIOANAL CHEM*, **3**, 416-426.
120. Houseman, BT. and Mrksich, M., Carbohydrate arrays for the evaluation of protein binding and enzymatic modification.(2002). *CHEM BIOL*, **4**, 443-454.
121. Kruger, N.J., Errors and artifacts in coupled spectrophotometric assays of enzyme activity. (1995). *PHYTOCHEMISTRY*, **5**, 1065-1071.
122. Houston, CT., Taylor, WP., Widlanski, TS. and Reilly, JP., Investigation of enzyme kinetics using quench-flow techniques with MALDI-TOF mass spectrometry. (2000). *ANAL CHEM*, **14**, 3311-3319.

123. Bungert, D., Heinzle, E. and Tholey, A., Quantitative matrix-assisted laser desorption/ionization mass spectrometry for the determination of enzyme activities. (2004). *ANAL CHEM*, **2**, 167-175.
124. Greis, K., Mass spectrometry for enzyme assays and inhibitor screening: An emerging application in pharmaceutical research. (2007). *MASS SPECTROM REV*, **3**, 324-339.
125. Walker, RW., Vandenne, WJ., Ahn, HS. and Mandel, LR., Identification of N,N-dimethyltryptamine product of an in-vitro enzymic methylation. (1972). *ANAL BIOCHEM*, **47**, 228-234.
126. Bettencourt, A., Lhoest, G., Roberfroid, M. and Mercier, M., Gas-chromatographic and mass fragmentographic assays of carcinogenic polycyclic hydrocarbon epoxide hydratase activity. (1977). *J CHROMATOGR A*, **2**, 323-330.
127. Blakley, C., Carmody, J. and Vestal, M., A new soft ionization technique for mass-spectrometry of complex-molecules. (1980). *J AM CHEM SOC*, **18**, 5931-5933.
128. Blakley, C. and Vestal, M., Thermospray interface for liquid chromatography mass spectrometry. (1983). *ANAL CHEM*, **55**, 750-754.
129. Newton, R., Bayliss, MA., Khan, JA., Bastani, A., Wilkins, ACR., Games, DE., Walton, TJ., Brenton, AG. And Harris, FM., Kinetic analysis of cyclic CMP-specific and multifunctional phosphodiesterases by quantitative positive-ion fast-atom bombardment mass spectrometry. (1999). *RAPID COMMUN MASS SP*, **7**, 574-584.
130. Walton, T., Bayliss, MA., Pereira, ML., Games, DE., Genieser, HG., Brenton, AG., Harris, FM. And Newton, RP., Fast-atom bombardment tandem mass spectrometry of cyclic nucleotide analogues used as site-selective activators of cyclic nucleotide-dependent protein kinases. (1998). *RAPID COMMUN MASS SP*, **8**, 449-455.
131. Kim, Y., Oh, E., Oh, YH., Moon, DW., Lee, TG. And Kim, HS., Protein kinase assay on peptide-conjugated gold nanoparticles by using secondary-ion mass spectrometric imaging. (2007). *ANGEW CHEM INT EDIT*, **36**, 6816-6819.
132. de Boer, A., Lingeman, H., Niessen, WMA. And Irth, H., Mass spectrometry-based biochemical assays for enzymeinhibitor screening. (2007). *TRAC-TREND ANAL CHEM*, **9**, 867-883.
133. Liesener, A. and Karst, U., Assessing protease activity pattern by means of multiple substrate ESI-MS assays. (2005). *ANALYST*, **6**, 850-854.
134. Liesener, A., Perchuc, AM., Schöni, R., Wilmer, M. and Karst, U., Screening for proteolytic activities in snake venom by means of a multiplexing electrospray

- ionization mass spectrometry assay scheme. (2005). *RAPID COMMUN MASS SP*, **20**, 2923-2928.
135. Tang, K., Allman, S.L., Jones, R.B. and Chen, C.H., Quantitative-analysis of biopolymers by matrix-assisted laser-desorption. (1993). *ANAL CHEM*, **15**, 2164-2166.
  136. Tholey, A., Zabet-Moghaddam, M. and Heinzle, E., Quantification of peptides for the monitoring of protease-catalyzed reactions by matrix-assisted laser desorption/ionization mass spectrometry using ionic liquid matrixes. (2006). *ANAL CHEM*, **1**, 291-297.
  137. Pei, J., Li, Q. and Kennedy, R., Rapid and Label-Free Screening of Enzyme Inhibitors Using Segmented Flow Electrospray Ionization Mass Spectrometry. (2010). *J AM SOC MASS SPECTR*, **7**, 1107-1113.
  138. Nichols, K.P., Azoz, S. and Gardeniers, H.J., Enzyme kinetics by directly imaging a porous silicon microfluidic reactor using desorption/ionization on silicon mass spectrometry. (2008). *ANAL CHEM*, **21**, 8314-8319.
  139. Houseman, B.T., Huh, J.H., Kron, S.J. and Mrksich, M., Peptide chips for the quantitative evaluation of protein kinase activity. (2002). *NAT BIOTECHNOL*, **3**, 270-274.
  140. Reineke, U., Volkmer-Engert, R. and Schneider-Mergener, J. Applications of peptide arrays prepared by the SPOT-technology. (2001). *CURR OPIN BIOTECH*, **1**, 59-64.
  141. Falsey, J.R., Renil, M., Park, S., Li, S.J. and Lam, K.S., Peptide and small molecule microarray for high throughput cell adhesion and functional assays. (2001). *BIOCONJUGATE CHEM*, **3**, 346-353.
  142. Min, D.H., Su, J. and Mrksich, M., Profiling kinase activities by using a peptide chip and mass spectrometry. (2004). *ANGEW CHEM INT EDIT*, **44**, 5973-5977.
  143. Min, D.H., Tang, W.J. and Mrksich, M., Chemical screening by mass spectrometry to identify inhibitors of anthrax lethal factor. (2004). *NAT BIOTECHNOL*, **6**, 717-723.
  144. Shen, Z., Go, E., Gamez, A., Apon, J., Fokin, V., Greig, M., Ventura, M., Crowell, J., Blixt, O., Paulson, J., Stevens, R., Finn, M. and Siuzdak, G., A mass spectrometry plate reader: Monitoring enzyme activity and inhibition with a desorption/ionization on silicon (DIOS) platform. (2004), *CHEMBIOCHEM*, **5**, 921-927.
  145. Himpel, S., Tegge, W., Frank, R., Leder, S., Joost, H.G. and Becker, W., Specificity determinants of substrate recognition by the protein kinase DYRK1A. (2000). *J BIOL CHEM*, **4**, 2431-2438.



146. Duan, Y. and Laursen, RA., Protease substrate specificity mapping using membrane-bound peptides. (1994). *ANAL BIOCHEM*, **2**, 431-438.
147. Gan, ZB., Marquardt, RR. and Xiao, H., Protease and protease inhibitor assays using biotinylated casein coated on a solid phase. (1999). *ANAL BIOCHEM*, **1**, 151-156.
148. Kim, C., Cheng, CY., Saldanha, SA. and Taylor, SS., PKA-I holoenzyme structure reveals a mechanism for cAMP-dependent activation. (2007). *CELL*, **6**, 1032-1043.
149. Zhang, J., Adrián, FJ., Jahnke, W., Cowan-Jacob, SW., Li, AG., Jacob, RE., Sim, T., Powers, J., Dierks, C., Sun, F., Guo, GR., Ding, Q., Okram, B., Choi, Y., Wojciechowski, A., Deng, X., Liu, G., Fendrich, G., Strauss, A., Vajpai, N., Grzesiek, S, Tuntland, T., Liu, Y., Bursulaya, B., Azam, M., Manley, PW., Engen, JR., Daley, GQ., Warmuth, M., and Gray, NS., Targeting Bcr-Abl by combining allosteric with ATP-binding-site inhibitors. (2010). *NATURE*, **7280**, 501-506.
150. Greis, KD., Zhou, ST., Burt, TM., Carr, AN., Dolan, E., Easwaran, V., Evdokimov, A., Kawamoto, R., Roesgen, J. and Davis, GF., MALDI-TOF MS as a label-free approach to rapid inhibitor screening. (2006). *J AM SOC MASS SPECTR*, **6**, 815-822.
151. Ozbal, CC., LaMarr, WA., Linton, JR., Green, DF., Katz, A., Morrison, TB. and Brenan, CJ., High throughput screening via mass spectrometry: a case study using acetylcholinesterase. (2004). *ASSAY DRUG DEV TECHN*, **4**, 373-381.
152. Hodgson, RJ., Besanger, TR., Brook, MA., and Brennan, JD., Inhibitor screening using immobilized enzyme reactor chromatography/mass spectrometry. (2005). *ANAL CHEM*, **23**, 7512-7519.
153. Rathore, R., Corr, JJ., Lebre, DT., Seibel, WL. and Greis, KD., Extending matrix-assisted laser desorption/ionization triple quadrupole mass spectrometry enzyme screening assays to targets with small molecule substrates. (2009). *RAPID COMMUN MASS SP*, **20**, 3293-3300.
154. Rathore, R., Corr, J. Scott, G. Vollmerhaus, P. and Greis, KD., Development of an inhibitor screening platform via mass spectrometry. (2008). *J BIOMOL SCREEN*, **10**, 1007-1013.
155. Ruegg, UT. and Burgess, GM., Staurosporine, K-252 and UCN-01: potent but nonspecific inhibitors of protein kinases. (1989). *TRENDS BIOCHEM SCI*, **6**, 218-220.
156. Kerkela, R. Grazette, L., Yacobi, R., Iliescu, C., Patten, R., Beahm, C., Walters, B., Shevtsov, S., Pesant, S., Clubb, FJ., Rosenzweig, A., Salomon, RN., Van Etten, RA., Alroy, J., Durand, JB. and Force, T., Cardiotoxicity of the cancer therapeutic agent imatinib mesylate. (2006). *NAT MED*, **8**, 908-916.

157. Druker, BJ., Tamura, S., Buchdunger, E., Ohno, S., Segal, GM., Fanning, S., Zimmermann, J. and Lydon, NB., Effects of a selective inhibitor of the Abl tyrosine kinase on the growth of Bcr-Abl positive cells. (1996). *NAT MED*, **5**, 561-566.
158. Buchdunger, E., Zimmermann, J., Mett, H., Meyer, T., Müller, M., Druker, BJ. and Lydon, NB., Inhibition of the Abl protein-tyrosine kinase in vitro and in vivo by a 2-phenylaminopyrimidine derivative. (1996). *CANCER RES*, **1**, 100-104.
159. Brasher, BB. and Van Etten, RA., c-Abl has high intrinsic tyrosine kinase activity that is stimulated by mutation of the Src homology 3 domain and by autophosphorylation at two distinct regulatory tyrosines. (2000). *J BIOL CHEM*, **45**, 35631-35637.
160. Nic, M., Jirat, J. and Kosata, B., "Enantiomer excess", IUPAC Compendium of Chemical Terminology. (2006). The Gold Book, 2201
161. Gawley, R., Do the terms "% ee" and "% de" make sense as expressions of stereoisomer composition or stereoselectivity? (2006). *J ORG CHEM*, **6**, 2411-2416.
162. Porte, A., Reibenspies, J. and Burgess, K., Design and optimization of new phosphine oxazoline ligands via high-throughput catalyst screening. (1998). *J AM CHEM SOC*, **36**, 9180-9187.
163. Reetz, M., Combinatorial and evolution-based methods in the creation of enantioselective catalysts. (2001). *ANGEW CHEM INT EDIT*, **2**, 284-310.
164. Okamoto, Y. and Yashima, E., Polysaccharide derivatives for chromatographic separation of enantiomers. (1998). *ANGEW CHEM INT EDIT*, **8**, 1020-1043.
165. Fales, H. and Wright, G., Detection of chirality with chemical ionization mass-spectrometry-meso ions in gas-phase. (1977). *J AM CHEM SOC*, **7**, 2339-2340.
166. Tao, W. and Cooks, R., Parallel reactions for enantiomeric quantification of peptides by mass spectrometry. (2001). *ANGEW CHEM INT EDIT*, **4**, 757-760.
167. Guo, JH., Wu, JY., Siuzdak, G. and Finn, MG., Measurement of enantiomeric excess by kinetic resolution and mass spectrometry. (1999). *ANGEW CHEM INT EDIT*, **12**, 1755-1758.
168. Karas, M., Bachmann, D. and Hillenkamp, F., Influence of the wavelength in high-irradiance ultraviolet-laser desorption mass-spectrometry of organic-molecules. (1985). *ANAL CHEM*, **57**, 2935-2939.
169. Berkenkamp, S., Menzel, C., Karas, M. and Hillenkamp, F., Performance of infrared matrix-assisted laser desorption/ionization mass spectrometry with lasers

- emitting in the 3  $\mu$  m wavelength range. (1997). *RAPID COMMUN MASS SP*, **11**, 1399-1406.
170. Romano, L. and Levis, R., Nondestructive laser vaporization of high-molecular-weight, single-stranded-DNA. (1991). *J AM CHEM SOC*, **113**, 9665-9667.
171. Tang, K., Allman, SL., Jones, RB. and Chen, CH., Comparison of rhodamine dyes as matrices for matrix-assisted laser desorption ionization mass-spectrometry. (1992). *ORG MASS SPECTROM*, **27**, 1389-1392.
172. Yang, C., Visible wavelength MALDI study, in *Faculty of Graduate Studies*, 2009, University of Western Ontario: London, Ont.
173. Cornett, D., Duncan, M. and Amster, I., Liquid-mixtures for matrix-assisted laser-desorption. (1993). *ANAL CHEM*, **65**, 2608-2613.
174. Smith, C., Chang, S. and Yeung, E., Characterization of neutral red as a visible-wavelength MALDI matrix. (1995). *J MASS SPECTROM*, **30**, 1765-1767.
175. Chen, LC., Asakawa, D., Hori, H. and Hiraoka, K., Matrix-assisted laser desorption/ionization mass spectrometry using a visible laser. (2007). *RAPID COMMUN MASS SP*, **21**, 4129-4134.
176. Hu, X., Lacey, D., Li, J., Yang, C., Loboda, AV. and Lipson, RH., Visible wavelength MALDI using Coumarin laser dyes. (2008). *INT J MASS SPECTROM*, **278**, 69-74.
177. Yang, CY., Hu, XK., Loboda, AV. and Lipson, RH., A Useful Binary Matrix for Visible-MALDI of Low Molecular Weight Analytes. (2010). *J AM SOC MASS SPECTR*, **21**, 294-299.
178. Yang, CY., Hu, XK., Loboda, AV. and Lipson, RH., A fragmentation study of the Rhodamine 610 cation using visible-laser desorption ionization. (2010). *J MASS SPECTROM*, **45**, 909-914.
179. Chen, LC., Mori, K., Hori, H. and Hiraoka, K., Au-assisted visible laser MALDI. (2009). *INT J MASS SPECTROM*, **279**, 41-46.
180. Chen, LC., Ueda, T., Sagisaka, M., Hori, H. and Hiraoka, K., Visible laser desorption/ionization mass spectrometry using gold nanorods. (2007). *J PHYS CHEM C*, **111**, 2409-2415.
181. Kim, J., Paek, K. and Kang, W., Visible surface-assisted laser desorption/ionization mass spectrometry of small macromolecules deposited on the graphite plate. (2002). *B KOR CHEM SOC*, **23**, 315-319.

182. Xu, DS., Guo, GL., Gui, LL., Tang, YQ., Zhang, BR. and Qin, GG., Optical absorption and photoluminescence studies of free-standing porous silicon films with high porosities. (1999). *J PHYS CHEM B*, **103**, 5468-5471.
183. Xu, SY. Li, YF. Zou, HF. Qiu, JS. Guo, Z. and Guo, BC., Carbon nanotubes as assisted matrix for laser desorption/ionization time-of-flight mass spectrometry. (2003). *ANAL CHEM*, **75**, 6191-6195.
184. Shenar, N., Martinez, J. and Enjalbal, C., Laser desorption/ionization mass spectrometry on porous silica and alumina for peptide mass fingerprinting. (2008). *J AM SOC MASS SPECTR*, **19**, 632-644.
185. Hua, L., Chen, JR., Ge, L. and Tan, SN., Silver nanoparticles as matrix for laser desorption/ionization mass spectrometry of peptides. (2007). *J NANOPART RES*, **9**, 1133-1138.
186. Kawasaki, H., Yonezawa, T., Watanabe, T. and Arakawa, R., Platinum nanoflowers for surface-assisted laser desorption/ionization mass spectrometry of biomolecules. (2007). *J PHYS CHEM C*, **111**, 16278-16283.
187. Novikov, A., Caroff, M., Della-Negra, S., Lebeyec, Y., Pautrat, M., Schultz, JA., Tempez, A., Wang, HYJ., Jackson, SN. and Woods, AS., Matrix-implanted laser desorption/ionization mass spectrometry. (2004). *ANAL CHEM*, **76**, 7288-7293.
188. Kawasaki, H., Sugitani, T., Watanabe, T., Yonezawa, T., Moriwaki, H. and Arakawa, R., Layer-by-layer self-assembled multilayer films of gold nanoparticles for surface-assisted laser desorption/ionization mass spectrometry. (2008). *ANAL CHEM*, **80**, 7524-7533.
189. Sonderegger, H., Rameshan, C., Lorenz, H., Klauser, F., Klerks, M., Rainer, M., Bakry, R., Huck, CW. and Bonn, GK., Surface-assisted laser desorption/ionization-mass spectrometry using TiO<sub>2</sub>-coated steel targets for the analysis of small molecules. (2011). *ANAL BIOANAL CHEM*, **401**, 1963-1974.
190. Lachheb, H., Puzenat, E., Houas, A., Ksibi, M., Elaloui, E., Guillard, C. and Herrmann, JM., Photocatalytic degradation of various types of dyes (Alizarin S, Crocein Orange G, Methyl Red, Congo Red, Methylene Blue) in water by UV-irradiated titania. (2002). *APPL CATAL B-ENVIRON*, **39**, 75-90.
191. Knochenmuss, R., Ion formation mechanisms in UV-MALDI. (2006). *ANALYST*, **131**, 966-986.
192. Ludemann, H., Redmond R., and Hillenkamp, F., Singlet-singlet annihilation in ultraviolet matrix-assisted laser desorption/ionization studied by fluorescence spectroscopy. (2002). *RAPID COMMUN MASS SP*, **16**, 1287-1294.
193. Horneffer, V., Dreisewerd, K., Ludemann, HC., Hillenkamp, F., Lage, M. and Strupat, K., Is the incorporation of analytes into matrix crystals a prerequisite for matrix-assisted laser desorption/ionization mass spectrometry? A study of five

- positional isomers of dihydroxybenzoic acid. (1999). *INT J MASS SPECTROM*, **185**, 859-870.
194. Michael, LG. and Caprioli, RM., Ionization Methods, in *Encyclopedia of mass spectrometry*, Armentrout, P. and Caprioli, RM. Editors. 2007, Elsevier: Amsterdam ; Boston.
195. Setz, P. and Knochenmuss, R., Exciton mobility and trapping in a MALDI matrix. (2005). *J PHYS CHEM A*, **109**, 4030-4037.
196. Vertes, A., Balazs, L. and Gijbels, R., Matrix-Assisted Laser Desorption/Ionization Peptides in Transmission Geometry. (1990). *RAPID COMMUN MASS SP*, **4**, 263-266.
197. Johnson, R., Models for Matrix-Assisted Laser Desorption/Ionization by a laser-pulse. (1994). *INT J MASS SPECTROM*, **139**, 25-38.
198. Bencsura, A., Navale, V., Sadeghi, M. and Vertes, A., Matrix-guest energy transfer in matrix-assisted laser desorption. (1997). *RAPID COMMUN MASS SP*, **11**, 679-682.
199. Zhigilei, L. and Garrison, B., Microscopic mechanisms of laser ablation of organic solids in the thermal and stress confinement irradiation regimes. (2000). *J APPL PHYS*, **88**, 1281-1298.
200. Dreisewerd, K., Schurenberg, M., Karas, M. and Hillenkamp, F., Influence of the laser intensity and spot size on the desorption of molecules and ions in Matrix-Assisted Laser Desorption/Ionization with a uniform beam profile. (1995). *INT J MASS SPECTROM*, **141**, 127-148.
201. Vogel, A. and Venugopalan, V., Mechanisms of pulsed laser ablation of biological tissues. (2003). *CHEM REV*, **103**, 577-644.
202. Karas, M. and Kruger, R., Ion formation in MALDI: The cluster ionization mechanism. (2003). *CHEM REV*, **103**, 427-439.
203. Mukamel, S. and Abramavicius, D., Many-body approaches for simulating coherent nonlinear spectroscopies of electronic and vibrational excitons. (2004). *CHEM REV*, **104**, 2073-2098.
204. Ehring, H., Karas, M. and Hillenkamp, F., Role of photoionization and photochemistry in ionization processes of organic-molecules and relevance for Matrix-Assisted Laser Desorption/Ionization mass-spectrometry. (1992). *ORG MASS SPECTROM*, **27**, 472-480.
205. Ehring, H. and Sundqvist, B., Studies of the MALDI process by luminescence spectroscopy. (1995). *J MASS SPECTROM*, **30**, 1303-1310.

206. Karas, M., Gluckmann, M. and Schafer, J., Ionization in matrix-assisted laser desorption/ionization: singly charged molecular ions are the lucky survivors. (2000). *J MASS SPECTROM*, **35**, 1-12.
207. Krutchinsky, A., Dolguine, A. and Khodorkovski, M., Matrix-Assisted Laser Desorption/Ionization of neutral clusters composed of matrix and analyte molecules. (1995). *ANAL CHEM*, **67**, 1963-1967.
208. Pshenichnyuk, S., Asfandiarov, NL., Falko, VS. and Lukin, VG., Temperature dependencies of negative ions formation by capture of low-energy electrons for some typical MALDI matrices. (2003). *INT J MASS SPECTROM*, **227**, 259-272.
209. Kruger, R., Pfenninger, A., Fournier, I., Gluckmann, M. and Karas, M., Analyte incorporation and ionization in matrix-assisted laser desorption/ionization visualized by pH indicator molecular probes. (2001). *ANAL CHEM*, **73**, 5812-5821.
210. Karbach, V. and Knochenmuss, R., Do single matrix molecules generate primary ions in ultraviolet matrix-assisted laser desorption/ionization. (1998). *RAPID COMMUN MASS SP*, **12**, 968-974.
211. Chen, X., Carroll, J. and Beavis, R., Near-ultraviolet-induced matrix-assisted laser desorption/ionization as a function of wavelength. (1998). *J AM SOC MASS SPECTR*, **9**, 885-891.
212. Mowry, C. and Johnston, M., Simultaneous detection of ions and neutrals produced by Matrix-Assisted Laser-Desorption. (1993). *RAPID COMMUN MASS SP*, **7**, 569-575.
213. Quist, A., Huthfehre, T. and Sundqvist, B., Total yield measurements in Matrix-Assisted Laser-Desorption using a quartz-crystal microbalance. (1994). *RAPID COMMUN MASS SP*, **8**, 149-154.
214. Carr, S. and Cassady, C., Reactivity and gas-phase acidity determinations of small peptide ions consisting of 11 to 14 amino acid residues. (1997). *J MASS SPECTROM*, **32**, 959-967.
215. Harrison, A., The gas-phase basicities and proton affinities of amino acids and peptides. (1997). *MASS SPECTROM REV*, **16**, 201-217.
216. Mormann, M., Bashir, S. Derrick, PJ. and Kuck, D., Gas-phase basicities of the isomeric dihydroxybenzoic acids and gas-phase acidities of their radical cations. (2000). *J AM SOC MASS SPECTR*, **11**, 544-552.
217. Burton, RD., Watson, CH. Eyler, JR. Lang, GL. Powell, DH. and Avery, MY., Proton affinities of eight matrices used for matrix-assisted laser desorption/ionization. (1997). *RAPID COMMUN MASS SP*, **11**, 443-446.

218. Breuker, K., Knochenmuss, R. and Zenobi, R., Gas-phase basicities of deprotonated matrix-assisted laser desorption/ionization matrix molecules. (1999). *INT J MASS SPECTROM*, **184**, 25-38.
219. Zenobi, R. and Knochenmuss, R., Ion formation in MALDI mass spectrometry. (1998). *MASS SPECTROM REV*, **17**, 337-366.
220. Macha, S., McCarley, T. and Limbach, P., Influence of ionization energy on charge-transfer ionization in matrix-assisted laser desorption/ionization mass spectrometry. (1999). *ANAL CHIM ACTA*, **397**, 235-245.
221. McCarley, T., McCarley, R. and Limbach, P., Electron transfer ionization in matrix assisted laser desorption/ionization mass spectrometry. (1998). *ANAL CHEM*, **70**, 4376-4379.
222. Zubarev, RA., Horn, DM., Fridriksson, EK., Kelleher, NL., Kruger, NA., Lewis, MA., Carpenter, BK. and McLafferty, FW., Electron capture dissociation for structural characterization of multiply charged protein cations. (2000). *ANAL CHEM*, **72**, 563-573.
223. Frankevich, V., Knochenmuss, R. and Zenobi, R., The origin of electrons in MALDI and their use for sympathetic cooling of negative ions in FTICR. (2002). *INT J MASS SPECTROM*, **220**, 11-19.
224. McCombie, G., Staab, D., Stoeckli, M. and Knochenmuss, R., Spatial and spectral correlations in MALDI mass spectrometry images by clustering and multivariate analysis. (2005). *ANAL CHEM*, **77**, 6118-6124.
225. Beavis, R. and Chait, B., High-accuracy molecular mass determination of proteins using matrix-assisted laser desorption mass-spectrometry. (1990). *ANAL CHEM*, **62**, 1836-1840.
226. Allwood, DA., Dreyfus, RW., Perera, IK. and Dyer, PE., UV optical absorption of matrices used for matrix-assisted laser desorption/ionization. (1996). *RAPID COMMUN MASS SP*, **10**, 1575-1578.
227. Puretzky, A. and Geohegan, D., LIF imaging and gas-phase diagnostics of laser desorbed MALDI-matrix plumes. (1998). *APPL SURF SCI*, **127**, 248-254.
228. Yau, PY., Chan, TWD., Cullis, PG., Colurn, AW. and Derrick, PJ., Threshold fluences for production of positive and negative-ions in matrix-assisted laser desorption/ionization using liquid and solid matrices. (1993). *CHEM PHYS LETT*, **202**, 93-100.
229. Westmacott, G., Ens, W., Hillenkamp, F., Dreisewerd, K. and Schurenberg, M., The influence of laser fluence on ion yield in matrix-assisted laser desorption ionization mass spectrometry. (2002). *INT J MASS SPECTROM*, **221**, 67-81.

230. Ens, W., Mao, Y., Mayer, F. and Standing, KG., Properties of matrix-assisted laser desorption – measurements with a time-to-digital converter. (1991). *RAPID COMMUN MASS SP*, **5**, 117-123.
231. Dreisewerd, K., Schurenberg, M., Karas, M. and Hillenkamp, F., Matrix-assisted laser desorption/ionization with nitrogen lasers of different pulse widths. (1996). *INT J MASS SPECTROM*, **154**, 171-178.
232. Wang, B., Bahr, U., Dreisewerd, K., Karas, M. and Hillenkamp, F., Gas-phase cationization and protonation of neutrals generated by matrix-assisted laser desorption. (1993). *J AM SOC MASS SPECTR*, **4**, 393-398.
233. Kussmann, M., Nordhoff, E., Rahbeknielsen, H., Haebel, S., Rossellarsen, M., Jakobsen, L., Gobom, J., Mirgorodskaya, E., KrollKristensen, A., Palm, L. and Roepstorff, P., Matrix-assisted laser desorption/ionization mass spectrometry sample preparation techniques designed for various peptide and protein analytes. (1997). *J MASS SPECTROM*, **32**, 593-601.
234. Cohen, S. and Chait, B., Influence of matrix solution conditions on the MALDI-MS analysis of peptides and proteins. (1996). *ANAL CHEM*, **68**, 31-37.
235. Bornsen, KO., Gass, MAS., Bruin, GJM., vonAdrichem, JHM., Biro, MC., Kresbach, GM. and Ehrat, M., Influence of solvents and detergents on matrix-assisted laser desorption/ionization mass spectrometry measurements of proteins and oligonucleotides. (1997). *RAPID COMMUN MASS SP*, **11**, 603-609.
236. Gluckmann, M., Pfenninger, A., Kruger, R., Thierolf, M., Karas, M., Horneffer, V., Hillenkamp, F. and Strupat, K., Mechanisms in MALDI analysis: surface interaction or incorporation of analytes? (2001). *INT J MASS SPECTROM*, **210**, 121-132.
237. Canham, L., Silicon quantum wire array fabrication by electrochemical and chemical dissolution of wafers. (1990). *APPL PHYS LETT*, **57**, 1046-1048.
238. Kovalev, D., Polisski, G., BenChorin, M., Diener, J. and Koch, F., The temperature dependence of the absorption coefficient of porous silicon. (1996). *J APPL PHYS*, **80**, 5978-5983.
239. Law, K. and Larkin, J., Recent advances in SALDI-MS techniques and their chemical and bioanalytical applications. (2011). *ANAL BIOANAL CHEM*, **399**, 2597-2622.
240. Maus, M., Gantefor, G. and Eberhardt, W., The electronic structure and the band gap of nano-sized Si particles: competition between quantum confinement and surface reconstruction. (2000). *APPL PHYS A-MATER*, **70**, 535-539.



241. Luo, G., Chen, Y., Siuzdak, G. and Vertes, A., Surface modification and laser pulse length effects on internal energy transfer in DIOS. (2005). *J PHYS CHEM B*, **109**, 24450-24456.
242. Nordstrom, A., Apon, JV., Uritboonthal, W., Go, EP. and Siuzdak, G., Surfactant-enhanced desorption/ionization on silicon mass spectrometry. (2006). *ANAL CHEM*, **78**, 272-278.
243. Alimpiev, S., Nikiforov, S., Karavanskii, V., Minton, T. and Sunner, J., On the mechanism of laser-induced desorption-ionization of organic compounds from etched silicon and carbon surfaces. (2001). *J PHYS CHEM-US*, **115**, 1891-1901.
244. Luo, G., Chen, Y., Daniels, H., Dubrow, R. and Vertes, A., Internal energy transfer in laser desorption/ionization from silicon nanowires. (2006). *J PHYS CHEM B*, **110**, 13381-13386.
245. Heuberger, M., Zach, M. and Spencer, N., Density fluctuations under confinement: When is a fluid not a fluid? (2001). *SCIENCE*, **292**, 905-908.
246. Alimpiev, S., Grechnikov, A., Sunner, J., Karavanskii, V., Simanovsky, Y., Zhabin, S. and Nikiforov, S., On the role of defects and surface chemistry for surface-assisted laser desorption ionization from silicon. (2008). *J CHEM PHYS*, **128**, 1-19.
247. Chen, YF., Chen, HY., Aleksandrov, A. and Orlando, TM., Roles of water, acidity, and surface morphology in surface-assisted laser desorption/ionization of amino acids. (2008). *J PHYS CHEM C*, **112**, 6953-6960.
248. Li, Q., Ricardo, A., Benner, SA., Winefordner, JD. and Powell, DH., Desorption/ionization on porous silicon mass spectrometry studies on pentose-borate complexes. (2005). *ANAL CHEM*, **77**, 4503-4508.
249. Peterson, D.S., Matrix-free methods for laser desorption/ionization mass spectrometry. (2007). *MASS SPECTROM REV*, **26**, 19-34.
250. Okuno, S., Nakano, M., Matsubayashi, G., Arakawa, R. and Wada, Y., Reduction of organic dyes in matrix-assisted laser desorption/ionization and desorption/ionization on porous silicon. (2004). *RAPID COMMUN MASS SP*, **18**, 2811-2817.
251. Wong, C. and Chan, T., Cationization processes in matrix-assisted laser desorption/ionization mass spectrometry: Attachment of divalent and trivalent metal ions. (1997). *RAPID COMMUN MASS SP*, **11**, 513-519.
252. Nakajima, A., Itakura, T., Watanabe, S. and Nakayama, N., Photoluminescence of porous Si, oxidized then deoxidized chemically. (1992). *APPL PHYS LETT*, **61**, 46-48.

253. Pusel, A., Wetterauer, U. and Hess, P., Photochemical hydrogen desorption from H-terminated silicon (111) by VUV photons. (1998). *PHYS REV LETT*, **81**, 645-648.
254. Timoshenko, V., Dittrich, T., Sieber, I., Rappich, J., Kamenev, BV. and Kashkarov, PK., Laser-induced melting of porous silicon. (2000). *PHYS STATUS SOLIDA*, **182**, 325-330.
255. Herino, R., Perio, A., Barla, K. and Bomchil, G., Microstructure of porous silicon and its evolution with temperature. (1984). *MATER LETT*, **2**, 519-523.
256. Broughton, J. and Li, X., Phase-diagram of silicon by molecular-dynamics. (1987). *PHYS REV B*, **35**, 9120-9127.
257. Northen, TR., Woo, HK., Northen, MT., Nordstrom, A., Uritboonthail, W., Turner, KL. and Siuzdak, G., High surface area of porous silicon drives desorption of intact molecules. (2007). *J AM SOC MASS SPECTR*, **18**, 1945-1949.
258. Chen, Y. and Vertes, A., Adjustable fragmentation in laser desorption/ionization from laser-induced silicon microcolumn arrays. (2006). *ANAL CHEM*, **78**, 5835-5844.
259. Zou, J. and Balandin, A., Phonon heat conduction in a semiconductor nanowire. (2001). *J APPL PHYS*, **89**, 2932-2938.
260. Sokolov, V. and Shelykh, A., Some characteristics of porous silicon (reflection, scattering, refractive index, microhardness). (2008). *TECH PHYS LETT*, **34**, 196-198.
261. Trauger, SA., Go, EP., Shen, ZX., Apon, JV., Compton, BJ., Bouvier, ESP., Finn, MG. and Siuzdak, G., High sensitivity and analyte capture with desorption/ionization mass spectrometry on silylated porous silicon. (2004). *ANAL CHEM*, **76**, 4484-4489.
262. Crouch, CH., Carey, JE., Warrender, JM., Aziz, MJ., Mazur, E. and Genin, FY., Comparison of structure and properties of femtosecond and nanosecond laser-structured silicon. (2004). *APPL PHYS LETT*, **84**, 1850-1852.
263. Wu, C., Crouch, CH., Zhao, L., Carey, JE., Younkin, R., Levinson, JA., Mazur, E., Farrell, RM., Gothoskar, P. and Karger, A., Near-unity below-band-gap absorption by microstructured silicon. (2001). *APPL PHYS LETT*, **78**, 1850-1852.
264. Arakawa, R., Shimomae, Y., Morikawa, H., Ohara, K. and Okuno, S., Mass spectrometric analysis of low molecular mass polyesters by laser desorption/ionization on porous silicon. (2004). *J MASS SPECTROM*, **39**, 961-965.

265. Chin, S., Multiphoton ionization of molecules.(1971). *PHYS REV A-GEN PHYS*, **4**, 992-996.
266. Biaggioni, I., Paul, S., Puckett, A. and Arzubiaga, C., Caffeine and theophylline as adenosine receptor anagonists in humans. (1991). *J PHARMACOL EXP THER*, **258**, 588-593.
267. Lee, K., Chiang, CK. Lin, ZH. and Chang, HT., Determining enediol compounds in tea using surface-assisted laser desorption/ionization mass spectrometry with titanium dioxide nanoparticle matrices. (2007). *RAPID COMMUN MASS SP*, **21**, 2023-2030.
268. Hanna, SJ., Campuzano-Jost, P., Simpson, EA., Robb, DB., Burak, I., Blades, MW., Hepburn, JW. and Bertram, AK., A new broadly tunable (7.4-10.2 eV) laser based VUV light source and its first application to aerosol mass spectrometry. (2009). *INT J MASS SPECTROM*, **279**, 134-146.
269. Kim, D., Kim, HM., Yang, KY., Kim, SK. and Kim, NJ., Molecular beam resonant two-photon ionization study of caffeine and its hydrated clusters. (2008). *J CHEM PHYS*, **128**, 134311-134316.
270. Lorkiewicz, P. and M. Yappert, Titania Microparticles and Nanoparticles as Matrixes for in Vitro and in Situ Analysis of Small Molecules by MALDI-MS. (2009). *ANAL CHEM*, **81**, 6596-6603.
271. Chen, Z., Lee, T. and Bosman, G., Electrical band-gap of porous silicon. (1994). *APPL PHYS LETT*, **64**, 3446-3448.
272. Vernardou, D., Drosos, H., Spanakis, E., Koudoumas, E., Savvakis, C. and Katsarakis, N., Electrochemical and photocatalytic properties of WO<sub>3</sub> coatings grown at low temperatures.(2011). *J MATER CHEM*, **21**, 513-517.
273. Zheng, LX., Cheng, H., Liang, FX., Shu, SW., Tsang, CK., Li, H., Lee, ST. and Li, YY., Porous TiO<sub>2</sub> Photonic Band Gap Materials by Anodization.(2012). *J PHYS CHEM C*, **116**, 5509-5515.
274. Jafari, GR., Saberi, AA., Azimirad, R., Moshfegh, AZ. and Rouhani, S., The effect of annealing temperature on the statistical properties of WO<sub>3</sub> surface. (2006). *J STAT MECH-THEORY E*, **9**, 9-17.
275. Yu, IG., Kim, YJ., Kim, HJ., Lee, C. and Lee, WI., Size-dependent light-scattering effects of nanoporous TiO<sub>2</sub> spheres in dye-sensitized solar cells. (2011). *J MATER CHEM*, **21**, 532-538.
276. Sokolov, V. and Shelykh, A., Some characteristics of porous silicon (reflection, scattering, refractive index, microhardness). ( 2008). *TECH PHYS LETT*, **34**, 196-198.

277. Gonzalez-Borrero, PP., Sato, F., Medina, AN., Baesso, ML., Bento, AC., Baldissera, G., Persson, C., Niklasson, GA., Granqvist, CG. and da Silva, AF., Optical band-gap determination of nanostructured WO<sub>3</sub> film. (2010). *APPL PHYS LETT*, **96**, 1-3
278. Ofir, A., Dor, S., Grinis, L., Zaban, A., Dittrich, T. and Bisquert, J., Porosity dependence of electron percolation in nanoporous TiO<sub>2</sub> layers. (2008). *J CHEM PHYS*, **128**.
279. Kang, SH., Choi, SH., Kang, MS., Kim, JY., Kim, HS., Hyeon, T. and Sung, YE., Nanorod-based dye-sensitized solar cells with improved charge collection efficiency. (2008). *ADV MATER*, **20**, 54-60.
280. Shinoda, H., Nakajima, T., Ueno, K. and Koshida, N., Thermally induced ultrasonic: emission from porous silicon. (1999). *NATURE*, **400**, 853-855.
281. Wang, HT., Xu, YB., Goto, M., Tanaka, Y., Yamazaki, M., Kasahara, A. and Tosa, M., Thermal conductivity measurement of tungsten oxide nanoscale thin films. (2006). *MATER TRANS*, **47**, 1894-1897.
282. Tan, Z., Wang, L. and Shi, Q., Study of heat capacity enhancement in some nanostructured materials. (2009). *PURE APPL CHEM*, **81**, 1871-1880.
283. Roth, J., Protein N-glycosylation along the secretory pathway: Relationship to organelle topography and function, protein quality control, and cell interactions. (2002). *CHEM REV*, **102**, 285-303.
284. Shi, YJ., Hu, XK., Mao, DM., Dimov, SS. and Lipson, RH., Analysis of xanthate derivatives by vacuum ultraviolet laser time-of-flight mass spectrometry. (1998), *ANAL CHEM*, **70**, 4534-4539.
285. Shi, Y. J.; Consta, S.; Das, A. K.; Mallik, B.; Lacey, D.; Lipson, R. H., A 118 nm vacuum ultraviolet laser. (2002). *J CHEM PHYS*, **116**, 6990-6999.
286. Shi, Y. and Lipson, R., An overview of organic molecule soft ionization using vacuum ultraviolet laser radiation. (2005). *CAN J CHEM*, **83**, 1891-1902.

## VITA

**Name: Jin Li**

**Post-secondary Education and Degrees:**

Ph.D. candidate, The University of Western Ontario, 2010-2012

M.Sc. degree, The University of Western Ontario, 2006-2008

M.Sc. degree, Wuhan University, China, 1996 - 1999

Bachelor degree, Hubei University, China, 1991- 1994

**Related Work Experience:**

Teaching Assistant, University of Western Ontario, 2010-2012 & 2006 – 2008

Research Assistant, Dalian Chemistry and Physics Research Institute, Chinese Academy of Sciences, China, 2004-2006

Lecturer, Preventive Medicine Department, Guangdong College of Pharmacy, China, 1999 – 2004

**Publications:**

1. Li, J., Hu, X. K. and Lipson, R. H., On-chip enrichment and analysis of peptide subsets using maleimide-functionalized fluoruous affinity biochip and nanostructure initiator mass spectrometry. *To be submitted.*
2. Li, J., Hu, X. K. and Lipson, R. H., Lable-free and matrix-free kinase activity assay and inhibitor screening using fluoruous-affinity NIMS chip. *To be submitted.*
3. Li, J. and Lipson, R. H., Study of Surface Assisted Laser Desorption/Ionization mechanism by measuring the ion signal as a function of laser fluence. *In process.*
4. Li, J. and Lipson, R. H., Analyses of pharmaceutical compounds and peptides using visible-NIMS. *In process.*

5. Li, J. and Lipson, R. H., Measurement of enantiomeric excess by kinetic resolution and NIMS-MS. *In process*.
6. Li, J.; Lu, C.; Hu, X. K.; Yang, X. J.; Loboda, A. V.; Lipson, R. H., Nanostructured porous silicon by laser assisted electrochemical etching. *International Journal of Mass Spectrometry*.(2009), **285**, 137-142.
7. Li, J., The preparation of porous microcolumn arrays of silicon, and post-ionization of neutral particles from DIOS-MS. Faculty of Graduate Studies, The University of Western Ontario: London, Ont., **2008**.
8. Hu, X.K., Lacey, D. Li, J. Yang, C. Y., Loboda, A.V. and Lipson, R.H., Visible wavelength MALDI using Coumarin laser dyes, *International Journal of Mass Spectrometry*. (2008), **278**, 69-74.
9. Wang, H., Li, J., Yang, TX. and Zhang, HS., N-Hydroxysuccinimidyl Fluorescein-O-Acetate for Precolumn Fluorescence Derivatization of Amino Acids and Oligopeptides in Liquid Chromatography, *Journal of Chromatographic Science*. (2001), **39**, 365-369.
10. Wang, H., Li, J., Yang, TX. and Zhang, HS., N-Hydroxysuccinimidyl Fluorescein-O-acetate as a Fluorescent Derivatizing Reagent for Catecholamines in Liquid Chromatography, *Analytical Biochemistry*. (2000), **281**, 15-20.
11. Wang, H., Li, J., Liu, X. and Zhang, HS., N-hydroxysuccinimidyl fluorescein-O-acetate as a highly fluorescent derivatizing reagent for aliphatic amines in liquid chromatography, *Analytica Chimica Acta*. (2000), **423**, 77-83.

#### **Posters and Presentation:**

1. Li, J. and Lipson, R. H., On-chip enrichment and NIMS analysis of peptide subsets and a kinase activity assay using a maleimide-functionalized fluoruous affinity biochip. 95<sup>th</sup> Conference of the Canadian Society of Chemistry, Calgary, Alberta, May26-30, **2012**.
2. Li, J., Hu, XK. and Lipson, RH., Nanostructure-initiator mass spectrometry for analysis of peptides, *NanoOntario 2010*, The University of Western Ontario, London, Ontario, May 16-18, **2010**.

3. Li, J., Hu, XK., Lu, C. and Lipson, RH., The preparation of porous microcolumn arrays of silicon, and post-ionization of neutral particles from DIOS-MS, *Symposium on Chemical Physics 2008*, Waterloo, Ontario, Canada, Nov. 7-9, **2008**.
4. Li, J. and Lipson, RH., The preparation of porous microcolumn arrays of silicon, and its application on DIOS-MS, *The 23<sup>rd</sup> WESTERN RESEARCH FORUM 2011*, The University of Western Ontario, London, Ontario, Feb 26<sup>th</sup>, **2011**, Scheduled talk.
5. Lipson, RH. and Li, J., Laser Desorption Ionization Mechanisms and Applications for Mass Spectrometry and Spectroscopy. 95<sup>th</sup> Conference of the Canadian Society of Chemistry, Calgary, Alberta, May 26-30, **2012**. Invited talk.